Design and Development of Ruthenium-Based Prussian Blue Analogue–Derived Bimetallic and Chalcogenide Electrocatalysts for Hydrogen Evolution

By

Manisha Sadangi

CHEM11202104004

National Institute of Science Education and Research (NISER), Bhubaneswar, Odisha-752050

A thesis submitted to the

Board of Studies in Chemical Sciences

In partial fulfillment of requirements for the Degree of

DOCTOR OF PHILOSOPHY
of
HOMI BHABHA NATIONAL INSTITUTE

December, 2025

Homi Bhabha National Institute[1]

Recommendations of the Viva Voce Committee

As members of the Viva Voce Committee, we certify that we have read the dissertation prepared by Manisha Sadangi entitled "Design and Development of Ruthenium-Based Prussian Blue Analogue–Derived Bimetallic and Chalcogenide Electrocatalysts for Hydrogen Evolution" and recommend that it may be accepted as fulfilling the thesis requirement for the award of Degree of Doctor of Philosophy.

S. No.	Doctoral Committee	Name	Signature	Date	In-Person/Online
1.	Chairman	Prof. A. Srinivasan		15.04.26	In-Person
2.	Guide/Convener	Prof. J. N. Behera		15.04.26	In-Person
3.	Co-Guide (if any)				
4.	Examiner	Prof. D. Pradhan		15-04-26	Online
5.	Member - 1	Prof. M. Sarkar		15.04.26	In-Person
6.	Member - 2	Dr. C. S. Purohit		15/04/26	In-Person
7.	Member - 3	Dr. S. Patra		15/4/2026	In-Person

Final approval and acceptance of this thesis is contingent upon the candidate's submission of the final copies of the thesis to HBNI.

I hereby certify that I have read this thesis prepared under my direction and recommend that it may be accepted as fulfilling the thesis requirement.

Date: 15/04/26

Place: NISER, Bhubaneswar

Signature

Guide: Prof. J. N. Behera

[1] This page is to be included only for final submission after successful completion of viva voce.

STATEMENT BY AUTHOR

This dissertation has been submitted in partial fulfillment of requirements for an advanced degree at Homi Bhabha National Institute (HBNI) and is deposited in the Library to be made available to borrowers under rules of the HBNI.

Brief quotations from this dissertation are allowable without special permission, provided that accurate acknowledgement of source is made. Requests for permission for extended quotation from or reproduction of this manuscript in whole or in part may be granted by the Competent Authority of HBNI when in his or her judgment the proposed use of the material is in the interests of scholarship. In all other instances, however, permission must be obtained from the author.

Manisha Sadangi 15/04/2026

Manisha Sadangi

DECLARATION

I, hereby declare that the investigation presented in the thesis has been carried out by me. The work is original and has not been submitted earlier as a whole or in part for a degree / diploma at this or any other Institution / University.

Manisha Sadangi 15/04/2026

Manisha Sadangi

CERTIFICATION ON ACADEMIC INTEGRITY

Undertaking by the Student:

1. I **Manisha Sadangi**, HBNI Enrolment No**. CHEM11202104004** hereby undertake that the Thesis, titled "**Design and Development of Ruthenium-Based Prussian Blue Analogue-Derived Bimetallic and Chalcogenide Electrocatalysts for Hydrogen Evolution**" is prepared by me and is the original work undertaken by me.
2. I also hereby undertake that this document has been duly checked through a plagiarism detection tool and the document is found to be plagiarism free as per the guidelines of the Institute/UGC.
3. I am aware and undertake that if plagiarism is detected in my thesis at any stage in the future, suitable penalty will be imposed as applicable as per the guidelines of the Institute/UGC.

Manisha Sadangi 15/04/2026
Signature of the Student with date

Endorsed by the Thesis Supervisor:

4. I certify that the thesis written by the Researcher is plagiarism-free as mentioned above by the student.

15/04/2026
Signature of the Thesis Supervisor with Date

Name : Prof. J. N. Behera
Designation : Professor
Department : School of Chemical Sciences
Name of the CI/ OCC: NISER Bhubaneswar, Odisha-752050

List of Publications Arising from the Thesis

Journals

(a) Published

[#]**1.** "Ruthenium-doped cobalt sulphide electrocatalyst derived from a ruthenium–cobalt Prussian blue analogue (RuCo-PBA) for an enhanced hydrogen evolution reaction (HER)", **Manisha Sadangi** and J. N. Behera,* *Dalton Trans*., **2024**, *53*, 6667-6675.

[#]**2.** "Ru Prussian blue analogue-derived Ru nanoparticles composited with a trace amount of Pt as an efficacious electrocatalyst for the hydrogen evolution reaction", **Manisha Sadangi,** C. Chakravarty, J. Bhattacharjee* and J. N. Behera,* *Dalton Trans*., **2024**, *53*, 16384-16396.

[#]**3.** "Ruthenium cobalt nanoalloy derived from its Prussian blue analogue (RuCo-PBA) for efficient hydrogen evolution electrocatalysis", **Manisha Sadangi** and J. N. Behera,* *ChemCatChem.*, **2025**, *17*, e202500178 (1-10).

4. "Vanadium-doped cobalt selenide: an efficient bifunctional electrocatalyst for overall water splitting", A. Sahu, **Manisha Sadangi** and J. N. Behera,* *Sustain. Energy Fuels*, **2025**, *9*, 2718-2728.

5. "Synthesis of a paddlewheel-based 3D Co-MOF and its Co_3Se_4-derived composite as an electrocatalyst for water oxidation", L. K. Pradhan, R. K. Tiwari, **Manisha Sadangi** and J. N. Behera,* *Inorg. Chem.,* **2025**, *64*, 20308-20319.

6. "Tailoring supercapacitor performance via sulfur engineering in ternary CoNiMoS electrodes", T. T. Mishra, **Manisha Sadangi**, J. N. Behera,* M. Chakraborty* and D. Roy,* *Sustain. Energy Fuels*, **2026,** *10*, 364-374.

7. "Unraveling multicopper [Cu_3] and [Cu_6] clusters with Rare μ_3-sulfato and linear μ_2-oxido-bridges as potent antibiofilm agents against multidrug-resistant Staphylococcus aureus", S. Sujan, S. Bandyopadhyay, C. Sarkar, I. Das, A. Gupta, **Manisha Sadangi**, S. Mondal, M. Banerjee, G. Vijaykumar, J. N. Behera, S. Konar, S. Mandal,* M. Bera,* *ACS Appl. Bio Mater.,* **2024**, *7*, 2423-2449.

(b) Communicated

[#]**1.** "Prussian blue analogue (PBA)–derived Ru–$NiSe_2$ nanogranules as robust and efficient electrocatalysts for alkaline hydrogen evolution", **Manisha Sadangi** and J. N. Behera,* *ACS Appl. Energy Mater.,* **2026.** *(Accepted)*

([#] Pertaining to The Thesis)

Conferences

1. 1st HBNI INTERACTION MEETING in Chemical Sciences held during 18-20th January 2023 at NISER Bhubaneswar, Odisha, India. **(Poster Presentation)**

2. Emergent Materials for Energy and Environment (EMEE-2023) held during 4-5th March 2023 at IIT Roorkee, Uttarakhand, India. **(Poster Presentation)**

3. High End Workshop on ELECTROCHEMICAL INVESTIGATION TECHNIQUES (WEIT-2024) held during 1st-7th January 2024 at NIT Rourkela, Odisha, India. **(Participated)**

4. First DAE Conclave 2024 held during 22nd-26th of October 2024 at NISER Bhubaneswar, Odisha, India. **(Poster Presentation)**

5. Frontiers in Chemical Sciences-2024 (FICS-2024) held during 2nd-4th December 2024 at IIT Guwahati, Assam, India. **(Poster Presentation)**

6. DAE-BRNS Conference on Electrochemistry in Industry, Health and Environment (EIHE–2025) held during 21st-25th January 2025 at BARC Mumbai, Maharashtra, India. **(Poster Presentation)P**

Manisha Sadangi 15/04/2026

Manisha Sadangi

Dedicated to

(My Beloved Family)

ACKNOWLEDGEMENTS

I want to express my gratitude to **Prof. Jogendra Nath Behera, my supervisor**, for his continuous patience, encouragement, support, and freedom to think freely.

I am thankful to **Prof. Hirendra Nath Ghosh** (Director-NISER), **Prof. Sudhakar Panda** (Former Director-NISER), for the laboratory facilities and financial support.

I thank my Doctoral committee members, **Prof. A. Srinivasan**, **Dr. C. S. Purohit**, **Prof.**

Moloy Sarkar, **Dr. Srikanta Patra** and all the faculty members in SCS.

I would like to thank **Dr. Arun Kumar**, **Dr. Priyanka Pandey** and all the **SCS staff members.**

I warmly thank our collaborator, **Dr. Joydeep Bhattacharjee** (SPS, NISER).

I would like to thank all the CIS staff members.

I would like to thank all my past and present lab members, Dr. Ranjay K. Tiwari, Dr. Aneeya K. Samantara, Dr. Jiban K. Das, Dr. Rajat K. Tripathy, Dr. Malaya K. Sahoo, Dr. Abhisek Padhy, Dr. Nachiketa Sahu, Litun, Kismat, Ankita, Debayan, Sunil, Goutam Pratik, Prayash, Satya, Ashutosh, Ashish, Abhipsa, Sunita, Arnub, Mubashirah for their continuous support and valuable discussions.

I am grateful to all of my friends for their support and scientific discussions. Above all, I want to thank my family for their care and support throughout this challenging yet amazing journey.

CONTENTS

MOTIVATION AND OBJECTIVE

Fossil fuels continue to be the primary energy source for industrial productions around the world. Environmental pollution and a drastic change in the climate are the dangerous effects of utilising fossil fuels. Finding alternative green fuel sources is crucial since the constantly dwindling fossil fuel supplies have made the energy situation worse. Hydrogen (H_2) has been considered one of the most effective clean energy sources due to its high calorific value and lack of harmful combustion products. Among all the methods currently in operation, electrochemical water splitting is one of the most widely used and effective method for producing hydrogen that is powered by electricity. Pt is a noble metal based electrocatalyst and is regarded as the benchmark electrocatalyst for producing hydrogen by water splitting. The large-scale application is, however, limited by its high price, scarcity, and low abundance. For practical application, it is therefore desirable to create extremely stable and affordable electrocatalysts with significant catalytic performance. Prussian blue analogues (PBAs) are subclass of metal organic frameworks (MOFs) and have gathered enormous attention as a suitable material precursor because of their simple, reliable, and affordable synthesis. The PBA-derived technique is advantageous for the synthesis of various effective nanostructured materials because it optimises the electrochemically active surface area of the electrocatalyst, controls the morphology, increases electrical conductivity, and triggers the catalytic activity. Moreover, Ru-based PBA-derived electrocatalysts exhibit excellent performance towards HER. This is because Ru alters the materials' electronic structures and enhances intrinsic conductivity, charge transfer, electron delocalisation, and reaction kinetics. Furthermore, during the HER process, Ru inclusion reduces the energy barrier of the adsorption/desorption process leading towards the enhancement in the HER performance of the electrocatalysts.

SYNOPSIS

In this thesis, Prussian blue analogue (PBA)-derived nanomaterials are utilised as electrocatalysts for electrochemical hydrogen evolution reaction (HER). The thesis consists of 5 chapters. **Chapter 1** contains the introduction, which explains the rationale for the search for a suitable electrocatalyst for use in the electrochemical HER. **Chapter 2** describes the synthesis techniques and the fundamental characterisation methods of the freshly synthesised electrocatalyst, along with the fundamental electrochemical parameters for the hydrogen evolution reaction. **Chapter 3** demonstrates a detailed study on RuCo-PBA-derived Ru-doped cobalt sulphide i.e. Co_9S_8/Ru nanoparticles as an effective electrocatalyst for HER. **Chapter 4** illustrates the designing of PtRu nanocomposite i.e. Ru@C/Pt from Ru-PBA for HER application. **Chapter 5** represents the synthesis of RuCo-PBA-derived RuCo nanoalloy and its application towards the HER. **Chapter 6** deals with the synthesis of NiRu-PBA-derived Ru incorporated $NiSe_2$ and its application towards the alkaline HER. Lastly, **Chapter 7** is the summary of the present thesis.

Chapter 1: Overview of Electrochemical Hydrogen Evolution Reaction

Worldwide, the main energy source for industrial output is still fossil fuels. The hazardous consequences of using fossil fuels include environmental pollution and a significant shift in the climate. Finding alternative green fuel sources is essential because the energy situation has gotten worse due to the steadily decreasing supply of fossil fuels. Hydrogen (H_2) has been regarded as one of the most efficient clean energy sources due to the absence of hazardous combustion products and its high calorific value. In comparison to all the techniques available, electrochemical water splitting is one of the most popular and efficient electricity-powered hydrogen production

techniques currently in operation. HER can take place in both acidic and alkaline medium. A noble metal-based catalyst Pt is the bench-mark electrocatalyst for hydrogen production through water splitting process. However, its high cost, scarcity, and low abundance restrict its widespread application. Therefore, it is desirable to develop highly stable, reasonably priced electrocatalysts with notable catalytic performance for practical use. Prussian blue analogues (PBAs) are subclass of metal organic frameworks (MOFs) and have gathered enormous attention as a suitable material precursor because of their simple, reliable, and affordable synthesis. Prussian blue analogues (PBAs), a subclass of metal organic frameworks (MOFs), have attracted a lot of interest as a potential material precursor due to their straightforward, reliable, and reasonably priced production. The PBA-derived technique is highly beneficial for the synthesis of various effective nanostructured materials because it controls the morphology, optimises the electrochemically active surface area of the electrocatalyst, triggers the catalytic activity and increases electrical conductivity. All these properties led towards the excellent performance of the electrocatalyst.

Chapter 2: Experimental Methods and Characterisation Techniques

After the synthesis of the materials by utilising a variety of synthesis techniques such as the coprecipitation method, solvothermal method, annealing process etc., they are characterised by using various characterisation techniques. The structure and composition of the materials are determined by powder X-ray diffraction, energy dispersive X-ray spectroscopy, inductively coupled plasma optical emission spectroscopy and X-ray photoelectron spectroscopy. The morphological analysis can be carried out by using the field emission scanning microscopy and transmission electron microscopy. The electrochemical characterisations are done by carrying out the cyclic voltammetry, linear sweep voltammetry, Tafel slope, electrostatic impedance

spectroscopy, chronopotentiometry/chronoamperometry etc. techniques in a three electrode system containing working, reference and counter electrode. After the long-term stability test the structural, compositional and morphological analysis was done to determine the changes occurred in the material during the long-term electrolysis process. Smaller is the value of overpotential, Tafel slope, charge transfer resistance and higher is the value of ECSA, better is the performance of the electrocatalyst towards the process of electrocatalysis.

Chapter 3: Ruthenium doped cobalt sulphide electrocatalyst derived from ruthenium cobalt Prussian blue analogue (RuCo-PBA) for enhanced hydrogen evolution reaction (HER)

In this work we have successfully synthesised RuCo-PBA by a coprecipitation method at the room temperature. Then a series of Ru-doped Co_9S_8 by varying the reaction time from 24 to 48 then to 72 hours were synthesised by using the hydrothermal method. The obtained products thus obtained after 24, 48 and 72 h of reaction time were named as Co_9S_8/Ru@24h, Co_9S_8/Ru@48h and Co_9S_8/Ru@72h respectively. For comparison purpose we have also synthesised bare CoS_x by following the same reaction scheme but replaced RuCo-PBA with $Co(NO_3)_2.6H_2O$. The electrochemical measurement of all the synthesised materials was carried out in a 3-electrode system by taking a sample-modified GCRDE as the working electrode, Ag/AgCl as the reference electrode and Pt as the counter electrode. Among all the synthesised materials Co_9S_8/Ru@48h showed best performance towards the hydrogen evolution reaction by requiring a small value of overpotential i.e. 94 mV to produce the bench-mark current density of 10 mA cm^{-2}. Other materials were found to show poor performance in comparison to Co_9S_8/Ru@48h. Also, it shows a lower Tafel slope value of 84 mV dec^{-1} and a lower charge transfer resistance of 17.5 Ω which indicates towards the faster electrode

kinetics and faster charge transfer reaction at the electrode-electrolyte interface respectively. Additionally, a large value of electrochemically active surface area (431 μF cm^{-2}) was also observed for Co_9S_8/Ru@48h indicating towards the presence of large number of active sites for the desired reaction to take place. It also exhibits long-term durability for 20 hours in the harsh electrolytic environment of 0.5 M H_2SO_4. The post-catalytic data of Co_9S_8/Ru@48h reveals no change in the phase of the material and the FESEM analysis shows slight agglomeration of particles. These analysis shows the robustness of the electrocatalyst. The best performance of the electrocatalyst Co_9S_8/Ru@48h can be attributed to the presence of doped ruthenium in the Co_9S_8. Doping of Ru into Co_9S_8 modifies the electronic environment of the material and enhances the conductivity as well as activated the inherent catalytic activity of the cobalt sulphide. PBA also played an important role by providing the uniform distribution of nanosheet like morphology throughout the surface of the material. This uniform distribution leads towards the exposure of larger number of active sites for the desired reaction to take place. PBA also provided the C and N moiety. These C and N along with the presence of doped Ru facilitates the conductivity and prevents the agglomeration as well as the corrosion of the active species during the long-term electrolysis process. The time-variation also provided the well-defined nanosheet like morphology for Co_9S_8/Ru@48h. The poor performance of the other time varied materials Co_9S_8/Ru@24h and Co_9S_8/Ru@72h can be attributed to presence of slightly and highly agglomerated sheet like morphology respectively. Due to the particle agglomeration large number of active sites get blocked, it is also evident from their poor ECSA i.e. 178 μF cm^{-2} (Co_9S_8/Ru@24h) and 29.1 μF cm^{-2} (Co_9S_8/Ru@72h). The performance of the bare CoS_x was also not up to the mark. Its poor performance is due to the absence of synergy between Ru and Co. Since it was synthesised by using

$Co(NO_3)_2.6H_2O$ and not PBA, it possesses thick agglomerated sheet like morphology which has least number of active sites for the reaction to occur as evident from its lower ECSA value (8.9 μF cm^{-2}). The use of the RuCo-PBA precursor in the hydrothermal approach opens up a new avenue for developing Ru-doped Co_9S_8 material, which excel as outstanding electrocatalysts for H_2 production.

Chapter 4: Ru Prussian blue analogue-derived Ru nanoparticles composited with a trace amount of Pt as an efficacious electrocatalyst for the hydrogen evolution reaction

In this work we have successfully synthesised Ru-PBA by a hydrothermal method. From it we have derived a series of RuPt nanocomposite by first annealing the RuPBA in Ar atmosphere which resulted into Ru@C and then adding a varied concentration of $PtCl_2$ (0.1, 0.5 and 1.0 mmol) to a solution of Ru@C followed by reduction with $NaBH_4$. The obtained composite with 0.1, 0.5 and 1.0 mmol concentration of $PtCl_2$ are termed as $\underline{Ru@C/Pt_{0.1}}$, $Ru@C/Pt_{0.5}$ and $\underline{Ru@C/Pt_{1.0}}$ respectively. The electrochemical analysis was carried out in a 3-electrode system with 0.5 M H_2SO_4 electrolyte. The sample coated GCRDE, Ag/AgCl and graphite rod was taken as the working, reference and counter electrodes respectively. Among all the synthesised materials $\underline{Ru@C/Pt_{0.5}}$ was exhibiting best performance towards the acidic hydrogen evolution reaction. It requires a very low value of overpotential i.e. 32 mV to produce the benchmark current density of 10 mA cm^{-2}. The performance of the catalyst is comparable to that of the state-of-the-art catalyst Pt/C which requires an overpotential of 29 mV to produce 10 mA cm^{-2}. The performance of $\underline{Ru@C/Pt_{0.5}}$ was comparable to that of Pt/C. But it was observed that Pt/C requires larger value of overpotential i.e. 178 mV to produce the higher current density value of 100 mA cm^{-2} in comparison to $\underline{Ru@C/Pt_{0.5}}$ which requires only 140 mV. The Tafel slope was also found to be least for the $\underline{Ru@C/Pt_{0.5}}$

i.e. 26 mV dec^{-1} comparison to all the synthesised material along with the benchmark catalyst Pt/C and commercial RuO_2 as well as RuC. This shows the faster kinetics at the electrode surface. The ECSA of the loaded Pt was also observed to be highest i.e. 205 cm^2 for the Ru@C/$Pt_{0.5}$ indicating towards the larger number of active sites present in the material. Ru@C/$Pt_{0.5}$ also exhibited least value of charge transfer resistance and highest value of turn over frequency (TOF = 5.6 s^{-1}) in comparison to all the synthesised materials suggesting towards the faster charge transfer process at the electrode-electrolyte interface and high efficiency of the electrocatalyst towards the HER respectively. Further, the chronopotentiometry test for 50 hours reveals the high stability of Ru@C/$Pt_{0.5}$ in 0.5 M H_2SO_4. The excellent performance of Ru@C/$Pt_{0.5}$ can be attributed to the synergistic effect between the Pt and Ru which modifies the electronic structure of the material and provides the optimised H adsorption and desorption energies for the HER. Ru@C/$Pt_{0.5}$ was showing remarkable performance when compared to the other concentration varied materials Ru@C/$Pt_{0.1}$ and Ru@C/$Pt_{1.0}$. This is so because when the concentration is low i.e. 0.1 mmol, it's insufficient to bring about the optimised energy required for the process to take place but when the concentration was high i.e. 1.0 mmol, the Pt nanoparticles got agglomerated among themselves and blocked the active sites for the reaction to take place. This was confirmed by their lower ECSA values. Hence a trace amount of Pt is a necessary condition for obtaining an excellent electrocatalyst for HER. This was also proved by the theoretical studies. First-principles computational simulations show that charge retention on Ru close to the Pt Island corners results in electrostatic repulsion, which lowers the binding strength of H at the nearby Ru interstitial fcc sites. However, in line with experimental findings, when Pt islands get bigger, the adsorption of H atoms at the fcc sites begins to stabilise once more due to the softening of phonon modes

surrounding the Pt islands, which raises the overpotential. Additionally, the under-coordinated peripheral Pt atoms block the Ru fcc sites at the edge of the Pt islands, which effectively reduces the amount of active Ru fcc sites by over-binding H atoms strongly to prevent their simple desorption. Hence the trace amount of Pt is a necessary condition for the good performance of the electrocatalyst. Additionally, Ru@C/$Pt_{0.5}$ was showing good performance when compared to Ru@C, this suggests the efficiency of the synergistic interaction between the Ru and Pt. The effective catalysis by Ru@C/$Pt_{0.5}$ described in this work may open the door for such composites to successfully replace Pt/C as the main catalyst, making commercial water splitting economically feasible for widespread use.

Chapter 5: Ruthenium cobalt nanoalloy derived from its Prussian blue analogue (RuCo-PBA) for efficient hydrogen evolution electrocatalysis

In this work we have successfully synthesised a RuCo-PBA by following a coprecipitation method. A series of RuCo-PBA-derived RuCo nanoalloys were synthesised by annealing the mixture of RuCo-PBA with acetylene black (AB) for 3 hours at a temperature ranging from 500-800 °C. The obtained materials are termed as RuCoNA/AB@T, T = 500–800. For comparison purpose Ru-PBA derived Ru nanoparticles i.e. RuNP/AB@600 and Co-PBA derived Co nanoparticles i.e. CoNP/AB@600 were synthesised by following the same reaction procedure. Among all the synthesised electrocatalysts RuCoNA/AB@600 was observed to showing best electrocatalytic performance by requiring only 129 mV of overpotential to produce the bench mark current density in acidic condition of 0.5 M H_2SO_4. RuCoNA/AB@600 also displays least value of Tafel slope (122 mV dec^{-1}) and R_{ct} (18.69 Ω) indicating towards the faster kinetics and faster charge-transfer reaction at the electrode-electrolyte interface respectively. It also exhibits higher value of ECSA suggesting the

presence of large number of active sites for the desired reaction to take place and better performance towards the HER. Additionally, the chronopotentiometry test shows the long-term stability of RuCoNA/AB@600 during 96 hours of electrolysis. The excellent performance of RuCoNA/AB@600 can be attributed to the synergistic effect that arises due to the alloying of Ru and Co which leads to effective change in the electronic structure by causing the d-orbitals to overlap. The use of PBA as a precursor provided both the metal centres simultaneously and no second step for metal incorporation was needed. PBA also provided the uniform distribution of nanogranules like particles throughout the surface of the material, this exposes large number of the active sites for the reaction. Here temperature variation also played a remarkable role by providing well-defined and smaller size of nano granules throughout the surface of the RuCoNA/AB@600. Other temperature varied materials were found to having agglomerated nanogranules like morphology throughout the surface of the material. Due to this aforementioned reason other temperature varied nanoalloys are exhibiting poor HER performance. The PBA along with the AB provided N-doped graphitised C, this enhanced the conductivity of the material and provided stability to the material during the long term chronopotentiometry test in 0.5 M H_2SO_4. The not so good performance of the RuNP/AB@600 and CoNP/AB@600 is attributed to the absence of synergistic effect between the two metal centres. Further the performance of RuCoNA/AB@600 was compared to that of RuCoNA@600 which was synthesised by using the same process but without AB. RuCoNA@600 exhibited poor performance in comparison to RuCoNA/AB@600 due to the absence of N-doped graphitised C which enhances the conductivity of the material as well as creates defects in the material which enhances the electrocatalytic activity of the material. The post-catalytic studies of RuCoNA/AB@600 reveal no change in the phase of the material. The FESEM analysis

also showed only a small agglomeration of the particles. This shows the robustness of the material as an electrocatalyst. The synthesis of RuCoNA/AB@600 through a facile annealing process, which involves the annealing of RuCo-PBA precursor along with acetylene black, creates a new pathway for the development of RuCo nano-alloy with N-doped graphitised carbon, which acts as an exceptional electrocatalyst for the H_2 production.

Chapter 6: Prussian blue analogue (PBA)–derived Ru–$NiSe_2$ nanogranules as robust and efficient electrocatalysts for alkaline hydrogen evolution

In this work NiRu-PBA was synthesised by using a facile coprecipitation method. A series of Ru incorporated $NiSe_2$ was derived from it by using a hydrothermal process and varying the reaction time from 24-72h. Thus, obtained materials are named as Ru-$NiSe_2$@T, where T=24h, 48h and 72h. T represents the reaction time. Among all the time-varied materials Ru-$NiSe_2$@48h was exhibiting remarkable performance by requiring only 84 mV of overpotential to produce the bench-mark current density in 1.0 M KOH electrolyte. It also displayed least value of Tafel slope i.e. 89 mV dec^{-1} indicating towards the faster kinetics at the electrode surface and lower R_{ct} value of 57 Ω shows that faster charge transfer process is taking place at the electrode electrolyte interface as compared to all the synthesised materials. Among all the synthesised materials, larger value of ECSA was observed for Ru-$NiSe_2$@48h suggesting towards the presence of larger number of electroactive sites for water reduction to occur. The Ru-$NiSe_2$@48h also exhibited long-term stability in 1 M KOH for 72 hours of duration. The remarkable performance of the Ru-$NiSe_2$@48h can be attributed to the presence of incorporated Ru in the $NiSe_2$ lattice. The synergistic interaction between Ru and Ni altered the electronic structure of the material which provides an optimised energy for the H adsorption and desorption process. The insertion of Ru into $NiSe_2$ leads towards

the formation of defects in the material which facilitates the electrolyte diffusion and ultimately enhances the performance of the materials. The PBA provided both the metal centres simultaneously and helped to achieve the homogeneous distribution of the nanogranules like morphology throughout the surface of the material. PBA also provided the C and N moiety which along with the presence of Ru enhances the conductivity of the material as well as provided stability to the material during the long-term stability test. The time-variation also helped in achieving the well-defined nanogranules morphology for Ru-$NiSe_2$@48h. Other time-varied materials were observed to having agglomerated nanogranules like morphology. These agglomerated morphology leads to the blocking of active-sites and hampers the process of electrolysis leading towards the poor performance of the materials. Further, for the comparison purpose $NiSe_2$@48h was synthesised by following the same reaction conditions but replacing the NiRu-PBA with $Ni(NO_3)_2.6H_2O$. $NiSe_2$@48h was unable to match the performance of Ru-$NiSe_2$@48h towards the alkaline HER process due to the absence of the synergistic interaction between Ru and Ni. Also, due to the absence of PBA precursor, agglomerated larger size spherical nanoparticles morphology was observed in the FESEM images for $NiSe_2$@48h, which blocks the active sites for the reaction to occur. After all the electrochemical studies, the post-catalytic study of Ru-$NiSe_2$@48h reveals no change in the phase of the material and FESEM images revealed slightly agglomerated nanogranules due to the long-term electrolysis for 72 hours. The XPS also reveals no significant changes in the oxidation state of material, only Ru^{3+} were converted into Ru^0 due to the long-term electrolysis. All these post-catalytic data reveal the robustness of the material towards the alkaline HER. This research will open up a new avenue for the development of NiRu-PBA-derived Ru-incorporated $NiSe_2$, a high-performance electrocatalyst for H_2 production in an alkaline medium.

Chapter 7: Thesis Summary and Future Perspectives

In summary, various PBA-derived electrocatalysts have been developed, and their performance towards the hydrogen evolution reaction has been explored. Chapter 1 discusses the rationale for looking for an alternative electrocatalyst for implementing electrochemical energy conversion. Chapter-2 demonstrates the synthetic methods and the basic techniques for characterising the newly developed electrocatalyst, alongwith the fundamental electrochemical parameters associated with electrochemical energy conversion. Chapter-3 shows a complete investigation of RuCo-PBA-derived nanosheet-like Ru-doped Co_9S_8 nanoparticles as an excellent electrocatalyst for the hydrogen evolution reaction in acidic electrolytic conditions. The impact of temperature change on the material's morphology and catalytic activity is also investigated. Chapter-4 reveals the electrocatalytic performance of RuPt nanocomposite derived from Ru-PBA, followed by the addition of Pt using a reduction method towards the acidic HER. The role of concentration variation has also been studied in detail. Chapter-5 describes the synthesis, characterisation and electrochemical studies of RuCo-PBA and its derived RuCo nanoalloy. The effect of annealing temperature has been discussed in the present work on the electrocatalytic performance of the electrocatalyst. Chapter-6 illustrates the systematic characterisation and electrochemical studies of NiRu-PBA and its derived Ru-incorporated $NiSe_2$ towards the alkaline hydrogen evolution reaction. The effect of time variation and Ru incorporation has been studied in this work.

LIST OF SCHEMES

LIST OF FIGURES

LIST OF TABLES

LIST OF ABBREVIATIONS

HER	Hydrogen evolution reaction
OER	Oxygen evolution reaction
MOF	Metal-organic framework
PB	Prussian blue
PBA	Prussian blue analogue
TMCs	Transition metal chalcogenides
PXRD	Powder X-ray diffraction
FTIR	Fourier transform infrared spectroscopy
FESEM	Field emission scanning electron microscope
EDS	Energy dispersive X-ray spectroscopy
TEM	Transmission electron microscope
HRTEM	High-resolution transmission electron microscopy
SAED	Selected area electron diffraction
XPS	X-ray photoelectron spectroscopy
ICP-OES	Inductively coupled plasma-optical emission spectroscopy
BET	Brunauer-Emmett-Teller
GC	Gas chromatography
CV	Cyclic voltammetry
LSV	Linear sweep voltammetry
TOF	Turn-over frequency
EIS	Electrochemical impedance spectroscopy
R_s	Solution resistance
R_{ct}	Charge transfer resistance

C_{dl}	Double-layer capacitance
CPE	Constant phase elements
ECSA	Electrochemically active surface area
CP	Chronopotentiometry
CA	Chronoamperometry
WE	Working electrode
GCE	Glassy carbon electrode
RE	Reference electrode
CE	Counter electrode
RHE	Reversible hydrogen electrode
DFT	Density functional theory
h	Hour
min	Minute
mL	Milliliter
mg	Milligram
g	Gram
mmol	Millimole
μL	Microliter
PEM	Proton exchange membrane
AEM	Anion exchange membrane
FCs	Fuel cells
WEs	Water electrolyzers
LIB	Lithium-ion battery
SIB	Sodium-ion battery
JCPDS	Joint committee on powder diffraction standards
COD	Crystallography open database
1D	One dimensional
2D	Two dimensional
3D	Three dimensional

CHAPTER-1

Overview of Electrochemical Hydrogen Evolution Reaction

1.1 Introduction

1.2 Water Electrolyser

1.2.1 Electrochemical Water Splitting

1.2.2 Types of Electrolysers

(a) Alkaline Electrolyser

(b) Proton Exchange Membrane Electrolyser

(c) Solid Oxide Electrolysers

(d) Comparison of Electrolyser Types

1.3 Water Splitting Reaction Mechanism in Different Media

1.3.1 Hydrogen Evolution Reaction (HER) Mechanism

1.3.2 Oxygen Evolution Reaction (HER) Mechanism

1.4 Fuel Cells

1.4.1 Types of Fuel Cells

1.5 Theoretical Aspects of Hydrogen Evolution Reaction

1.6 Electroactive Materials for Hydrogen Evolution Reaction

1.6.1 Noble Metal-Containing Electrocatalysts

1.6.2 Non-Noble Metal-Containing Electrocatalysts

1.6.3 Metal-Organic Frameworks (MOFs) as Electrocatalysts

1.6.4 MOF-Derived Electrocatalysts

1.6.5 Prussian Blue and its Analogues

1.1 Introduction

Our reliance on non-renewable resource-based energy technology has grown enormously in recent years. The world's energy needs significantly increased in the beginning of the 18th century as a result of a higher reliance on machines and technology. The demand for energy services is rising due to a number of factors, including population growth, global economic expansion, and technological improvements.[1] There has been an exponential increase in the world's annual energy consumption from a variety of fossil fuels, including wood, coal, natural gas, and petroleum. In a matter of decades, the energy that had been conserved for over a billion years was depleted. More than 80% of usable energy comes from fossil fuels like gas, coal, and petroleum.[2] Without a doubt, these fuels generate electricity pretty effectively, but they are not meant for long-term use. If the current rate of consumption continues unchecked, the planet's limited fossil fuel supplies are expected to run out entirely by the end of this century. Furthermore, significant amounts of greenhouse gases have been released into the Earth's atmosphere as a result of the widespread usage of fossil fuels.[3,4] Additionally, the use of fossil fuels has produced pollutants such as sulphur dioxide (SO_2), nitrogen oxide (NO_x), ammonia

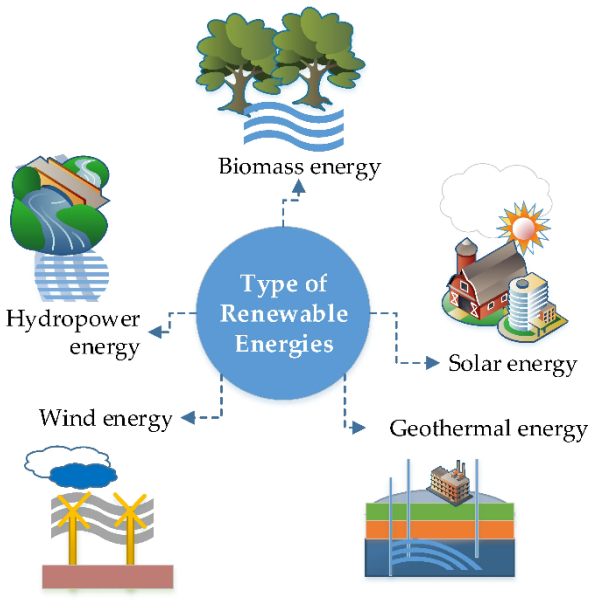

Figure 1.1: Renewable energy sources.[7]

(NH_3), volatile organic compound (VOC) gases, and heavy metal compounds, all of which have become global air quality concerns. Such pollution is associated with an increasing risk to ecosystems and human health. There have been alarming incidents of problems like acid rain, and the number of cancer occurrences has increased in comparison to data from forty years ago, suggesting a worrying health impact, especially for those who live in areas with high pollution levels.[5] Environmental degradation and the scarcity of fossil fuels are urgent worldwide concerns.[6] A concentrated effort has been made to investigate different renewable energy sources in an attempt to reduce our reliance on fossil fuels and address the growing energy demands of contemporary human activities.[5] To solve these issues, sustainable energy sources like hydropower, wind, solar, geothermal, and biomass are essential **(Figure 1.1)**.[6,7] Extensive study has been devoted to renewable energy, its conversion, and storage, due to escalating worries regarding global climate change and the rising energy demand, essential for sustainable human growth.[8]

Developing eco-friendly technologies like fuel cells, metal-air batteries, and water-splitting devices has become essential to addressing these issues. Among these, hydrogen

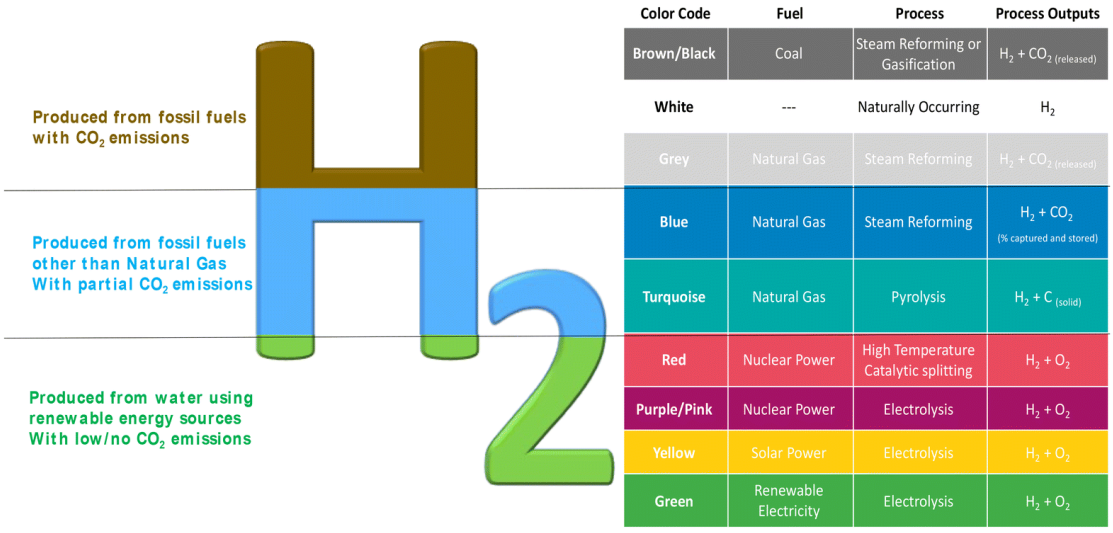

Color Code	Fuel	Process	Process Outputs
Brown/Black	Coal	Steam Reforming or Gasification	$H_2 + CO_2$ (released)
White	---	Naturally Occurring	H_2
Grey	Natural Gas	Steam Reforming	$H_2 + CO_2$ (released)
Blue	Natural Gas	Steam Reforming	$H_2 + CO_2$ (% captured and stored)
Turquoise	Natural Gas	Pyrolysis	$H_2 + C$ (solid)
Red	Nuclear Power	High Temperature Catalytic splitting	$H_2 + O_2$
Purple/Pink	Nuclear Power	Electrolysis	$H_2 + O_2$
Yellow	Solar Power	Electrolysis	$H_2 + O_2$
Green	Renewable Electricity	Electrolysis	$H_2 + O_2$

Figure 1.2: Different colours of H_2 depending on the synthesis process.[15]

- a clean, renewable, and high-energy-density fuel has shown promise as a way to address the world's growing energy needs while reducing greenhouse gas emissions.[9–12] In addition to the energy applications, hydrogen is widely used in the petroleum and chemical industries.[13] Despite its abundance, hydrogen is not available in nature in its free form.[14]

Hydrogen has several benefits, but its environmental impact varies depending on its generation technique. Based on production techniques, hydrogen is categorised by colour, such as black, white, grey, blue, turquoise, red, pink, yellow and green, as shown in **Figure 1.2**. H_2 can be broadly divided into three categories: grey, blue, and green hydrogen.[15] Grey hydrogen is produced by the method of steam methane reforming of the liquified natural gas, but it releases carbon into the environment. Blue hydrogen is also produced by using the same steam methane reforming method, but it includes carbon capture and storage technology, which prohibits the emission of carbon into the environment. But both the grey as well as the blue H_2 are obtained from the fossil fuels. Green hydrogen, on the other hand, is created by electrolysing water with electricity to make hydrogen without producing any hazardous byproducts.[16] By using renewable electricity to produce ultra-pure hydrogen, electrochemical water splitting reduces reliance on fossil fuels and promotes carbon neutrality. "Electrolyser" and "Fuel cell" will be crucial for the generation and utilisation of green hydrogen, respectively, in the future decades.

1.2 Water Electrolysers

1.2.1 Electrochemical Water Splitting

One common phrase for electrolysis is "water splitting". The water-splitting reaction takes place in a particular kind of cell called an electrolyser. Electrolysis transforms

water molecules into hydrogen and oxygen by applying an external voltage to the electrode in an aqueous electrolyte medium. The hydrogen evolution reaction (HER) at the catalyst-modified cathode electrode and the oxygen evolution reaction (OER) at the catalyst-coated anode electrode surface are typically the two half-cell reactions involved. This method produces carbon-free, environmentally friendly molecular hydrogen and oxygen gas.[17,18] **Figure 1.3** demonstrates the water splitting reaction in an electrolyser. Oxygen bubbles formed at the anode during water splitting, while hydrogen bubbles emerged at the cathode side.[19–21] **Figure 1.3** displays the polarisation curves for anodic OER as well as the cathodic HER water splitting reaction.[22]

Theoretically, the thermodynamic potential for HER and OER through water splitting is 0 and 1.23 V, respectively. Hence, the overall theoretical thermodynamic potential for water splitting is 1.23 V.[23,24] However, some additional energy is required to overcome the energy barrier associated with the electrochemical water splitting. This extra potential is the overpotential, which is the discrepancy between the thermodynamic and experimental potentials.[25] The benchmark catalysts require the least value of

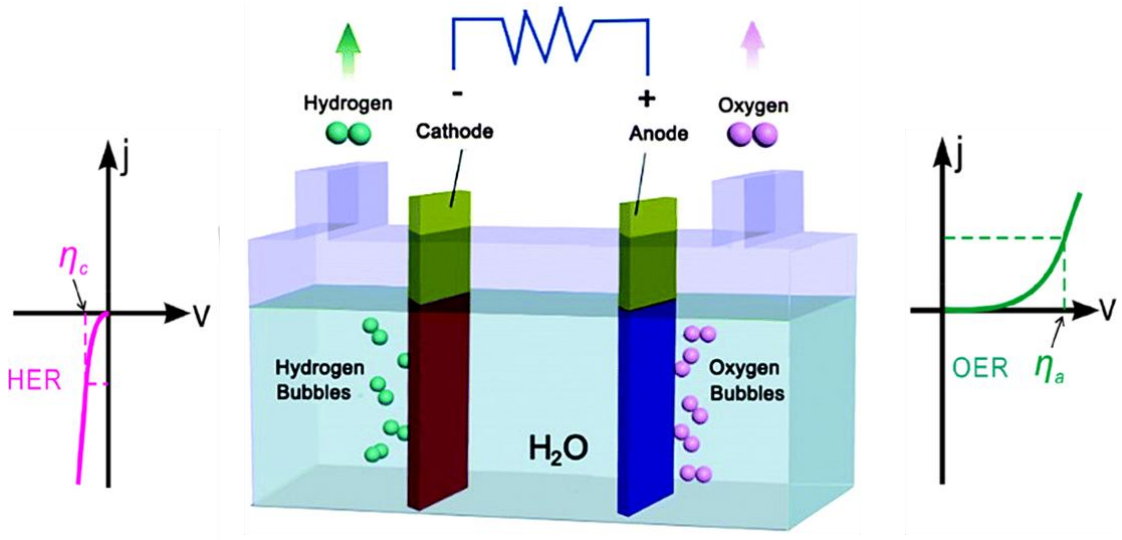

Figure 1.3: Electrolytic cell showing water splitting process and the polarisation. curves for hydrogen and oxygen evolution reaction.[22]

overpotentials for HER and OER. The benchmark catalysts for HER are the Pt-based electrocatalysts. Similarly, the benchmark catalysts for OER are the Ru and Ir oxides. However, their extensive usage for water splitting is limited by their high cost and scarcity. Therefore, the synthesis of low cost electrocatalysts for exceptional performance towards HER and OER is necessary.[26,27]

1.2.2 Types of Electrolysers

An electrolyser can be built and set up in a number of ways, and different electrolytes can be utilised. Unipolar and bipolar electrolysers are the two main varieties. Whereas the unipolar design typically uses a liquid electrolyte (alkaline liquids), the bipolar design uses a solid polymer electrolyte (proton exchange membranes). An electrolyser, which is built very similarly to a battery or fuel cell, consists of a cathode, an anode, a diaphragm and an electrolyte. A diaphragm prevents the released gases from combining and only allows ions to go through it.[28]

(a) Alkaline Electrolyser (AE)

A 30% concentrated potassium hydroxide solution is the suitable electrolyte for the majority of applications; however, sodium chloride and sodium hydroxide are also appropriate alternatives. Diaphragms can be made of a variety of materials, including polymers like polypropylene and polyphenylene sulphide and ceramic oxides like potassium titanate and asbestos. Conventional AE cells have traditionally used asbestos diaphragms, which are usually 3 mm thick. However, due to health concerns and operating temperature restrictions (not exceeding 80 °C), alternatives have been investigated. There is commonly a 5 mm separation between the two electrodes, with the cathode being made of steel having a catalyst coating and the anode being made of steel containing a nickel coating. Commercial alkaline electrolysers have current densities

between 100 and 400 mA cm^{-2}. **Equations (1.1)** and **(1.2)** take place in the cathode and anode of an AE cell, respectively.[28]

$$4H_2O(l) + 4e^- \rightarrow 2H_2(g) + 4OH^-(aq) \quad (1.1)$$

$$4OH^-(aq) \rightarrow O_2(g) + e^- \quad (1.2)$$

An alkaline electrolyser has a straightforward overall construction. An aqueous electrolyte solution suspends the two metal electrodes in their unipolar form. When electricity is applied to each electrode, oxygen and hydrogen gases are produced.

(b) Proton Exchange Membrane Electrolyser (PEME)

PEME cells consist of the gas-tight, thin, cross-linked polymeric membrane which is usually less than 0.2 mm thick and has an acidic character due to the presence of sulfonic acid functional groups. By means of an ion exchange mechanism, these groups enable proton conduction throughout the material. The most widely used membrane in PEME cells for water electrolysis is Nafion, a DuPont trademark. **Equations 1.3** and **1.4** illustrate the reactions that occur in a PEME cell's anode and cathode, respectively.[28]

$$4H_2O(l) \rightarrow O_2(g) + 4H^+(aq) + 4e^- \quad (1.3)$$

$$4H^+(aq) + 4e^- \rightarrow 2H_2(g) \quad (1.4)$$

PEME technology, a common electrolyser type, is used in the construction of many modern electrolysers. Water supplied to the cathode may easily cool the cell, and water management is simpler because the positive electrode must be saturated with water. This type of electrolyser produces high-quality hydrogen. The only issue is the water vapour in the system. Electrolyte designers use a number of techniques to stop water from diffusing into electrolytes, as it happens in fuel cells as well.[14] One common method is to use electrolytes that are considerably thicker than those used in fuel cells.

(c) Solid Oxide Electrolysers (SOE)

SOE technology was developed with the intention of lowering energy usage and, consequently, operating costs. Hydrogen is produced somewhat differently by solid oxide electrolysers, that utilise a solid ceramic material as the electrolyte which predominantly conducts the negatively charged oxygen ions (O^{2-}) at elevated temperatures. Negatively charged oxygen ions and hydrogen gas are produced when steam at the cathode reacts with electrons from the external circuit. After passing through the solid ceramic membrane, the oxygen ions react at the anode to produce the oxygen gas and electrons needed for the external circuit. Solid oxide electrolysers must run at temperatures high enough for the solid oxide membranes to function well (about 700 to 800 °C), in contrast to PEM electrolysers, which run at 70 to 90 °C, and commercial alkaline electrolysers, which typically operate at less than 100 °C. By utilising heat that is accessible at these extreme temperatures (from a variety of sources, including nuclear energy), the solid oxide electrolysers can effectively lower the electrical energy needed to produce hydrogen from water.

Yttria-stabilized zirconia (YSZ), the electrolyte used in SOE, takes use of the oxygen vacancies in its mixed oxide structure to provide improved ionic conductivity even at high working temperatures. The cathode is a cermet consisting of nickel and YSZ, whereas the anode is a mixture of YSZ and perovskites intended to improve electrocatalysis by utilising structural and electrical flaws.[28,29] The reactions occur in the cathode and anode of an SOE cell, according to **Equations 1.5** and **1.6,** respectively.[28]

$$2H_2O(g) + 4e^- \rightarrow 2H_2(g) + 2O_2^- \quad (1.5)$$

$$2O_2^- \rightarrow O_2(g) + 4e^- \quad (1.6)$$

(d) Comparison of Electrolyser Types

While SOE technology is still in its early stages of development, AE and PEME technologies are currently commercially feasible. Compared to PEMEs, AEs are less expensive overall and have a longer lifespan. Nevertheless, their low operational pressure and current density result in greater system volumes and hydrogen generation costs. However, PEMEs are attractive for integration into power grids, especially those with a large percentage of renewable energy sources, due to their high cell efficiency and quick system dynamics. However, the exorbitant cost and short lifespan of platinum catalysts impede PEMEs. By making it possible to recycle CO_2 into useful fuels and supporting the hydrogen economy, SOE shows promise as a technology for promoting sustainable development. Furthermore, because SOEs operate at high temperatures, they are more efficient than AEs and PEMEs.

1.3 Water Splitting Reaction Mechanism in Different Media

1.3.1 Hydrogen Evolution Reaction (HER) Mechanism

Pure hydrogen production is a difficult endeavour. Electrocatalytic water splitting is one of the environmentally friendly ways to produce pure H_2. The hydrogen evolution reaction, sometimes referred to as the electrolyser's cathodic half-reaction, typically happens when protons are reduced into molecular hydrogen following their adsorption on the catalyst surface. This cathodic half-cell reaction produces H_2 from water via a two-electron transfer pathway that is dependent on the pH of the water (neutral, acidic or alkaline). In a neutral or acidic environment, HER typically occurs either through Volmer-Heyrovsky or Volmer-Tafel steps. In the Volmer step, the H^+ ion adheres to the surface of the electrocatalyst M to create an adsorbed hydrogen atom and is represented as M-H. If the reaction further proceeds through the Heyrovsky step, then the electron-

coupled hydronium ion (H^+) will combine with the already adsorbed hydrogen to form H_2. If the reaction proceeds through the Tafel step, then two adsorbed H combine with each other and result in H_2. Here, M in the reaction mechanism represents the catalytic site. In an acidic or neutral medium, the HER follows three steps **(Equation 1.7-1.9)**:

$$M + H^+ + e^- \rightarrow M\text{-}H \text{ (Volmer step)} \quad (1.7)$$

$$M\text{-}H + H^+ + e^- \rightarrow H_2 \text{ (Heyrovsky step)} \quad (1.8)$$

$$2M\text{-}H \rightarrow H_2 \text{ (Tafel step)} \quad (1.9)$$

In an alkaline medium, the HER takes place by following the same reaction mechanism as in an acidic medium, but the source of protons here is H_2O. In the first step, i.e. the Volmer step, a proton from a H_2O molecule combines with an electron, resulting in adsorbed H on the catalytic site, i.e. M-H. After the first step, the reaction can either proceed through the Heyrovsky step or the Tafel step to produce the molecular H_2. In the Heyrovsky step another H from a second water molecule combines with an electron and the already adsorbed H to produce H_2. In the Tafel step, two adsorbed H combine

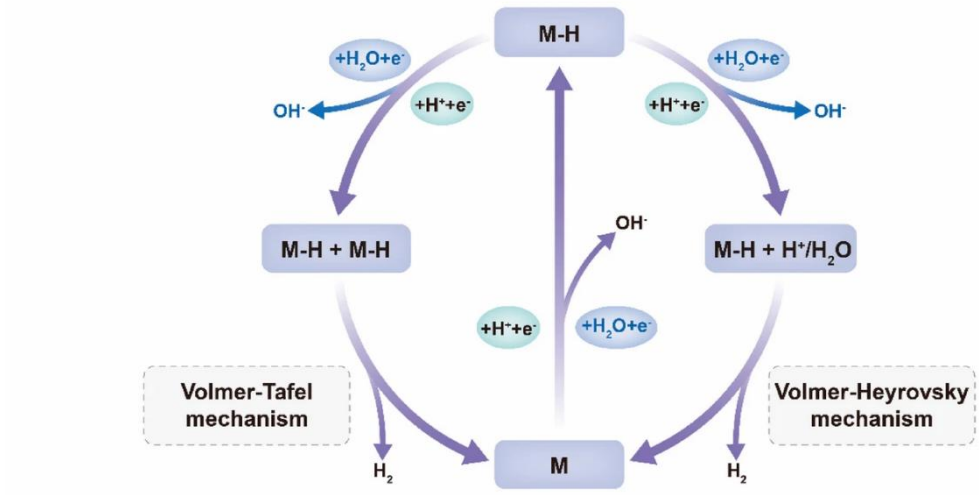

Figure 1.4: Mechanism of HER in neutral/acidic and alkaline media.[30]

with each other, resulting in the formation of H_2. The mechanism for HER in alkaline medium is as follows **(Equation 1.10-1.12)**:

$$M + H_2O + e^- \rightarrow M\text{-}H + OH^- \text{ (Volmer step)} \quad (1.10)$$

$$M\text{-}H + H_2O + e^- \rightarrow OH^- + H_2 + M \text{ (Heyrovsky step)} \quad (1.11)$$

$$2M\text{-}H \rightarrow H_2 \text{ (Tafel step)} \quad (1.12)$$

Figure 1.4 shows the schematic HER mechanism in neutral/acidic and alkaline media.[30]

1.3.2 Oxygen Evolution Reaction (HER) Mechanism

The electrolyser's anodic half-cell reaction, known as the oxygen evolution reaction (OER), uses a four-electron transfer pathway to oxidise water into molecular oxygen. In contrast to HER, it has slow reaction kinetics due to the kinetic and thermodynamic barriers at every stage, making it the electrolyser's overall efficiency bottleneck. Thermodynamically, 1.23 V is needed to complete the process; however, additional potential is needed because each stage involves an energy barrier. Therefore, it creates a

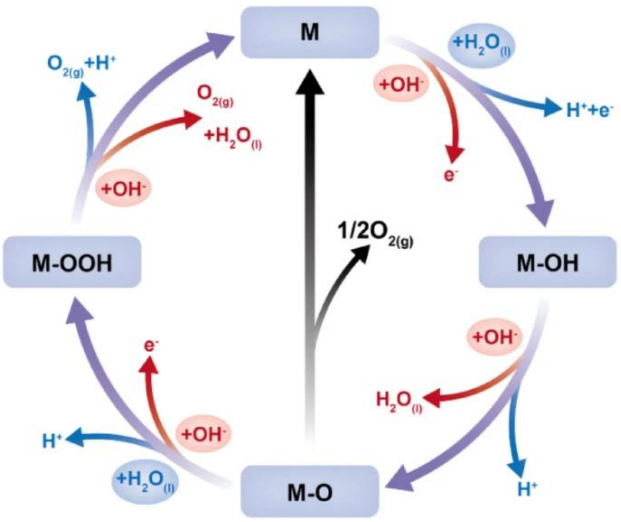

Figure 1.5: Mechanism of OER in neutral/acidic and alkaline media.[30]

difficulty for the technological improvement of the electrolyser, even if the total

economics of hydrogen generation is reduced. Additionally, as shown in **Figure 1.5**, OER uses many reaction pathways and is highly dependent on the pH of the water used.

Hydroxide ions are deposited on the catalyst surface in a neutral or acidic solution when water molecules lose an electron and a proton. Adsorbed hydroxo species then undergo an additional electron and proton loss to create oxo species. These oxo species are transformed into peroxo species by another water molecule losing an electron and a proton. These peroxo species then split into a proton and an electron, releasing molecular oxygen. Therefore, two water molecules are oxidised into molecular oxygen and create four protons and electrons in an acidic and neutral medium. The OER mechanism is as follows in the acidic or neutral medium **(Equation 1.13-1.17)**:

$$M + H_2O \rightarrow MOH + H^+ + e^- \quad (1.13)$$

$$MOH + OH^- \rightarrow MO + H_2O + e^- \quad (1.14)$$

$$2MO \rightarrow 2M + O_2 \quad (1.15)$$

$$MO + H_2O \rightarrow MOOH + H^+ + e^- \quad (1.16)$$

$$MOOH + H_2O \rightarrow M + O_2 + H^+ + e^- \quad (1.17)$$

The water splitting reaction can also take place in an alkaline medium. Hydroxide ions are readily available in the alkaline media and are directly adsorbed on the catalyst surface to generate hydroxo species. A proton is taken from it by another hydroxide ion, forming the oxo species, which is then attacked by another hydroxide to produce the peroxo species. Ultimately, the proton is extracted by another hydroxide ion, freeing the oxygen molecule. As a result, two water molecules and one oxygen molecule were produced from four hydroxide molecules in an alkaline medium. The OER follows the mechanism below in alkaline medium **(Equation 1.18-1.22)**:

$$M + OH^- \rightarrow MOH \quad (1.18)$$

$$MOH + OH^- \rightarrow MO + H_2O \quad (1.19)$$

$$2MO \rightarrow 2M + O_2 \quad (1.20)$$

$$MO + OH^- \rightarrow MOOH + e^- \quad (1.21)$$

$$MOOH + OH^- \rightarrow M + O_2 + H_2O \quad (1.22)$$

Figure 1.5 shows the schematic representation of OER in acidic/neutral and alkaline media.[30]

1.4 Fuel Cells

An electrochemical device or cell known as a fuel cell can convert chemical energy into electrical energy by employing an electrode to catalyse an electrochemical reaction. Fuel cells can continuously produce energy as long as fuel is available.[31] In a fuel cell, hydrogen and oxygen fuels are supplied to the anode and cathode compartments. Hydrogen oxidation takes place at the anode, where hydrogen is transformed into the hydronium ion (H_3O^+) (HOR). At the cathode, O_2 reduction results in the formation of

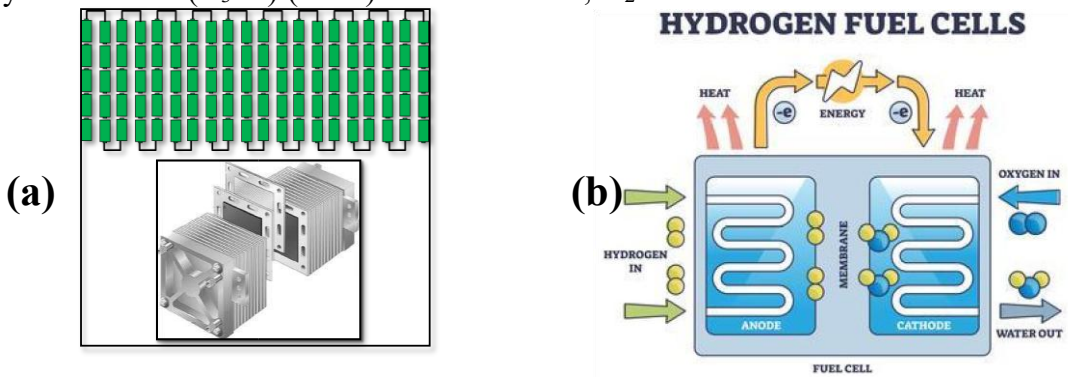

Figure 1.6. Representation of the Fuel cell stack along with the working principle (a and b). (Adapted from Jolt Plastics innovation and hydrogen fuel news)

hydroxide ion (OH^-) (ORR). When the anodic H_3O^+ ions and the OH^- ion of the cathodic compartment interact, water is produced. When an electron moves from the anode to the

cathode via an external circuit, electricity is generated. By connecting multiple independent fuel cells, we can easily produce large amps of power, as shown in **Figures 1.6a and b**.

1.4.1 Types of Fuel Cells

There are various types of fuel cells. Some of the fuel cells are listed here:

(a) Alkaline Fuel Cell (AFC)

(b) Proton Exchange Membrane Fuel Cell (PEMFC)

(c) Solid Oxide Fuel Cell (SOFC)

(d) Molten Carbonate Fuel Cell (MCFC)

(e) Phosphoric Acid Fuel Cell (PAFC)

Compared to traditional FCs, PEMFC has several advantages, such as a low operating temperature, increased power capability, portability due to its small size, and inexpensive cost.

1.5 Theoretical Aspects of Hydrogen Evolution Reaction

Density functional theory (DFT) combined with the Sabatier principle is a ground-breaking method for understanding patterns in catalytic activity. The Sabatier principle is one of the oldest laws in catalysis for a two-step reaction involving an adsorbed intermediate, such as the hydrogen evolution reaction. This principle states that "A good catalyst must bind reaction intermediates neither too strongly nor too weakly". The ideal

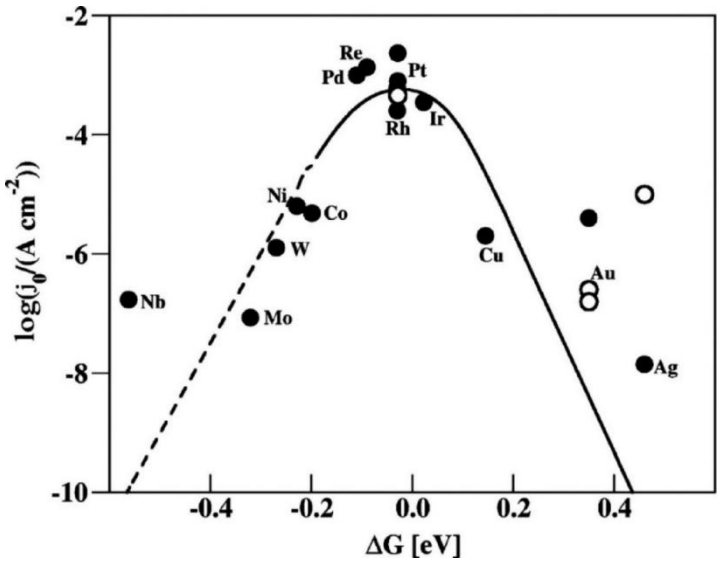

Figure 1.7: Volcano plot.

catalyst should have modest binding strength, allowing for a rapid adsorption and desorption process at the electrode surface.[32] Numerous studies have described the relative electrocatalytic activity of different electrode materials as a descriptor. One unique element that governs the catalytic process is the descriptor. In the electrocatalytic water-splitting process, this descriptor can be conceptualised as the interaction between the catalytic surface and the reaction intermediate. Parsons proposed a volcano-like picture for the electrocatalytic HER to connect j_0 to the thermodynamically derived ΔG_{H^*}.[33] The volcano-like pattern is observed because j_0 may be expressed as $(\theta_H)^{\alpha}(1 - \theta_H)^{1-\alpha}$ as a function of ΔG_{H^*};[34] where α represents the relative slope of the energy curves of the initial and final states at their intersection. The volcano reaches its peak at $\theta_H = 1 - \theta_H = 0.5$ ($\alpha = 1 - \alpha = 0.5$), or $\Delta G_{H^*} = 0$. At $\Delta G_{H^*} = 0$, the two linear branches of the volcano plot are symmetrical. j_0 grows exponentially with decreasing ΔG_{H^*} when ΔG_{H^*} is greater than zero (very weak H* adsorption). Similarly, j_0 decreases exponentially with a fall in ΔG_{H^*} when ΔG_{H^*} is lower than zero (very strong H* adsorption).[33] By correlating the measured hydrogen temperatures of adsorption with a wide range of j_0 values discovered for polycrystalline metal surfaces, Trasatti created a different kind of

volcano map in response to Parsons's findings.[35] Low j_0 values are seen in metals with strong hydrogen adsorption (Mo, Ta, W) as well as weak hydrogen adsorption (Ag, Zn, Al). Only metals with significant hydrogen adsorption, including Pt, Pd, and Rh, have high values of j_0. Additionally, Trasatti,[35] Conway, and Bockris[36] observed that there is a simple phenomenological linear relationship between the logarithm of j_0 and the work function (Φ) for all of these metal surfaces. Since Φ solely depends on a metal's Fermi energy, there should be some inherent relationship between the electrical properties of metals. Due to the availability of enormous computational potential, DFT can now easily examine the highly accurate electronic structures of the catalysts. As demonstrated by Nørskov *et al.*, DFT calculations started to play an increasingly significant role in determining ΔG_{H^*} values for constructing volcano-type displays for various systems.[37] DFT has been successfully used to represent a wide range of surfaces, including metals,[37] sulphides,[38] alloys,[39] metal carbides,[40] and even non-metallic surfaces that were not described by conventional heat of adsorption data. The calculated ΔG_{H^*} values provide the volcano-type plots shown in **Figure 1.7** after correlation with the measured j_0.[41] As expected, the peak of the activity volcano contains Pt-family metals with large j_0 and low absolute values of ΔG_{H^*}. Since the theoretical maximum of j_0 is located at the peak of the volcano curve with $\Delta G_{H^*} = 0$, research on the design and fabrication of highly active catalysts strives to climb the "electrocatalytic activity" volcano.

1.6 Electroactive Materials for Hydrogen Evolution Reaction

According to theoretical research, water electrolysis can produce molecular hydrogen by using the two-electron reaction mechanism at thermodynamic potential of 0 V (against RHE). The electrocatalytic process that splits water requires a large overpotential value. The different precious and non-precious metals have an enormous

effect on the electrocatalytic production of renewable hydrogen molecules. Noble metals like palladium (Pd) and platinum (Pt) are considered as efficient catalysts for the hydrogen evolution process because they require very less value of overpotential to do so. But due to the high cost of these noble metal-based catalysts, along with their scarcity and poor performance during the long-term electrolysis process, researchers are focusing towards the synthesis of materials that are low in cost, show good catalytic performance and greater stability in the electrolytic conditions.

1.6.1 Noble Metal-Containing Electrocatalysts

Various noble metal-based electrocatalysts have been synthesised and studied to date for HER by combining them with other metals to bring down the cost of catalyst production and enhance the catalytic activity. Yuan and coworkers have synthesised TiO_2 nano-polyhedrons decorated with Pt nanoparticles on the integrated electrode using titanium fibres ($Pt/TiO_2/Ti$) via electrodeposition after a hydrothermal process. The electrocatalyst was observed to deliver the benchmark current density of 10 mA cm^{-2} by requiring a small overpotential of 23 mV.[42] In another work, Zhai and coworkers have synthesised $Pt@CoO_x$ catalyst which also exhibits good HER activity by requiring an overpotential of only 82 mV to produce 10 mA cm^{-2} in a neutral medium.[43] Wang and coworkers have successfully fabricated MOF-derived Pt/CuO nanoclusters loaded directionally on nitrogen-doped porous carbon arrays. With an overpotential of 39 mV at 10 mA cm^{-2}, the optimised electrocatalyst demonstrated outstanding HER catalytic activity in an alkaline medium of 1 M KOH.[44]

1.6.2 Non-Noble Metal-Containing Electrocatalysts

Noble metal-based electrocatalysts are not widely used in industry due to their high cost and low stability. The study of electrochemical water splitting has recently investigated several non-noble metal-based catalysts that contain electrocatalysts of V, Co, Ni, Fe, Cu, Mo, and W.[45,46] Among numerous non-precious transition metal-containing electrocatalysts, transition metal oxides, phosphides, and carbides stand out as the best options for energy conversion applications due to their inherent catalytic activity.[47–49] Xu and coworkers have synthesised MoS_2 which exhibits a lower overpotential of 164 mV at 10 mA cm^{-2} current density for HER in 0.5 M H_2SO_4.[50] Du and coworkers have synthesised a bimetallic NiCoP coupled with C_{60}. The optimised electrocatalyst needed only 97 mV of overpotential to produce the benchmark current density.[51] Zhou and coworkers have synthesised (3D) porous $NiSe_2$/Ni hybrid foams which show good HER performance in the acidic electrolyte by requiring only 143 mV of overpotential for producing 10 mA cm^{-2}.[52] Wu and coworkers have synthesised CoO_x electrocatalyst for HER by following the solvothermal reaction process. It requires an overpotential of 112 mV to reach 20 mA cm^{-2} current density in the alkaline medium.[53]

1.6.3 Metal-Organic Frameworks (MOFs) as Electrocatalysts

As a new class of porous materials made by metal nodes (ions/clusters) and organic linkers through coordinated interactions, metal-organic frameworks (MOFs) have many structural and component advantages, including intrinsic designable and tunable structures, high crystallinity, adjustable chemical components, high porosity, large surface area, diverse topologies, etc. The **Figure 1.8** shows that metal ions and organic linkers can coordinate to each other and result in the formation of 1D, 2D and 3D MOF. A huge, independent one-layer sheet of two-dimensional supramolecular polymer

(2DSP) containing triphenylene-fused nickel bis(dithiolene) complexes was created by Dong *et al.*[54] These 2DSPs exhibit remarkable catalytic sites for hydrogen evolution by requiring an overpotential of 333 mV at a current density of 10 mA cm^{-2}. *Li et al.* used a straightforward hydrothermal process to create 2D polyhalogenated Co(II) coordination isostructural polymers.[55] They found that the coupling of Co-MOF and acetylene black increased the reactivity of hydrogen production in acidic conditions, and that the HER electrocatalytic activity of Co-Cl_4-MOF was significantly higher than that of Co-Br_4-MOF and Co-F_4-MOF. Because of their lower Tafel slope of 86 mV dec^{-1}, and smaller overpotential of 283 mV at a current density of 10 mA cm^{-2}, the AB and Co–Cl_4-MOF (3:4) exhibit the best HER activity among all composites.

Although MOFs have several properties but their direct application is limited by their

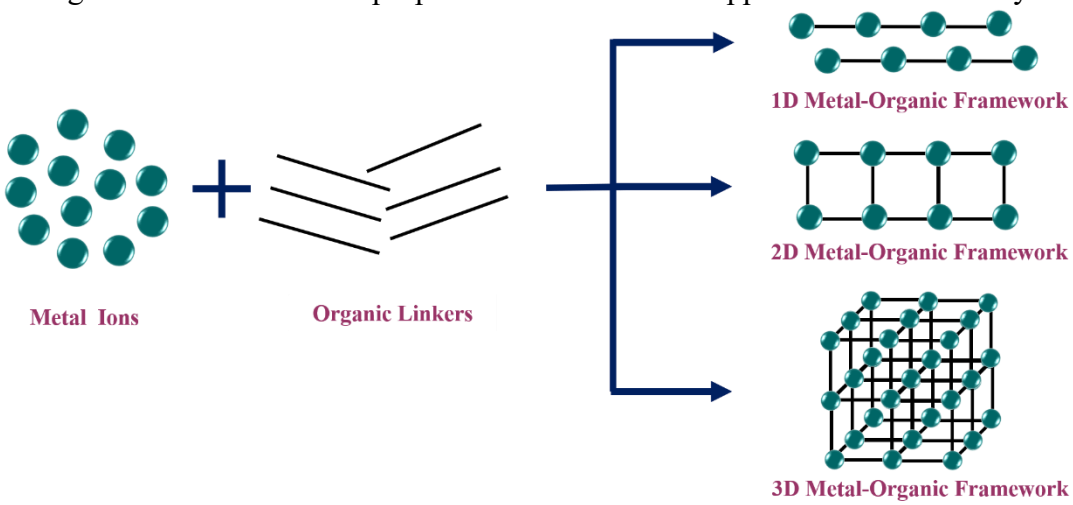

Figure 1.8: Metal-organic frameworks.

higher value of overpotentials, intrinsic instability in alkaline, acidic, or oxidative conditions. Additionally, MOFs' metal–ligand linkages are prone to breaking down, which reduces their catalytic activity. Therefore, owing to their outstanding properties, MOFs have garnered a lot of attention as a precursor to derive electrocatalysts from them.[56]

1.6.4 MOF-Derived Electrocatalysts

Many MOFs' potential for usage in the energy industry, especially electrochemical energy conversion, is severely limited by their inadequate electrical conductivity and stability under operating conditions.[57] Therefore by employing MOFs as a sacrificial template, researchers are concentrating on creating a range of functional materials with remarkable performance for HER. By carefully controlling the chemical or thermal processes, pure MOFs and MOF composites can be converted into a variety of nanoarchitectures, such as metal compound nanoparticles, metal nanoparticles/carbon composites, and MOF-derived carbon.[58–60] The electrocatalysts derived from MOF possess the inherent large surface area, regulated porosity, hollow and porous structure, and a well-designed morphology. Additionally, they also possess an enhanced number of active sites, increased conductivity, as well as accelerated mass transport for the electrocatalytic applications.[59,61,62] By carefully selecting metal nodes and organic ligands, carefully regulating experimental conditions, and post-synthetic modification, MOFs can be used as excellent sacrificial templates to synthesise MOF-derived nanomaterials with intended structural and compositional properties.[63,64]

Do and coworkers have synthesised Co-MOF-derived $Co/Co_3O_4/C$ particles. The optimised electrocatalyst required a low overpotential of 160 mV to generate 10 mA cm^{-2} in 1 M KOH.[65] In another study, Feng and coworkers have synthesised MOF-derived carbon-MoS_2 composite. In an acidic electrolyte of 0.5 M H_2SO_4 it requires only 200 mV at 10 mA cm^{-2} current density.[66] Duan and coworkers have utilised a Co-MOF and produced CoP/C by both direct and indirect phosphating techniques. The direct one showed good performance in the acidic electrolyte by requiring 136 mV at 10 mA cm^{-2}.[67]

1.6.5 Prussian Blue and its Analogues

Prussian blue (PB) and its analogues (PBAs) are a subclass of MOFs with distinctive properties. Prussian blue (PB) is a dark blue compound with the formula $Fe_4[Fe(CN)_6]_3.xH_2O$. It was discovered in 1706 in Berlin. Berlin served as the capital of the newly established Kingdom of Prussia since 1701. The nation where this new pigment was discovered inspired its name i.e Prussian blue. The mixed-valence transition metal complex Prussian blue has a maximum absorption of visible light at about 700 nm. As shown in the **Figure 1.9** Fe(II)–C–N–Fe(III)–N–C sequences make up its cubic lattice structure.[68] In the ideal configuration, high-spin Fe(III) has six nitrogen atoms as neighbours, while low-spin Fe(II) is octahedrally surrounded by six carbon atoms. For charge compensation, cations like K^+ are intercalated at interstitial locations in the Prussian blue lattice in this ideal structure.[69] Initially PB was first employed as the pigment in paint, Japanese woodblock printing and making blueprints. PB also showed application as an antidote for curing the Cs^+ and Tl^+ poisoning. The application of PB was further explored in sensors, rechargeable batteries, electrochemical energy conversion and storage applications, etc.[69]

When one or both of the Fe are replaced by some other metals, the obtained compounds are known as Prussian blue analogues (PBAs). PBAs have the following formula: $A_xM_A[M_B(CN)_6]\cdot nH_2O$, where A is an alkaline ion (Li, Na, K), M_A and M_B represent the transition metals (M_A and M_B = Mn, Fe, Co, Ni, Cu, Zn, Ru, etc.) **(Figure 1.10)**.[70] They all have metal ions bridged by cyanide ions. Some PBAs are even better than the PB itself for a number of applications. PBAs are also of great interest for usage in sensors, batteries and also possess high interest in the field of nanomedicines as well. PBAs can be used as electrodes for supercapacitors with organic or aqueous electrolytes

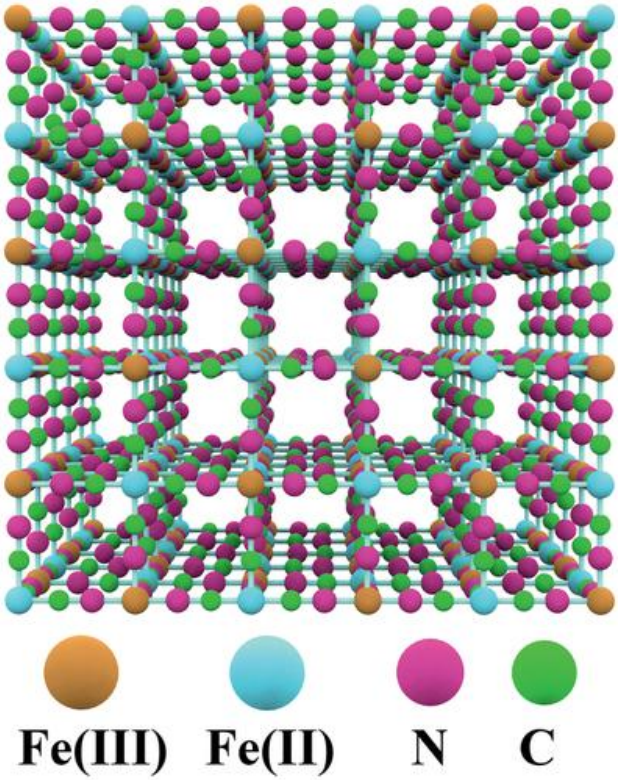

Figure 1.9: Structure of Prussian blue (PB).[68]

and cathode materials for alkaline ion batteries (Li^+, Na^+, K^+, etc.) because of their open framework, which allows the alkaline ions to be removed or intercalated reversibly from/into the PBAs. Since PBAs are generally prepared in aqueous solution, some defects and crystal water will unavoidably remain in them. Hence, they can serve as the host for hydrogen storage. Additionally, PBAs and their derivatives can be used as catalysts for the HER and OER because of the framework's abundance of transition metals.[71]

PBAs retain the basic characteristics of MOF materials, together with their specific benefits in electrochemical applications.[72] There are various advantages of PBAs over the traditional MOFs:

(i) PBAs possess high thermal and structural stability owing to the presence of strong cyanide linkage between the metal centres whereas MOFs' metal–ligand linkages are vulnerable to deterioration, which reduces their catalytic activity.

(ii) PBAs have mixed-valence metal which allows electron hopping and results in better conductivity of the material while most of the traditional MOFs are insulating unless they are designed with conjugated linkers. This restricts their capacity to transport electrons effectively during electrocatalysis.

(iii) Synthesis of PBA is simple, cost-effective and can be obtained at room temperature but MOFs generally required solvothermal synthesis, costly ligands as well as solvents.

(iv) PBAs enable substitution of the metal sites and intrinsic vacancy engineering, which enhances the electrochemical activity and catalysis.

(v) PBA exhibits better electrochemical stability in comparison to various MOFs which often collapse under electrochemical conditions,

(vi) PBAs have high porosity, large 3D cubic channels and open diffusion pathways which makes them excellent for various electrocatalytic applications whereas pore blockage or poor structural design frequently restrict the density and accessibility of active sites in MOFs.

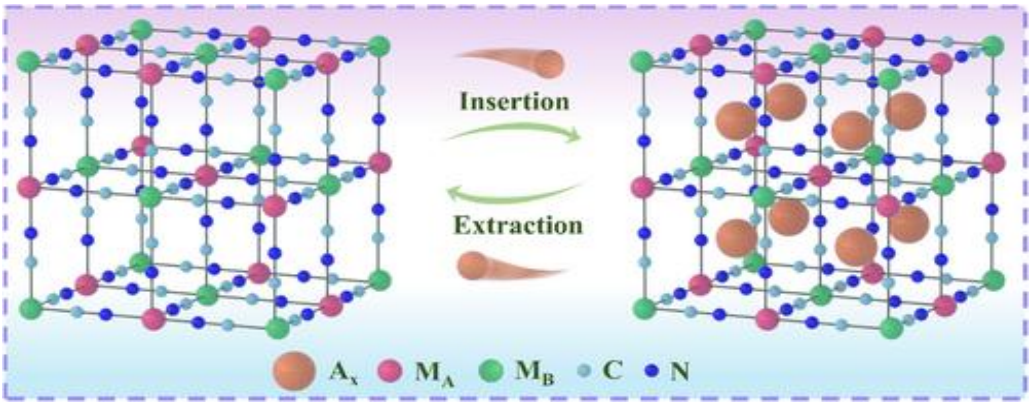

Figure 1.10: Structure of Prussian blue analogue (PBA).[70]

As a result of the aforementioned properties, they have been identified as promising starting materials for the development of extremely efficient energy storage/conversion materials.[56,68,73–76]

1.6.6 PBA-Derived Electrocatalysts

However, the activity of PB and PBA are not remarkable when compared to that of benchmark catalysts owing to their poor stability as well as the constrained conductivity. Nowadays, PBA-based materials have a wide range of potential applications and comparatively good HER activity.[30] PBA-based catalysts outperform pristine PBAs in terms of structural stability, ionic conductivity, tuned electrochemical properties, reduced water sensitivity, and optimised morphology. Derivatisation methods can remove structural defects and vacancies that impair cycle performance in pristine PBAs. Nevertheless, surface changes and compositional tweaking in PBA derivatives optimise their redox-active transition metals structural characteristics, and multifunctional capabilities for energy conversion. PBA-derived catalysts are especially attractive because they may be tailored to overcome the intrinsic limitations of pure PBAs, such as capacity fading owing to structural instability and poor performance due to inadequate electronic conductivity. PBA-based catalysts are ideal for a variety of applications due to their great structural flexibility, increased surface areas, low skeletal density, and improved chemical stability. PBA-derived catalysts are becoming increasingly attractive because of their ability to retain the advantageous open framework structure while introducing functional alterations that improve certain performance metrics.[30,77]

Further, due to platinum's high cost and scarcity, there is a growing interest in exploring low-cost and efficient replacements. The well-tuned compositional and structural properties of PBAs make PBA derivatives ideal electrocatalysts with varied active

phases, active species, and more exposed active sites. Alternative electrocatalysts include metal alloys, sulphides, selenides, phosphides, etc.

(a) PBA-Derived Alloys

Alloy materials consist of two or more different kinds of metal elements, which offer significant development potential in the field of electrocatalysis because of the synergistic action between the metals. Metal nanoparticles enwrapped in carbon materials show great promise as electrocatalysts due to their enhanced activity, thermal and chemical stability.[68,70] As revealed by Tavakkoli and co-workers and Deng and co-workers, transition metals and their alloys enclosed in carbon materials have been proposed as prospective HER catalysts with improved activity and stability. However, they required costly or complicated multi-step synthesis methods.[78,79] Yang and coworkers gained crucial success in preparing a FeCo alloy wrapped by in situ produced nitrogen-doped graphene layers via direct annealing of $Fe_3[Co(CN)_6]_2$ spheres under a nitrogen environment. The graphene layers will inhibit the aggregation of FeCo nanoparticles, offering more active sites for HER. Electrochemical experiments in 0.5 M H_2SO_4 revealed that the S-600 has the highest catalytic activity for HER, with an overpotential of 262 mV to produce 10 mA cm^{-2} current density compared to the reversible hydrogen electrode (RHE). This high activity is also attributed to nitrogen dopants in graphene layers, as well as the synergistic effect between the graphene and metal.[80] In another study Li and coworkers have synthesised FeCo alloy nanoparticles on a carbon cloth by using a thermal technique from FeCo-PBA precursor. The FeCo alloy nanoparticles require only 161 mV overpotential to generate 10 mA cm^{-2} current density in 1.0 M KOH. Strong electronic interactions between Fe and Co enhances the

electron transfer from Fe to Co and play an important role in regulating hydrogen adsorption energy and promoting the faster charge transfer process.[81]

(b) PBA-Derived Sulphides

The sulphides have unique physicochemical properties, such as an abundance of surface-active sites, adjustable electronic structures, chemical stability, and good electrical conductivity, making them suitable for HER. Sulphide materials exhibit good performance towards HER by facilitating hydrogen activation and lowering the energy barrier related to the proton reduction.[82] Yu and coworkers used a solvothermal reaction between $Ni_3[Co(CN)_6]_2 \cdot 12H_2O$ nanocubes and ammonium thiomolybdate ($(NH_4)_2MoS_4$) to create bimetal-incorporated MoS_2 nanoboxes (Ni−Co−MoS_2) made of ultrathin nanosheets. In an acidic electrolyte, the synthesised electrocatalyst requires a low overpotential value of 155 mV to produce the benchmark current density of 10 mA cm^{-2}. The increased activity of the electrocatalyst was attributed to the following five factors: i) the high surface area resulting from the ultrathin nanosheet building blocks and hollow structure, ii) enhanced electroactive edge sites, iii) supplementary active edge sites generated from the defect-rich structure, iv) the modulated electronic structure resulted by Co and Ni doping, and v) the synergistic effects between various coexisting metal sulphide phases.[83] In another work, Ding and coworkers have developed an iron-doped NiS/$Ni(OH)_2$/CC composite by using a hydrothermal sulphurization technique of bimetallic NiFe-PBA precursors grown on 3D $Ni(OH)_2$ nanosheets. Fe-NiS/$Ni(OH)_2$/CC requires a low overpotential of only 103 mV to produce a current density of 10 mA cm^{-2} in 1.0 M KOH electrolyte. Fe-NiS/$Ni(OH)_2$/CC exhibits outstanding catalytic activity because to its distinctive 3D structure, homogeneous iron

doping due to the in-situ PBA development, and high conductivity owing to the self-supported electrode carbon cloth.[84]

(c) PBA-Derived Selenides

Transition metal-based selenides exhibit enhanced electrochemical activity. This can be attributed to the less electronegativity of Se when compared to that of S and O, which leads to a decrease in the covalent character and improving the redox kinetics at the metal centres.[85] Guo and coworkers have synthesised NiFe-PBA-derived NiFeSe/CFP (carbon fiber paper). Here, NiFeSe is deposited on the CFP through the selenization at 450 °C. It produced the 10 mA cm^{-2} of current density by requiring only 186 mV. The unique 3D porous configuration inherited from the PBA templates, enhanced charge transfer at the heterogeneous interface due to the synergistic effect between the bimetallic phases, and high conductivity improved by the formation of amorphous carbon shells during selenization, all contribute to NiFeSe/CFP's improved electrocatalytic performance.[86] In another study, Wang and coworkers have developed $CoSe_2$-$FeSe_2$ bimetallic sulphide anchored on the carbon nanotube (CNT) surface by following the annealing process. The $CoSe_2$-$FeSe_2$/CNT hybrid synthesised from CoFe-PBA precursor requires only 205 mV to produce 10 mA cm^{-2} current density in 0.5 M H_2SO_4. The exceptional HER performance is attributed to the synergistic effects of bi-metallization and porous nanoarchitecture. The bi-metallization enhances charge transfer at interfaces and reconfigures the partial electron structure, while the porous nanoarchitecture allows for close contact between active sites and electrolyte, accelerating gas bubble formation.[87] Sun and coworkers generated a series of $Ni_xCo_{(1-x)}Se_2$ from NiCo-PBA by altering the concentration of Ni and Co precursors during PBA synthesis to examine the influence of concentration on the material's performance.

Among all the synthesised materials, $Ni_{0.631}Co_{0.369}Se_2$ requires only 168, 155, and 294 mV of overpotential to produce the benchmark current density of 10 mA cm^{-2} in acidic, alkaline, and neutral media, respectively. Optimising the nickel/cobalt stoichiometric ratio resulted in increased HER activity.[88]

(d) PBA-Derived Phosphides

Transition metal phosphides (TMPs) have recently emerged as a new class of water splitting electrocatalysts due to their affordability and reactivity. Specifically, certain nanostructured phosphides of cobalt, nickel, iron, and molybdenum have been investigated as effective electrocatalysts for HER with appreciable overpotentials.[89,90] Bulk TMPs, however, display sluggish conductivity, relatively larger overpotential, and slower charge transfer kinetics than contemporary electrocatalysts for HER. Some of the aforementioned problems can be resolved by introducing the second metal during the synthesis of the materials. By utilising the bimetallic PBA precursors, phosphides with two metal centres can be obtained, which will enhance the overall performance of the catalyst towards the process of electrolysis. Ding and the coworkers have fabricated Co_2P/Ni_2P/CNT composite by utilising a CoNi-PBA precursor which delivers the current density of 10 mA cm^{-2} by requiring an overpotential of 151 and 202 mV in 0.5 M H_2SO_4 and 1 M KOH for HER, respectively. Co_2P/Ni_2P/CNT exhibits outstanding HER performance because of the strong interaction between the bimetallic phosphide and CNT, resulting in improved reaction kinetics, quick electron transfer, and higher specific surface area. The strong coupling between Co_2P/Ni_2P and CNT, which exhibits the better reaction kinetics of the bimetallic phosphide, fast electron transfer, and improved specific surface area, is responsible for the enhanced HER performance of Co_2P/Ni_2P/CNT.[91] In a different study, Wang and coworkers have developed NiFeP

phosphide film by using NiFe-PBA as the starting material. Under an alkaline electrolytic environment, it requires only 99 mV of overpotential to deliver the 10 mA cm^{-2} current density.[92]

In addition to HER, PBA-derived materials exhibit excellent performance in other energy conversion and storage applications as well. Some of them are discussed below.

1.6.6 (i) Supercapacitors

In recent years, extensive studies and exploration have been undertaken on PBA materials in the fields of energy storage and transformation. Supercapacitors are regarded as extremely promising technologies for energy storage. This is mostly owing to their outstanding benefits, which include high power density, a long operating lifespan, quick charge/discharge capabilities, and cost effectiveness.[76] In a study, Hu and coworkers have developed silver-decorated cobaltosic oxide $Ag@Co_3O_4$ and bismuth–iron oxide $Bi_2O_3@BiFeO_3$ by using the PBA precursors. The optimised $Ag@Co_3O_4$, when taken as a cathode material, demonstrates a discharge-specific capacity of 1027 C g^{-1}, and $Bi_2O_3@BiFeO_3$, when taken as the anode material, displays a capacity of 615 C g^{-1} at a current density of 1 A g^{-1}. Notably, the assembled ASC device $Ag@Co_3O_4$ // $Bi_2O_3@BiFeO_3$ obtained an energy density of 55 Wh kg^{-1} at a power density of 1640 W kg^{-1} within a voltage window of 1.8 V.[93] In another study, Huo and coworkers have utilised NiCoFe-PBA to derive iron-cobalt-nickel selenide nanomaterial. The AS assembled with the iron-cobalt-nickel selenide as positive material and activated carbon as the negative material, delivers an energy density of 15.8 Wh kg^{-1} at a power density of 800 W kg^{-1} within a wide voltage window of 1.6 V.

1.6.6 (ii) Battery

The field of electrochemical energy storage is undergoing a paradigm change away from traditional lithium-ion chemistry, driven by the pursuit of affordability, sustainability, and resource availability. Potassium-ion (PIBs), sodium-ion (SIBs), and zinc-ion batteries (ZIBs) are at the forefront of this transition, sharing the fundamental intercalation or "rocking-chair" mechanism that underpins LIB success (except for ZIBs' unique conversion chemistry in particular configurations). However, they have major differences in operational principles and material requirements.[76] In a study Lei and coworkers have derived FeCoNi alloy supported on N-doped porous carbon by using a FeCo-PBA. The synthesised material, when applied in a Zn-air battery, exhibited an enhanced specific capacity of 791 mAh g_{Zn}^{-1} along with the long-term cycling stability when compared to the commercial Pt/C + RuO_2.[94]

1.6.6 (iii) Oxygen Evolution Reaction

The overall reaction kinetics of OER are likewise slow when compared to HER. The goal of developing new electrocatalysts for water oxidation is to reduce overpotential while still achieving high current density. At the same time, developing a stable catalyst system capable of producing a steady current for days piques interest for practical applications. Electrochemical OER takes place at the anode and is a more complex reaction than HER. This is due to the formation of high-energy intermediates in various steps, such as H_2O adsorption on the surface of the catalyst, electron transfer, and O-O bond formation. Zhang and coworkers have taken the CoFe-PBA precursor and synthesised the CoP-FeP material. The material requires a low overpotential of only 230 mV to produce the benchmark current density of 10 mA cm^{-2}. Additionally, it displays a lower Tafel slope of 35.5 mV dec^{-1}. The combined impact of their composition and

structure is responsible for the exceptional OER activity of CoP-FeP nanoboxes (CoP-FeP NBs).[95] In another study, Lee and coworkers have developed P-HNCP@NiCoOOH catalyst by using a NiCo-PBA precursor. The catalyst exhibits good activity towards the OER application. It requires an overpotential of 360 mV to produce a current density of 10 mA cm^{-2}.[96]

1.7 Ru - Based Electrocatalysts for HER

In order to obtain electrocatalysts which can outperform the benchmark catalyst in terms of performance as well as price, we need to incorporate some metals into the transition metal-based compounds. Ru is the best choice for this purpose. This is because ruthenium is more affordable than the other Pt-group metals, such as Pt, Pd, and Ir. The cost is only 0.61 times that of Pt. Additionally and importantly, Ru has a similar metal-hydrogen bond strength when compared to Pt (~65 kcal mol^{-1}).[97] Additionally, Ru has performed better in OH chemisorption and water dissociation than other metals.[98] However, under the electrochemical operating conditions, metallic Ru dissolves and becomes unstable during the long-term electrolysis process. Creating bimetallic Ru-based core–shell nanomaterials and alloying Ru with other metals have also been observed to be efficient ways to increase the HER activity. Because of the synergistic effect between various metals and altered electronic structure resulting from the incorporation of Ru. The catalysts obtained by alloying Ru with different metals are found to be highly effective and possess robust stability. Additionally, the catalyst's activation throughout the HER process is favoured by the synergistic impact of several metals.[99] The incorporation of Ru in the material system has been proven to stabilise the active phase and tailor the electronic structure for increased durability and activity in the various electrolytic environments.[100] Numerous studies have been published so far that

demonstrate how the materials' effectiveness increases in the presence of Ru. These aforementioned benefits make it a suitable alternative to the Pt.

1.7.1 Ru and Noble Metal-Based Catalysts

Pd, Pt, and Ru are the precious metals that are regarded of as the best HER catalysts because Ru has effective water dissociation capabilities while Pd and Pt have exceptional hydrogen atom recombination properties.[98] Li et al. created Ru nanoparticles that were homogeneously anchored on a porous carbon sphere and alloyed with trace amounts of Pt (PtRu@RFCS). The catalyst was easily made by condensing resorcinol and formaldehyde with a combination of $RuCl_3$ and H_2PtCl_6. It required a low overpotential of 19.7 mV to obtain a current density of 10 mA cm^{-2}. Due to the metallic Pt nanocluster on PtRu alloy nanoparticles, which causes weak hydrogen bonding and quick hydrated proton dissociation, PtRu@RFCS performs better than the commercial Pt/C. Additionally, by shielding the metals from aggregation, size expansion, detachment, and dissociation, the carbon spheres significantly increase the catalysts' longevity.[101] Further, in another study Liu and coworkers have used a simple solid-liquid phase chemical procedure to create new cation vacancies in a five-fold twinned anisotropic structure (v-$Pd_3Pt_{29}Ru_{62}Te_6$ AS). It exhibited excellent catalytic performance towards HER by requiring a very low overpotential of only 22 and 39 mV in alkaline and acidic media, respectively.[102]

1.7.2 Ru and Non-Noble Metal-Based Catalysts

Ru-based HER catalysts have been developed with non-precious metals such molybdenum (Mo), nickel (Ni), cobalt (Co) etc., according to a number of research investigations.[98] Liu and coworkers have developed Ru/MoS_2/CP by using a

hydrothermal process to create Ru–MoS_2 hybrid nanocomposites on carbon paper which resulted in vertically aligned MoS_2 nanosheets on CP. The $RuCl_3$ solution was used for chemical modification to create the composites, which were then further annealed in an H_2 environment. The material exhibited good performance in alkaline media by requiring only 13 mV of overpotential for 10 mA cm^{-2}. Due to Ru's ability to efficiently dissociate water molecules into OH^- ions, the synthesised electrocatalyst demonstrated exceptional performance in alkaline conditions. Unsaturated Mo and/or S atoms, which may encourage H_{ads} adsorption and their recombination into H_2, as well as the distinctive porous shape of vertically orientated MoS_2 nanosheets, which may offer an abundance of exposed reaction sites, were responsible for its excellent performance.[103] Additionally, Demir *et al.* reported that Ru^{3+} ions impregnated on nanoceria were reduced using $NaBH_4$ to create ceria (CeO_2)-supported Ru^0 nanoparticles (Ru^0/CeO_2). In an acidic solution, the hybrid nanocomposite containing Ru demonstrated exceptional electrocatalytic efficacy with a small overpotential value (47 mV at 10 mA cm^{-2}).[104]

1.7.3 MOF-Derived Ru Containing Electrocatalysts

Because of their large surface area, adjustable structure, and configurable porosity, MOFs have been widely exploited as sacrificial template as a novel approach to create electrocatalysts.[105,106] A MOF-assisted method has been used to create Ru-based catalysts using additional metals. Xu *et al.* synthesised low-ruthenium containing NiRu alloy nanoparticles enwrapped in nitrogen-doped carbon by Ru doping in Ni-based MOF, followed by pyrolysis technique under a nitrogen atmosphere at 800 °C. During thermal annealing, N-doped carbon shell formed on NiRu alloy nanoparticles enhances the HER activity and durability of the electrocatalyst by protecting the agglomeration of the particles and corrosion of the material. To produce the current density of 10 mA cm^{-}

^{2} the material required an overpotential of 50 and 32 mV in 0.5 M H_2SO_4 and 1 M KOH respectively.[107] In another study, a Ru–MoO_2 nanohybrid was created by Jiang *et al.* because the strong electronic connection between Ru and Mo would increase electrical conductivity and effectively lower the intermediate energy barriers. The catalysts were prepared by a facile in situ pyrolysis of a Ru-modified Mo-MOF under an inert environment. In both alkaline (29 mV in 1 M KOH) and acidic (55 mV in 0.5 M H_2SO_4) conditions, the nanocomposites showed low overpotential at 10 mA cm^{-2} due to the strong electronic connections between MoO_2 and Ru nanoparticles caused by the synergistic interaction.[108]

1.7.4 PBA-Derived Ru Containing Electrocatalysts

With the aid of PBAs and a one-step thermal treatment utilising a $Co_3[Co(CN)_6]_2$ precursor and $RuCl_3$, *Su et al.* created Ru–Co bimetallic nanoalloys enwrapped in N-doped graphene layers (RuCo@NC). It requires a low overpotential of 28 mV in 1 M KOH to produce 10 mA cm^{-2}. Because of the protection provided by the carbon cage, this new catalyst demonstrated exceptional durability over 10,000 cycles and high catalytic activity realised by the synergistic action of RuCo alloys.[109] In a similar study, Yan and coworkers used Co-PBA and $RuCl_3$ as precursors, the obtained material was then subjected to phosphidation which resulted in the Ru-incorporated CoP (Ru-CoP). The optimised catalyst required a low overpotential of 51 mV to reach the benchmark current density value in 1 M KOH electrolyte.[110]

1.8 Conclusion

The goal of HER electrocatalyst research is to produce H_2 on an industrial scale in a stable and effective manner. In order to satisfy the realistic demands of long-term and high-load operation, plans for the large-scale production of high-efficiency catalysts must be developed. Additionally, the catalytic materials must have excellent thermal and chemical stability.[111] To effectively catalyse the electrochemical processes, the electrocatalysts should be able to ensure rapid electron and mass movement as well as plenty of areas for surface reactions. Conversely, complex nanoarchitectures impede catalytic activity, leading to poor electrochemical performance for HER.

As discussed, noble-metal-based catalysts show good performance for the HER. However, their broad practical use is limited by high cost, low abundance, and poor electrochemical stability. Therefore, researchers are investing considerable effort in developing noble-metal-free electrocatalysts that can perform more effectively in electrochemical reactions than noble metal-based catalysts. While non-noble metal catalysts are more affordable and durable, their performance toward the HER is not as remarkable as that of state-of-the-art catalysts.[24,27] Although MOFs have a large surface area and structural tunability, their direct application is limited by intrinsic instability in alkaline, acidic, or oxidative conditions. The metal–ligand linkages in MOFs are susceptible to degradation, which diminishes their catalytic activity. Over prolonged operation, MOFs can undergo phase changes or active site leaching, even though pyrolysis can increase their stability by producing carbonaceous or metallic derivatives. Since their organic linkers are often insulating, most of the traditional MOFs are inherently poor conductors, restricting their ability to transfer electrons efficiently during electrocatalysis. Although MOF-derived materials, like carbonised derivatives, exhibit

improved conductivity, achieving excellent performance often requires additional modifications such as doping or hybridisation with conductive components. Pore blockage or suboptimal structural design often limits the density and accessibility of active sites in MOFs. Some active sites may be lost due to sintering, aggregation, or insufficient exposure when MOFs are converted into derived materials. Even while MOFs function well in lab conditions, low current densities at industrial scale, large overpotentials, and inadequate stability restrict their practical use.[56]

Additionally, so far, there have been encouraging breakthroughs in research on the PBA-derived electrocatalysts for batteries, supercapacitors, OER and HER. However, while people across the world continue to make progress, there are still many issues that must be addressed. While PBA-derived materials have benefits including rapid ion channels, tunability, and open frameworks, their main disadvantages are structural water, flaws, low conductivity, and stability problems, particularly in non-aqueous batteries. While many efforts have been made to make PBA-derived materials a viable alternative to the traditional state-of-the-art catalyst for HER and OER, attaining equivalent or better activity necessitates additional attention. The PBA-derived materials show good performance in the supercapacitor application, but their poor energy density limits their widespread applicability. To improve crystal stability, increase the reversibility of oxidation-reduction reactions, optimise the carrier ion diffusion dynamics, increase electrical conductivity in ionic/electronic systems, raise the working voltage of electrodes, reduce undesirable side reactions, and increase the contributions of capacitance to the electrode capacity, more research into more complex synthesis techniques is imperative.[76] Additionally, designing supercapacitors with exceptionally high energy densities comparable to batteries remains a major hurdle.[76,112] Nonetheless,

obtaining higher activity electrocatalysts through creative modification and putting them into large-scale industrialisation remains a significant issue.[113]

The Ru-based electrocatalysts have shown exceptional HER activity in both alkaline and acidic electrolytes. More significantly, Ru is highly affordable than other precious metals and is electrochemically durable. Numerous techniques have been used to enhance HER performance, including increasing electrical conductivity through the use of carbon materials to facilitate electron transport, increasing electrocatalytic activity by incorporating heteroatoms and/or transition metals, increasing the number of active sites through nanostructuring, lowering the Ru content through MOF-assisted methods, and other novel techniques. Ru containing catalysts for the HER have demonstrated exceptional performance across all pH ranges, according to several studies. In particular, Ru-based catalysts have outperformed Pt/C under alkaline circumstances because of their exceptional H_2O dissociation characteristics, which are evidenced by their binding energies of H_2O and OH. Furthermore, it is crucial for the creation of safe and commercially feasible water splitting technologies. The development of hydrogen as a sustainable and clean energy source that can substitute fossil fuels might result from such efforts.[98] The **Table 1.1** summarises various electrocatalysts and their performance for HER.

1.9 Challenges and Our Approach Towards the Electrocatalyst Design

Although the HER performance of the present catalysts has been significantly improved during the past few years under laboratory conditions but their insufficient stability, excessive overpotentials, and low current densities at industrial scales restrict the real-world usability of the existing catalysts. In addition to unlocking their potential in

electrocatalysis, resolving these issues will increase their practicality in other fields, including sensing, gas separation, and energy storage.[56,77]

By taking into consideration the above discussion, Prussian blue analogues containing transition metals such as Ni and Co, along with Ru can be synthesised and utilised as a precursor to derive electrocatalysts from them for HER application. Ni and Co-based materials can show good performance towards the HER, as evident from the Volcano plot **(Figure 1.7)**. The Ni and Co are also inexpensive and abundantly available. But the performance exhibited by the Ni and Co based materials are not up to the mark when compared with that of the state-of-the-art catalyst. However, improved catalytic efficiency has been achieved by strategies such as heterostructure assembly, elemental doping, strain modulation, and defect engineering. Electronic structure modification via cation insertion is particularly efficient, as introducing secondary metal species can change the crystal field, optimise hydrogen adsorption free energy, and synergistically improve reaction kinetics. The presence of Ru in PBA or PBA-derived materials enhances the activity of the redox centre as well as makes the Faradaic reactions faster. This is so because, unlike many 3d metals, which are restricted to 1-2 redox couples, ruthenium can access numerous stable oxidation states ($Ru^{2+}/Ru^{3+}/Ru^{4+}/Ru^{+}$). The Ru modifies the electronic structures of the materials and improves the reaction kinetics, charge transfer process, intrinsic conductivity and electron delocalization process. In addition to this, Ru incorporation lowers the energy barrier of the adsorption/desorption process during the HER process.[110,114]

Therefore, by keeping in mind all the aforementioned discussions, we have successfully synthesised RuCo-PBA, RuNi-PBA and Ru-Ru-PBA. We have derived chalcogenide electrocatalysts from RuCo-PBA and NiRu-PBA. Furthermore, we have synthesised a nanoalloy and a nanocomposite from RuCo-PBA and RuRu-PBA, respectively. We have

studied the electrochemical performances of the synthesised electrocatalysts towards HER.

Table 1.1 Electrocatalysts and their performance towards HER in different media.

Sl No.	Electrocatalysts	Overpotential at 10 mA cm^{-2} (mV)	Tafel Slope (mV dec^{-1})	Electrolyte	References
1	Au@PdAgNRBs	26.2	30	0.5 M H_2SO_4	115
2	Ru-MoO_2	29	31	1.0 M KOH	108
3	Ru-NC-700	12	14	0.5 M H_2SO_4	116
4	Ni-MOF	350	60	0.5 M H_2SO_4	117
5	Co-MOF	101	121	0.5 M H_2SO_4	118
6	Co@Co_3O_4-NC	221	77.3	1.0 M KOH	119
7	Ni_2PNS	168	63	1.0 M KOH	120
8	ZIF-67	256	127.2	0.5 M H_2SO_4	121
9	Co-BDC/MoS_2	155	86	1.0 M KOH	122
10	FeCo@nitrogen doped graphene	262	74	0.5 M H_2SO_4	80
11	PdCo@nitrogen doped graphene	80	31	0.5 M H_2SO_4	123
12	IrCo@nitrogen doped graphene	24	23	0.5 M H_2SO_4	124
13	CoP@FeCoP/NC	141	56.34	1.0 M KOH	125
14	Co_3S_4@MoS_2	136	74	1.0 M KOH	126

Sl No.	Electrocatalysts	Overpotential at 10 mA cm^{-2} (mV)	Tafel Slope (mV dec^{-1})	Electrolyte	References
15	Mo-CoNCs	127	55	0.5 M H_2SO_4	127
16	NHPBA	70	52	0.5 M H_2SO_4	128
17	Pt-$Ni_3[Fe(CN_6)]_2$	59	31	0.5 M H_2SO_4	129
18	FeHCF/GA	150	65	0.5 M H_2SO_4	130
19	RuP_x@NPC	74	70	1.0 M KOH	131

1.10 References

1. R. G. Newell, D. Raimi and G. Aldana, *Resour. Futur.*, 2019, 46.

2. B. Johnston, M. C. Mayo and A. Khare, *Technovation*, 2005, **25**, 569–585.

3. N. Kumar, K. Naveen, M. Kumar, T. C. Nagaiah, R. Sakla, A. Ghosh, V. Siruguri, S. Sadhukhan, S. Kanungo and A. K. Paul, *ACS Appl. Energy Mater.*, 2021, **4**, 1323–1334.

4. S. Ghosh and R. N. Basu, *Nanoscale,* 2018, **10**, 11241–11280.

5. J. Jia and Y. Lan, *Molecules,* 2023, **28**, 7383.

6. N. Farooq, Z. ur Rehman, M. I. Khan, S. Asghar, M. Saleem, R. Irshad, A. Sheikh, A. Shanableh, S. Manzoor and Z. U. Khan, *New J. Chem.*, 2024, **48**, 8933–8962.

7. R. Avtar, N. Sahu, A. K. Aggarwal, S. Chakraborty, A. Kharrazi, A. P. Yunus, J. Dou and T. A. Kurniawan, *Resources,* 2019, **8**, 149.

8. W. J. Ong, N. Zheng and M. Antonietti, *Nanoscale,* 2021, **13**, 9904 -9907.

9. J. O. M. Bockris, *Int. J. Hydrogen Energy*, 2002, **27**, 731–740.

10. P. Hota, A. Das and D. K. Maiti, *Int. J. Hydrogen Energy, 2023,* **48**, 523–541.

11. B. H. R. Suryanto, Y. Wang, R. K. Hocking, W. Adamson and C. Zhao, *Nat. Commun.*, 2019, **10**, 1–10.

12. S. Wang, A. Lu and C. J. Zhong, *Nano Converg.,* 2021, **8**, 1–23.

13. Y. Wang, C. Wang, M. Chen, Z. Tang, Z. Yang, J. Hu and H. Zhang, *Fuel Process. Technol.*, 2019, **192**, 227–238.

14. P. Nikolaidis and A. Poullikkas, *Renew. Sustain. Energy Rev.,* 2017, **67**, 597-611.

15. V. Balasubramanian, S. K. Butti, N. V. Choudary, R. Parthasarathy and S. K. Bhargava, *Chem. Commun.,* 2025, **61**, 15494-15509.

16. Y. Choi, J. H. Lee and D. H. Youn, *Molecules*, 2024, **29**, 4975.

17. Q. Wang, C. S. Cha, J. Lu and L. Zhuang, *Phys. Chem. Chem. Phys.*, 2009, **11**, 679–687.

18. A. Raveendran, M. Chandran and R. Dhanusuraman, *RSC Adv.,* 2023, **13**, 3843 3876.

19. Y. Han, X. Yue, Y. Jin, X. Huang and P. K. Shen, *J. Mater. Chem. A*, 2016, **4**, 3673–3677.

20. M. Plevová, J. Hnát and K. Bouzek, *J. Power Sources,* 2021, **507**, 230072.

21. H. Yang, M. Driess and P. W. Menezes, *Adv. Energy Mater.,* 2021, **11**, 2102074.

22. X. Zou and Y. Zhang, *Chem. Soc. Rev.*, 2015, **44**, 5148–5180.

23. S. Liu, M. Li, C. Wang, P. Jiang, L. Hu and Q. Chen, *ACS Sustain. Chem. Eng.*, 2018, **6**, 9137–9144.

24. N. T. Suen, S. F. Hung, Q. Quan, N. Zhang, Y. J. Xu and H. M. Chen, *Chem. Soc. Rev.,* 2017, **46**, 337–365.

25. M. Chatenet, B. G. Pollet, D. R. Dekel, F. Dionigi, J. Deseure, P. Millet, R. D. Braatz, M. Z. Bazant, M. Eikerling, I. Staffell, P. Balcombe, Y. Shao-Horn and H. Schäfer, *Chem. Soc. Rev.,* 2022, **51**, 4583–4762.

26. J. Song, C. Wei, Z. F. Huang, C. Liu, L. Zeng, X. Wang and Z. J. Xu, *Chem. Soc. Rev.*, 2020, **49**, 2196–2214.

27. J. Zhu, L. Hu, P. Zhao, L. Y. S. Lee and K. Y. Wong, *Chem. Rev.,* 2020, **120**, 851–918.

28. M. Tofighi-Milani, S. Fattaheian-Dehkordi and M. Lehtonen, *IEEE Access*, 2025, **13**, 39870-39885.

29. A. Ursua, L. M. Gandia and P. Sanchis, *Proc. IEEE*, 2012, **100**, 410–426.

30. Y. Li, C. Yang, H. Wang, L. Ma and Y. Wang, *Discov. Electrochem.*, 2025, **2** (39), 1–41.

31. M. Winter and R. J. Brodd, *Chem. Rev.*, 2004, **104**, 4245–4269.

32. H. Ooka, J. Huang and K. S. Exner, *Front. Energy Res.*, 2021, **9**, 654460.

33. R. Parsons, *Trans. Faraday Soc.,* 1958, **54**, 1053-1063.

34. B. E. Conway and B. V Tilak, *Electrochim. Acta,* 2002, **47**, 3571-3594.

35. S. Trasatti, *J. Electroanal. Chem. Interfacial Electrochem.*, 1972, **39**, 163–184.

36. B. E. Conway and J. O'M Bockris, *J. Chem. Phys.*, 1957, **26**, 532–541.

37. J. K. Nørskov, T. Bligaard, A. Logadottir, J. R. Kitchin, J. G. Chen, S. Pandelov and U. Stimming, *J. Electrochem. Soc.*, 2005, **152**, J23.

38. C. Tsai, F. Abild-Pedersen and J. K. Nørskov, *Nano Lett.*, 2014, **14**, 1381–1387.

39. J. Greeley, J. K. Nørskov, L. A. Kibler, A. M. El-Aziz and D. M. Kolb, *ChemPhysChem*, 2006, **7**, 1032–1035.

40. R. Michalsky, Y. J. Zhang and A. A. Peterson, *ACS Catal.*, 2014, **4**, 1274–1278.

41. E. Skúlason, V. Tripkovic, M. E. Björketun, S. Gudmundsdóttir, G. Karlberg, J. Rossmeisl, T. Bligaard, H. Jónsson and J. K. Nørskov, *J. Phys. Chem. C*, 2010, **114**, 18182–18197.

42. H. Yuan, J. Li, Z. Tang, Y. Wang, T. Wu, M. Huang, L. Zhao, Z. Zhao, H. Liu, C. Xu, X. Liu and W. Zhou, *Chem. Eng. J.*, 2024, **492**, 152339.

43. L. Zhai, X. She, L. Zhuang, Y. Li, R. Ding, X. Guo, Y. Zhang, Y. Zhu, K. Xu, H. J. Fan and S. P. Lau, *Angew. Chemie - Int. Ed.*, 2022, **61**, e202116057.

44. P. Wang, Y. Yan, P. Wang, Z. Ye, X. Zheng and W. Cai, *Chem. Eng. J.*, 2023, **455**, 140856.

45. J. Verma and S. Goel, *Int. J. Hydrogen Energy*, 2022, **47**, 38964–38982.

46. R. Y. Fan, J. Y. Xie, N. Yu, Y. M. Chai and B. Dong, *Int. J. Hydrogen Energy*, 2022, **47**, 10547–10572.

47. J. Jiang, Q. Liu, C. Zeng and L. Ai, *J. Mater. Chem. A*, 2017, **5**, 16929–16935.

48. Y. Zhang, Q. Fu, B. Song and P. Xu, *Accounts Mater. Res.*, 2022, **3**, 1088–1100.

49. A. Parra-Puerto, K. L. Ng, K. Fahy, A. E. Goode, M. P. Ryan and A. Kucernak, *ACS*

Catal., 2019, **9**, 11515–11529.

50. J. Xu, G. Shao, X. Tang, F. Lv, H. Xiang, C. Jing, S. Liu, S. Dai, Y. Li, J. Luo and Z. Zhou, *Nat. Commun.*, 2022, **13**, 2193.

51. Z. Du, N. Jannatun, D. Yu, J. Ren, W. Huang and X. Lu, *Nanoscale*, 2018, **10**, 23070–23079.

52. H. Zhou, Y. Wang, R. He, F. Yu, J. Sun, F. Wang, Y. Lan, Z. Ren and S. Chen, *Nano Energy*, 2016, **20**, 29–36.

53. Y. Wu, R. Sun and J. Cen, *Front. Chem.*, 2020, **8**, 386.

54. R. Dong, M. Pfeffermann, H. Liang, Z. Zheng, X. Zhu, J. Zhang and X. Feng, *Angew. Chemie - Int. Ed.*, 2015, **54**, 12058–12063.

55. Y. S. Li, J. W. Yi, J. H. Wei, Y. P. Wu, B. Li, S. Liu, C. Jiang, H. G. Yu and D. S. Li, *J. Solid State Chem.*, 2020, **281**, 1–7.

56. E. S. Sowbakkiyavathi, P. Dhandapani, S. Ramasamy, J. H. Oh, I. In, S. J. Lee and A. Subramania, *RSC Sustainability,*2025, **3**, 3628–3651.

57. Y. Peng, S. Sanati, A. Morsali and H. García, *Angew. Chemie - Int. Ed.,* 2023, **62**, e202214707.

58. H. F. Wang, L. Chen, H. Pang, S. Kaskel and Q. Xu, *Chem. Soc. Rev.,* 2020, **49**, 1414–1448.

59. Z. Liang, R. Zhao, T. Qiu, R. Zou and Q. Xu, *EnergyChem,* 2019, **1**, 100001.

60. X. Qin, D. Kim and Y. Piao, *Carbon Energy,* 2021, **3**, 66–100.

61. Q. Wang, Y. Song, D. Sun and L. Zhang, *ACS Omega*, 2021, **6**, 11077–11082.

62. Z. Abbas, N. Hussain, I. Ahmed and S. M. Mobin, *Inorg. Chem.*, 2023, **62**, 8835–

8845.

63. E. Vijayakumar, S. Ramakrishnan, C. Sathiskumar, D. J. Yoo, J. Balamurugan, H. S. Noh, D. Kwon, Y. H. Kim and H. Lee, *Chem. Eng. J.*, 2022, **428**, 131115.

64. K. Srinivas, Y. Chen, X. Wang, B. Wang, M. Karpuraranjith, W. Wang, Z. Su, W. Zhang and D. Yang, *ACS Sustain. Chem. Eng.*, 2021, **9**, 1920–1931.

65. H. H. Do, M. A. Tekalgne, V. A. Tran, Q. Van Le, J. H. Cho, S. H. Ahn and S. Y. Kim, *Fuel,* 2022, **329**, 125468.

66. J. Feng, H. Zhou, J. Wang, T. Bian, J. Shao and A. Yuan, *Int. J. Hydrogen Energy*, 2018, **43**, 20538–20545.

67. D. Duan, J. Feng, S. Liu, Y. Wang and X. Zhou, *J. Electroanal. Chem.*, 2021, **892**, 115300.

68. X. Song, S. Song, D. Wang and H. Zhang, *Small Methods,* 2021, **5**, 2001000.

69. A. Kraft, *ChemTexts*, 2018, **4**,16.

70. Y. Wei, M. Zheng, W. Zhu and H. Pang, *Carbon Neutralization,* 2023, **2**, 271–299.

71. W. J. Li, C. Han, G. Cheng, S. L. Chou, H. K. Liu and S. X. Dou, *Small,* 2019, **15**, 1900470.

72. K. Zhang, M. Xu, J. Wang and Z. Chen, *Nanoscale*, 2023, **15**, 17525–17533.

73. J. Gao, Q. Huang, Y. Wu, Y. Q. Lan and B. Chen, *Adv. Energy Sustainability Res.,* 2021, **2**, 2100033.

74. U. J. Ryu, S. Jee, P. C. Rao, J. Shin, C. Ko, M. Yoon, K. S. Park and K. M. Choi, *Coord. Chem. Rev.,* 2021, **426**, 213544.

75. C. Chen, D. Xiong, M. Gu, C. Lu, F. Y. Yi and X. Ma, *ACS Appl. Mater. Interfaces*,

2020, **12**, 35365–35374.

76. K. Wu, G. Zhang, B. Yan and H. Pang, *ChemSusChem,* 2025, e202501886.

77. G. Janani, S. Park, S. Surendran, Y. Lim, D. J. Moon, G. H. Jeong, H. Choi, G. Kwon, X. Lu, K. Jin and U. Sim, *Next Materials,* 2025, **9**, 100930.

78. J. Deng, P. Ren, D. Deng and X. Bao, *Angew. Chemie - Int. Ed.*, 2015, **54**, 2100–2104.

79. M. Tavakkoli, T. Kallio, O. Reynaud, A. G. Nasibulin, C. Johans, J. Sainio, H. Jiang, E. I. Kauppinen and K. Laasonen, *Angew. Chemie*, 2015, **127**, 4618–4621.

80. Y. Yang, Z. Lun, G. Xia, F. Zheng, M. He and Q. Chen, *Energy Environ. Sci.*, 2015, **8**, 3563–3571.

81. D. Li, S. Xie, H. Dong, B. Gao, X. Zhang, P. K. Chu and X. Peng, *Int. J. Hydrogen Energy*, 2024, **87**, 401–408.

82. J. Shi, Y. Bao, R. Ye, J. Zhong, L. Zhou, Z. Zhao, W. Kang and S. B. Aidarova, *Catal. Sci. Technol.*,2025, **15**, 2104–2131.

83. X. Y. Yu, Y. Feng, Y. Jeon, B. Guan, X. W. D. Lou and U. Paik, *Adv. Mater.*, 2016, **28**, 9006–9011.

84. X. Ding, M. Zhang, X. Chang and X. Zhou, *Dalt. Trans.*, 2022, **52**, 1680–1686.

85. R. Wang, C. Qian, Z. Zhang, H. Shen, J. Xia, D. Cui, K. Sun, H. Liu, C. Guo, F. Yu, J. Li and W. Bao, *Small,* 2023, **19**, 2206848.

86. Y. Guo, Y. Liu, Y. Liu, C. Zhang, K. Jia, J. Su and K. Wang, *Catalysts,* 2022, **12**, 739.

87. B. Wang, X. Zhang and Y. Chen, *J. Phys.: Conf. Ser.*, 2021 **1838**, 012018.

88. J. Sun, N. Sha, T. Xu, C. Sun, Y. Xie, C. Lv and X. Wang, *New J. Chem.*, 2025, **49**, 12986–12994.

89. C. G. Read, J. F. Callejas, C. F. Holder and R. E. Schaak, *ACS Appl. Mater. Interfaces*, 2016, **8**, 12798–12803.

90. Q. Kang, M. Li, J. Shi, Q. Lu and F. Gao, *ACS Appl. Mater. Interfaces*, 2020, **12**, 19447–19456.

91. Z. Ding, H. Yu, X. Liu, N. He, X. Chen, H. Li, M. Wang, Y. Yamauchi, X. Xu, M. A. Amin, T. Lu and L. Pan, *J. Colloid Interface Sci.*, 2022, **616**, 210–220.

92. D. W. Wang, Y. Di Zhu, S. Lei, S. M. Chen, Z. G. Gu and J. Zhang, *J. Solid State Chem.*, 2021, **293**, 121779.

93. B. Hu, J. Jiang, P. Wang, H. Cheng, D. Li, Z. Zhou, Y. Deng, N. Zhao, X. Yuan and Z. Li, *ACS Appl. Nano Mater.*, 2025, **8**, 720–732.

94. Y. Lei, F. Zhang, G. Li, J. Yang, Y. Xie, H. Hu, Y. Shen, X. Zhang and X. Wang, *Energy and Fuels*, 2024, **38**, 8277–8284.

95. S. Zhang, Y. Cheng, Z. Ni, X. Lei, B. Wang, X. Liu and R. Guo, *J. Power Sources*, 2024, **623**, 235454.

96. S. Lee, J. Kim, O. Kwon, J. Lee, P. chen Su and J. Kim, *Appl. Surf. Sci.*, 2025, **700**, 163206.

97. C. Li and J. B. Baek, *ACS Omega,* 2020, **5**, 31-40.

98. S. Y. Bae, J. Mahmood, I. Y. Jeon and J. B. Baek, *Nanoscale Horiz.,*2020, **5**, 43-56.

99. S. Han, Q. Yun, S. Tu, L. Zhu and Q. Lu, *J. Mater. Chem. A*, 2019, **7**, 24691–24714.

100. H. Li, X. Qian, C. Xu, S. Huang, C. Zhu, X. Jiang, L. Shao and L. Hou, *ACS Appl. Mater. Interfaces*, 2017, **9**, 28394–28405.

101. K. Li, Y. Li, Y. Wang, J. Ge, C. Liu and W. Xing, *Energy Environ. Sci.*, 2018, **11**, 1232–1239.

102. S. Liu, X. Mu, W. Li, M. Lv, B. Chen, C. Chen and S. Mu, *Nano Energy*, 2019, **61**, 346–351.

103. J. Liu, Y. Zheng, D. Zhu, A. Vasileff, T. Ling and S. Z. Qiao, *Nanoscale*, 2017, **9**, 16616–16621.

104. E. Demir, S. Akbayrak, A. M. Önal and S. Özkar, *ACS Appl. Mater. Interfaces*, 2018, **10**, 6299–6308.

105. H. Furukawa, K. E. Cordova, M. O'Keeffe and O. M. Yaghi, *Science*, 2013, **341**, 1230444.

106. N. Stock and S. Biswas, *Chem.Rev.*, 2012, **112**, 933–969.

107. Y. Xu, S. Yin, C. Li, K. Deng, H. Xue, X. Li, H. Wang and L. Wang, *J. Mater. Chem. A*, 2018, **6**, 1376–1381.

108. P. Jiang, Y. Yang, R. Shi, G. Xia, J. Chen, J. Su and Q. Chen, *J. Mater. Chem. A*, 2017, **5**, 5475–5485.

109. J. Su, Y. Yang, G. Xia, J. Chen, P. Jiang and Q. Chen, *Nat. Commun.*, 2017, **8**, 1–10.

110. Y. Yan, J. Huang, X. Wang, T. Gao, Y. Zhang, T. Yao and B. Song, *Front. Chem.*, 2018, **6**, 521.

111. F. Yang, X. Huang, C. Su, E. H. Song, B. X. Liu and B. B. Xiao, *ChemPhysChem,* 2024, **25**, e202400640.

112. P. Huo, J. Zhang, Y. Huang, J. Zheng, X. Yang, X. Gao and Y. Guo, *Clean Energy*, 2025, zkaf067.

113. Y. Qi, L. Qiu, X. Ma, J. Wu, J. Xiang, C. Guo, J. Yu, K. Li, Z. Tao and Y. Lv, *Int. J. Hydrogen Energy*, 2024, **83**, 520–544.

114. P. Jain and P. P. Ingole, *Chem. Phys. Impact*, 2024, **9**, 100693.

115. Z. Fan, Z. Luo, X. Huang, B. Li, Y. Chen, J. Wang, Y. Hu and H. Zhang, *J. Am. Chem. Soc.*, 2016, **138**, 1414–1419.

116. B. Lu, L. Guo, F. Wu, Y. Peng, J. E. Lu, T. J. Smart, N. Wang, Y. Z. Finfrock, D. Morris, P. Zhang, N. Li, P. Gao, Y. Ping and S. Chen, *Nat. Commun.*, 2019, **10**, 631.

117. V. Khrizanforova, R. Shekurov, V. Miluykov, M. Khrizanforov, V. Bon, S. Kaskel, A. Gubaidullin, O. Sinyashin and Y. Budnikova, *Dalt. Trans.*, 2020, **49**, 2794–2802.

118. Y. Zhou, W. Dong, M. Jiang, Y. Wu and D. Li, *J. Solid State Chem.*, 2019, **279**, 120929.

119. C. Bai, S. Wei, D. Deng, X. Lin, M. Zheng and Q. Dong, *J. Mater. Chem. A*, 2017, **5** (20), 9533–9536.

120. Q. Wang, Z. Liu, H. Zhao, H. Huang, H. Jiao and Y. Du, *J. Mater. Chem. A,* 2018, **6** (38), 18720–18727.

121. H. Zong, R. Qi, K. Yu and Z. Zhu, *Electrochim. Acta*, 2021, **393**, 1–10.

122. D. Zhu, J. Liu, Y. Zhao, Y. Zheng and S. Z. Qiao, *Small*, 2019, **15** (14), 1–8.

123. J. Chen, G. Xia, P. Jiang, Y. Yang, R. Li, R. Shi, J. Su and Q. Chen, *ACS Appl.*

Mater. Interfaces, 2016, **8**, 13378–13383.

124. P. Jiang, J. Chen, C. Wang, K. Yang, S. Gong, S. Liu, Z. Lin, M. Li, G. Xia, Y. Yang, J. Su and Q. Chen, *Adv. Mater.*, 2018, **30**, 1705324.

125. J. Shi, F. Qiu, W. Yuan, M. Guo and Z. Lu, *Chem. Eng. J.*, 2021, **403**, 126312.

126. Y. Guo, J. Tang, Z. Wang, Y. Kang and Y. Bando, *Nano Energy*, 2018, **47**, 494–502.

127. B. K. Kang, S. Y. Im, J. Lee, S. H. Kwag, S. Bin Kwon, S. Tiruneh, M.-J. Kim, J. H. Kim, W. S. Yang, B. Lim and D. H. Yoon, *Nano Res.*, 2019, **12**, 1605–1611.

128. S. Zhu, J. Ge, C. Liu and W. Xing, *EnergyChem*, 2019, **1**, 100018.

129. J. Guo, X. Zhang, Y. Sun, L. Tang, Q. Liu and X. Zhang, 2017, **2**, 3–9.

130. L. Li, Y. Huang and Y. Li, *EnergyChem*, 2020, **2**, 100024.

131. J. Chi, W. Gao, J. Lin, B. Dong, K. Yan and J. Qin, *ChemSusChem*, 2018, **11**, 743–752.

CHAPTER-2

Experimental Methods and Characterisation Techniques

2.1 Materials

2.2 Synthesis Techniques

2.2.1 Synthesis of PB and PBA

(a) Coprecipitation Approach

(b) Solvothermal Approach

(c) Electrodeposition Approach

2.2.2 PB/PBA-Derived Electrocatalysts

2.2.3 Ru-Based PBAs and their Derivatives

2.3 Instrumental Techniques

(a) X-Ray Diffraction (XRD)

(b) Fourier Transform Infrared Spectroscopy (FTIR)

(c) Field Emission Scanning Electron Microscopy (FESEM)

(d) Transmission Electron Microscopy (TEM)

(e) Energy-Dispersive X-ray Spectroscopy (EDS)

(f) Brunauer-Emmett-Teller (BET) Surface Area

(g) X-ray Photoelectron Spectroscopy (XPS)

(h) Raman Spectroscopy

(i) Inductively Coupled Plasma-Optical Emission Spectroscopy (ICP-OES)

(j) Gas Chromatography (GC)

2.4 Electrochemical Measurements

2.4.1 Construction of Electrochemical Cell and Electrode Fabrication

2.4.2 Electrochemical Characterisation Techniques Associated with Water Splitting

(a) Cyclic Voltammetry

(b) Overpotential

(c) Tafel Slope

(d) Electrochemical Impedance Spectroscopy (EIS)

(e) Turn-Over Frequency (TOF)

(f) Electrochemical Active Surface Area (ECSA)

(g) Stability

2.5 References

The characterisation techniques utilised in this current thesis are X-ray diffraction (XRD), Fourier transform infrared spectroscopy (FTIR), field-emission scanning electron microscopy (FESEM), transmission electron microscopy (TEM), X-ray photoelectron spectroscopy (XPS), Raman spectroscopy, energy dispersive X-ray (EDX), gas chromatography (GC), inductively coupled plasma-optical emission spectroscopy (ICP-OES) and physisorption technique (BET). These techniques provide information on a range of material characteristics, such as oxidation states, redox, thermal, structural, and morphological characteristics. These methods' basic principles are briefly explained. Various synthetic techniques to synthesise PB/PBA along with their derivatives are also discussed. A thorough explanation of the various experimental configurations utilised to carry out studies on hydrogen evolution reaction (HER) utilising locally designed and built catalysts is also provided.

2.1 Materials

All the materials used in this thesis were received from the company mentioned in front of them **(Table 2.1)** without additional purification.

Table 2.1 List of chemicals along with their formula and company.

Chemical formula	Chemical Name	Name of Company
Pt/C	Platinum carbon	Sigma Aldrich
C_2H_5OH	Ethanol	Merck
H_2SO_4	Sulfuric acid	Himedia
KOH	Potassium hydroxide	Sigma Aldrich
$PtCl_2$	Platinum chloride	Sigma Aldrich
$RuCl_3$	Ruthenium chloride	Sigma Aldrich

Chemical formula	Chemical Name	Name of Company
RuO_2	Ruthenium oxide	Sigma Aldrich
$Co(NO_3)_2.6H_2O$	Cobalt nitrate hexahydrate	Sigma Aldrich
$Ni(NO_3)_2.6H_2O$	Nickel nitrate hexahydrate	Sigma Aldrich
$NaBH_4$	Sodium borohydride	Sigma Aldrich
S	Sulphur powder	Sigma Aldrich
$K_4[Ru(CN)_6].xH_2O$	Potassium hexacyanoruthenate(II) hydrate	Sigma Aldrich
$Ru(O_2C_5H_7)_3$	Ruthenium acetylacetonate	Sigma Aldrich
$C_7HF_{13}O_5S.C_2F_4$	Sulphonated tetrafluoroethylene copolymer (Nafion)	Alfa Aesar and Sigma Aldrich
$Na_3C_6H_5O_7$	Trisodium citrate	Sigma Aldrich
C	Acetylene black	Sigma Aldrich
$K_3[Co(CN)_6.xH_2O$	Potassium hexacyanocobaltate (III) hydrate	Sigma Aldrich
Se	Selenium powder	TCI
$H_2NNH_2.H_2O$	Hydrazine monohydrate	Sigma Aldrich

2.2 Synthesis Techniques

2.2.1 Synthesis of PB and PBA

PB/PBA synthesis techniques are generally divided into three primary categories (a) the coprecipitation approach, (b) the solvothermal method, and (c) the electrodeposition technique, as shown in **Figure 2.1**.[1]

(a) Coprecipitation Approach

The coprecipitation method, which is the most traditional way to synthesise PB/PBAs, has the benefits of being inexpensive and simple. In this method, a solution of a metal hexacyano complex is added slowly in a dropwise manner to another solution containing a metal ion salt. The resultant precipitate is the PBA, and it possesses random morphology due to the rapid reaction between the metal ions and the ligands. Coordination agents like sodium citrate are used to slow the reaction rates in order to regulate the morphology of PBAs synthesised by the precipitation process.

(b) Solvothermal Approach

Prussian blue microparticles are commonly prepared by employing the hydrothermal process, in which the Fe^{3+}/Fe^{2+} obtained by decomposition of $Fe(CN)_6^{4-}$ in the acidic solution reacts with the remaining $Fe(CN)_6^{4-}$ to generate PB.[2] Co-PBA i.e. $Co_3[Co(CN)_6]_2$ has also been synthesised by both acid as well as non-acid assisted solution by using the solvothermal method from a single precursor $K_3[Co(CN)_6]$. Therefore, PBAs containing a single transition metal can be synthesised using this technique.[3]

(c) Electrodeposition Approach

Besides the two methods discussed above, PBAs can also be synthesised by using the approach of electrodeposition. The process of facilitating the migration of negative and positive ions present in the electrolytic solution to the electrode surface while applying an external electric field is known as electrodeposition. This leads to electrochemical processes which result in deposition. By altering the electrolyte's composition and the deposition parameters, it is possible to precisely control the nucleation and growth

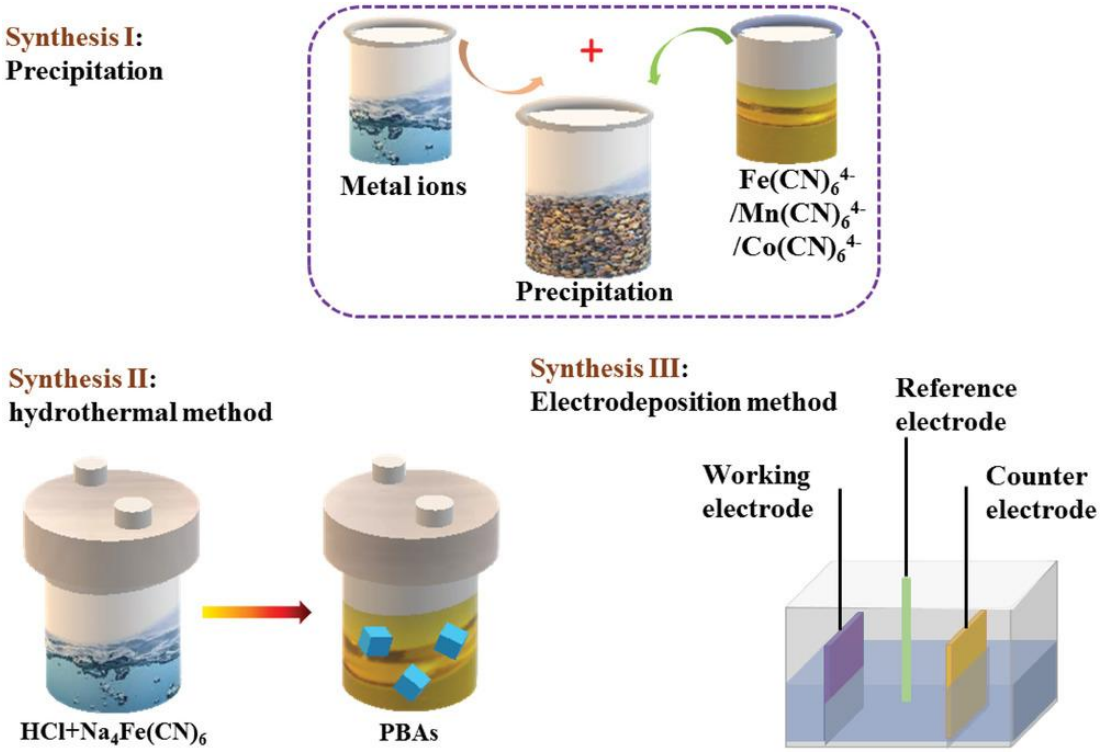

Figure 2.1: Synthesis procedure of Prussian blue and its analogues.[1]

process of PBA on the surface of substrate as well as the material's structure, purity, and shape. Because of their excellent adherence to the conductive substrate, catalysts made via the electrodeposition approach do not require additional binders, preventing the loss of active sites. However, the self-supporting catalysts made by the electrodeposition method have a smaller geometric area than the catalysts made by the aforementioned methods due to the instrument's present limitations, which prevents their use in the production of industrial-grade catalysts.

2.2.2 PB/PBA-Derived Electrocatalysts

PBA-derived synthesis involves three basic steps: pre-treatment, derivatisation, and post-treatment. The process can be complex and time-consuming. Derivatisation is the crucial process in converting a PBA into other materials such as oxides, sulphides, and carbides. Sometimes a pre-treatment is conducted before derivatisation, followed by post-treatment to complete the whole process **(Figure 2.2)**. These procedures are intentionally

chosen to enhance the material's performance in the required application by tuning its morphological, physical, or chemical characteristics.

Pre-treatment processes are typically used to regulate the morphology of PBA. However, morphology engineering is only possible for particles with a minimum size to accommodate complex design. Some of the most commonly used pre-treatment techniques are: templating and direct growth, ion exchange, etching, coating and formation of hybrid or composite materials. Further, derivatisation is an important process in defining PBA-derived chemistry. To maintain the pre-treatment structure, process parameters must be tightly controlled during this transition in chemistry. The derivatisation can be achieved by using various techniques such as annealing in the presence of gas or powders, the solvothermal method, etc., as shown in **Figure 2.2**. The derivatisation technique solely depends on the choice of the product. Finally, post-treatment processes are employed to fine-tune the product by removing undesired products or adding porosities. The post-treatment basically involves techniques such as annealing, etching, and incorporation of a second material to obtain the desired products. However, this requires high temperatures and harsh acids.[4]

2.2.3 Ru-Based PBAs and their Derivatives

The Ru-based PBAs can be synthesised by following the coprecipitation method as discussed in the section 2.2.1a by choosing a suitable metal salt and a metal hexacyano complex. They can also be synthesised in solvothermal manner by taking required precursors in an autoclave and heating the final solution at a required temperature. Thus, obtained PBAs can be used as precursors to obtain other derivatives like chalcogenides, alloys, phosphides, nitrides etc., by subjecting them with appropriate reagents in solvothermal or pyrolysis methods as discussed in section 2.2.2.

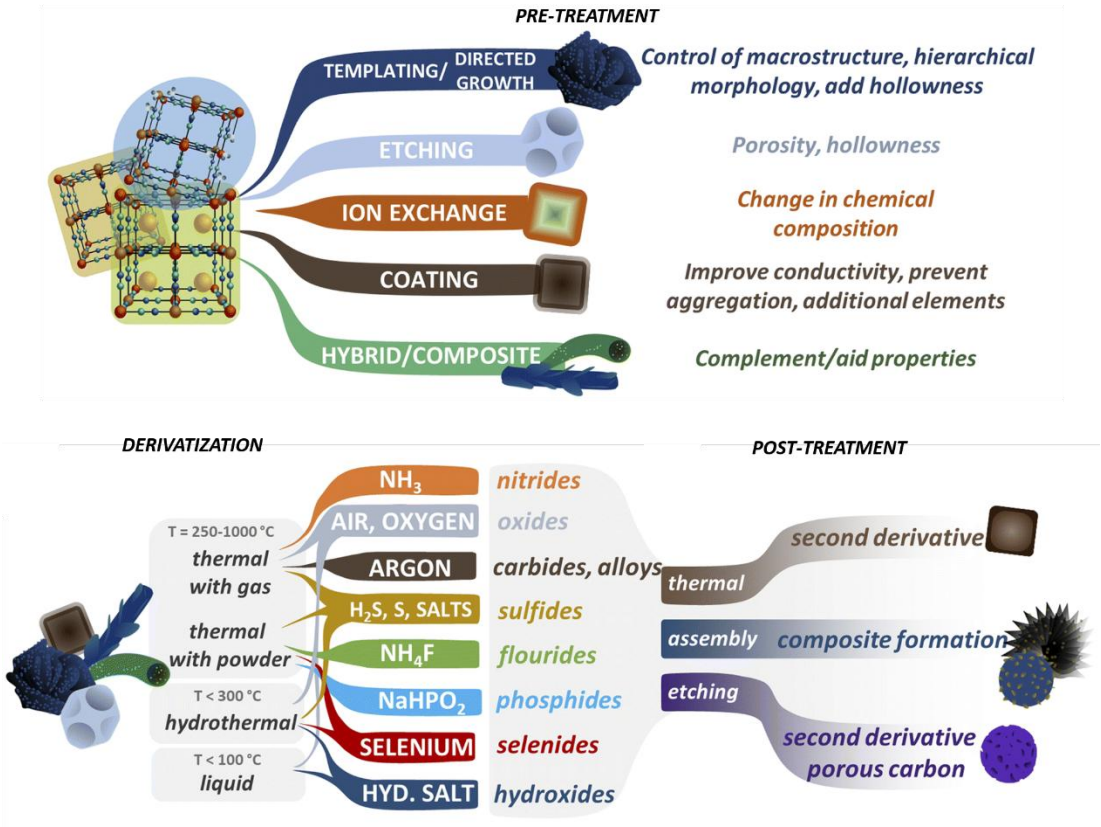

Figure 2.2: Synthesis of PB/PBA-derived materials.[4]

2.3 Instrumental Techniques

(a) X-Ray Diffraction (XRD):[5,6]

XRD is a powerful non-destructive analytical method for examining the phase composition, orientation, and crystal structure of solid, liquid, and powdered materials. Since X-rays are the light source utilised in XRD and have wavelengths in the nanometre range, the material's X-ray scattering produces an interference pattern. The three primary components of X-ray equipment are an XRD detector, a sample holder, and an X-ray source. A heated tungsten tube housed in a clear ceramic vessel serves as the cathode of the X-ray tube, which generates X-rays, while cooled copper foil serves as the anode. the tungsten-emitted electrons are propelled towards a metal (under water cooling) and liberate electrons from the interior shells of Cu atoms. This causes the valence electron

to unwind into an inward position and results in X-beam formation. Cu-source can generate X-beams with two different wave lengths (Cu K_β and Cu K_α, with λ values of 0.139 and 0.154 nm). For effective obstruction, the X-ray should be monochromatic, and using a nickel channel ensures that just K_β is emitted. From the emission beam centred on the sample, the detector determines the scattered beam. The angle formed by the entering and departing directions of the beam is two theta. The scattered X-rays of the sample can interfere in both constructive and destructive manners. The detectors can only read out a signal at angles where constructive interference occurs. The components of a crystalline material are represented by the dots on the graph. The incident X-ray beam is scattered by the material at many planes. As a result, the diffracted X-rays' optical path length is changed. The X-ray beam's incidence angle and the distances between the crystal planes are the only factors that affect the path length's magnitude. This is summarised by the well-known Bragg Equation **(Equation 2.1)**:

$$n\lambda = 2d\ sin\Theta \qquad (2.1)$$

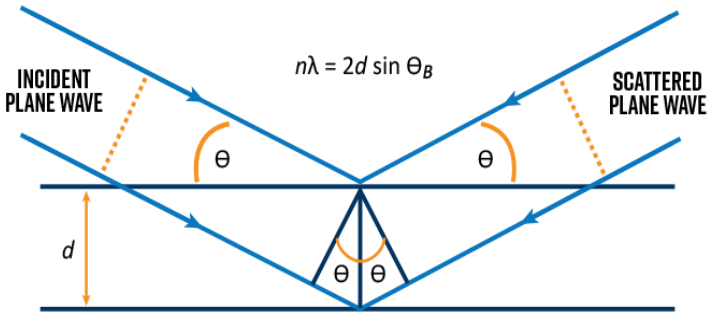

Figure 2.3: Demonstration of X-ray scattering. (adopted from nanoscience Instruments)

where λ and θ are the wavelength of the incident beam and the angle formed by the incident ray and the lattice plane, and n is the interference order. The following terms can be used to represent this equation: constructive interference occurs when the path difference (as calculated by 2d sinθ) is a multiple (n = 1, 2, ..., etc.) of the X-ray

wavelength, **(Figure 2.3)**. We may determine the distance between the material's lattice planes using XRD tests as the wavelength is known and the angles at which constructive interference takes place are observed. The obtained result after measurement is known as the diffractogram. In this instance, the X-ray intensity is displayed on the y-axis and the angle between the incident and diffracted beam, 2θ, is represented on the x-axis. A Bruker diffractometer (DAVINCI D8 ADVANCE) with Cu Kα radiation and wavelength of 0.154 nm was utilised to collect the X-ray spectra for this thesis.

(b) Fourier Transform Infrared Spectroscopy (FTIR)

The molecule's vibration band interacts with light in the infrared spectrum. When the sample is exposed to infrared light, some of the light intensity is absorbed by the vibration and some is reflected. A fingerprint vibrational band is present in the functional groups. Thus, functional groups are identified using FTIR spectroscopy.

(c) Field Emission Scanning Electron Microscopy (FESEM)[7]

FESEM is used to provide high-resolution three-dimensional images of the material's morphology. After being emitted by the electron cannon's cathode, electrons are accelerated by the anode in a high vacuum. A raster pattern is used to scan surface samples while focusing on a comparatively small area. A primary electron interacts with a surface sample atom, producing secondary emissions which are captured and used to

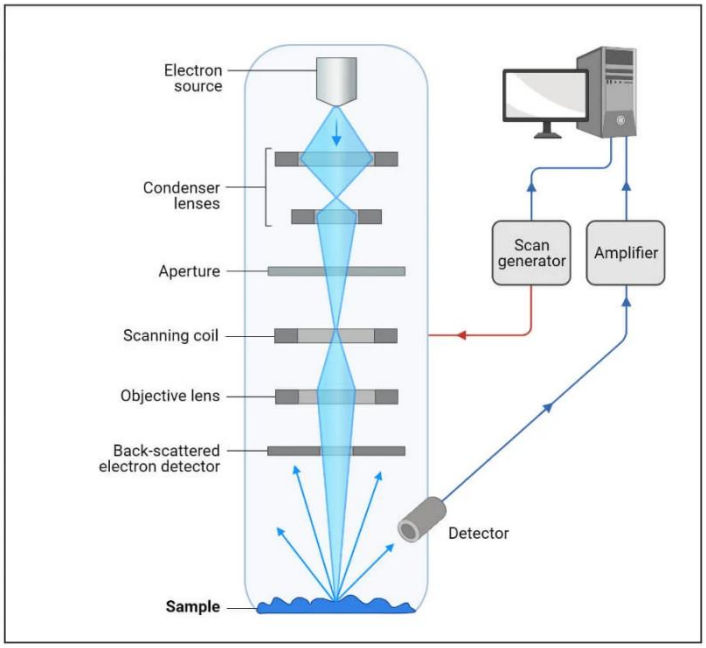

Figure 2.4: Schematic representation of FE-SEM. (adapted from microbenotes)

produce an image. The angle and speed of the secondary beam are closely linked to the material's surface structure. This thesis uses data from a field-emission scanning electron microscope (FESEM) made by Carl Zeiss, Germany (Model: ∑igma) **(Figure 2.4).**

(d) Transmission Electron Microscopy (TEM)[8]

The TEM functions similarly as the principle of a light microscope. The main difference is that a light microscope utilises light rays to focus and produce a picture, whereas a TEM uses an electron beam to concentrate on the material. Electrons have a shorter wavelength than light, which has a longer one. In a TEM, the resolution power enhances as the specimen is irradiated by electrons, increasing the wavelength of electron transmission, whereas in a light microscope, the resolution power increases when the wavelength of light decreases. Because electrons possess a wavelength of 0.005 nm, which is 100,000X shorter than that of light, TEM has a resolution that is around 1000 times better than that of a light microscope. In material research, TEM is

widely used to examine the quality, density, and morphologies of various nanoparticles, including quantum dots and nanowires. A monochromatic electron beam is produced by the electron canon and by the condenser lenses this stream is focused into a narrow coherent beam. The condenser aperture confines the beam and removes high angle electrons. The thickness and transparency of the specimen determine how much energy is conveyed upon impact. This transmitted component is transformed into an image by the objective lens. The image is expanded at each stage as it travels down the column via the intermediate and projection lenses. Light is produced when the picture is received by the fluorescent screen **(Figure 2.5)**. HRTEM creates an interference picture that displays the sample image using both scattered and transmitted electron beams. Surface structures, dislocations, and point defects can be accurately characterised by analysing the lattice defects and crystal structures of various materials in the atomic unit range. We may ascertain the d-spacing of crystals using the indices supplied by the selected area

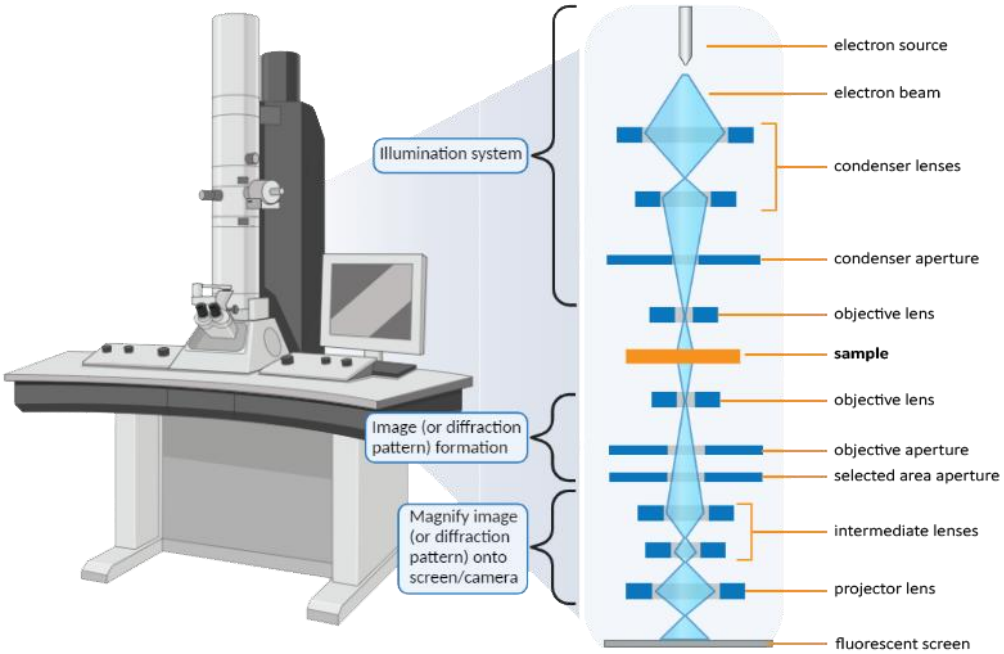

Figure 2.5 Simplified TEM graphic illustrating the important components. (adopted from nanoscience Instruments)

electron diffraction (SAED) pattern. The pattern we get can also tell us about the samples' crystallinity. According to Bragg's law, the sample's crystal planes that run parallel to the electron beam's path will diffract. The electron's periodic potential was subjected to a Fourier transform to produce this diffraction pattern. The interference between the primary electrons and the diffracted electrons results in the back transformation, also called the inverse Fourier transform, which creates a picture. In this thesis, the morphologies of the materials were examined using a transmission electron microscope, model number JEOL F200, operating at a voltage of 200 kV.

(e) Energy-Dispersive X-ray Spectroscopy (EDS)

Elemental composition may be identified and examined using EDS spectroscopy. There is no requirement for an additional device because EDS is present in a SEM or TEM. An electron-hole pair is produced when the sample interacts with incoming X-rays. When a strong bias voltage is supplied across the crystal, the electrons and holes move to electrodes on opposing sides, sending a charge signal to the pulse processor. The energy of the incoming X-rays determines the signal's intensity **(Figure 2.6)**. As a result, the

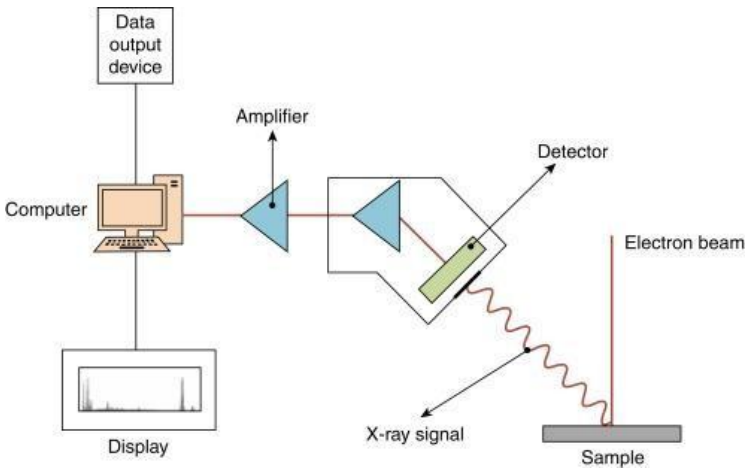

Figure 2.6: Representation of energy dispersive X-ray spectroscopic (EDX) analysis.

current produced by each X-ray may be used to calculate its energy. The energy dispersive spectrometer (EDS) studies of the samples were obtained from the Carl Zeiss spectrometer (made in Germany; model: ∑igma).

(f) Brunauer-Emmett-Teller (BET) Surface Area[9]

To remove any impurities from the surface, samples are first dried under a vacuum or inert gas flow. The sample is exposed to cryogenic temperatures in order to allow a probe gas to physically adsorb to its surface **(Figure 2.7)**. The volume of probe gas adsorbed is measured to determine how much gas is required to cover the sample's surface. The Brunauer, Emmett, and Teller (BET) theory is then applied to the adsorption data to get the specific surface area, which is then given in units of area per mass of sample ($m^2 g^{-1}$). A sample's surface area may be influenced by a number of physical characteristics, including particle size, pore volume, pore size, and surface roughness. For this thesis, the Quantachrome physisorption device (Anton Paar) was used to perform BET surface area analysis.

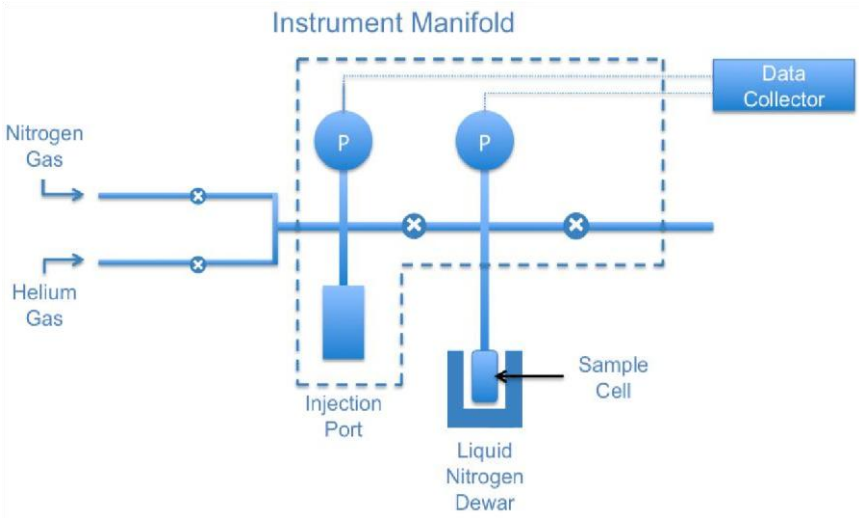

Figure 2.7: Representation of Brunauer Emmett Teller (BET) surface area instrument. (Adopted from particletechlabs and LibreTexts Chemistry)

(g) X-ray Photoelectron Spectroscopy (XPS)[10]

Surface analysis, or gathering quantitative chemical data from the substance, is done using XPS. The empirical formula, elemental composition, and electronic state of the material may all be ascertained using this approach. When the energy of an X-ray with a certain wavelength is known (for Al Kα X-rays, Ephoton = 1486.7 eV) and the kinetic energies of the liberated electrons are determined, the photoelectric effect equation **(Equation 2.2)** may be used to calculate the electron binding energy of each released electron.

$$E_{binding} = E_{photon} - (E_{kinetic} + \Phi) \qquad (2.2)$$

The electron's binding energy (BE), the energy of the X-ray photons, the work function, and the electron's kinetic energy are represented by the symbols $E_{binding}$, E_{photon}, α, and $E_{kinetic,}$ respectively **(Figure 2.8)**[11]. The conservation of energy is represented by this equation. The work function-like component ¸ which may be thought of as an adjustable instrumental correction factor, compensates for the photoelectron's loss of a few eV of

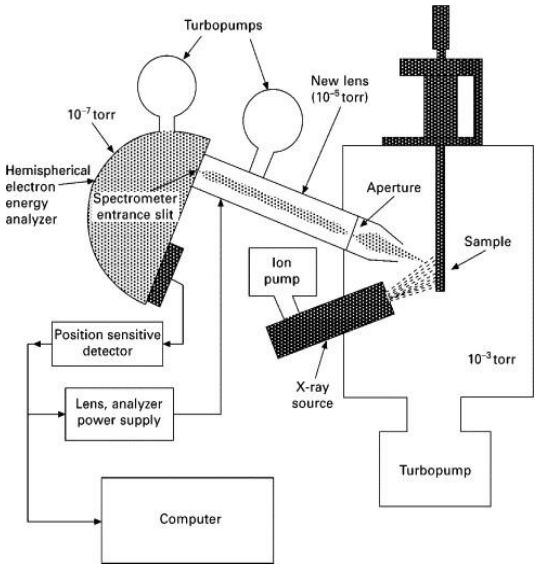

Figure 2.8 Representation of X-ray photoelectron spectroscopy (XPS) working principle.[11]

kinetic energy when it is released from the bulk and absorbed by the detector. In practice, it is a constant that rarely needs to be changed. The intensity and binding energy of the photoelectron peak can be used to calculate an element's quantity and chemical state. Since these photo-electrons originate from a depth of 10 nm, the data obtained for XPS measurement is consequently from inside this depth.[10] XPS measurements were carried out in ultra-high vacuum utilising a monochromatic Al kα X-ray source. XPS PHI Versa Probe III and AXIS Supra Kratos analytical XPS instruments were used to obtain the XPS spectra in this thesis.

(h) Raman Spectroscopy[12]

Raman spectroscopy is a molecular spectroscopic method that uses the manner in which light interacts with matter to reveal information about the composition or properties of a material. Most of the photons that are released when light interact with molecules in a gas, liquid, or solid have the same energy as the incident photons, this phenomenon is called as elastic or Rayleigh scattering. Just one out of every ten million of these photons will disperse at a frequency distinct from the incoming photon. This process is referred

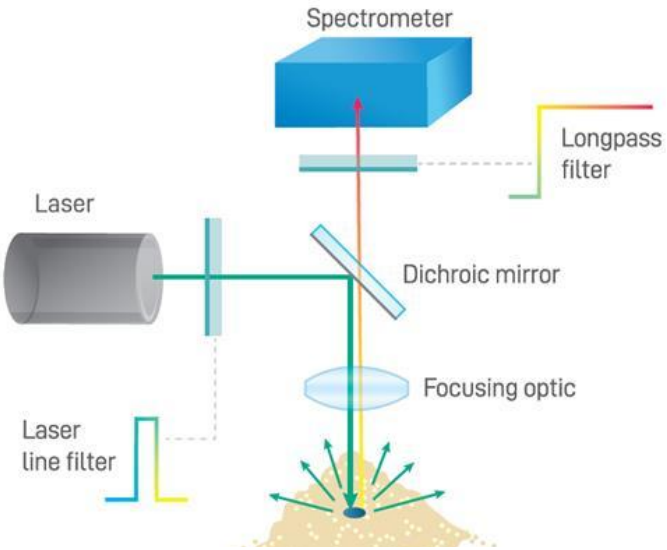

Figure 2.9: Representation of Raman spectrometer. (Adopted from Wasatch photonics)

to as inelastic scattering, or the Raman effect, in honour of Sir C.V. Raman, who pioneered the discovery and was awarded the 1930 Nobel Prize in Physics. Since then, the Raman spectroscopy has been utilised to many other fields, including medical diagnostics, reaction analysis, and material research. By collecting a molecule's vibrational signature using Raman, one can learn more about its composition and interactions with nearby molecules **(Figure 2.9)**. Raman analysis was performed for this thesis using the LabRAM HR Evolution apparatus (Horiba Scientific).

(i) Inductively Coupled Plasma-Optical Emission Spectroscopy (ICP-OES)[13]

It is a strictly analytical procedure that is used to identify the constituent elements. Finding traces of metal in any substance, including food and water, is very beneficial. It essentially uses a flame method, with flame temperatures between 6000 and 10,000

K. The ICP-OES instrument consists of both the analyser and the atomiser. The inductive coupling plasma functions as an atomiser and optical emission spectroscopy as an analyser. The spontaneous emission of photons produced by ions or atoms that have been

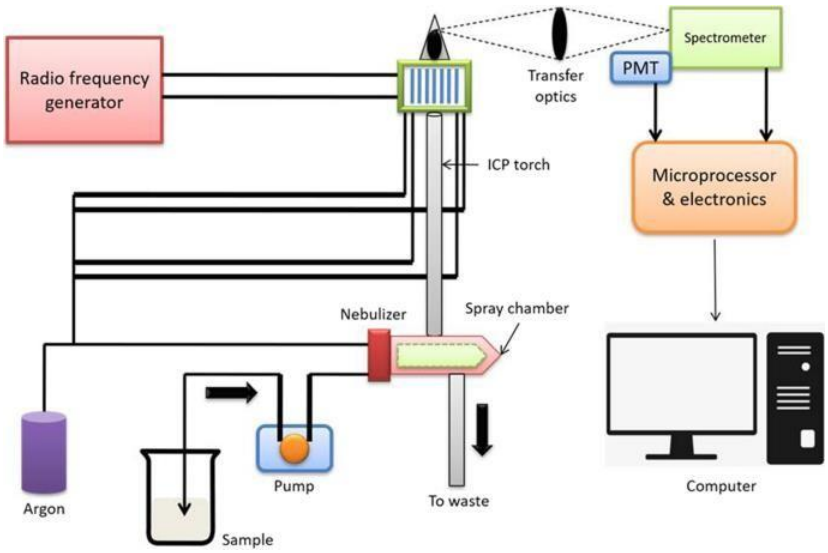

Figure 2.10: Representation of ICP-OES. (adopted from Springer Nature)[14]

energized by a radio frequency discharge is the fundamental idea behind ICP-OES. Using

a sample injection technique, the samples were first put into an inductively coupled argon plasma which atomizes and ionizes molecules before they are excited. Ionic or atomic emission, the name for the photons emitted by ions and atoms as electrons return from an excited energy level to a lower energy level, are collected using Echelle or Rowland circle optics, which distinguish different emission wavelengths from one another. The detector then measures the strength of the emission signal at the proper wavelengths, which match the energy difference between the electron's excited and ground states. The amount of the element in the plasma affects the intensity of the emission signal. Compared to other experiment types, ICP-OES measurements offer several advantages, such as:

(a) Multiple elements can be measured simultaneously using the ICP-OES approach.

(b) Very little chemical interference and ionisation.

(c) The technique is extremely sensitive and can measure down to parts per billion.

(d) It can yield a consistent outcome.

The fundamental components and layout of a typical ICP-OES instrument are shown in **(Figure 2.10)**.[14] The ICP-OES equipment consists of nebulisers, sample injectors, ICP torches, spray chambers, RF generators, spectrometer optics, emission detectors, signal processing, and software. ICP OES was performed for this thesis using the iCAP 7000 Series (Thermo Scientific).

(j) Gas Chromatography (GC)

A combination of components can be measured and separated using the GC technique. For element separation in a column of solid or liquid stationary phase, the retention coefficients of each individual element in GC are essential. The injector, column, and

detector are its three main parts. The column is linked between the injector and detector and placed in what is referred to as the oven. The oven, column, and injector may be heated to different temperatures based on the requirements of the samples. A constant flow of argon, the carrier gas, is sent through the column at a specific pace (sccm). The electrochemical cell's headspace is sampled (H_2, O_2, CH_4, C_2H_s, etc), and the sample is then injected into the injection port using a gas-tight syringe. The sample gas was then drawn through the column by the carrier gas, and the analytes reached the detector in different streams at different times based on their individual retention coefficients. For the gas phase investigation, argon (Ar) is used as a carrier gas in a thermal conductivity detector (TCD).

This study used Agilent Micro GC 990 equipment for GC analysis. An integrated micro-machined injector is present in this device. This enables incredibly accurate insertion of tiny sample quantities in a compact format without the need for splitting.

2.4 Electrochemical Measurements

2.4.1 Construction of Electrochemical Cell and Electrode Fabrication:

The electrolysis occurs in an electrochemical cell which is composed of three electrodes. These are working, reference and counter electrode. In general working electrodes can be sample modified glassy carbon electrodes (GCEs)/graphite sheets/carbon cloth/Ni foam etc. In this thesis the electrochemical measurements are done by taking the GCEs. The reference electrodes are mercury/mercury chloride (calomel electrode, Hg/Hg_2Cl_2), silver/silver chloride (Ag/AgCl) or mercury/mercury oxide (Hg/HgO). Bare platinum or graphite rod acts as the counter electrode. **Figure 2.11** shows the standard configuration of a three-electrode measuring setup.

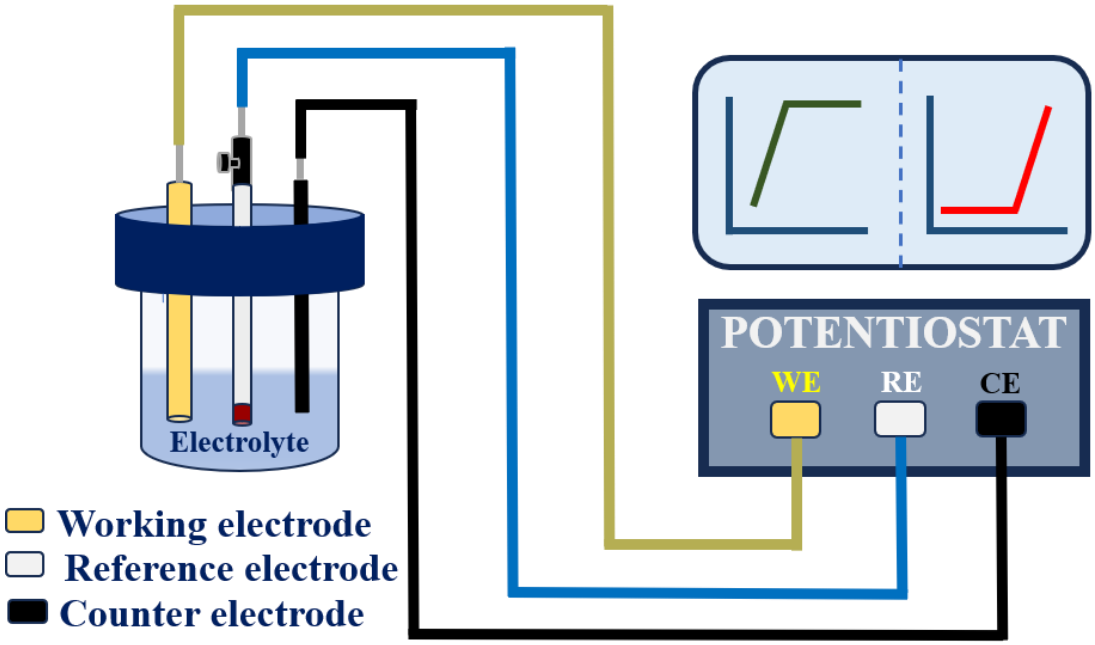

Figure 2.11: Electrochemical setup of three-electrodes for water splitting process.

A homogenous catalyst slurry is created by ultrasonically treating a suitable amount of the as-prepared catalyst with a solvent (such as ethanol) and a binder (such as Nafion). The electrode's surface is polished with alumina powder and cleaned with ethanol. The mixture is then drop-cast onto the GCE's surface. The electrode is dried well under a table lamp prior to the use. In order to initiate the electrolysis process, some potential must be supplied even when the pertinent electrodes are immersed in the aqueous electrolytes for water splitting. The as-obtained potential values for the corresponding HER and OER are calibrated into the reversible hydrogen electrode (RHE) scale by using the well-known Nernst equation as follows **(Equation 2.3-2.5)**:

For Ag/AgCl reference electrode:

$$E_{RHE} = E_{Ag/AgCl} + E^{0}_{Ag/AgCl} + 0.059\,pH \qquad (2.3)$$

In case of Hg/HgO reference electrode:

$$E_{RHE} = E_{Hg/HgO} + E^{0}_{Hg/HgO} + 0.059\,pH \qquad (2.4)$$

Similarly, for Hg/Hg_2Cl_2 reference electrode:

$$E_{RHE} = E_{Hg/Hg_2Cl_2} + E^0_{Hg/Hg_2Cl_2} + 0.059\,pH \qquad (2.5)$$

2.4.2 Electrochemical Characterisation Techniques Associated with Water Splitting

A catalyst's activity and durability must be examined, and it must be compared with other state-of-the-art catalysts as well as reported materials before it can be commercialised. The electrochemical parameters that are essential to comprehending the water splitting process include overpotential, Nyquist plot (which deals with charge transfer dynamics involved in the catalytic process), Tafel slope (which shows the kinetics of the desired reaction), electrochemical active surface area (ECSA) (which are responsible for the splitting of water to H_2 and O_2) and long-term stability test (chronoamperometry/chronopotentiometry reveals the robustness of the electrocatalyst). The real reaction mechanism involved in the catalytic process can also be deduced using these parameters.

(a) Cyclic Voltammetry

Cyclic voltammetry (CV) is a potent and widely used electrochemical method that is frequently used to study the oxidation and reduction processes of molecular species. Additionally, CV is very useful for studying chemical reactions that are initiated by electron transfer, such as catalysis. **Figure 2.12** shows the voltammograms, often known as cyclic voltammograms. The y-axis shows the response, in this case the passing current (i), while the x-axis shows a parameter that is applied on the system, in this case the applied potential (V).[15] In cyclic voltammetry (CV), potential progressions occur instantly from one potential V_1 to another V_2, and then from V_2 to V_1. Voltammetry can

show a current versus potential plot of many contact processes, however it may be challenging to pinpoint the activity.

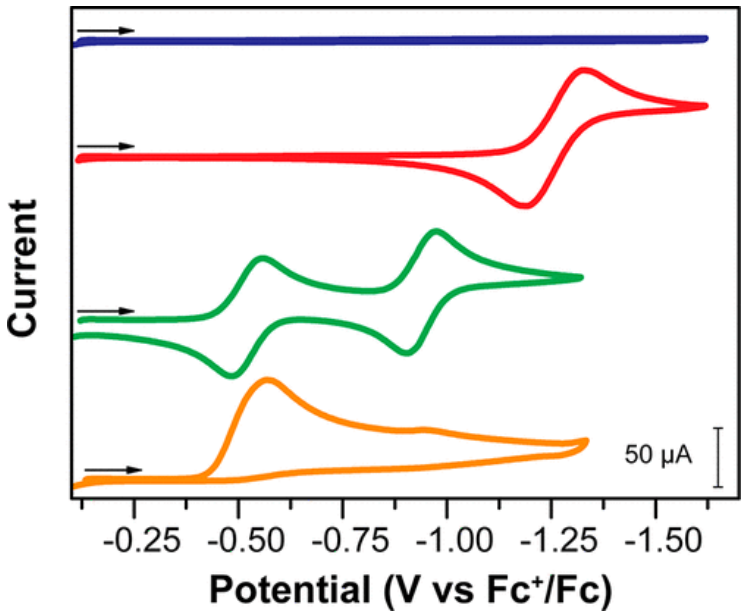

Figure 2.12: Cyclic voltammograms.[15]

(b) Overpotential

According to thermodynamics, it requires 0.0 V for HER at the cathodic counterpart and 1.23 V for OER at the anodic counterpart. However, in reality, the kinetic barrier in these multistep reactions requires extra energy in the form of additional potential at each step, this supplementary potential is known as overpotential.[16,17] Lower is the value of overpotential possessed by an electrocatalyst better is its performance towards the process of electrolysis. Therefore, creating effective electrocatalysts with lower overpotential values is one of the main focuses of researchers worldwide. Three important factors raise the difference between the thermodynamic and experimental potential for the catalytic process. Depending on this, overpotentials are divided into three main groups: concentration overpotential, activation overpotential, and overpotential related to the ohmic drop.[18,19] Concentration overpotential is the

overpotential linked to ionic species availability and ion transport at the electrode-electrolyte interface. It can be reduced by continuously stirring the electrolyte and

optimising the pH of the solution. The activation overpotential is the actual factor that is the catalyst's intrinsic property, which may be reduced by selecting the right catalyst and is dependent on the catalyst's active sites, active surface area, and surface energy. The ohmic overpotential is the result of electrochemical resistance between the electrode and electrolyte, as well as additional contact resistance. It is calculated from the Nyquist impedance spectra.

The overpotential of an electrocatalyst is determined by linear sweep voltammetry (LSV) technique. LSV is recorded after optimising the concentration along with the operational conditions. LSV is plotted between the potential in the RHE scale and the obtained current density. The actual potential (activation potential) of a catalyst is then calculated by subtracting the ohmic drop (iR) and the corresponding thermodynamic

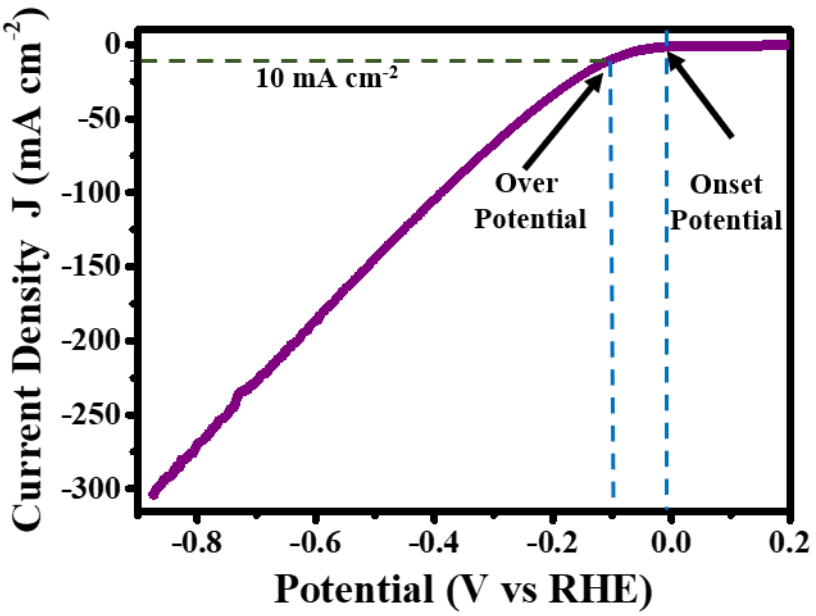

Figure 2.13: Linear sweep voltammetry curve showing the onset and overpotential.

potential.[20,21] Overpotential is displayed at a specific current density since it is a relative number, such as the onset-overpotential, which is the overpotential at the beginning of the reaction. The overpotential is typically determined at a current density of 10 mA cm^{-2}, which is commonly used to assess the electrocatalyst's performance because 12.3 % of solar to fuel conversion efficiency generates nearly 10 mA cm^{-2} current density, which is the benchmark for the performance of a solar to fuel device.[22,23] The evaluation of onset potential and overpotential from an LSV graph of HER is represented in the **Figure 2.13**. Similarly, the onset and overpotential parameters can be determined from the LSV for OER.

(c) Tafel Slope:

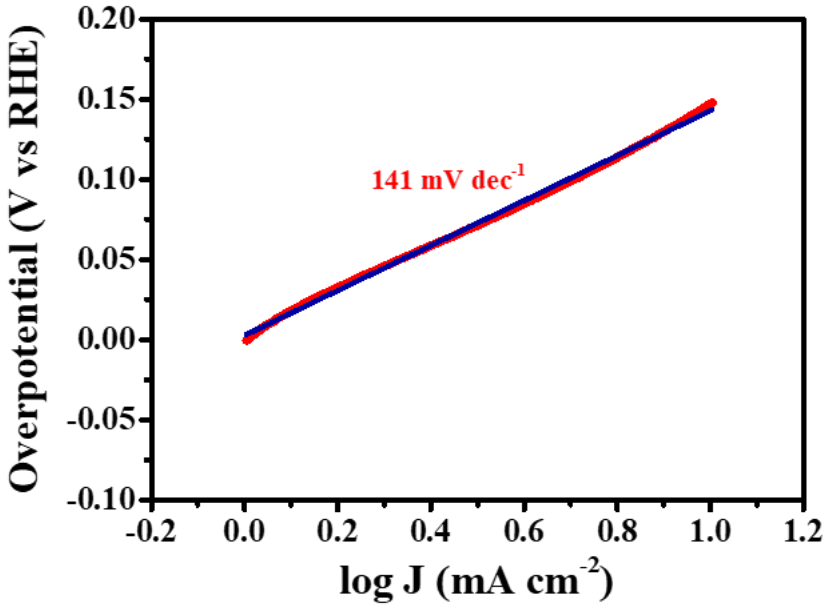

Figure 2.14: Tafel graph.

The intrinsic kinetics information of the electrocatalyst can be effectively examined using the Tafel plot, which is obtained from the experimentally recorded polarisation curves. The Tafel plot is a graph between the logarithm of current density and the overpotential in the RHE scale. It is obtained by fitting the linear region of the curve. The following equation establishes the relationship between log (J) and potential (V)

(Equation 2.6):

$$\eta = a + b\log(J) \qquad (2.6)$$

where 'η' is overpotential, 'a' represents the Tafel constant, 'b' is the Tafel slope and 'J' is current density.[24,25] The smaller value of Tafel slope indicates towards the faster kinetics at the electrode surface.[26,27] Additionally, the Tafel plot's extrapolation, which meets the X-axis at a specific point, is used to calculate the exchange current density value. A greater exchange current density value indicates that the catalyst surface has more active sites.[28] **Figure 2.14** displays a fitted linear region of the Tafel plot. In simple terms, the compound with the lowest Tafel slope value among a group of compounds is considered to be a better catalyst with appropriate kinetics for water splitting (HER and OER).

(d) Electrochemical Impedance Spectroscopy (EIS)

Charge transfer characteristics are a crucial indicator of an electrocatalyst's activity in an electrochemical reaction, and they can be assessed using the EIS measuring method within a suitable frequency range by the Nyquist plot. It is a plot of real impedance

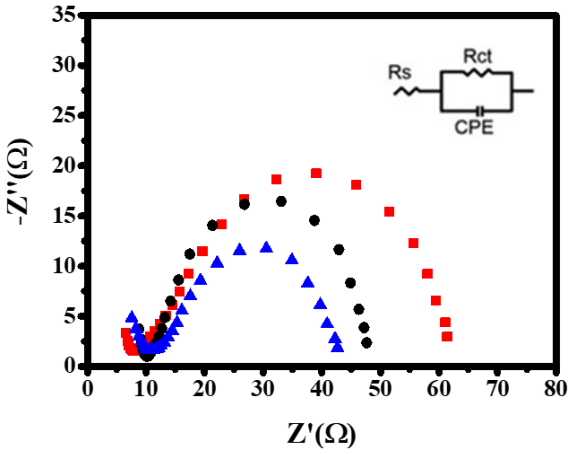

Figure 2.15: EIS or Nyquist plot of the electrocatalysts.

(Z') on the x-axis and imaginary impedance (Z") on the y-axis **(Figure 2.15)**. The AC frequency is varied from the higher to lower range while maintaining a constant applied voltage and amplitude in order to get the data.[29,30] EIS measurements are typically carried out over an applied potential beyond the onset potential (the catalysts should exhibit considerable activity at this potential). From the charge transfer resistance, we can determine the charge transfer process. In particular, (i) the resistance at the high-frequency region i.e. the solution resistance (R_s) can be utilised to assess the resistances between electrode and catalyst interface, the inherent resistance of electrode as well as the resistance due to electrolyte ions owing to the non-Faradaic process because the high-frequency region is independent of the applied potential; (ii) the resistance in the medium frequency region shows the charge transport within the catalyst and; (iii) the resistance at low frequencies is utilised to investigate the charge transfer resistance (R_{ct}) of the electrocatalyst-electrolyte interface.[31] For both HER and OER EIS plot provides a semicircle data. The diameter of the obtained semicircle is the charge transfer resistance (R_{ct}).[32]

Charge transfer resistance truly represents the resistance that results from the transfer of electric charge between the ionic species of the electrode and electrolyte at the interface during the discharge of ions at the catalyst surface. Hence, a lower charge transfer resistance results in a much better electrochemical conductivity of the catalyst and faster charge transfer between the electrode and electrolyte. So, an appropriate catalyst must have the lowest R_{ct} value. A straightforward Randles circuit fitting can reveal the circuit components implicated in the Nyquist plot. The following formula can be used to determine the double-layer capacitance value (C_{dl}) **(Equation 2.7)**:

$$C_{dl} = \frac{1}{2\pi f_{max} R_{ct}} \qquad (2.7)$$

The frequency at the greatest Z" value or frequency at the highest Z" in the semicircle is denoted by f_{max}.

(e) Turn-Over Frequency (TOF)

Currently, the differentiation of overpotential at comparable current density is the primary method used to assess electrocatalytic performance. However, different methods are consistent with different electrocatalyst loading masses, which makes assessing the electrocatalytic activity difficult. TOF is carefully employed as a crucial metric to evaluate the electrocatalytic performance in order to resolve this issue. The intrinsic electrocatalytic activity of the catalysts has been evaluated by measuring the number of molecular hydrogens/oxygens released per unit active site of the catalyst per second is called TOF. The material that has a higher TOF value performs exceptionally well. In practice, it is nearly impossible to have all atoms with equally accessible and catalytically active nanoparticles.[33] However, such findings may still be pertinent and helpful when comparing identical nanomaterials. TOF is determined by utilising the following equation for HER process **(Equation 2.8)**:[33]

$$\text{TOF} = \frac{J \times S}{2Fn} \tag{2.8}$$

Here, "J" stands for the obtained current density, "S" for the working electrode's geometrical surface area, "2" for the hydrogen evolution reaction's two-electron process and it will be "4" for oxygen evolution reaction, "F" for the faraday constant, and "n" for the number of metal sites in the loaded catalyst, which can be found using ICP-OES, ICP-MS, or the following formula **(Equation 2.9)**:

$$n = \frac{\text{Loaded mass} \times \text{NA}}{M.W.} \tag{2.9}$$

(f) Electrochemical Active Surface Area (ECSA)

In contrast to the BET surface area, which displays all accessible surface areas, it reflects the electrochemically active surface of the catalyst. It is computed from the double-layer capacitance because it is a surface phenomenon that provides capacitance via the adsorption of ions on the electrochemically active surfaces of a catalyst but solely follows the adsorption process, and is represented by the symbol C_{dl}.[34] ECSA can be determined by using the following **Equation 2.10**:

$$ECSA = \frac{C_{dl}}{C_s} \qquad (2.10)$$

Here C_s represents the specific capacitance of the atomically smooth surface. C_s = 35 μF cm^{-2} in acidic medium of 0.5 M H_2SO_4 and C_s = 40 μF cm^{-2} in the alkaline medium of 1.0 M KOH.

In order to determine the ECSA value, at first CV is taken between potential and current. The obtained CV consists of both non-Faradaic and Faradaic region. Further for ECSA calculation CVs at different scan rates are taken in the non-Faradaic region **(Figure 2.16a)** where just ion adsorption is favoured rather than any redox reaction. Since it solely involves the adsorption of ions, which are extremely reversible and quick physiochemical processes without any chemical reactions, the current produced from the CV in the EDLC region is exactly proportional to the scan rate (ν) and related to the C_{dl} by **Equation 2.11**.

$$I = \nu \times C_{dl} \qquad (2.11)$$

C_{dl} is obtained by measuring the slope of the plot between different scan rates and half of the difference of anodic and cathodic current **(Figure 2.16b)**.[35–37] So, higher is the

value of C_{dl}, higher will be the value of ECSA i.e. higher is the number of active sites for the desired reaction to take place.[38]

Further, in order to evaluate an ECSA-based specific catalytic activity of Pt and Pt-based electrocatalysts, the charge associated with the electrochemical oxidation of monolayers of adsorbed species, such as H_{upd} (Q_H), is first measured. The surface area-specific charge of an ideal one-electron transfer, 210 μC cm^{-2} (H_{upd}), is then used to normalise this obtained charge Q_H. The intrinsic surface area of Pt catalyst is determined in this manner.[39]

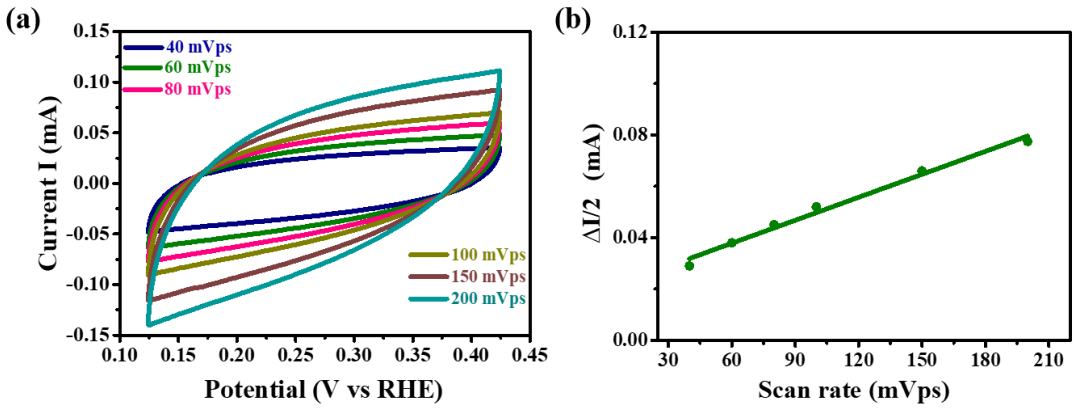

Figure 2.16: CV curves at different scan rates in the non-Faradaic region (a) and C_{dl} evaluation from the slope of the plot (b).

(g) Stability

Aside from intrinsic activity, time-dependent stability of the material is a significant metric for the potential applications, particularly at the high current densities. Electrocatalyst stability can be assessed using numerous methods, including chronopotentiometry (CP), chronoamperometry (CA), and accelerated degradation studies. The chronopotentiometry is the study of change in overpotential with respect to time to achieve a constant current value **(Figure 2.17a)**. If the overpotential value increases, it shows that the material is losing its capacity to perform the required reaction

over time. However, if a drop in the value of overpotential is determined, it means that the activity of the electrocatalyst is boosted throughout the long-term electrolysis

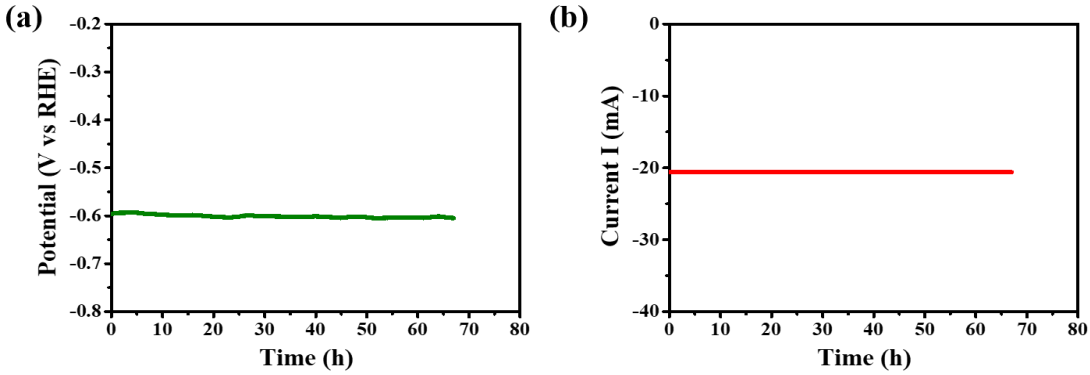

Figure 2.17: Chronopotentiometry (a) and chronoamperometry (b) plots.

process. The loss in activity is caused by the loss of sample from the electrode's surface, as well as particle agglomeration, which results in the blocking of active sites for the reaction to occur. Whereas, the improvement in performance might be attributed to the development of a new active phase or the dissolving of inactive catalyst components in the electrolyte, which exposes the material's active sites for the required reaction process. Similarly, chronoamperometry is the study of the change in current with time to achieve a constant potential value **(Figure 2.17b)**. The accelerated degradation technique differs from the previous two stability methods, it uses cyclic voltammetry at a high scan rate (100/200 mV/s) to record the full CV curves in the OER/HER range. After 1000 or 2000 cycles, the overpotential obtained before and after tests is compared to analyse stability. If both the overpotential values remain the same or only a minute shift is observed after the long-term test, then the material is considered as highly robust for the electrolysis process.[40–42] It is also critical to investigate whether any changes occurred to the material's composition, phase, or morphology as a result of the long-term electrolysis process. XRD, FESEM, TEM, XPS, ICP-OES, and other techniques are used to describe probable changes in the catalyst and determine the reasons responsible for the variations in activity of the electrocatalyst.

2.5 References

1. W. J. Li, C. Han, G. Cheng, S. L. Chou, H. K. Liu and S. X. Dou, *Wiley-VCH Verlag*, 2019.

2. M. Hu, J. Sen Jiang, R. P. Ji and Y. Zeng, *CrystEngComm*, 2009, **11**, 2257–2259.

3. M. Cao, X. Wu, X. He and C. Hu, *Chem. Commun.*, 2005, 2241–2243.

4. B. Bornamehr, V. Presser, A. J. G. Zarbin, Y. Yamauchi and S. Husmann, *J. Mater. Chem. A,* 2023, **11**, 10473-10492

5. W. H. Bragg and W. L. Bragg, *Proceedings of the Royal Society of London. Series A, Containing Papers of a Mathematical and Physical Character*, 1997, **88**, 428-438.

6. A. R. West, *Solid State Chemistry and its Applications*, Wiley, 2022.

7. K. C. A. Smith and C. W. Oatley, *British J. Appl. Phys.*, 1955, **6**, 391.

8. S. Amelinckx, D. van Dyck, J. van Landuyt and G. van Tendeloo, *Electron Microscopy: Principles and Fundamentals*, Wiley, 2008.

9. D. N. P. R. Jayakantha, N. Gunawardhana, H. M. N. Bandara, E. Comini, N. M. Gunawardana and S. M. M. L. Karunarathne, *Instrument. Sci. Technol.,* 2021, **50**, 47-56.

10. J. F. Moulder and J. Chastain, *Handbook of X-ray Photoelectron Spectroscopy: A Reference Book of Standard Spectra for Identification and Interpretation of XPS Data,* Physical Electronics Division, Perkin-Elmer Corporation, 1992.

11. H. Bluhm, in *In Situ Characterisation of Thin Film Growth*, eds. G. Koster and G. Rijnders, Woodhead Publishing, 2011, 75-98.

12. Z. Li, M. J. Deen, S. Kumar and P. R. Selvaganapathy, *Sensors*, 2014, 17275-17303.

13. Y. R. Sharma, *Elementary Organic Spectroscopy*, S. Chand Limited, 2007.

14. S. R. Khan, B. Sharma, P. A. Chawla and R. Bhatia, *Food Anal. Methods*, 2022, **15**, 666-688.

15. N. Elgrishi, K. J. Rountree, B. D. McCarthy, E. S. Rountree, T. T. Eisenhart and J. L. Dempsey, *J. Chem. Educ.*, 2018, **95**, 197–206.

16. J. Zhu, L. Hu, P. Zhao, L. Y. S. Lee and K. Y. Wong, *Chem. Rev.*, 2020, **120**, 851–918.

17. W. Zhang, L. Cui and J. Liu, *J. Alloys Compd.*, 2020, **821**, 153542.

18. S. Anantharaj, S. R. Ede, K. Sakthikumar, K. Karthick, S. Mishra and S. Kundu, *ACS Catal.*, 2016, **6**, 8069–8097.

19. J. H. Kim, K. Kawashima, B. R. Wygant, O. Mabayoje, Y. Liu, J. H. Wang and C. B. Mullins, *ACS Appl. Energy Mater.*, 2018, **1**, 5145–5150.

20. Y. Shi and B. Zhang, *Chem. Soc. Rev.*, 2016, **45**, 1529–1541.

21. J. K. Das, A. K. Samantara, A. K. Nayak, D. Pradhan and J. N. Behera, *Dalton Trans.*, 2018, **47**, 13792–13799.

22. J. D. Benck, T. R. Hellstern, J. Kibsgaard, P. Chakthranont and T. F. Jaramillo, *ACS Catal.,* 2014, **4**, 3957–3971.

23. Q. Gao, W. Zhang, Z. Shi, L. Yang and Y. Tang, *Adv. Mater.*, 2019, **31**, 1–35.

24. Y. Wang, Z. Zhang, X. Liu, F. Ding, P. Zou, X. Wang, Q. Zhao and H. Rao, *ACS Sustain. Chem. Eng.*, 2018, **6**, 12511–12521.

25. Y. Lu, Y. Deng, S. Lu, Y. Liu, J. Lang, X. Cao and H. Gu, *Nanoscale*, 2019, **11**, 21259–21265.

26. Y. Pan, Y. Chen, Y. Lin, P. Cui, K. Sun, Y. Liu and C. Liu, *J. Mater. Chem. A*, 2016, **4**, 14675–14686.

27. Y. C. Zhang, C. Han, J. Gao, L. Pan, J. Wu, X. D. Zhu and J. J. Zou, *ACS Catal.,* 2021, **11**, 12485–12509.

28. L. Ma, X. Shen, H. Zhou, G. Zhu, Z. Ji and K. Chen, *J. Mater. Chem. A*, 2015, **3**, 5337–5343.

29. Y. Guo, C. Zhang, J. Zhang, K. Dastafkan, K. Wang, C. Zhao and Z. Shi, *ACS Sustain. Chem. Eng.*, 2021, **9**, 2047–2056.

30. Q. Wang, G. C. Xu, D. J. Liu, H. Ding and L. Zhang, *Int. J. Hydrogen Energy*, 2023, **48**, 12712–12722.

31. X. Zhang, Y. Guo and C. Wang, *Energy Mater.*, 2024, **4**, 400044.

32. H. Jin, J. Wang, D. Su, Z. Wei, Z. Pang and Y. Wang, *J. Am. Chem. Soc.*, 2015, **137**, 2688–2694.

33. A. Ali and P. K. Shen, *Carbon Energy,* 2020, **2**, 99–12134.

34. G. Cao, Z. Chen, J. Cui, L. Gan, H. Dai, X. Yang and P. Wang, *ACS Catal.*, 2018, **8**,

5062–5069.

35. S. Jung, C. C. L. McCrory, I. M. Ferrer, J. C. Peters and T. F. Jaramillo, *J. Mater. Chem. A*, 2016, **4**, 3068–3076.

36. X. Wang, F. Li, W. Li, W. Gao, Y. Tang and R. Li, *J. Mater. Chem. A*, 2017, **5**, 17982–17989.

37. F. Song and X. Hu, *Nat. Commun.*, 2014, **5**, 4474.

38. H. Lu, Y. Zhang, Y. Huang, C. Zhang and T. Liu, *ACS Appl. Mater. Interfaces*, 2019, **11**, 3372–3381.

39. H. A. Gasteiger, S. S. Kocha, B. Sompalli and F. T. Wagner, *Appl. Catal. B: Environ.*, 2005, **56**, 9–35.

40. Z. F. Huang, J. Song, K. Li, M. Tahir, Y. T. Wang, L. Pan, L. Wang, X. Zhang and J. J. Zou, *J. Am. Chem. Soc.*, 2016, **138**, 1359–1365.

41. S. Ju, Y. Liu, H. Chen, F. Tan, A. Yuan, X. Li and G. Zhu, *ACS Appl. Energy Mater.*, 2019, **2**, 4439–4449.

42. H. Liang, D. Jiang, S. Wei, X. Cao, T. Chen, B. Huo, Z. Peng, C. Li and J. Liu, *J. Mater. Chem. A*, 2018, **6**, 16235–16245.

CHAPTER-3

Ruthenium-Doped Cobalt Sulphide Electrocatalyst Derived from Ruthenium-Cobalt Prussian Blue Analogue (RuCo-PBA) for Enhanced Hydrogen Evolution Reaction (HER)

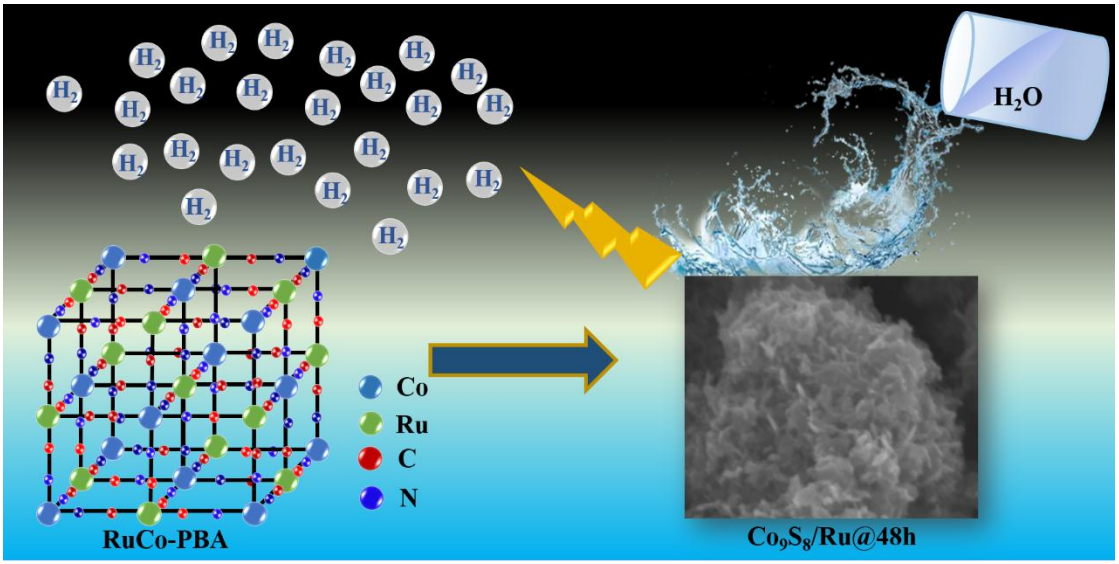

3.1 Abstract

The designing of efficient electrocatalysts for hydrogen generation is essential for the practical application of water-splitting devices. With numerous electrochemical advantages, transition metal sulphides are regarded as the most promising candidates for catalysing the hydrogen evolution reaction (HER) in acidic media. In the present study, Ru-doped cobalt sulphide nanosheets, termed Co_9S_8/Ru@t (t =24 h,48 h, and 72 h), were obtained by varying the reaction time from 24 h to 72 h from a RuCo-PBA precursor. The role of the time period for the synthesis of Co_9S_8/Ru@48h is vital in increasing the number of electroactive sites and optimising the hydrogen adsorption–desorption phenomena leading to an increment in the HER activity. The electrochemical outcomes demonstrate that the optimized Co_9S_8/Ru@48h requires a low overpotential of just 94 mV to produce 10 mA cm^{-2} current density, and also exhibits a lower Tafel slope value of 84 mV dec^{-1} defining its faster reaction kinetics. The as-synthesized Co_9S_8/Ru@48h was stable for up to 20 h of constant electrolysis signifying its outstanding durability. The optimized synthetic approach and impressive electrochemical results make Co_9S_8/Ru@48h a suitable alternative to noble metal-based electrocatalysts for the HER.

3.2 Introduction

The current energy crisis requires a solution due to the scarcity of prime energy sources (natural gas, and coal). Additionally, the environmental pollution created by their usage must be efficiently regulated. In recent years, massive efforts have been made to present clean energy sources as potential replacements for traditional fossil fuels.[1–4] Hydrogen (H_2) energy, with no carbon content and a high energy density of 146 kJ g^{-1}, has piqued people's interest as an environmentally friendly and clean energy source. At present, H_2 is primarily produced in industries by steam reforming of natural gas, which is environmentally hazardous. On the other hand, the electrochemical water splitting is a cost-effective and highly desirable method of producing hydrogen with high purity (> 99%).[5] However, the sluggish reaction kinetics associated with water electroly sis slows down the overall conversion process. Therefore, a highly efficient and stable electrocatalyst is urgently required to speed up the slow reaction rate of the HER at the cathode. Pt is regarded as the prime choice for efficiently catalysing the HER but it has inherent limitations, such as stability, scarcity and very high cost, that constrain its widespread application.[6] For the HER, several metal-free and non-noble metal-based electrocatalysts have been developed over the last few decades, but their poor stability and activity make them insufficient replacements for Pt-based electrocatalysts for the HER.

Recently, a number of Earth-abundant non-noble transition metal sulphides such as Fe_7S_8, CoMoS, Ni_2S_3, NiS_2, Co_9S_8, CoS_2, WS_2, VS_2, MoS_2, and others, have recently been intensively investigated as potential substitutes for Pt.[7–17] Among them Co metal-based transition metal sulphides, especially Co_9S_8, have received enormous attention because of their theoretically excellent electrocatalytic activity of Co, environmental friendliness, earth abundance, and very high stability in basic as well as acidic media.[18]

However, the catalytic performance of Co_9S_8 is still constrained by its low conductivity and small specific surface area.[19] Both theoretical as well as experimental studies revealed that the HER activities of Co-based TMSs (transition metal sulphides) must be improved in order to compete with noble metal-containing electrocatalysts. Numerous studies have been conducted on Co_9S_8 electrodes, either by improving Co_9S_8 nanostructures or by compounding with conductive substrates.[20–23] By altering the reaction conditions, various morphologies of Co_9S_8 in bulk form have been investigated, including hollow cubes,[22] polyhedrons,[21] nanoflakes[20] and so on. However, bulk Co_9S_8 still possesses numerous demerits for catalysing HER owing to their high value of additional energy, limited electroactive sites and gradual agglomeration during long-term electrolysis. Furthermore, to achieve a better catalytic performance for HER, researchers have driven their research towards synthesizing bimetallic and trimetallic sulphides.[24–28] Additionally, metal ion doping in Co_9S_8 enhances the specific surface area of the material and exposes the catalytic active sites for HER. Doping can promote the synergistic effect between the involved metal ions and further improve the catalytic activity leading to an enhancement in the HER performance of the Co_9S_8-based materials.[29–31] The hydrogen bond strength (65 kcal mol^{-1}) of platinum (Pt) and ruthenium (Ru) are similar, which opens the window for the fabrication of a Ru-based HER electrocatalyst as a suitable alternative for Pt. Additionally, the cost of Ru is one-fifth the cost of Pt, making it comparatively an economical electrocatalyst for HER.[32]

A metal-organic framework (MOF), also known as a coordination polymer, is composed of metal centres with various organic ligands. In general, MOFs are associated with several disadvantages, such as poor conductivity and substandard stability in acidic as well as basic media. Therefore, due to the above-mentioned limitations, MOFs have recently attracted a significant amount of interest as a possible precursor for the

construction of efficient electroactive materials for a variety of applications, including electrochemical water splitting.[33–36] Prussian Blue Analogues (PBA) are a special class of MOFs having a large specific surface area with a facile synthetic route.[37] Metal sulphides derived from PBAs have several advantages over bulk metal sulphides such as higher electrochemically active surface area (ECSA), a lower overpotential value, and improved stability in both alkaline and acidic media, resulting in enhanced electrochemical performance towards HER.[38] Furthermore, optimising the doping of a secondary metal ion, such as Ru, into the obtained PBA-derived sulphide will further increase the efficiency of the catalyst towards the electrochemical HER by exposing the active sites of the electrocatalyst and promoting the synergistic effect of the involved metal ions.

In the current work, we have successfully synthesised a series of Ru-doped Co_9S_8 nanosheets by varying the reaction time, and named them as Co_9S_8/Ru@t, where t represents the reaction time. First, we synthesised RuCo-PBA, and by utilizing the RuCo-PBA cubes, we have derived Ru-doped Co_9S_8 nanosheet-like particles which show high electrochemical activity for the HER including low overpotential, high ECSA, lower Tafel slope value, and long-term durability in an acidic medium of 0.5 M H_2SO_4. Generally, an additional Ru source is required for Ru doping, but in our work, Ru was already present in the precursor that paved the way for the synthesis of Ru-doped Co_9S_8. This synthetic method ultimately reduces the complexity of the reaction process, making it a feasible approach for synthesizing efficient electrocatalysts.

3.3 Experimental Section

3.3.1 Materials

Cobalt nitrate hexahydrate, trisodium citrate, sulphur powder, hydrazine hydrate and potassium hexacyanoruthenate (II) hydrate ($K_4[Ru(CN)_6].xH_2O$) were acquired from Sigma Aldrich chemicals and utilized as supplied with no alterations. Nafion solution from Alfa Aesar and absolute ethanol from Merck were purchased to prepare the catalyst ink. The entire experiment was performed by using DI water.

3.3.2 Synthesis of RuCo-PBA

RuCo-PBA was synthesised by a co-precipitation method. In a typical synthesis, a solution was made by adding 0.2 mmol $K_4[Ru(CN)_6].xH_2O$ (0.0862 g) to 10 mL DI water and stirring for 15 minutes. Another solution was prepared by adding cobalt nitrate hexahydrate (0.3 mmol, i.e., 0.0873 g) and trisodium citrate (0.46 mmol, i.e., 0.134 g) to 10 mL DI water and stirring for 15 minutes. The subsequent solution was added drop by drop to the first prepared solution, followed by 30 minutes of continuous stirring. The final solution was then allowed to stand for 24 hours at room temperature. After 24 hours, the material was washed three times with 10 mL DI water and three times with ethanol before being dried overnight at 60 °C. A blue powder material was obtained, which was named as RuCo-PBA.

3.3.3 Synthesis of Co_9S_8/Ru@t Nanoparticles

The Co_9S_8/Ru@t nanoparticles were obtained using a hydrothermal method, where t represents the reaction time. In this method, 8 mL of 1 M KOH was added to 50 mg of the previously prepared RuCo-PBA and stirred for 30 minutes. During continuous stirring, 50 mg of sulphur powder was added to the above solution. 2 mL of hydrazine hydrate was added to the above solution in a dropwise manner after 15 minutes. The final

solution was transferred to an acid digestion bomb and heated at a temperature of 200 °C in a hot air oven for 24, 48, and 72 hours. The resulting material was washed three times with DI water and three times with ethanol before drying overnight at 60 °C. The materials thus obtained after 24, 48, and 72 hours were designated as Co_9S_8/Ru@24h, Co_9S_8/Ru@48h and Co_9S_8/Ru@72h, respectively.

3.3.4 Synthesis of CoS_x

The CoS_x was synthesised using the same hydrothermal route that was used to synthesise Co_9S_8/Ru@t, but instead of RuCo-PBA, cobalt nitrate hexahydrate was used. In detail, 8 mL of 1 M KOH was mixed with 50 mg of cobalt nitrate hexahydrate and was stirred for about 30 minutes. 50 mg of sulphur powder was added to the above solution while it was being stirred continuously. After 15 minutes, 2 mL of hydrazine hydrate was added to the above solution. The final solution was transferred to an acid digestion bomb and heated in a hot air oven for 48 hours at 200 °C. The material was then washed 3 times with DI water and ethanol. The material thus obtained after drying at 60 °C was named as CoS_x.

Attempts to synthesize Co_9S_8 from CoPBA following the previously outlined procedure yielded unsuccessful results.

3.4 Characterisation

The crystallinity and phase purity of the samples were determined by using the Bruker D8 Advance diffractometer system (XRD) with Cu Kα radiation of wavelength (λ = 1.5418Å). The surface morphology and elemental distributions were characterised by transmission electron microscopy (TEM, equipped with HRTEM, JEOL 2100F, at 200kV) and field-emission scanning electron microscopy (FESEM, Zeiss Pvt. Ltd., Germany). A very dilute suspension of the sample in ethanol was prepared for the TEM

analysis and cast onto the 200-mesh carbon-coated copper grid. Before being used for morphology analysis, the grid was thoroughly dried under a table lamp. The specific surface area of the as-synthesised materials was analysed by using Brunauer−Emmett−Teller (BET) desorption/adsorption study using Quanta Chrome Instruments (version 5.21) at 77 K. Further, by using X-ray photoelectron spectroscopy (XPS, PHI Versa Probe III), the elemental composition and corresponding oxidation states of the elements present in the synthesized materials were determined.

3.5 Electrochemical Measurements

A Biologic Electrochemical Workstation (SP-200) three-electrode electrocatalytic cell setup was used to study the electrocatalytic HER performance of the synthesized materials RuCo-PBA, Co_9S_8/Ru@24h, Co_9S_8/Ru@48h and Co_9S_8/Ru@72h in 0.5 M H_2SO_4 electrolyte. The catalyst ink was prepared by dispersing 1 mg of each sample in 95 µL of ethanol and 5 µL of Nafion solution followed by ultrasonication treatment. Before the analysis, the glassy carbon rotating disk electrode (GCRDE, surface area 0.19 cm^2) was polished with 0.05 µ alumina slurry in DI water and dried in a vacuum desiccator. Bare platinum wire, Ag/AgCl (sat. KCl) and catalyst ink-modified GCRDE were used as a counter, reference and working electrodes respectively. The mass loading of the as-prepared sample slurry onto the GCRDE surface was taken as 0.26 mg cm^{-2}.To analyse the HER activity, the as-synthesized RuCo-PBA, Co_9S_8/Ru@24h, Co_9S_8/Ru@48h, Co_9S_8/Ru@72h and CoS_x were compared with Pt/C. The following equation was used to calibrate all electrochemical potentials to a reversible hydrogen electrode (RHE):

$$E_{RHE} = E_{(Ag/AgCl)} + 0.0591\ (pH) + 0.21\ V.$$

3.6 Results and Discussion

Co_9S_8/Ru@24h, Co_9S_8/Ru@48h and Co_9S_8/Ru@72h were synthesized by a two-step method. The synthesis was carried out as shown in **Scheme 3.1**. The first step involves the facile synthesis of RuCo-PBA followed by hydrothermal synthesis at 200 °C. The crystallinity and phase purity of RuCo-PBA, Co_9S_8/Ru@24h, Co_9S_8/Ru@48h and Co_9S_8/Ru@72h were determined by using PXRD. The PXRD pattern of RuCo-PBA **(Figure 3.1a)** consists of sharp peaks indicating the high crystallinity of the synthesised material. The pattern was found to be in good agreement with the JCPDS file number 01-077-1161, which is the PXRD pattern file for cobalt Prussian blue analogue compound. The PXRD pattern of Co_9S_8/Ru@24h, Co_9S_8/Ru@48h and Co_9S_8/Ru@72h **(Figure 3.1b)** are in good agreement with the (Powder Diffraction File (PDF) number 01-086-2273 of Joint Committee on Powder Diffraction Standards (JCPDS), which corresponds to the PXRD pattern of Co_9S_8. Furthermore, no extra peaks were obtained, indicating that the as-synthesised materials were phase pure. Also, no extra peaks for Ru were observed in the PXRD pattern, indicating the successful synthesis of the Ru-doped Co_9S_8. The PXRD pattern of CoS_x **Figure 3.1c** did not show any sharp peak of high

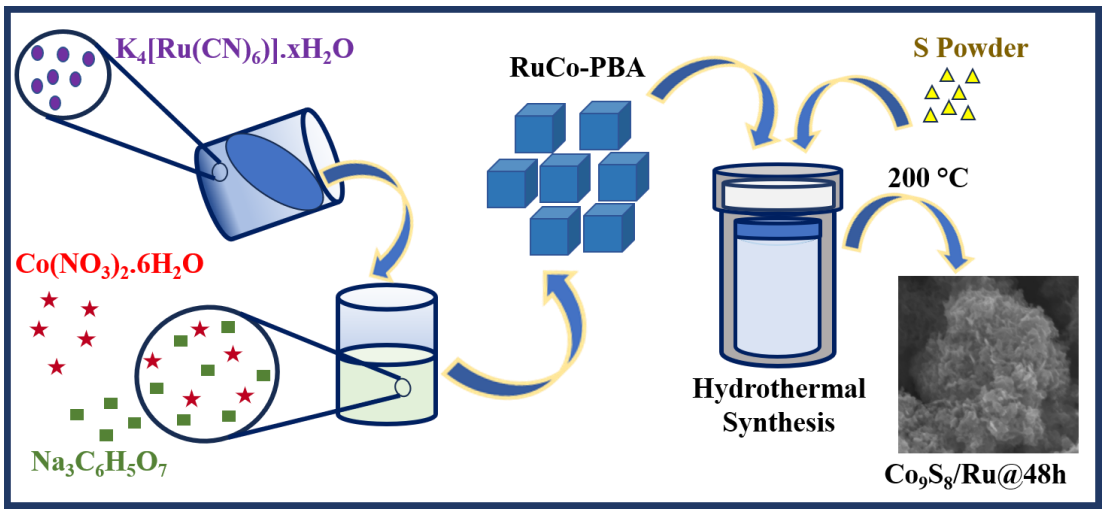

Scheme 3.1: Step wise synthesis process of Co_9S_8/Ru@48h.

intensity indicating the low crystallinity of CoS_x.The surface morphology of the RuCo-PBA, Co_9S_8/Ru@24h, Co_9S_8/Ru@48h and Co_9S_8/Ru@72h was investigated in detail by FESEM. The SEM image **(Figure 3.1d)** reveals nano-cube like morphology for RuCo-PBA. SEM images of Co_9S_8/Ru@48h **(Figure 3.2a-c)** depicted the uniform distribution of nanosheets throughout the surface at different scales of 500 nm, 100 nm and 5 µm. The presence and homogeneous distribution of Co, Ru, S, C and N in Co_9S_8/Ru@24h, Co_9S_8/Ru@48h and Co_9S_8/Ru@72h have been revealed through elemental mapping and energy dispersive X-ray absorption spectra (EDAX). The uniform distribution of Co, Ru, S, C, and N in the Co_9S_8/Ru@48h has been shown in **Figure 3.2d-h**. The nano sheet-

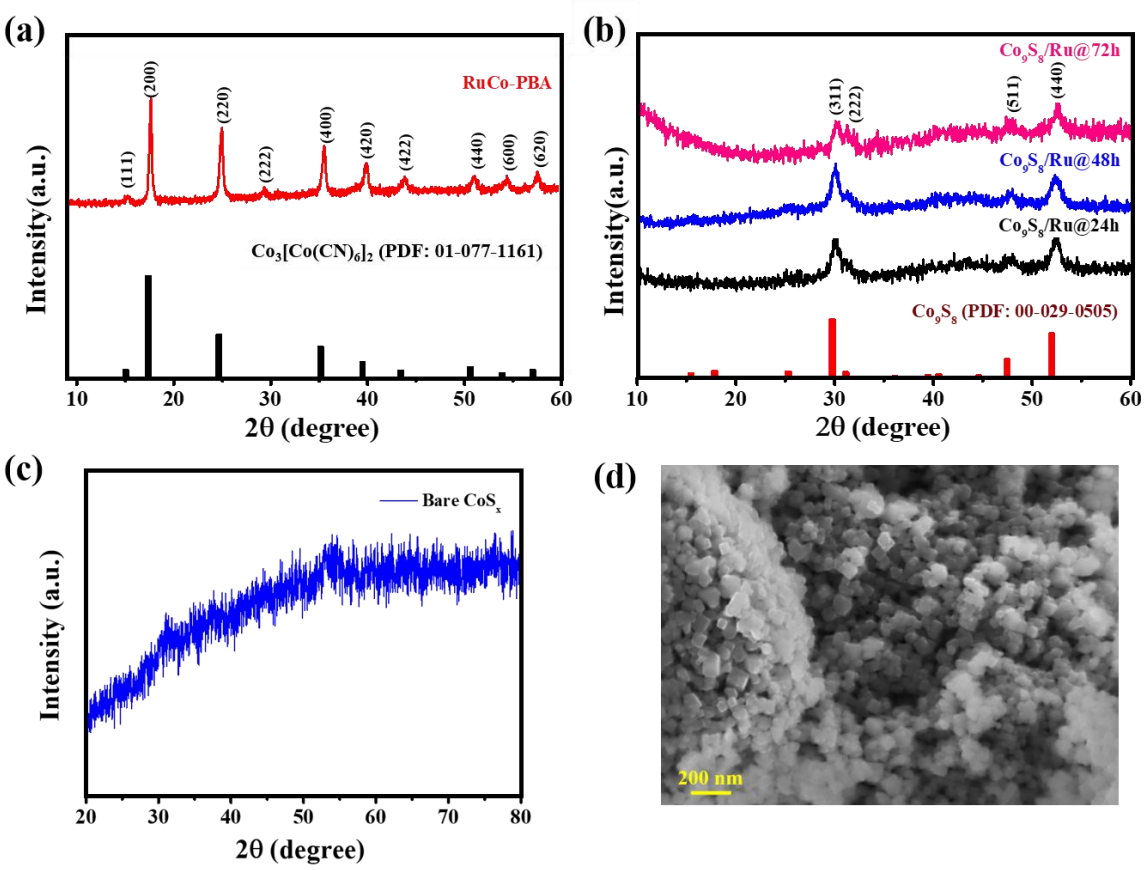

Figure 3.1: Powder X-ray diffraction of RuCo-PBA (a), Co_9S_8/Ru@24h, Co_9S_8/Ru@48h and Co_9S_8/Ru@72h (b), bare CoS_x (c) and FESEM image of RuCo-PBA (d).

like morphology was also observed in Co_9S_8/Ru@24h **(Figure 3.3a-c)** and Co_9S_8/Ru@72h **(Figure 3.4a-c)**, but there was no uniform distribution of the nanosheets, and some aggregation in the structures were observed. The elemental mapping for Co_9S_8/Ru@24h is shown in **Figure 3.3d-h**, and the same for Co_9S_8/Ru@72h is shown in **Figure 3.4d-h**, which also shows the uniform distribution of Co, Ru, S, C and N across the material surface. Also, agglomerated sheet-like morphology was obtained for CoS_x at different scales **(Figure 3.5)**. The TEM measurement further confirmed the nanosheet-like structure. As shown in the TEM images, **Figure 3.6a and 3.6b** of Co_9S_8/Ru@48h, the uniform distribution of nanosheet-like morphology throughout the surface is observed. The lattice fringe with interplanar spacings of 0.190, 0.176, 0.202, and 0.227 nm in the HRTEM image can be indexed to the (511), (440), (422), and (331) planes of the Co_9S_8 phase **(Figure 3.6c)**. The TEM image was found to be in good agreement with the obtained PXRD data for the Co_9S_8/Ru@48h, indicating the successful synthesis of the Co_9S_8/Ru@48h. In order to determine the specific surface area of the electrocatalysts,

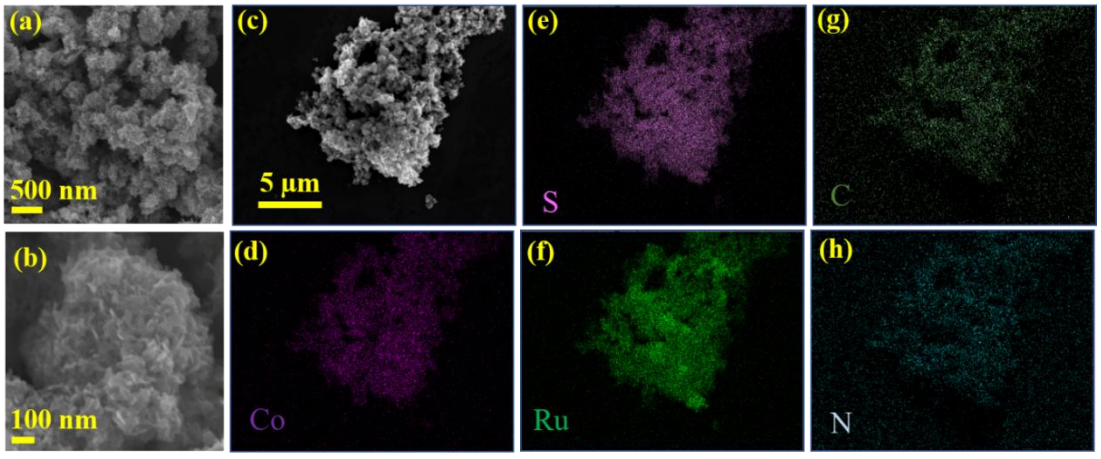

Figure 3.2: SEM images of Co_9S_8/Ru@48h at different scales (a-c) and elemental mapping of Co_9S_8/Ru@48h (d-h).

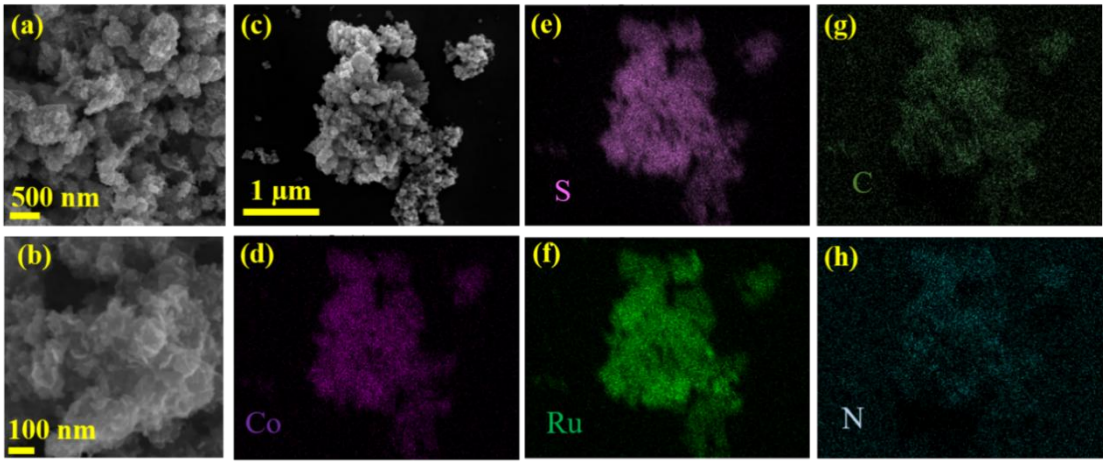

Figure 3.3: SEM images of Co_9S_8/Ru@24h at different scales (a-c) and elemental mapping of Co_9S_8/Ru@24h (d-h).

the Brunauer-Emmett-Teller (BET) isotherm was used. According to the N_2 adsorption-desorption isotherm, Co_9S_8/Ru@48h has the highest specific surface area of 43.6 m^2 g^{-1} **Figure 3.7b**, which is greater than Co_9S_8/Ru@24h (36.6 m^2 g^{-1}) **Figure 3.7a** and Co_9S_8/Ru@72h (36 m^2 g^{-1}) **Figure 3.7c**. The BET results reveal that the time optimisation factor of the solvothermal process is critical in optimising the specific surface area of the as-synthesised electrocatalysts, which subsequently proved advantageous in giving larger ECSA values for the HER. The elemental state and

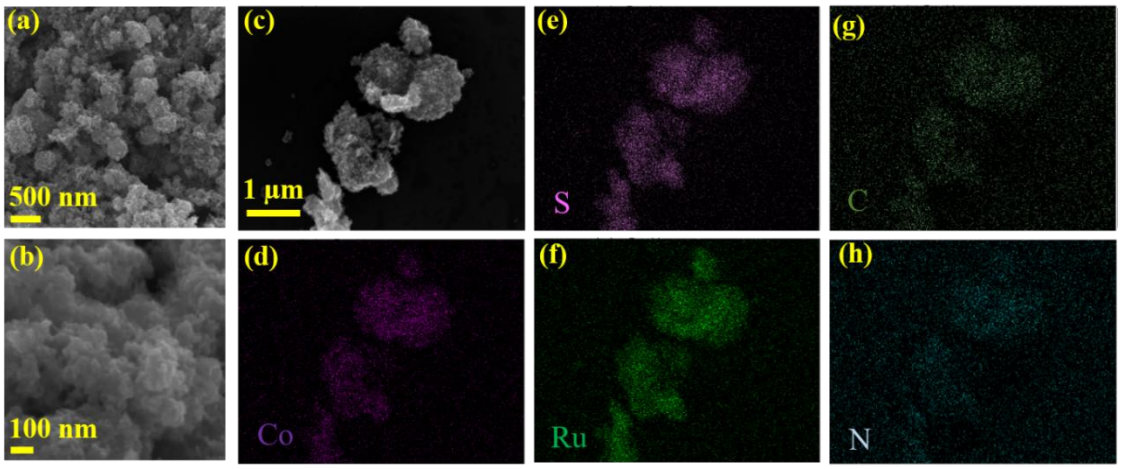

Figure 3.4: SEM images of Co_9S_8/Ru@72h at different scales (a-c) and elemental mapping of Co_9S_8/Ru@72h (d-h).

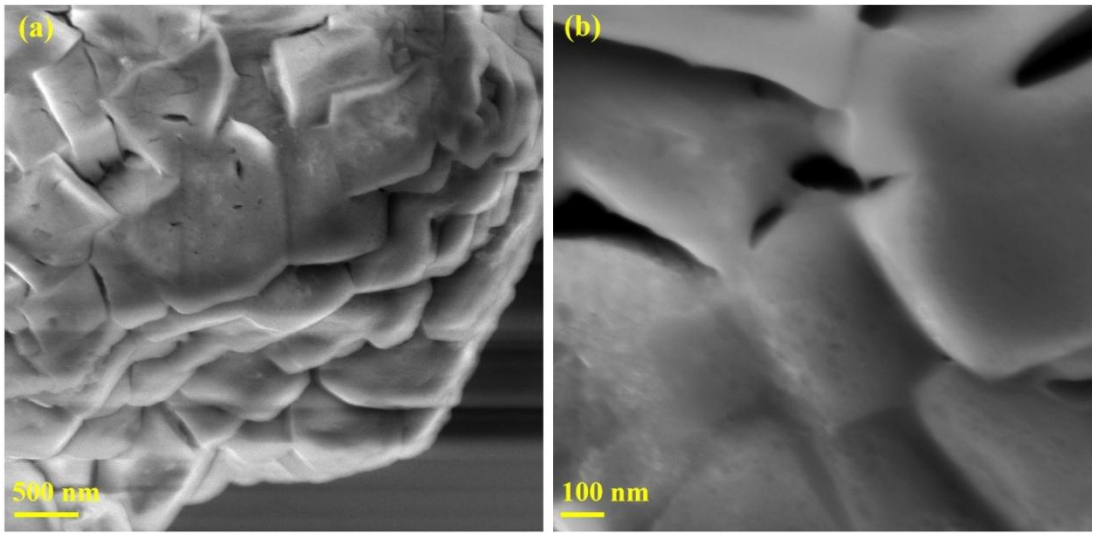

Figure 3.5: FESEM images of CoS_x at different scales (a & b).

chemical composition of the electrocatalyst Co_9S_8/Ru@48h were determined using XPS. **Figure 3.8a** depicts the full scan survey spectrum, which verifies the existence of Ru, S, Co, O, N, and C in the as-synthesised Co_9S_8/Ru@48h. The presence of an oxygen peak in the electrocatalyst can be attributed to the presence of unavoidable oxide species or to sample surface oxidation during areal exposure. **Figure 3.8b** depicts the presence of Co $2p_{3/2}$ and Co $2p_{1/2}$ peaks in a high-resolution Co 2p XPS spectrum. Both peaks were further deconvoluted into three peaks. The first peak was deconvoluted into three peaks at the binding energies of 778.1, 781.5 and 785.4 eV. The second peak was further deconvoluted into another three peaks at the binding energies of 792.9, 797.8 and 802.1 eV. The peaks at 781.5 and 797.8 are attributed to the Co^{2+} [11,39,40]. The peaks at 778.1 and 792.9 eV are ascribed to the Co^{3+} [11,39,40]. Additionally, due to the shakeup excitation of the high spin Co^{2+}, satellite peaks are caused at 785.4 and 802.1 eV [11,39,40]. **Figure 3.8c** depicts the XPS spectrum of S 2p, the peaks at 161.5 and 163.0 eV can be assigned to the $2p_{3/2}$ and $2p_{1/2}$ core levels of sulphur in Co_9S_8. The peaks at 164.8 and 166 eV can be assigned to the C-S $2p_{3/2}$ and $2p_{1/2}$, respectively.[41] The peak at 168 eV corresponds to the presence of oxysulphide species in the electrocatalyst.[11,39] Additionally, a peak at

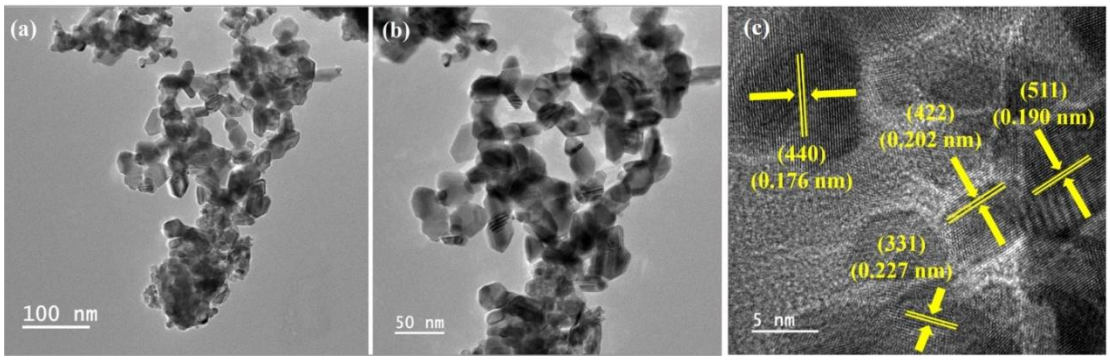

Figure 3.6: TEM images of Co_9S_8/Ru@48h at different scales (a and b). A high-resolution TEM image of Co_9S_8/Ru@48h (c).

226.8 eV was observed in the survey spectrum (**Figure 3.8a**) corresponds to the S 2s.[42] **Figure 3.8d** shows the XPS spectrum of Ru, the peak at 280.4 eV assigned to the Ru $3d_{5/2}$ corresponding to metallic ruthenium Ru (0). [32] In the full survey spectrum **(Figure 3.8a),** two peaks in the region from 450 eV to 500 eV correspond to Ru 3p peaks. These two peaks at 462.1 eV and 484.35 eV correspond to the Ru^{3+} $3p_{3/2}$ and $3p_{1/2,}$ respectively **(Figure 3.8e)**. [28] These results suggest some of the ruthenium (Ru^{3+}) is doped into Co_9S_8 and Ru (0) is also dispersed in the Co_9S_8 matrix. In **Figure 3.8d,** the peak at 284.6 corresponds to the C 1s. The XPS and XRD results correspond with the FESEM and TEM analysis suggesting the successful synthesis of Co_9S_8/Ru@48h.

For comparison purposes, the LSV (linear sweep voltammetry) curves for the as-prepared samples of RuCo-PBA, Co_9S_8/Ru@24h, Co_9S_8/Ru@48h, Co_9S_8/Ru@72h, CoS_x and commercial Pt/C were recorded at a sweep rate of 5 mV s^{-1} and an electrode rotation speed of 2000 rpm for the HER performances. Firstly, three consecutive LSVs (linear sweep voltammograms) were recorded and for the analysis of data, the 3rd LSV cycle was considered. The LSVs were normalized with the geometrical surface area of the working electrode. As shown in **Figure 3.9a**, commercial Pt/C shows the best performance towards HER with a low overpotential value of 29 mV. **Figure 3.9a** also

reveals that a very small overpotential of 94 mV is required by Co_9S_8/Ru@48h to attain the benchmark current density of 10 mA cm^{-2} as compared to Co_9S_8/Ru@24h and Co_9S_8/Ru@72h, which require an overpotential value of 125 mV and 136 mV, respectively. The overpotential of synthesised Co_9S_8/Ru@48h is lower than that of Co_9S_8/Ru@24h and Co_9S_8/Ru@72h, as well as various other metal sulphide electrocatalysts, as shown in **Table 3.1**. RuCo-PBA was found to be incapable of producing the benchmark current density of 10 mA cm^{-2}. Also, when the LSV of bare CoS_x was recorded to compare its performance to that of the synthesised electrocatalyst, it was found that the bare CoS_x was not able to deliver the current density of 10 mA cm^{-2}. This shows the efficiency of the electrocatalyst derived from the MOF, i.e., RuCo-PBA, as compared to the bulk material synthesised from the Co salt. The HER kinetics of the as-synthesized materials were determined through Tafel plots derived from the

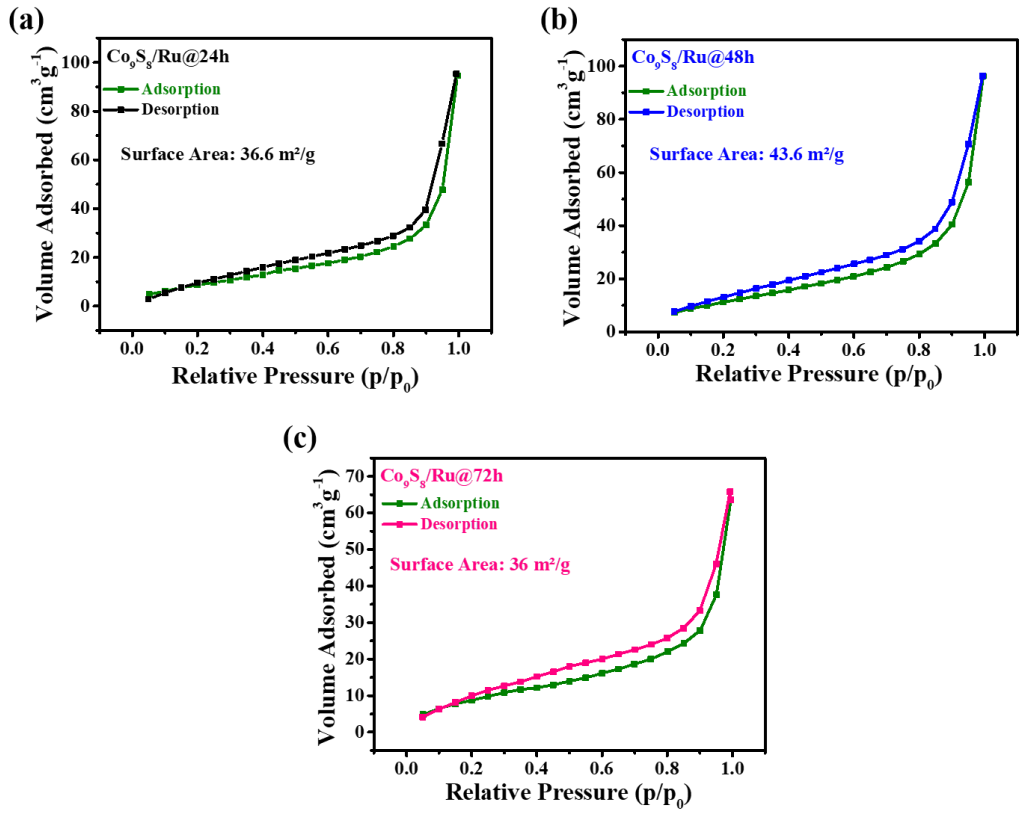

Figure 3.7: Nitrogen adsorption desorption isotherm for Co_9S_8/Ru@24h (a), Co_9S_8/Ru@48h (b), and Co_9S_8/Ru@72h (c).

LSV curves using equation η=b log j + a (b is the Tafel slope, j is the current density, a is the constant and η is overpotential).[43] As shown in the **Figure 3.9b** Co_9S_8/Ru@48h possess lowest Tafel slope value of 84 mV dec^{-1} as compared to Co_9S_8/Ru@24h and Co_9S_8/Ru@72h which are revealed to have Tafel slope value of 87 mV dec^{-1} and 96 mV

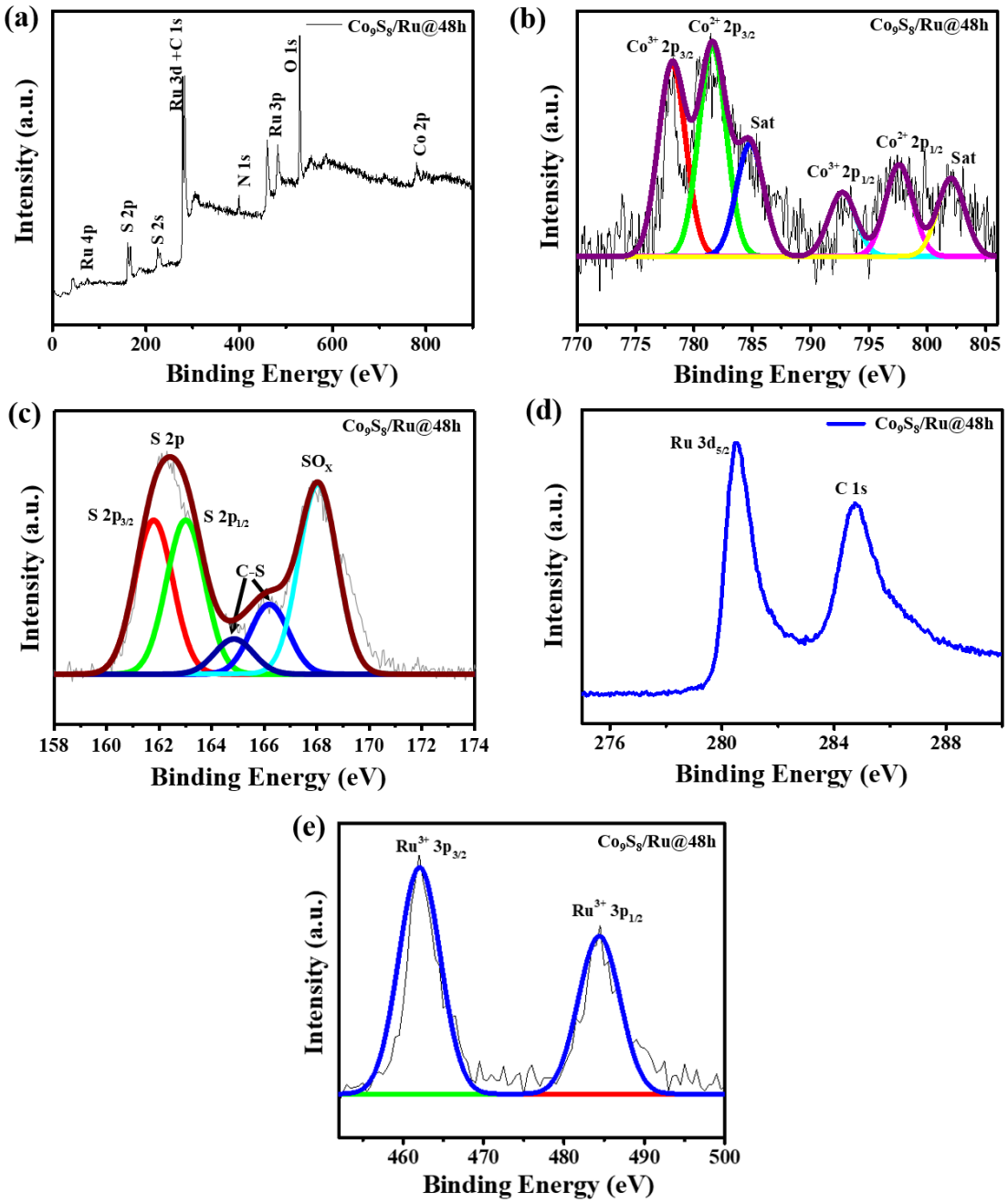

Figure 3.8: XPS full survey spectrum (a), Co 2p spectrum (b), S 2p spectrum (c), Ru 3d spectrum (d) and Ru 3p (e) spectrum of Co_9S_8/Ru@48h.

dec^{-1}, respectively. The smallest Tafel slope value indicates the faster rate kinetics in the case of Co_9S_8/Ru@48h, which is induced by the synergistic effect of Co and Ru.[29,44] The obtained Tafel slope value indicates that the rate-determining step in this case is the Heyrovsky step. It is worth noting that the present Co_9S_8/Ru@48h has electrocatalytic activity comparable to or greater than many previously reported HER catalysts in acidic

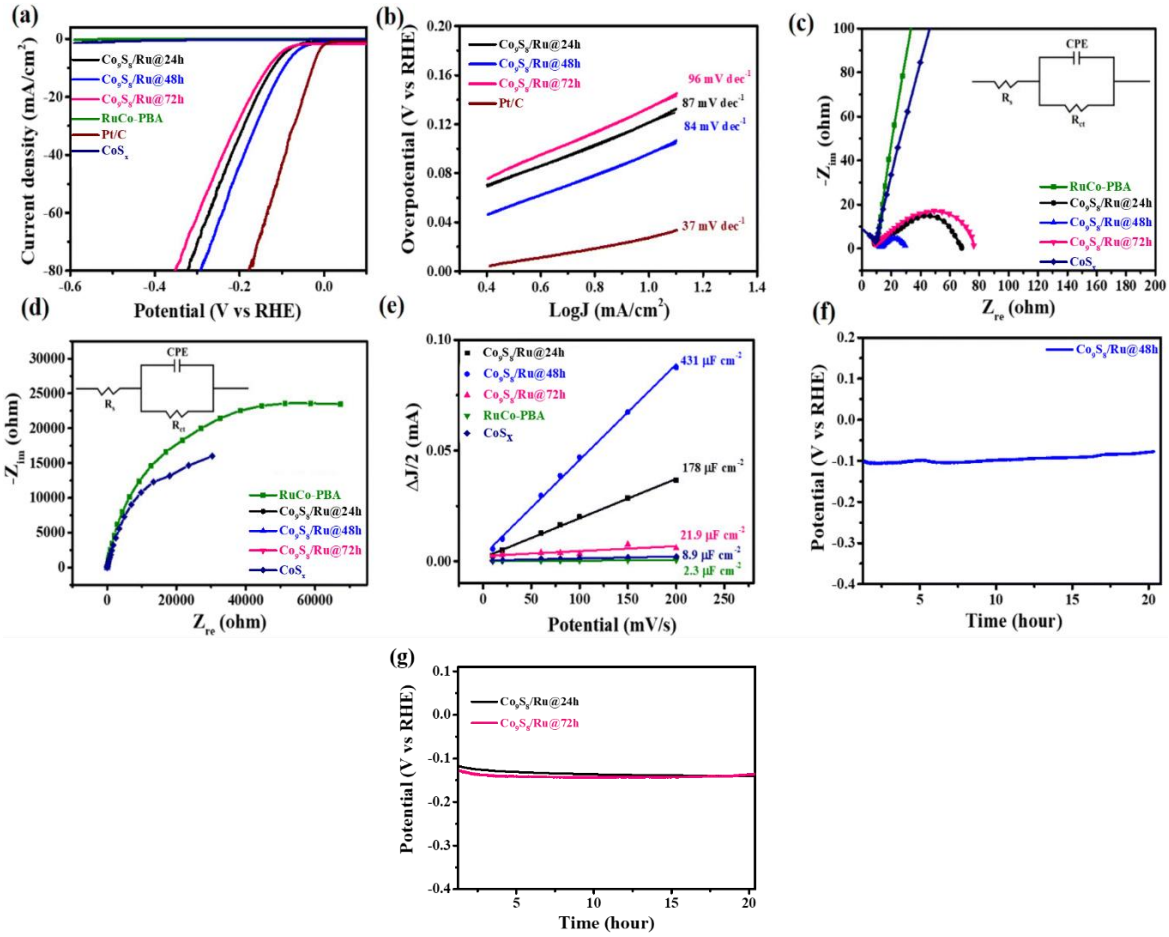

Figure 3.9 LSVs of RuCo-PBA, bare CoS_x, Co_9S_8/Ru@t products, and Pt/C (a). Tafel slopes of Co_9S_8/Ru@t products, bare CoS_x, and Pt/C (b). PEIS comparison at −360 mV of RuCo-PBA, bare CoS_x, Co_9S_8/Ru@t products (c & d). Estimated double-layer capacitance of RuCo-PBA, Co_9S_8/Ru@t products and bare CoS_x in 0.5 M H_2SO_4 at 0.105 V *vs*. RHE (e), chronopotentiometry test of Co_9S_8/Ru@48h in an acidic solution (f), chronopotentiometry test of Co_9S_8/Ru@24h, and Co_9S_8/Ru@72h in 0.5 M H_2SO_4 acidic solution (g).

electrolyte **(Table 3.1)**. towards the hydrogen evolution reaction. The charge transfer resistance of the synthesised materials was determined through impedance spectroscopy. The charge transfer resistance (R_{CT}) was measured for RuCo-PBA, Co_9S_8/Ru@24h, Co_9S_8/Ru@48h, Co_9S_8/Ru@72h and CoS_x by supplying 5 mV AC amplitude on a frequency scale of 1 MHz to 0.1 Hz at a potential value of 360 mV. **Figure 3.9c** shows that the lowest R_{CT} value of 17.5 Ω was obtained for Co_9S_8/Ru@48h, and the R_{CT} values obtained for Co_9S_8/Ru@24h and Co_9S_8/Ru@72h are 59 Ω and 68 Ω, respectively. The smaller R_{CT} value shows the faster electron diffusion between the supporting electrolyte and the catalyst-modified electrode.[45] The R_{CT} value was found to be very high for RuCo-PBA and CoS_x as shown in **Figure 3.9d**. This confirms the low conductivity of these catalyst, which is the reason behind their poor performances towards HER. The above-mentioned charge transfer resistance indicates the smallest value of resistance was found for Co_9S_8/Ru@48h, which leads to the higher conductivity of the catalyst. This significant reduction in R_{CT} observed from RuCo-PBA to Co_9S_8/Ru@48h could be attributed to the presence of the doped Ru in the Co_9S_8 that ultimately accelerated the electron transfer from the catalyst to the surface, ultimately contributing towards the HER performance.[32] Further, to investigate the HER activity of the synthesised materials, electrochemically active surface area (ECSA) was determined by performing the cyclic voltammetry (CV) experiment at different scan rates of 10, 20, 60, 80, 100, 150 and 200 mV s^{-1} in the non-faradaic region with a selected potential window of 0.01-0.21 V vs. RHE. The obtained CV curves have a rectangular shape **Figure 3.10** and this represents the simple process of electron and ion transfer. The double-layer capacitance C_{dl} is determined from the CV curves and this C_{dl} value is used to determine the number of electrochemically active sites present in the material. [46,47] C_{dl} values were obtained by plotting a graph of different scan rates, i.e., 10, 20, 60, 80, 100, 150 and 200 mV s^{-1}

against half of the difference between the cathodic and anodic current density at 0.105 V vs. RHE ($\Delta J=J_a-J_c$). The slope of the plotted data corresponds to the C_{dl} value. The C_{dl} value is directly related to the ECSA of the catalyst.[48] The obtained C_{dl} values are found to be 2.3, 178, 431, 21.9 and 8.9 μF cm^{-2} for RuCo-PBA, Co_9S_8/Ru@24h, Co_9S_8/Ru@48h, Co_9S_8/Ru@72h and CoS_x, respectively **(Figure 3.9e)**. Therefore, the highest value of the ECSA is found to be for Co_9S_8/Ru@48h, indicating its good catalytic

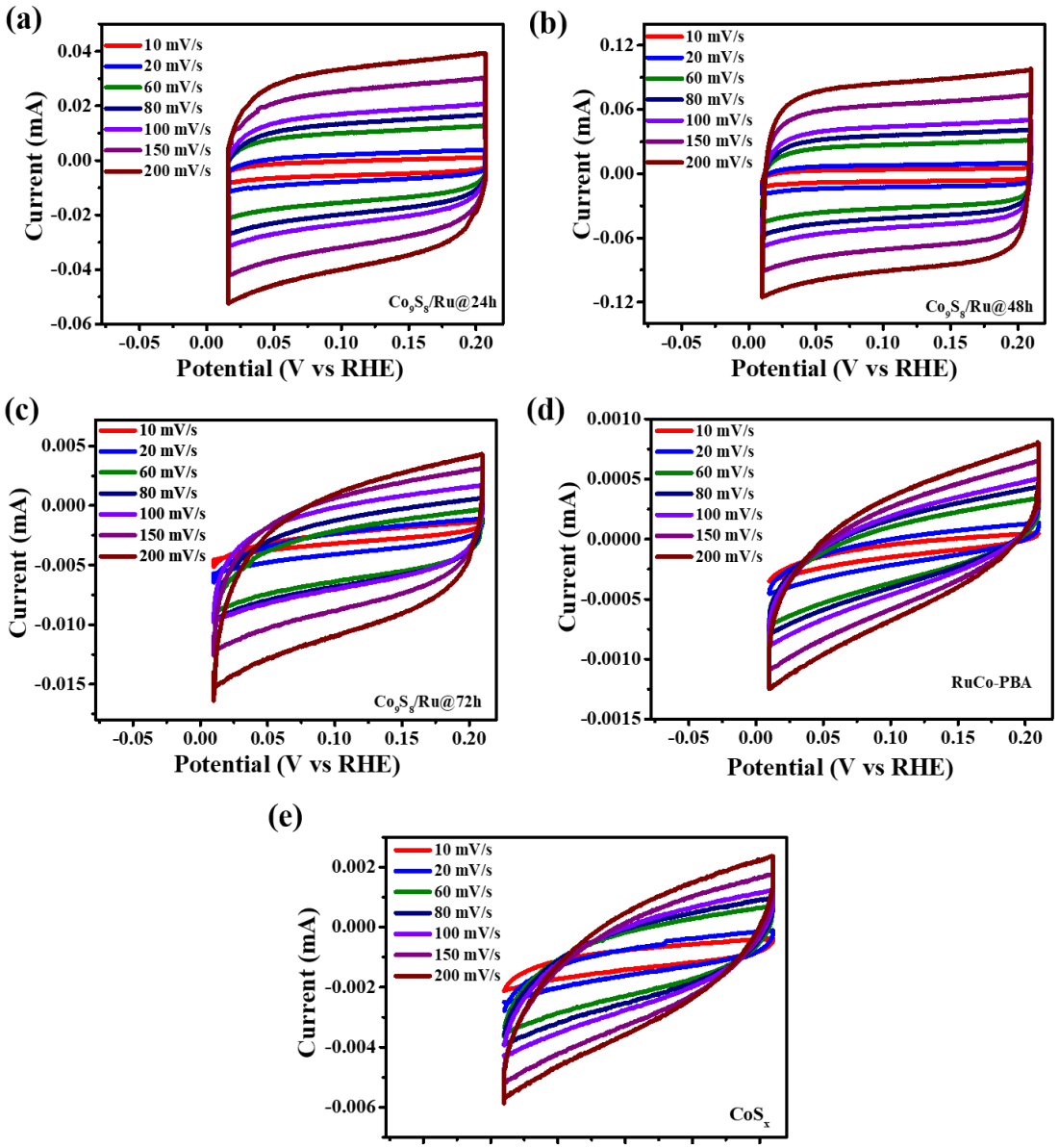

Figure 3.10: Cyclic voltammograms (CVs) of Co_9S_8/Ru@24h (a), Co_9S_8/Ru@48h (b), Co_9S_8/Ru@72h (c), RuCo-PBA (d) and bare CoS_x (e).

activity towards HER. The lesser value of ECSA obtained for CoS_x indicates that only a smaller number of electroactive sites are exposed, which leads to a decrease in the electrochemical performance of the electrocatalyst. The stability of the electrocatalyst is an important parameter in determining its practical application. The chronopotentiometry (CP) test was carried out at a constant current density of 10 mA cm^{-2} to investigate the long-term durability of the synthesized electrode material. **Figure 3.9f** demonstrates that the Co_9S_8/Ru@48h electrocatalyst was significantly robust up to 20 h of steady electrolysis with a minimal change in the overpotential value under severe acidic electrolytic conditions of 0.5 M H_2SO_4.[49,50] Co_9S_8/Ru@24h and Co_9S_8/Ru@72h were also found to be stable during the long-term electrolysis for 20 h but they requiring higher overpotential to produce a current density of 10 mA cm^{-2} as compared to that of the Co_9S_8/Ru@48h **(Figure 3.9g)**. Additionally, post-stability PXRD characterisation was carried out to investigate the changes that occurred to the electrocatalyst following long-term electrolysis. The PXRD pattern of Co_9S_8/Ru@48h after the durability test shows no change in the phase of the electrocatalyst, as presented in **Figure 3.11a**. FESEM investigation was conducted to support the results obtained from the PXRD data. The morphology has not changed significantly, as shown by the SEM images **(Figure 3.11b,c)**. This suggests the high stability of the Co_9S_8/Ru@48h in the acidic medium.The outstanding catalytic activity and endurance of the as-synthesised electrocatalyst can be attributed to the following factors. First, the presence of doped Ru in the obtained Co_9S_8 phase i.e. Co_9S_8/Ru@48h, led to the proper reaction intermediate energetics and improved electronic conductivity which thus led to the acceleration in reaction kinetics.[29–31] Second, the presence of Ru in the Co_9S_8/Ru@48h could optimise the adsorption energy due to the electronic interactions between Ru and Co_9S_8.[32] Third, the Co_9S_8/Ru@48h nanoparticles possess a greater specific surface area, which means a

higher ECSA. The uniform distribution of the nanosheet-like particles throughout the surface also played an important role by providing a larger electrochemically active surface area by exposing a large number of electrochemically active sites, which allows the proper diffusion of electrolyte and shortens the electron transfer path for the smooth progression of HER. Here, the PBA played an important role in providing the uniform

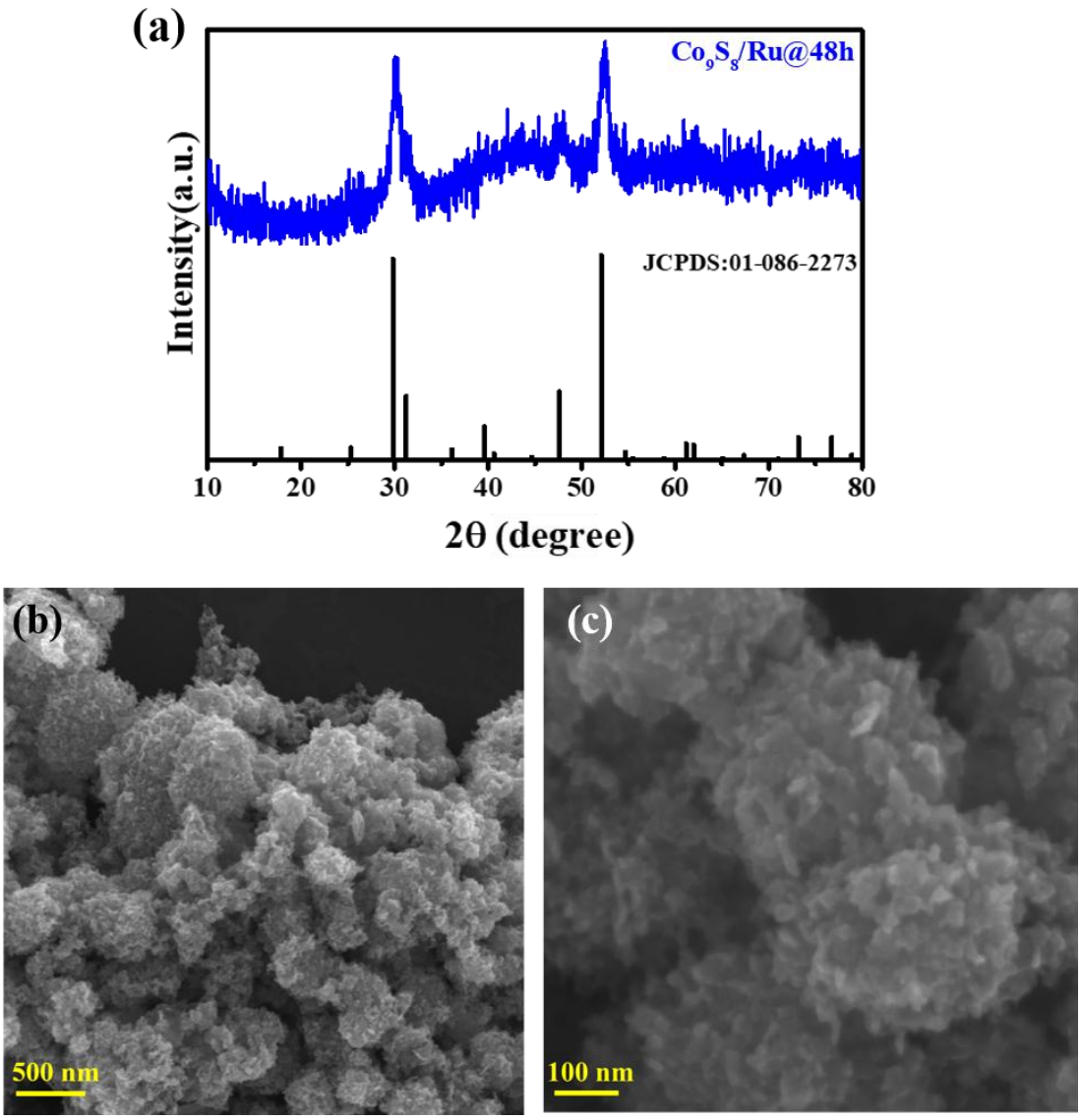

Figure 3.11: PXRD pattern (a) and FESEM images at different scales (b & c) of Co_9S_8/Ru@48h and after chronopotentiometry measurement of 20 h at 10 mA cm^{-2} current density under acidic electrolytic condition.

distribution of Ru-doped Co_9S_8 throughout the surface.[38] The above-mentioned systematic characterisation, as well as the improved electrochemical results of the Co_9S_8/Ru@48h, suggest that it could be used as a substitute for the most expensive electrocatalyst for HER. Our findings suggest a novel approach to developing PBA-derived electrocatalysts for electrochemical applications.

Table 3.1 Comparison of metal sulphide-based electrocatalysts for HER in 0.5 M H_2SO_4 electrolyte.

Electrocatalysts	Overpotential at 10 mA cm^{-2} (mV)	Tafel slope (mV dec^{-1})	References
Co_9S_8-30@MoS_x/CC	98	64.8	23
Co_9S_8-NDCL	149@20mA cm^{-2}	70	51
Co_9S_8/NC@MoS_2	117	68.8	21
MoS_2/Co_9S_8/MoC@CNT-N	174.2	84.7	52
CoS_2 nanowires	145	51.6	53
CoxSY	188	96	54
Co_9S_8@MoS_2	106	51.8	55
Zn-Co_9S_8@CF-(1-1)	278	85.2	56
Co_9S_8/Ru@48h	94	84	This work

3.7 Conclusions

In summary, we used the solvothermal method to prepare Ru-doped Co_9S_8 nanosheet-like particles from a bimetallic PBA, i.e., RuCo-PBA. The tuning of the surface area of the derived sulphide products was significantly influenced by varying the time for the hydrothermal process. For HER, the optimal Co_9S_8/Ru@48h electrocatalyst requires a

very low overpotential of 94 mV to obtain a 10 mA cm^{-2} current density and has an outstanding durability of 20 h in harsh acidic electrolytic conditions. It also shows a low Tafel slope value of 84 mV dec^{-1} and a small charge transfer resistance of 17.5 Ω. The notable catalytic performance can be attributed to the Ru-doped Co_9S_8 phase. Ru doping prevents the active species from agglomerating and corroding during long-term electrolysis under harsh conditions. The Ru doping also altered the electronic environment, which led to an increase in the conductivity as well as activated the inherent catalytic activity of the cobalt sulphide. The use of RuCo-PBA precursor in the hydrothermal approach opens up a new avenue for developing Ru-doped Co_9S_8 materials, which excels as an outstanding electrocatalyst for H_2 production.

3.8 References

1. Y. Yang, Z. Lun, G. Xia, F. Zheng, M. He and Q. Chen, *Energy Environ. Sci.*, 2015, **8**, 3563–3571.
2. C. G. Morales-Guio, L. A. Stern and X. Hu, *Chem. Soc. Rev.*, 2014, **43**, 6555–6569.
3. Y. Jiao, Y. Zheng, M. Jaroniec and S. Z. Qiao, *Chem. Soc. Rev.*, 2015, **44**, 2060–2086.
4. J. A. Turner, *Science*, 2004, **305**, 972–974.
5. C. C. L. McCrory, S. Jung, I. M. Ferrer, S. M. Chatman, J. C. Peters and T. F. Jaramillo, *J. Am. Chem. Soc.*, 2015, **137**, 4347–4357.
6. T. Wang, H. Xie, M. Chen, A. D'Aloia, J. Cho, G. Wu and Q. Li, *Nano Energy*, 2017, **42**, 69–89.
7. Q. Ma, C. Hu, K. Liu, S. F. Hung, D. Ou, H. M. Chen, G. Fu and N. Zheng, *Nano Energy*, 2017, **41**, 148–153.

8. C. Yang, M. Y. Gao, Q. B. Zhang, J. R. Zeng, X. T. Li and A. P. Abbott, *Nano Energy*, 2017, **36**, 85–94.

9. C. Guan, X. Liu, A. M. Elshahawy, H. Zhang, H. Wu, S. J. Pennycook and J. Wang, *Nanoscale Horiz.*, 2017, **2**, 342–348.

10. C. Zhang, Y. Shi, Y. Yu, Y. Du and B. Zhang, *ACS Catal.*, 2018, **8**, 8077–8083.

11. L. L. Feng, M. Fan, Y. Wu, Y. Liu, G. D. Li, H. Chen, W. Chen, D. Wang and X. Zou, *J. Mater. Chem. A*, 2016, **4**, 6860–6867.

12. Z. Liu, N. Li, C. Su, H. Zhao, L. Xu, Z. Yin, J. Li and Y. Du, *Nano Energy*, 2018, **50**, 176–181.

13. Y. Qu, M. Shao, Y. Shao, M. Yang, J. Xu, C. T. Kwok, X. Shi, Z. Lu and H. Pan, *J. Mater. Chem. A*, 2017, **5**, 15080–15086.

14. S. Chen, Z. Kang, X. Zhang, J. Xie, H. Wang, W. Shao, X. Zheng, W. Yan, B. Pan and Y. Xie, *ACS Cent. Sci*., 2017, **3**, 1221–1227.

15. Y. Jiang, X. Qian, C. Zhu, H. Liu and L. Hou, *ACS Appl. Mater. Interfaces*, 2018, **10**, 9379–9389.

16. F. Di, X. Wang, S. Farid and S. Ren, *Int. J. Hydrogen Energy*, 2023, **48**, 17758–17768.

17. P. M. Pataniya, V. Patel, P. Sahatiya, D. J. Late and C. K. Sumesh, *Surf. Interfaces*, 2022, **34**, 102319.

18. Y. Hou, M. Qiu, G. Nam, M. G. Kim, T. Zhang, K. Liu, X. Zhuang, J. Cho, C. Yuan and X. Feng, *Nano Lett.*, 2017, **17**, 4202–4209.

19. X. Yuan, J. Yin, Z. Liu, X. Wang, C. Dong, W. Dong, M. S. Riaz, Z. Zhang, M. Y. Chen and F. Huang, *ACS Appl. Mater. Interfaces*, 2018, **10**, 11565–11571.20

20. S. Deng, S. Shen, Y. Zhong, K. Zhang, J. Wu, X. Wang, X. Xia and J. Tu, *J. Energy Chem.*, 2017, **26**, 1203–1209.

21. H. Li, X. Qian, C. Xu, S. Huang, C. Zhu, X. Jiang, L. Shao and L. Hou, *ACS Appl. Mater. Interfaces*, 2017, **9**, 28394–28405.

22. A. Sivanantham, P. Ganesan and S. Shanmugam, *Adv. Funct. Mater.*, 2016, **26**, 4661–4672.

23. X. Zhou, X. Yang, M. N. Hedhili, H. Li, S. Min, J. Ming, K. W. Huang, W. Zhang and L. J. Li, *Nano Energy*, 2017, **32**, 470–478.

24. S. E. Fosdick, S. P. Berglund, C. B. Mullins and R. M. Crooks, *ACS Catal.*, 2014, **4**, 1332–1339.

25. J. Zhang, X. Bai, T. Wang, W. Xiao, P. Xi, J. Wang, D. Gao and J. Wang, *Nano-micro Lett*., 2019, **11**, 2.

26. X. Wang, Y. Zhu, A. Vasileff, Y. Jiao, S. Chen, L. Song, B. Zheng, Y. Zheng and S. Z. Qiao, *ACS Energy Lett*., 2018, **3**, 1198–1204.

27. T. Wang, R. Jin, X. Wu, J. Zheng, X. Li and K. Ostrikov, *J. Mater. Chem. A*., 2018, **6**, 9228–9235.

28. J. Zhang, X. Pang, J. Luo, X. Wang, S. Wang and Y. Zhou, *New J. Chem.*, 2023, **47**, 5169–5173.

29. X. Du, H. Su and X. Zhang, *J. Catal*., 2020, **383**, 103–116.

30. J. Duan, Y. Wang, H. Li, D. Wei, F. Wen, G. Zhang, P. Liu, L. Li, W. bing Zhang and Z. Chen, *Chem. Asian J*., 2020, **15**, 1613–1620.

31. L. Wu, K. Zhang, T. Wang, X. Xu, Y. Zhao, Y. Sun, W. Zhong and Y. Du, *ACS Appl. Nano Mater.*, 2018, **1**, 1083–1093.

32. W. Luo, Y. Wang and C. Cheng, *Mater. Today Phys*., 2020, **15**, 100274.

33. P. Q. Liao, J. Q. Shen and J. P. Zhang, *Coord. Chem. Rev.*, 2018, **373**, 22–48.

34. S. N. Zhao, X. Z. Song, S. Y. Song and H. jie Zhang, *Coord. Chem. Rev.*, 2017, **337**, 80–96.

35. J. S. Qin, D. Y. Du, W. Guan, X. J. Bo, Y. F. Li, L. P. Guo, Z. M. Su, Y. Y. Wang, Y. Q. Lan and H. C. Zhou, *J. Am. Chem. Soc.*, 2015, **137**, 7169–7177.

36. X. F. Lu, P. Q. Liao, J. W. Wang, J. X. Wu, X. W. Chen, C. T. He, J. P. Zhang, G. R. Li and X. M. Chen, *J. Am. Chem. Soc.*, 2016, **138**, 8336–8339.

37. L. Catala and T. Mallah, *Coord. Chem. Rev.*, 2017, **346**, 32–61.38

38. X. Y. Yu, Y. Feng, Y. Jeon, B. Guan, X. W. D. Lou and U. Paik, *Adv. Mater*., 2016, **28**, 9006–9011.

39. R. Liu, H. Zhang, X. Zhang, T. Wu, H. Zhao and G. Wang, *RSC Adv.*, 2017, **7**, 19181–19188.

40. B. Tian, W. Kolodziejczyk, J. Saloni, P. Cheah, J. Qu, F. Han, D. Cao, X. Zhu and Y. Zhao, *J. Mater. Chem. A*, 2022, **10**, 3522-3530.

41. H. Wang, J. Liu, H. Wang, X. Cai, X. Ye, L. Zhang, Z. Chen and Z. X. Shen, *J. Mater. Chem. A*, 2020, **8**, 14900–14907.

42. M. Kim, M. A. R. Anjum, M. Choi, H. Y. Jeong, S. H. Choi, N. Park and J. S. Lee, *Adv. Funct. Mater.,* 2020, **30**, 2002536

43. J. K. Das, A. K. Samantara, A. K. Nayak, D. Pradhan and J. N. Behera, *Dalton Trans.*, 2018, **47**, 13792–13799.

44. F. Yang, P. Zhao, X. Hua, W. Luo, G. Cheng, W. Xing and S. Chen, *J. Mater. Chem. A*, 2016, **4**, 16057–16063.

45. L. Yan, L. Cao, P. Dai, X. Gu, D. Liu, L. Li, Y. Wang and X. Zhao, *Adv. Funct. Mater*., 2017, **27**, 1703455.

46. N. Sahu, J. K. Das and J. N. Behera, *Inorg. Chem.,* 2022, **61**, 2835–2845.

47. J. Liang, Y. Yang, J. Zhang, J. Wu, P. Dong, J. Yuan, G. Zhang and J. Lou, *Nanoscale*, 2015, **7**, 14813–14816.

48. J. K. Das, A. K. Samantara, S. Satyarthy, C. S. Rout and J. N. Behera, *RSC Adv*., 2020, **10**, 4650–4656.

49. T. Tian, L. Huang, L. Ai and J. Jiang, *J. Mater. Chem. A*, 2017, **5**, 20985–20992.

50. J. Sun, Z. Huang, T. Huang, X. Wang, X. Wang, P. Yu, C. Zong, F. Dai and D. Sun, *ACS Appl. Energy Mater*., 2019, **2**, 7504–7511.

51. J. Mujtaba, L. He, H. Zhu, Z. Xiao, G. Huang, A. A. Solovev and Y. Mei, *ACS Appl. Nano Mater.*, 2021, **4**, 1776–1785.

52. M. Wang, K. Jian, Z. Lv, D. Li, G. Fan, R. Zhang and J. Dang, *J. Mater. Sci. Technol.*, 2021, **79**, 29–34.

53. M. S. Faber, R. Dziedzic, M. A. Lukowski, N. S. Kaiser, Q. Ding and S. Jin, *J. Am. Chem. Soc.*, 2014, **136**, 10053–10061.

54. X. Sun, H. Huang, C. Wang, Y. Liu, T. L. Hu and X. H. Bu, *ChemElectroChem*, 2018, **5**, 3639–3644.

55. V. Ganesan, S. Lim and J. Kim, *Chem. Asian J.*, 2018, **13**, 413–420.

56. B. Dong, J. Y. Xie, N. Wang, W. K. Gao, Y. Ma, T. S. Chen, X. T. Yan, Q. Z. Li, Y. L. Zhou and Y. M. Chai, *Renew. Energy*, 2020, **157**, 415–423.

CHAPTER-4

Ru Prussian Blue Analogue-Derived Ru Nanoparticles Composited with a Trace Amount of Pt as an Efficacious Electrocatalyst for the Hydrogen Evolution Reaction

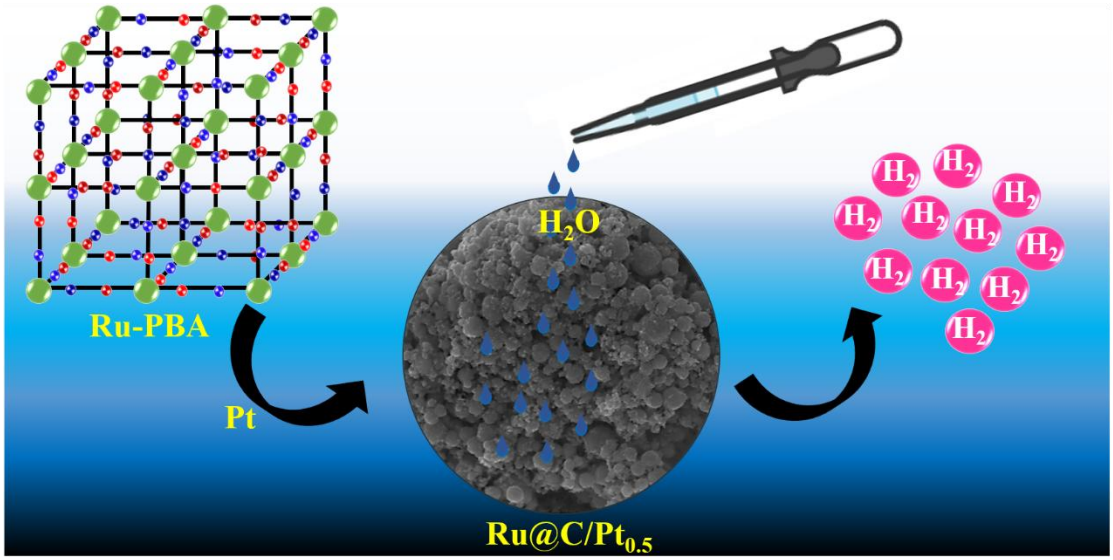

4.1 Abstract

In this work, we designed a straightforward and highly reproducible synthetic methodology to prepare Ru^0–Pt^0 composites. We report a significant improvement in the electrocatalytic performance upon compositing Ru with a very trace amount of Pt. In particular, Ru nanoparticles were derived from a Ru-Prussian blue analogue (Ru PBA) and composited with (0.1, 0.5, and 1 mmol) metallic platinum following an optimized chemical reduction method. Interestingly, the composite with 0.5 mmol of Pt (Ru@C/$Pt_{0.5}$) required low overpotentials of 32 and 140 mV to achieve current densities of 10 and 100 mA cm^{-2}, respectively. Furthermore, Ru@C/$Pt_{0.5}$ exhibited a smaller Tafel slope (26 mV dec^{-1}), robust durability with 50 hours of long-term stability and a higher turnover frequency (TOF: 5.6 $s^{-1}@\eta_{10\ mA\ cm^{-2}}$) than commercial Pt/C (TOF: 4.1 $s^{-1}@\eta_{10\ mA\ cm^{-2}}$). First-principles calculations using density functional theory (DFT) revealed that the existence of Pt islands on the Ru nanoparticles weakened the strength of the adsorption of hydrogen at the Ru interstitials due to electrostatic repulsion caused by charge retention at Ru atoms near the corner of the islands, leading to rapid dissociation of hydrogen. This created a significant impact on the improvement of the

electrocatalytic HER activity of the Ru@C/$Pt_{0.5}$ electrocatalyst. It appears that restricting the concentration of Pt to trace amounts is a necessary condition for the observed catalytic efficiency, as the catalytic efficiency decreases with an increasing island size due to stronger binding of atomic hydrogen on peripheral Pt atoms and stabilization of adsorbed atomic hydrogen caused by softening of phonon modes with increasing island size. This study opens up a novel avenue for the exploration of highly efficient electrocatalysts for hydrogen evolution reactions.

4.2 Introduction

Molecular hydrogen (H_2), presumed to be the greenest fuel ever with a high energy density, is nonetheless related with concerns such as safer transportation and storage.[1–4] Various techniques, either solely electrochemical or light-driven, have been developed for splitting water to produce hydrogen. However, electrochemical splitting of water using electrocatalysts remains the greenest and most effective method for producing H_2 on-site.[5] While the ideal strength of hydrogen bonding to platinum makes it the most promising electrocatalyst for the HER, its scarcity and high cost limit its widespread use in commercial applications.

Efforts have been undertaken to substitute platinum catalysts with earth-abundant transition metal sulfides, selenides, phosphides, nitrides, carbides, and other compounds.[6–21] Integrating these nanoparticles with conductive carbons in one dimension (carbon nanotubes) and two dimensions (graphene and its derivatives) improves catalytic performance.[22,23] The fair distribution of nanoparticles on these carbon materials enhances surface availability, which promotes electrocatalytic performance. The presence of a large number of electrochemically active sites leads to better performance in energy conversion application. The number of active sites can be

increased by tailoring the morphology,[24] porosity,[25] and size[26] of catalysts. The intrinsic activity of a catalyst can be enhanced by tuning its composition, phase, defect, and other properties. In this regard, defect engineering is an effective strategy since it leads to changes in the electronic structure of the material. This affects the interaction between the adsorbent and surface atoms, eventually leading to the modification of the adsorption energy of active sites, which enhances the performance of electrocatalysts in energy conversion applications.[27,28] However, most synthesis procedures in such directions require extra carbon precursors, whereas a single-step *in situ* method would be more favorable for scaling synthesis.

Metal–organic frameworks (MOFs), commonly referred to as coordination polymers, are made up of metal centres and various kinds of organic ligands. Significant drawbacks of MOFs include their low conductivity and unstable performance in basic and acidic environments. Owing to the above mentioned limitations, MOFs have attracted a lot of interest lately as a viable precursor for the development of effective electroactive materials for a wide range of applications, such as electrochemical water splitting.[29–32] Prussian blue analogues (PBA), a unique family of MOFs, have a large specific surface area and a feasible synthetic approach.[33] PBA-derived metal nanoparticles have several advantages over other nanoparticles, including higher electrochemical performance in HER due to their greater electrochemical active surface area (ECSA), lower overpotential value, and improved durability in both alkaline and acidic conditions.[34] PBA-derived electrocatalysts exhibit high stability under challenging electrolytic circumstances due to the carbon matrix around the material; it also provides protection against corrosion and prevents aggregation of the electrocatalyst particles. As an outcome, the particles are uniformly distributed across the electrocatalyst surface, increasing the number of active

sites readily accessible for the electrochemical reaction to take place and boosting the electrocatalyst's performance for the electrochemical application.[35]

An overview of the literature renders it abundantly evident that compositing non-noble metal nanoparticles with noble metals allows one to modify the lattice parameters, bond lengths, and binding energies of the nanoparticles.[1] The electrocatalytic performances of these composite nanoparticles improve as a result of a remarkable shift in the hydrogen adsorption energies. Many Ru and Pt-incorporated nanoparticles have been utilised as the primary electrocatalyst for a variety of energy conversion applications in recent years.[36–45] However, their further growth is hindered by their poor catalytic durability in acidic electrolytes. On the other hand, Ru and Pt have similar hydrogen bond strengths (65 kcal mol^{-1}), thereby making it facile for the hydrogen to undergo adsorption and desorption during the hydrogen evolution reaction.[46,47] The cost of metallic Ru is nearly 4% of the cost of Pt; therefore, it may be used as an alternative to the state-of-the-art Pt catalyst for HER.[48] Ru and its oxides have been shown to exhibit anti-corrosion capabilities in acidic environments, prompting more investigations into their electrocatalytic applications.[49,50] Therefore, strategies need to be established for the synthesis of ruthenium-based nanoparticles and their noble metal (Pt) based hybrids.

In this work, carbon-embedded Ru-nanoparticles (Ru@C) have been prepared from the Ru-Prussian blue analogue (Ru-PBA) by annealing in an inert atmosphere. Further, to achieve better HER electrocatalytic activity, the Ru@C nanoparticles were composited with tiny platinum nanoparticles (Ru@C/Pt). Here, we have synthesized Ru@C/Pt nanocomposites with variable amounts of platinum (0.1 mmol, 0.5 mmol, and 1 mmol), out of which $Ru@C/Pt_{0.5}$ showed better electrocatalytic activity. Particularly, it needs only 32 mV overpotential to deliver 10 mA cm^{-2} current density along with higher turnover frequency (5.6 $s^{-1}@\eta_{10\ mA\ cm^{-2}}$) and excellent electrocatalytic durability during

50 hours of continuous electrolysis. The as-prepared catalyst holds potential applications and shows better catalytic performance compared to the previously studied PBA-derived nanoparticles. In this study, carbon-embedded Ru nanoparticles (Ru@C) were synthesised by annealing the Ru-Prussian blue analogue (Ru-PBA) in an inert environment. To improve HER electrocatalytic performance, Ru@C nanoparticles were composited with tiny platinum nanoparticles (Ru@C/Pt). We synthesised the Ru@C/Pt nanocomposite with varying quantities of platinum (0.1 mmol, 0.5 mmol, and 1 mmol), with Ru@C/$Pt_{0.5}$ exhibiting higher electrocatalytic activity. It requires just 32 mV overpotential to achieve 10 mA cm^{-2} current density, a higher turnover frequency (5.6 $s^{-1}@\eta_{10\ mA\ cm^{-2}}$), and outstanding electrocatalytic durability during 50 hours of continuous electrolysis. The as-prepared catalyst holds potential application and shows greater catalytic activity as compared to the previously explored PBA-derived nanoparticles.[51–54]

4.3 Experimental Section

4.3.1 Materials

Potassium hexacyanoruthenate(ii) hydrate, $K_4[Ru(CN)_6]\cdot xH_2O$ and ruthenium acetylacetonate, $Ru(acac)_3$ were purchased from Sigma Aldrich chemicals and used as received without any further purification. Nafion solution (5% solution of Nafion 116 in lower hydrocarbon) and absolute ethanol (99.99%) were purchased from Alfa Aesar and Merck, respectively. In this work, all the solutions were prepared using deionized water.

4.3.2 Synthesis of Ru-PBA

Ru-PBA was synthesized using a single-step solvothermal method, following a previously reported procedure.[55] In detail, 0.310 mmol of $K_4[Ru(CN)_6]\cdot xH_2O$ (0.130 g) was added to 10 mL deionized water and stirred for 15 minutes. To it, 0.620 mmol $Ru(acac)_3$ (0.250 g) was added and stirred for 60 minutes. The final solution was

transferred to a Teflon-lined stainless-steel autoclave (volume: 23 mL) and placed in a hot air oven at 175 °C for 96 hours. The dark green residues obtained after cooling down to room temperature were washed with deionized water and absolute ethanol repeatedly, dried, and stored for further characterisation and modification.

4.3.3 Synthesis of PBA-derived Ru@C Nanoparticles (NPs) and Ru@C/Pt Nanocomposite

The Ru NPs were prepared by annealing the as-synthesized PBA in the argon atmosphere at 450 °C for one hour. Thereafter, the black-colored powder (Ru@C) so obtained was washed repeatedly with deionized water and absolute ethanol, dried, and stored for further characterisation and electrochemical study. Further, the Pt-doped Ru@C nanocomposite (Ru@C/Pt) was synthesized using a single-step wet chemical reduction method. In detail, 10 mg of Ru@C NPs was dispersed in 10 mL of (0.1 mmol, 0.5 mmol, and 1 mmol) $PtCl_2$ solution and left to stir for one hour. To the dispersion, freshly prepared aqueous $NaBH_4$ solution was added in a dropwise manner and left to stir for another 30 minutes. Thereafter, Ru@C/Pt was collected by washing repeatedly with deionized water, dried at 60 °C, and stored for further characterisation and electrochemical application study.

4.4 Characterisation

The crystallinity and phase purity of the synthesized samples were analyzed using the Bruker D8 advance diffractometer system with Cu Kα radiation (λ = 1.5418 Å). The surface morphology and elemental distributions were characterized by field-emission scanning electron microscope (FESEM, Zeiss Pvt. Ltd, Germany) and transmission electron microscope (JEOL, 2100F). For the TEM analysis, a very dilute suspension of the sample in a mixture of water and ethanol has been prepared and cast onto the 200-mesh carbon-coated copper grid. Thereafter, the grid was dried properly under the table

lamp and used for morphology analysis. Further, the elemental composition and corresponding oxidation states of the synthesized materials were determined through X-ray photoelectron spectroscopy (XPS, PHI Versa Probe III). The elemental composition of synthesized catalysts was verified by using an inductively coupled plasma-optical emission spectrophotometer (iCAP 7000 ICP-OES). The generated H_2 gas was analyzed using gas chromatography (Agilent 990 Micro GC).

4.5 Electrochemical Measurements

The electrocatalytic performance of the samples was assessed in a three-electrode electrochemical cell with a Biologic electrochemical workstation (SP-200). The sample cast on a glassy carbon rotating disk electrode (GCRDE), bare graphite rod, and aqueous Ag/AgCl were taken as the working, counter, and reference electrodes, respectively. The GCRDE (geometrical surface area: 0.19 cm^2) was polished to a mirror finish using alumina slurry, then washed with deionised water using a bath sonicator before being dried in a vacuum oven. Simultaneously, the electrocatalyst ink was prepared by mixing an optimized quantity of the electrocatalyst sample (1 mg) in absolute ethanol (0.095 mL) and Nafion (5% solution of Nafion in lower hydrocarbon) (0.005 mL) using a bath sonicator. The prepared catalyst ink was cast onto the polished GCRDE (with a loading of 0.263 mg cm^{-2}), dried properly, and used directly as a working electrode. Here, the linear sweep voltammograms were obtained at 5 mV s^{-1} and 2000 rpm in 0.5 M H_2SO_4 electrolyte. All electrochemical experiments were done using an Ag/AgCl reference electrode and the Nernst **Equation (4.1)**.

$$E_{RHE} = E_{Ag/AgCl} + 0.059\,pH + E^0_{Ag/AgCl} \quad (4.1)$$

Here, the pH of 0.5 M H_2SO_4 is 0.03, and the standard potential for the Ag/AgCl reference electrode $E^0_{Ag/AgCl}$ is 0.21 V. The electrochemical impedance spectrum, or Nyquist impedance, was measured under a static situation with an AC amplitude of 5 mV and a frequency range of 0.1 Hz to 1 MHz.

The TOF has been calculated using the following **Equation (4.2)**:

$$\text{TOF} = (J \times S)/(2 \times F \times n) \quad (4.2)$$

First, the moles of active sites (n) for each electrocatalyst were determined by dividing the mass of the material coated onto the electrode surface by their molecular mass. Following that, the turnover frequency (TOF) was estimated using the **Equation 4.2** given, assuming that all metal atoms participate in the catalytic process. J, S, and F represent the measured reduction current density, geometrical surface area of the working electrode, and Faraday constant (96 485.3 C mol^{-1}). Since two electrons are evolved per mole of H_2, 2 is used in the denominator in **Equation (4.2)**.[56]

4.6 Computational Details

First-principles calculations are performed by density functional theory (DFT),[57] as implemented in Quantum Espresso,[58] which expands wave functions on the basis of plane waves and allows ultrasoft pseudopotential for the valence electrons.[59] Many electron effects are represented by PBE-type exchange–correlation functionals.[60]

We considered a surface slab of Ru(002) with three atomic layers, each with 16 atoms. Ru(002) Pt, Ru(002) Pt_3, Ru(002) Pt_6, and Ru(002) Pt_9 models are designed by placing Pt atom (single) and clusters (of three/six/three above six) on fcc sites of the Ru(002) surface, as shown in **Figure 4.9**. Inter-slab separation of 25 Å is considered in order to

avoid the interaction between periodic images. All lattice parameters and ionic positions are optimized using the Broyden–Fletcher–Goldfarb–Shanno (BFGS) scheme.[61]

To ensure the convergence of total energy, all calculations are performed using plane-wave cutoff energy of 45 Ry and self-consistent field convergence criteria of 10–8 Ry. Variable cell-relaxation has been carried out until the total energies are converged below 10–5 Ry and forces are minimized below 10–4 Ry $Bohr^{-1}$. We have used 2 × 2 × 1 and 8 × 8 × 1 Monkhorst–Pack grid of *k*-points for slab vc-relaxation and calculation of energetics, respectively. Hydrogen adsorption has been tried on multiple high-symmetry surface positions, implying the fcc position to be the most stable. The hydrogen atom adsorption energies (E_{ads}) are calculated from total energies (E) as **(Equation 4.3)**,

$$E_{ads} = E_{RuH^*} - (E_{1/2H_2} + E_{Ru}) \quad (4.3)$$

where E_{RuH^*} corresponds to the energy of hydrogen adsorbed on Ru catalysts, E_{H_2} and E_{Ru} correspond to the energy of isolated H_2 molecules and Ru surface, respectively. At a temperature of 298.15 K, Gibb's free energy of hydrogen adsorption along the reaction coordinates is evaluated as **(Equation 4.4)**[62]

$$G_{H^*} = E_{ads}^{H} + \mathrm{ZPE} - TS \quad (4.4)$$

The zero-point energy (ZPE) is calculated by the relation **(Equation 4.5)**

$$\mathrm{ZPE} = \sum_i \hbar\omega_i/2 \quad (4.5)$$

where ω_i is a real normal mode frequency. The zero-point energy for a hydrogen molecule (H_2) thus calculated is 0.267 eV, implying 0.1335 eV per H atom. Entropy *S* is taken to be non-zero only for H_2 molecule in the gas phase and values are obtained from the standard table.[63] To approximately estimate the free energy G^{Ptn+2H^*} corresponding to the third step in the Volmer–Tafel mechanism, where two hydrogen atoms are adsorbed

in neighboring fcc sites, we have added ($G^{Ru2H*} - G^{RuH*}$), which is around −0.1 eV, to G^{PtnH*}.

4.7 Results and Discussion

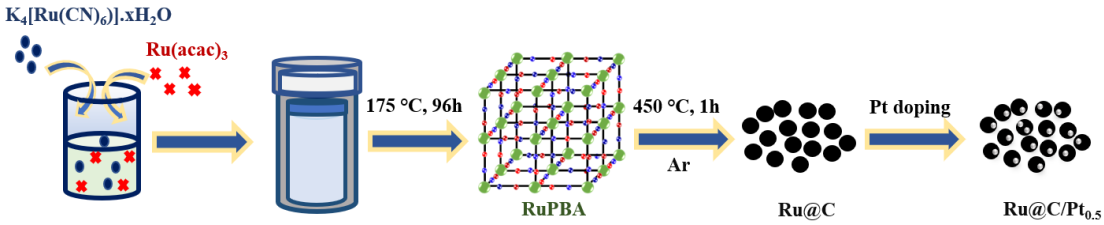

Scheme 4.1: Stepwise synthesis of Ru-PBA and its derived nanostructures (Ru@C and Ru@C/$Pt_{0.5}$).

The Prussian blue analogue (PBA) has been prepared from $K_4[Ru(CN)_6]\cdot xH_2O$ and $Ru(acac)_3$ in a single-step hydrothermal process. The hydrothermal synthesis method is highly advantageous compared to other growth methods for synthesizing nanomaterials due to its fast reaction kinetics, short processing times, ability to achieve phase purity, high crystallinity, high yield, low cost, environmental friendliness and reduced hazardous nature. These desirable characteristics make hydrothermal synthesis an ideal choice for producing nanomaterials. The mechanism of hydrothermal synthesis is a liquid nucleation model, and the parameters involved can be adjusted during hydrothermal processing to sustain a high synchronized nucleation rate and good size distribution.[64,65]

The as-prepared PBA was then annealed in an inert environment of Ar at various temperatures, resulting in the formation of Ru nanoparticles embedded in a carbon matrix (Ru@C). Furthermore, Pt nanoparticles were composited with Ru@C nanostructures using a one-step chemical reduction process. As indicated in **Scheme 4.1**, the Ru@C nanostructures were dispersed in varying quantities of aqueous $PtCl_2$ solution, followed by a dropwise addition of $NaBH_4$. The structure of the as-prepared catalysts was

characterized using powder X-ray diffraction analysis. As shown in **Figure 4.1a**, Ru-PBA is well indexed with a face-centered cubic (fcc) crystal structure with a space group of *Fm*3*m*.[36]

On the other hand, after annealing and composite formation with Pt NPs, the diffraction peaks (at 38.61°, 42.56°, 44.20°, 58.58°, 69.56° and 78.50°) for Ru@C NPs and Ru@C/$Pt_{0.5}$ were well indexed to the 100, 002, 101, 102, 110 and 103 facets of

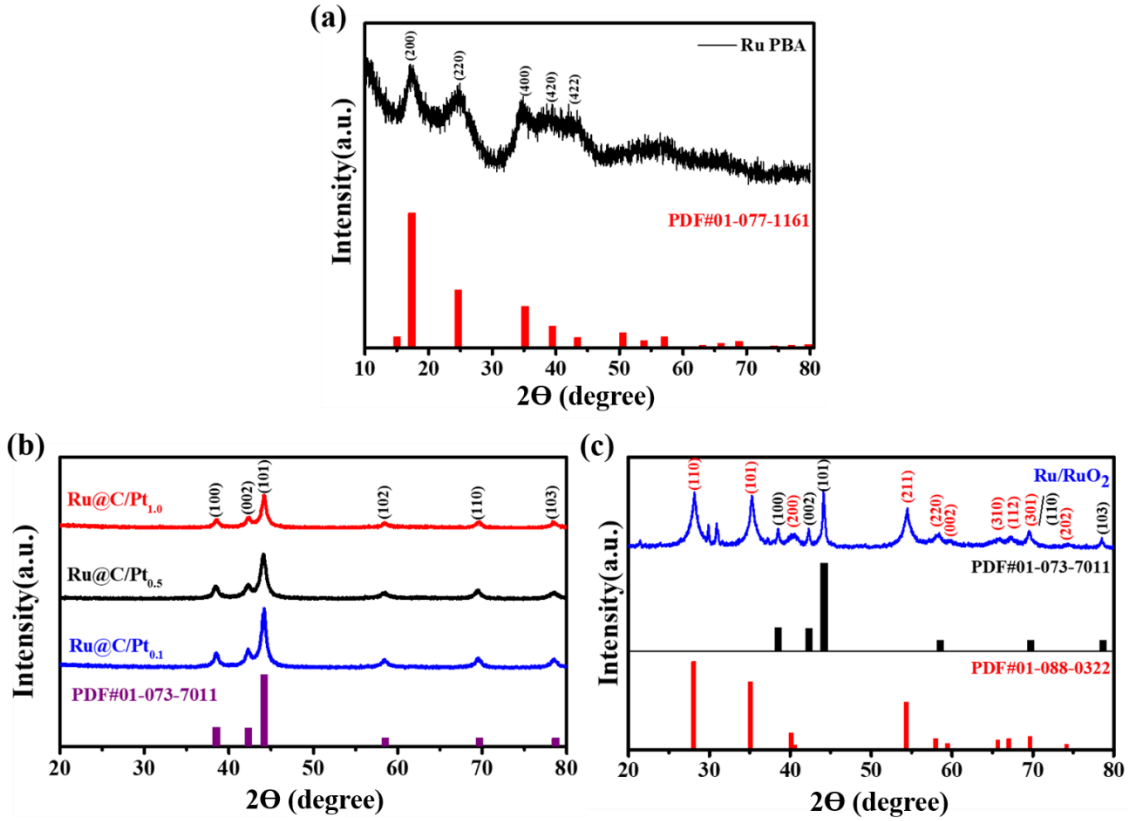

Figure 4.1: Powder X-ray diffraction for Ru-PBA (a), Ru@C/$Pt_{0.1}$, Ru@C/$Pt_{0.5}$, and Ru@C/$Pt_{1.0}$ (b), and Ru-PBA annealed in free air (c).

hexagonal close-packed (hcp) Ru nanocrystals (**Figure 4.2a**) with a space group *P*63/*mmc* (194) (PDF#01-073-7011). The PXRD pattern in **Figure 4.1b** clearly reveals a decrease in the crystallinity as we move from $Pt_{0.1}$ to $Pt_{0.5}$ and then to $Pt_{1.0}$.

However, annealing Ru-PBA in the air resulted in a combination of Ru@C NPs and RuO_2 **(Figure 4.1c)**. Images from the field emission scanning electron microscopy (FESEM) were utilised to verify the surface morphology and structure of the as-prepared Ru@C and Ru@C/Pt (at various Pt loadings). **Figure 4.2b** reveals that the as-prepared

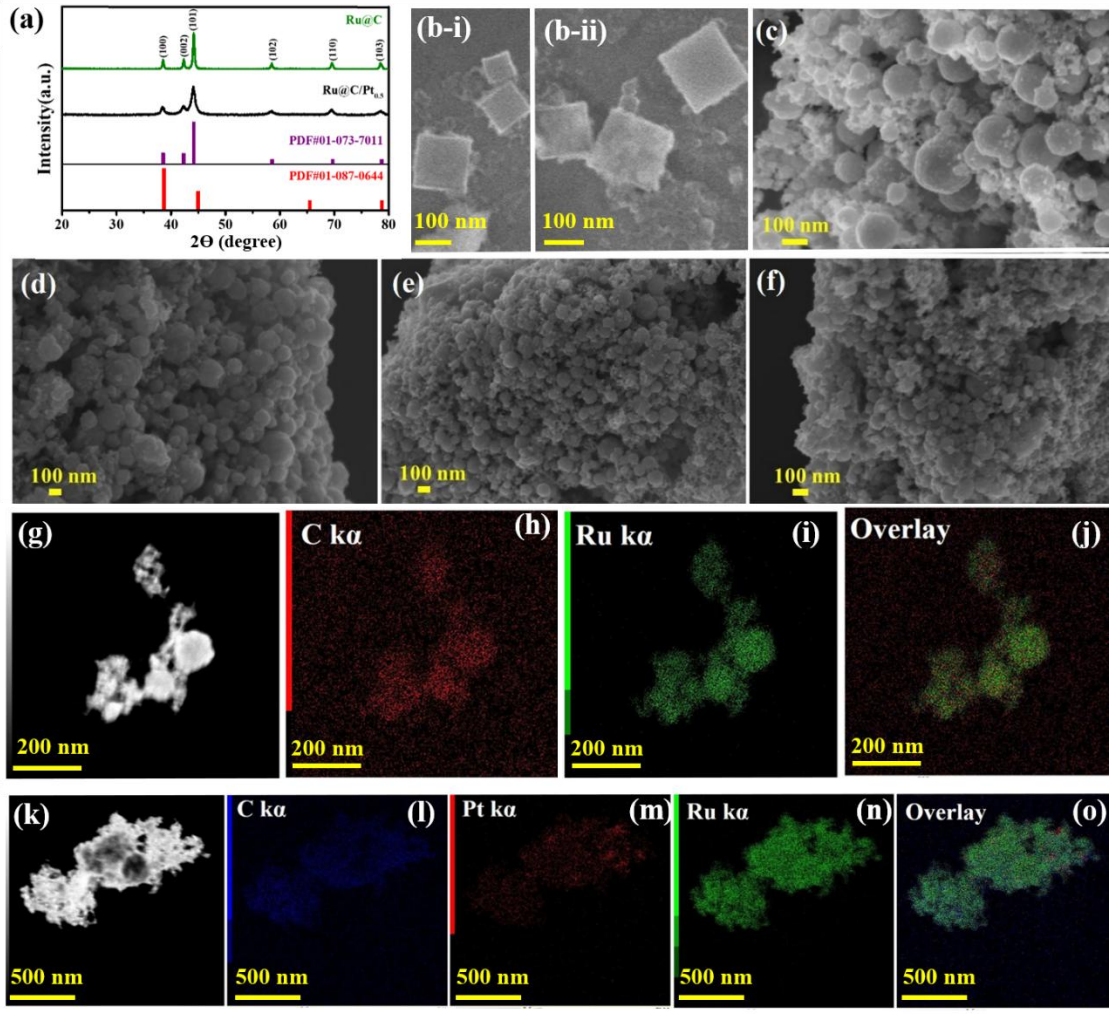

Figure 4.2: Powder XRD for Ru@C and Ru@C/$Pt_{0.5}$ (a). FESEM images for - Ru-PBA(b-i and b-ii), Ru@C (c), Ru@C/$Pt_{0.1}$ (d), Ru@C/$Pt_{0.5}$ (e), and Ru@C/$Pt_{1.0}$ (f). Elemental mapping of Ru@C (g–j) and Ru@C/$Pt_{0.5}$ (k–o).

Ru-PBA has a well-defined cube-like shape. However, annealing in an inert environment yields spherical-shaped Ru@C nanoparticles of varying sizes **(Figure 4.2c)**. Adding $PtCl_2$ to the annealed sample resulted in a uniform distribution of tiny Pt NPs on the

spheres, resulting in a Ru/Pt composite-like structure **(Figure 4.2d–f)**. **Figure 4.2d–f** reveals a decrease in the size of Ru nanoparticles with an increase in the Pt loading from 0.1 to 0.5 and finally to 1.0 mmol. This can be attributed to the change in the crystallinity of the electrocatalyst due to Pt loading **(Figure 4.1b)**. With a decrease in the crystallinity of the material, the size of nanoparticles decreases.[66] Furthermore, the composition of Ru@C and Ru@C/$Pt_{0.5}$ has been conferred from the EDS and elemental mapping, as shown in **Figure 4.2g–o**. **Figure 4.3a,b** and **Figure 4.3e,f** show the TEM images of Ru@C and Ru@C/Pt0.5, respectively. In the case of Ru@C, the high-resolution TEM images clearly show the lattice fringes of 0.213 nm and 0.205 nm assigned to the (002) and (101) facets of Ru **(Figure 4.3c)**. An additional spacing of 0.232 nm has been observed in Ru@C/$Pt_{0.5}$ assigned to the (111) plane of Pt **(Figure 4.3g)**. **Figure 4.3d** and **Figure 4.3h** reveal the SAED pattern for Ru@C and Ru@C/Pt0.5, respectively. The SAED pattern shows the high crystalline nature of both the materials. This clearly confirms the presence of Pt nanoparticles on the Ru spheres in the

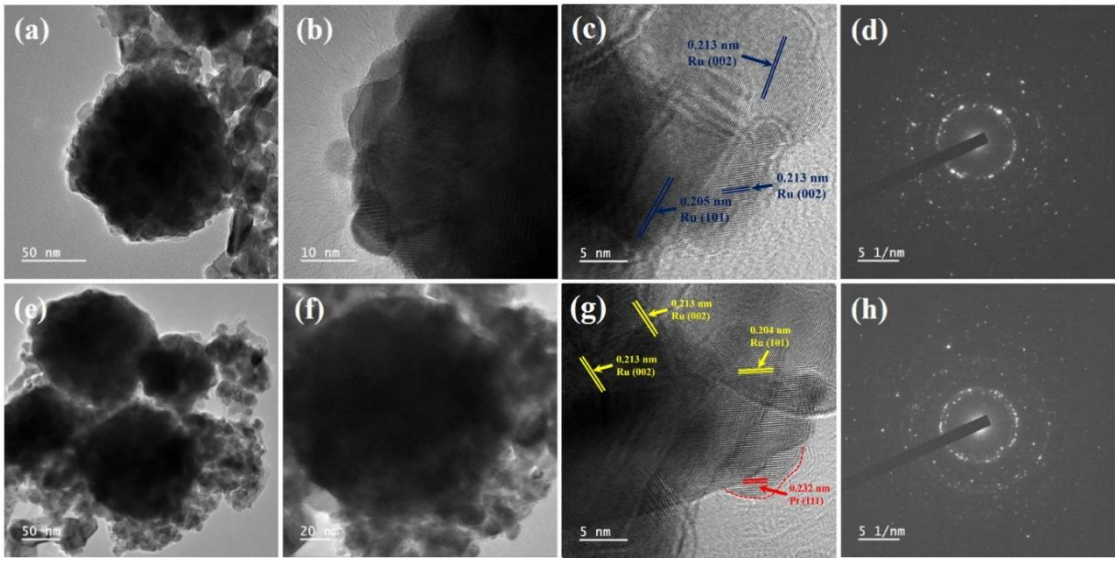

Figure 4.3: Transmission electron microscopic images, HRTEM and SAED pattern for Ru@C (a–d) and Ru@C/$Pt_{0.5}$ (e–h).

Ru@C/$Pt_{0.5}$ composite. Also, no more Pt nanoparticles were further observed in the TEM images, indicating that the trace amount of Pt atoms get dispersed on the Ru nanoparticles, resulting in the formation of a dilute composite.[67]

X-ray photoelectron spectroscopy has been utilised to determine the elements present in the composite material. The full survey spectrum **(Figure 4.4a)** shows the presence of Ru, Pt, and C along with a very trace amount of oxygen (the surface adsorbed oxygen).

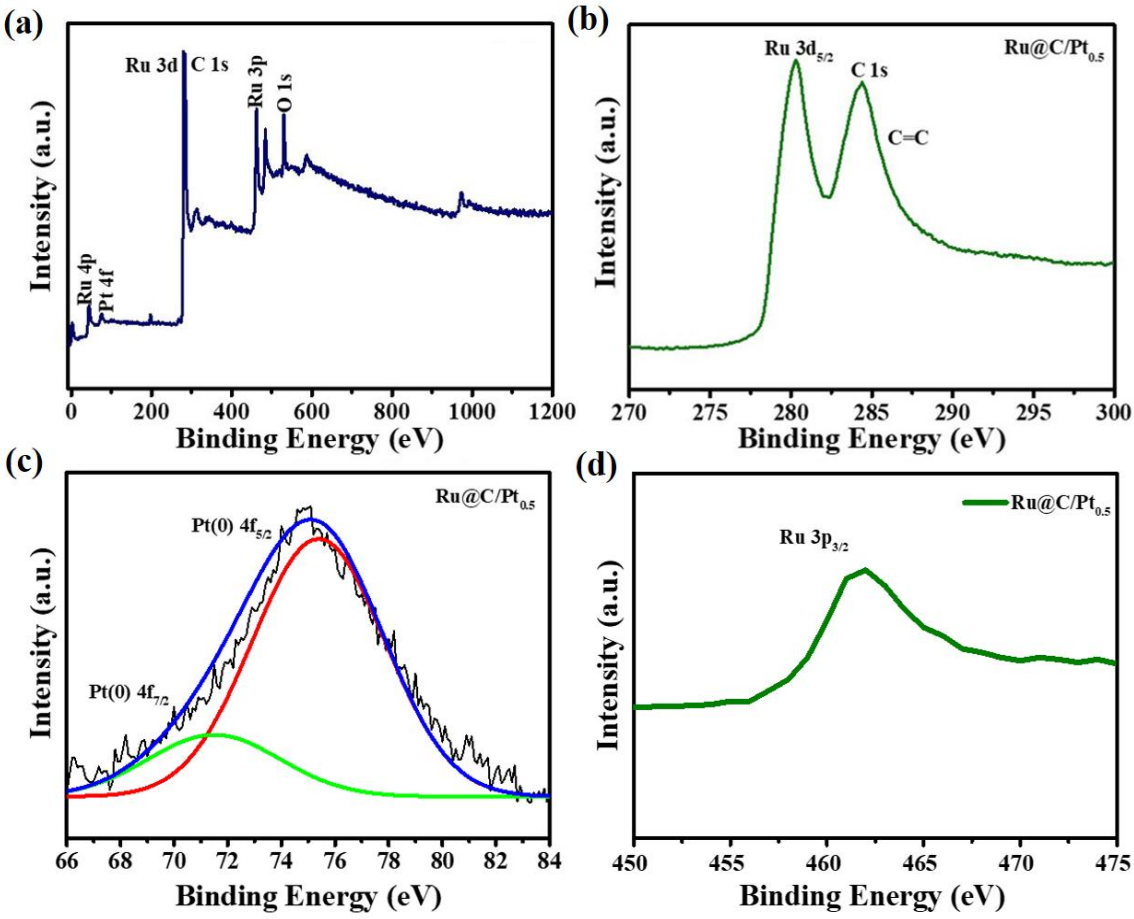

Figure 4.4: Full survey (a) and core-level X-ray photoelectron spectrum for Ru 3d and C 1s (b), Pt 4f (c) and Ru 3p (d) of Ru@C/$Pt_{0.5}$.

The peaks at 280.0 eV in **Figure 4.4b** and 461.85 eV in **Figure 4.4d** were assigned to the Ru $3d_{5/2}$ and Ru $3p_{3/2}$, respectively, for the metallic Ru (0). Further, in **Figure 4.4c**, the Pt 4f areas contain two major peaks (Pt $4f_{7/2}$ and Pt $4f_{5/2}$) ascribed to the metallic

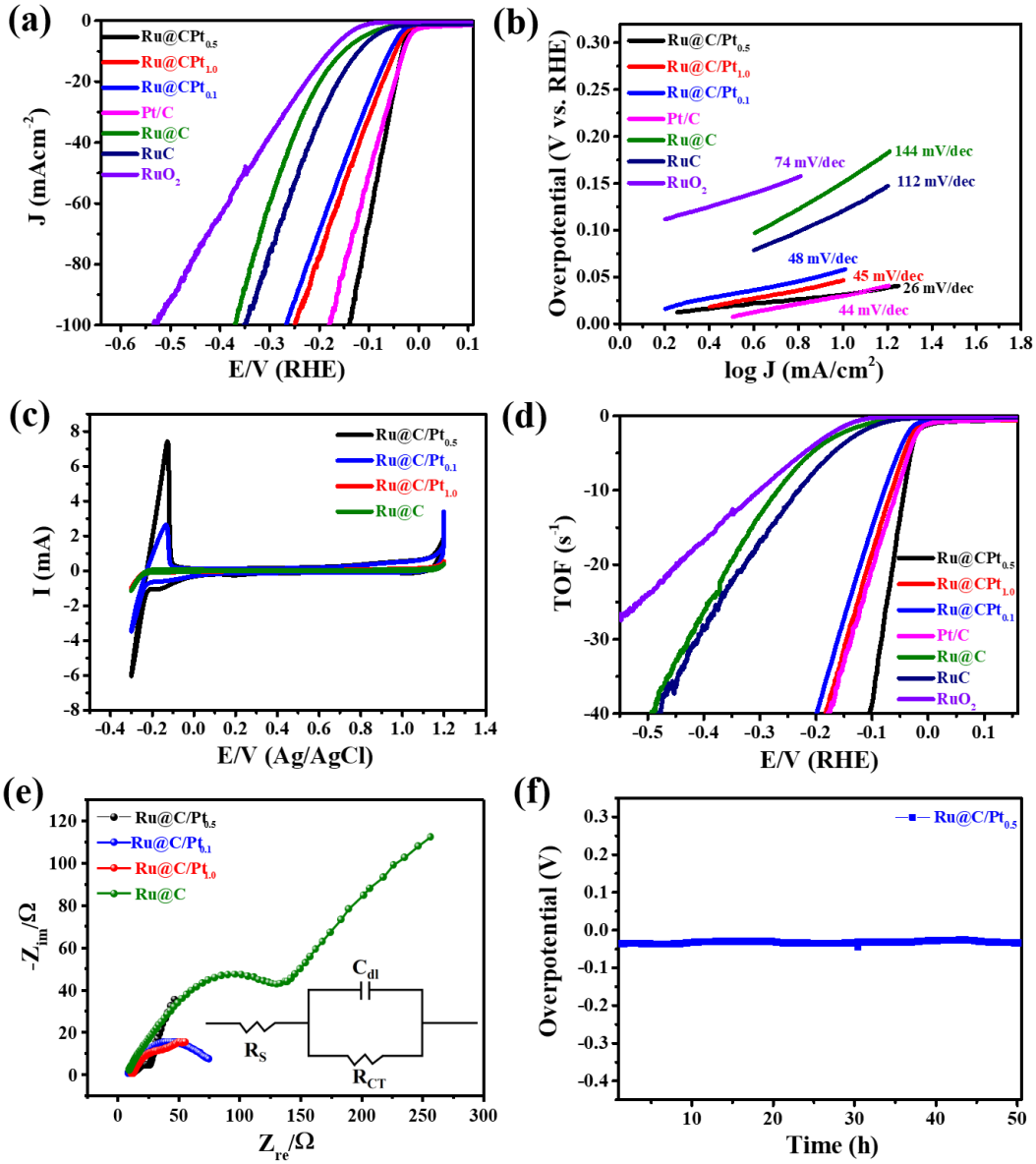

Figure 4.5: Linear sweep voltammogram (a), Tafel slopes (b), cyclic voltammograms (c), plot of turnover frequency against potential (d), EIS plot (e) and chronopotentiometric spectrum (f) for the electrocatalysts. The linear sweep voltammograms and cyclic voltammograms are recorded at sweep rates of 5 mV s^{-1} and 10 mV s^{-1}, respectively. The inset of (e) is the corresponding circuit diagram for the EIS plot.

Pt(0). The peak at 284.4 eV is attributed to the C 1s, and specifically, sp^2 hybridized carbon (C=C) of the graphitized carbon. This observation confirms the formation of a composite-like structure where both the Ru and Pt are in zero oxidation state with graphitized carbon, reflecting the improved stability because of higher corrosion resistance.[68,69]

After synthesis and characterisation, the electrocatalytic activity in the hydrogen evolution reaction was evaluated using a three-electrode electrochemical cell in an acidic electrolyte (0.5 M H_2SO_4). The electrocatalyst cast glassy carbon rotating disc electrode (GCRDE; the geometrical surface area is 0.19 cm^2), aqueous Ag/AgCl, and graphite rod serve as working, reference, and counter electrodes, respectively. Under the optimized temperature-dependent conditions, **Figure 4.5a** shows non-*iR* compensated linear sweep voltammograms of Ru@C, Ru@C/$Pt_{0.1}$, Ru@C/$Pt_{0.5}$, Ru@C/$Pt_{1.0}$ along with commercial Pt/C, Ru/C, and RuO_2 for comparison. The Ru@C/$Pt_{0.5}$ catalyst demonstrated superior electrocatalytic activity in comparison to other platinum-loaded catalysts, but its onset potential appears to be similar to that of Ru@C/$Pt_{0.1}$, Ru@C/$Pt_{1.0}$, and commercial Pt/C. Another crucial parameter for assessing the catalytic activity of a specific electrocatalyst is the cathodic current density at a given overpotential. This is determined using the reference of photo electrocatalytic water splitting, where the overpotential required to deliver 10 mA cm^{-2} current density is regarded as the benchmarked parameter and is compared with other materials to assess their catalytic activity.[70,71] In order to accomplish this, Ru@C/$Pt_{0.5}$ requires only 32 mV overpotential, which is significantly less than other electrocatalysts studied here **(Table 4.1)**. The performance of Ru@C/$Pt_{0.5}$ in different electrolytes, such as 0.5 M KOH (pH = 13.69), 0.5 M HCl (pH = 0.3) and 0.5 M Na_2SO_4 (pH = 7.2), has also been checked. The performance of Ru@C/$Pt_{0.5}$ has been checked in different electrolytes such as 0.5 M

KOH (pH=13.69), 0.5 M HCl (pH=0.3) and 0.5 M Na_2SO_4 (pH=7.2). The sample casted glassy carbon rotating disk electrode (GCRDE), bare graphite rod, and aqueous Ag/AgCl were taken as working, counter, and reference electrodes respectively for the electrolytes 0.5 M H_2SO_4, 0.5 M HCl and 0.5 M Na_2SO_4. The linear sweep voltammograms were obtained at 5 mV/s and 2000 rpm in all the electrolytes. The LSV in 0.5 M NaOH was carried out by using Hg/HgO, glassy carbon rotating disk electrode (GCRDE), and bare graphite rod as reference, working and counter electrode respectively. All the potentials were converted into RHE by using the following Nernst **Equation (4.6)**:

For Hg/HgO:

$$E_{RHE} = E_{Hg/HgO} + E^0_{Hg/HgO} + 0.059\,pH \qquad (4.6)$$

And for Ag/AgCl the **Equation 4.1** was utilised.

Figure 4.6a reveals the overpotentials required by Ru@C/$Pt_{0.5}$ to produce a current density of 10 mA cm^{-2} were 32 mV, 34 mV and 644 mV in 0.5 M H_2SO_4, 0.5 M HCl, and 0.5 M KOH, respectively. Ru@C/$Pt_{0.5}$ was not able to produce a current density of

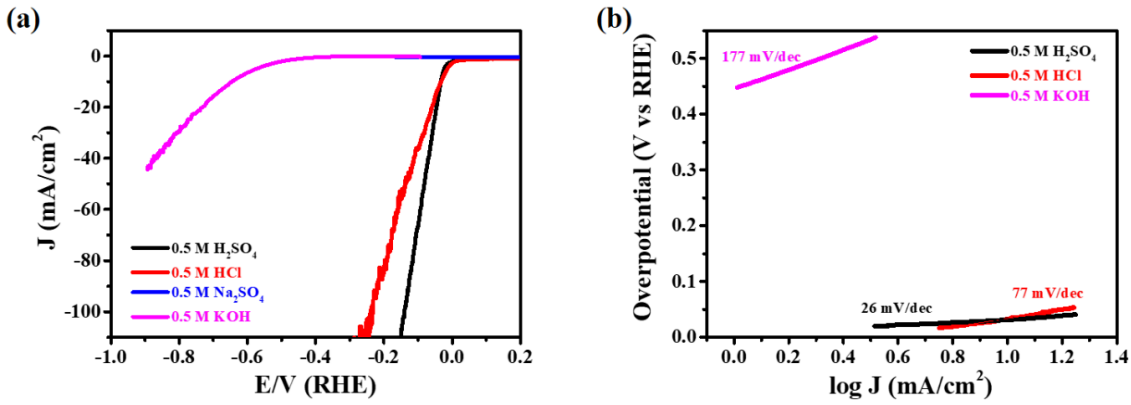

Figure 4.6: Linear sweep voltammograms (a) and Tafel slopes (b) for Ru@C/$Pt_{0.5}$ in 0.5 M H_2SO_4, 0.5 M HCl, 0.5 M Na_2SO_4 and 0.5 M KOH.

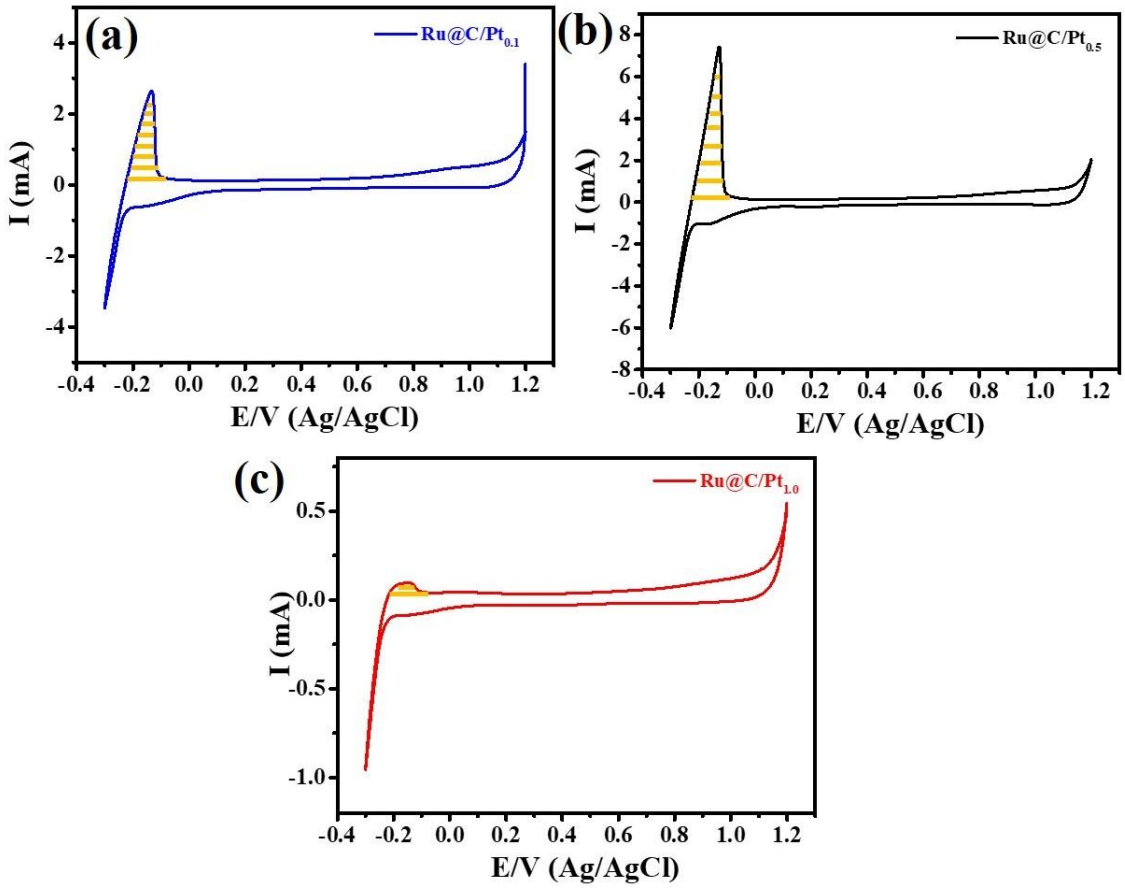

Figure 4.7: Cyclic voltammetric profile of Ru@C/$Pt_{0.1}$ (a), Ru@C/$Pt_{0.5}$ (b) and Ru@C/$Pt_{1.0}$ (c) electrode in 0.5 M H_2SO_4 at a sweep rate of 10 mV/s.

10 mA cm^{-2} in 0.5 M Na_2SO_4, *i.e.*, Ru@C/$Pt_{0.5}$ was inactive towards HER in 0.5 M Na_2SO_4. Although the overpotential required by Ru@C/$Pt_{0.5}$ to produce a current density of 10 mA cm^{-2} in 0.5 M H_2SO_4 and 0.5 M HCl was similar, **Figure 4.6b** reveals the Tafel slope for Ru@C/$Pt_{0.5}$ to be 26 mV dec^{-1} and 77 mV dec^{-1} in 0.5 M H_2SO_4 and 0.5 M HCl, respectively, indicating faster reaction kinetics in the case of 0.5 M H_2SO_4 as compared to 0.5 M HCl. Also to produce higher current densities, Ru@C/$Pt_{0.5}$ requires a very high overpotential in 0.5 M HCl than in 0.5 M H_2SO_4. This can be attributed to the fact that 0.5 M H_2SO_4 furnishes more H^+ ions as compared to 0.5 M HCl, which leads to an ultimate enhancement in the activity of the material towards HER. HCl also leads to

the production of Cl_2 gas at higher potentials, which can sometimes interfere with the HER. Hence, 0.5 M H_2SO_4 is a better electrolyte than 0.5 M HCl for HER.

Compared to the PBA-derived Ru@C nanoparticles, the Pt composite materials showed better catalytic behavior. Among different Pt-loaded composites, a significant improvement has been observed in the case of Ru@C/$Pt_{0.5}$. At lower loading (Ru@C/$Pt_{0.1}$), possibly the Pt nanoparticles get wrapped completely by the carbon matrix, decreasing the exposed active sites, which were also confirmed from the electrochemically activated surface area calculated from the charge involved in the hydrogen adsorption **(Figures 4.5c** and **4.7)**.

However, on increasing the Pt concentration (Ru@C/$Pt_{0.5}$), the ECSA increases, availing a greater number of catalytic active sites. But on further increase, as in the case of (Ru@C/$Pt_{1.0}$), the ECSA value decreases, which may be due to the agglomeration of Pt nanoparticles as the Pt loading concentration increased, which finally led to a drop in the number of active sites, resulting in a lower ECSA value.[72] In the case of acidic electrolytes such as 0.5 M H_2SO_4, the adsorption of hydrogen on the surface of platinum is attained by the application of sufficiently negative potentials to the electrode when the electrode is in contact with the electrolyte.

The reduction of H^+ ions and H atom adsorption becomes stronger with the application of more negative potentials:

$$H^+(aq) + e^- \rightarrow H(ad). \qquad (4.7)$$

This process continues as electrode potentials become increasingly negative until the formation of an H(ad) monolayer is attained. Once the Pt surface is fully covered by hydrogen atoms, the process of H_2 molecule adsorption will take place:

$$2H(ad) \rightarrow H_2(ad). \qquad (4.8)$$

These adsorbed molecules combine to generate hydrogen bubbles, which will exit the Pt electrode surface after they have grown large enough:

$$n\mathrm{H_2(ad)} \rightarrow n\mathrm{H_2(g)}. \quad (4.9)$$

At this moment, a high cathodic potential is applied to the electrode, exposing numerous free sites to the electrolyte solution. **Equations 4.7 - 4.9** occur successively at a faster rate, leading to a sharp increase in the cathodic current, known as hydrogen evolution. The formation of the H(ad) monolayer is readily detectable at the potential where the cathodic current rapidly increases. Opposite processes (*i.e.*, the anodic currents in the hydrogen region) occur when the potential is reversed.[73]

This promotional catalytic activity of Ru@C/$Pt_{0.5}$ was again verified from the kinetics of electrode reaction and associated interfacial processes. It can be determined from the rate-determining step of the reaction from the Tafel slope. The process of hydrogen evolution reaction (HER) takes place as follows in the acidic electrolyte:[74,75]

(i) A primary proton discharging and hydrogen adsorption step:

$$\mathrm{M + H^+ + e^- \rightarrow M–H\ (Volmer\ step)} \quad (4.10)$$

(ii) A recombination step:

$$\mathrm{M–H + M–H \rightarrow H_2\ (Tafel\ step)} \quad (4.11)$$

(iii) An electrochemical desorption step:

$$\mathrm{H^+ + e^- + M–H \rightarrow H_2\ (Heyrovsky\ step)} \quad (4.12)$$

The overall reaction mechanism of HER involves a combination of the Volmer step with either the Tafel or Heyrovsky step **(Equation 4.10-4.12).** The reaction mechanism of

HER on the catalyst surface has been elucidated from the Tafel slope determined from the following Tafel **Equation 4.13**,

$$\eta = a + b \log J. \quad (4.13)$$

Here, η, a, b, and J are the overpotential, Tafel constant, slope, and current density, respectively. Here, the Tafel slopes were obtained by linear fitting the Tafel plot and are presented in **Figure 4.5b**. In the present study, the rate-determining step is the Tafel step since the obtained Tafel slope for Ru@C/$Pt_{0.5}$ is 26 mV dec^{-1}, which is very low compared to that of other electrocatalysts studied here **(Table 4.1).** Here, the HER is taking place through the Volmer–Heyrovsky mechanism. This process begins with the electrodeposition of a proton **(4.10)**, followed by the electrochemical desorption step on the catalyst surface to generate H_2 directly **(4.12)**.[48] Furthermore,

Table 4.1 The comparison of the ECSA, Tafel slope, overpotential at 10 mA cm^{-2} current density, and turnover frequency (TOF) of the electrocatalysts studied here.

Electrocatalyst	ECSA of loaded platinum (cm^2)	Tafel slope (mV dec^{-1})	Overpotential ($\eta_{10\ mA\ cm^{-2}}$)	TOF (s^{-1}) ($\eta_{10\ mA\ cm^{-2}}$)
Ru@C	—	144	153 mV	2.25
Ru@C/$Pt_{0.1}$	97	48	57 mV	5.29
Ru@C/$Pt_{0.5}$	205	26	32 mV	5.60
Ru@C/$Pt_{1.0}$	8.38	45	45 mV	5.25
Pt/C (10% Pt)	—	44	30 mV	4.1
Ru/C	—	112	121 mV	2.11

Ru@C/$Pt_{0.5}$ exhibits an exchange current density value that is greater than that of the commercial Pt/C and even higher than that of the other catalysts examined here. By calculating the hydrogen turnover frequency (TOF), which measures the release of the number of molecular hydrogens per unit active site of the catalyst per second, the intrinsic electrocatalytic activity of the catalysts has been assessed. As depicted in **Figure 4.5d**, Ru@C/$Pt_{0.5}$ exhibits a TOF value of 5.6 H_2 per s at 10 mA cm^{-2} current density, which is higher than that of the bare Ru@C (2.25 H_2 per s), commercial Pt/C (4.1 H_2 per s), and Ru/C (2.11 H_2 per s). Here, a very trace quantity of platinum has been taken, and the significant improvement in the optimum composite has been ascribed to the synergistic activity of both metals in the composite structure. The content of metals in all the catalysts was determined through ICP-OES analysis **(Table 4.2)**. The Tafel slope is obtained by linear fitting the region between the onset potential and the overpotential of the LSV curve and was found to be 44 and 26 mV dec^{-1} for Pt/C and Ru@C$Pt_{0.5}$, respectively. The Tafel slope defines the kinetics of the reaction, and the Tafel slope value is found to be nearly the same for both materials. The Nernst equation specifies that mass transport losses happen at increasing current densities, suggesting that the overpotential due to the mass transport constraint enhances along with the concentration of the product species at the reaction interface. Mass transport

Table 4.2 ICP-OES analysis shows the content of Ru and Pt in Ru@C, Ru@C/$Pt_{1.0}$, Ru@C/$Pt_{0.5}$, and Ru@C/$Pt_{0.1}$.

	Ru	Pt
Ru@C	29.11%	0%
Ru@C/$Pt_{1.0}$	42.16%	7.255%
Ru@C/$Pt_{0.5}$	49.975%	2.6%
Ru@C/$Pt_{0.1}$	37.97%	0.16%

losses happen when the current density is high enough to keep the reactants from reaching active sites due to a high number of reacting molecules, which lowers the reaction rate.[76] Therefore, mass transport losses may lead to an increase in the overpotential value to produce a higher current density (100 mA cm^{-2}) by Pt/C (178 mV) since it has a high concentration of Pt as compared to Ru@C$Pt_{0.5}$ (140 mV), with a trace amount of Pt. As can be seen in **Figure 4.5e**, Ru@C/$Pt_{0.5}$ exhibits reduced charge transfer resistance in comparison to other electrocatalysts studied here, again supporting the electrocatalytic performance. Long-term durability is another important parameter of an electrocatalyst for evaluating its commercial approach. Therefore, the Ru@C/$Pt_{0.5}$ casted electrode was subjected to continuous electrolysis in an acidic electrolyte 0.5 M H_2SO_4. The chronopotentiometry study was carried out at a constant current density of 10 mA cm^{-2} and found a slight increase of only ~22 mV after 50 hours of electrolysis **(Figure 4.5f)**. This observation was also supported by the slight increase in the overpotential reflected from the comparison of initial and post-50-hours electrolysis linear sweep voltammogram **(Figure 4.8a)**.

Table 4.3 Gas chromatography measurement of generated H_2 during HER by using Ru@C/$Pt_{0.5}$ catalyst.

Time (min)	H_2 concentration (ppm)
0	0
5	1017.5
30	2431.5
Another 30 minutes	2576

In order to verify the structural deformation and phase transformation, we have conducted the microscopic and diffraction studies of Ru@C/$Pt_{0.5}$ after 50 hours **(Figure 4.8b,c)**. Interestingly, we did not find such a significant change in surface morphology, and even the crystal structure remained intact after the long-term stability test. It clearly demonstrates the robustness in durability to catalyze the HER process. The concentration of hydrogen gas generated by the catalyst Ru@C/$Pt_{0.5}$ at a current value of 10 mA cm^{-2} was analyzed by gas chromatography and was found to be nearly 2500 ppm after 30 minutes of electrolysis **(Table 4.3)**. In order to mechanistically understand the origin of enhancement of HER activity evidently only in the presence of a trace amount of Pt on the Ru(002) surface, we have explored the scope and energetics of hydrogen

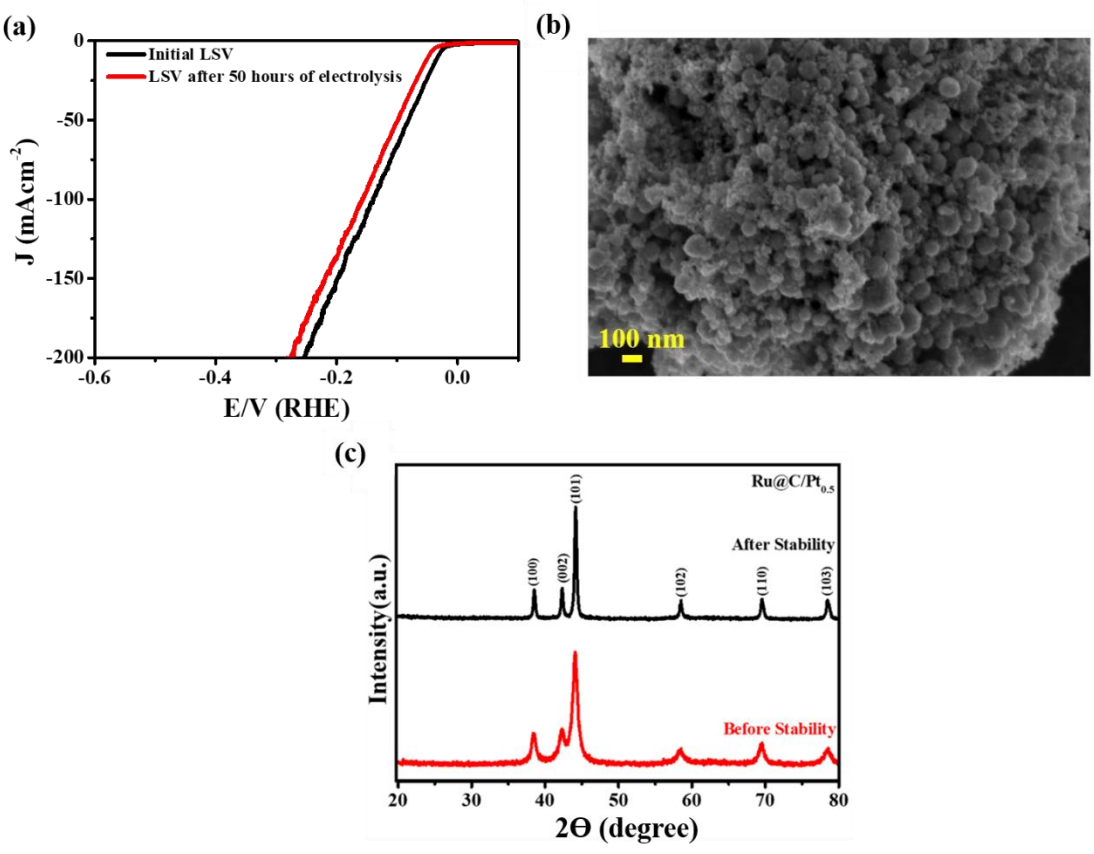

Figure 4.8: Linear sweep voltammogram of initial and after 50 hours of electrolysis (a), the sweep rate was 5 mV/s. FESEM (b) and PXRD pattern (c) of the Ru@C/$Pt_{0.5}$ after the stability test for 50 hours.

adsorption from first principles using density functional theory (DFT). We compare the ease of adsorption of atomic hydrogen at the preferred interstitial sites (fcc) on the Ru(002) surface in the vicinity of Pt atoms adsorbed on Ru interstitials, forming islands of increasing size. Specifically, Ru(002), Ru(002) Pt, Ru(002) Pt_3, Ru(002) Pt_6, and Ru(002) Pt_9 have been investigated in a slab geometry, as shown in **Figure 4.9(a–e)**, respectively. In **Figure 4.9**, we present a color map depicting the strength of adsorption of atomic H at different non-equivalent fcc sites. In $RuPt_1$ and $RuPt_3$, the strength of adsorption is comparable for "b, c, d, e" sites. For $RuPt_6$, at the "b" sites, marked in green, the strength of adsorption is the lowest among fcc sites, and thereby, should be catalytically the most active. On the contrary, the "a" sites, marked yellow, cannot adsorb atomic H since those H atoms migrate to passivate the under-coordinated Pt atom at the periphery of the Pt islands in the vicinity. In fact, these peripheral Pt atoms can chemisorb a second H atom as well, thus inhibiting desorption of the first H atom spontaneously upon exposure to the second H atom, leading to sustained blockade of the "a" sites. In

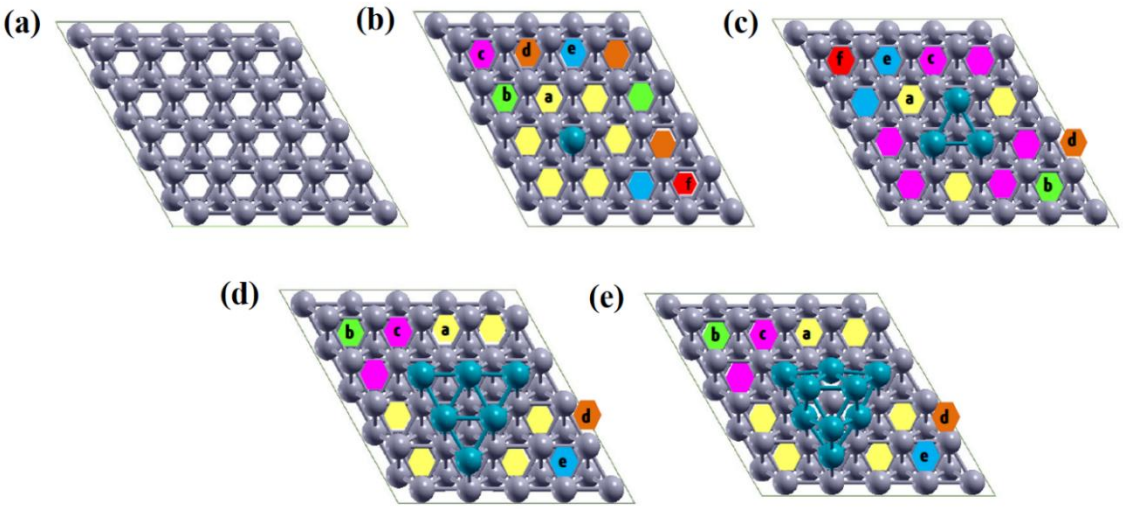

Figure 4.9: Top view of the optimized structure of Ru(002) (a), Ru(002) Pt (b), Ru(002) Pt_3 (c), Ru(002) Pt_6 (d), and Ru(002) Pt_9 (e). Color code, Pt: cyan, Ru: grey. Different colored hexagons represent the non-equivalent fcc sites for each system.

fact, desorption of hydrogen from such Pt atoms occurs only upon exposure of a third hydrogen atom, leading to a lowering of yield (as shown in **Figure 4.10**). As tabulated in **Table 4.4**, till $RuPt_3$, hydrogen adsorption energy (E_{ads}) reduces by 0.05 eV compared to that on the pure Ru(002) surface. However, upon the increase in size of the Pt island to $RuPt_6$, E_{ads} significantly reduces further by 0.06 eV, totaling a net reduction of 0.11 eV compared to pristine Ru(002). To understand the reason behind such lowering of strength of adsorption, we plot the difference charge density (CDD) for (a) Ru, (b) $RuPt_6$, and (c) $RuPt_6H$ in **Figure 4.11**. CDD being the difference between the ground state charge density of a given system and the sum of charge densities of individual constituent atoms, the red (blue) iso-surfaces imply accumulation (depletion) of charge upon the formation of bonds.

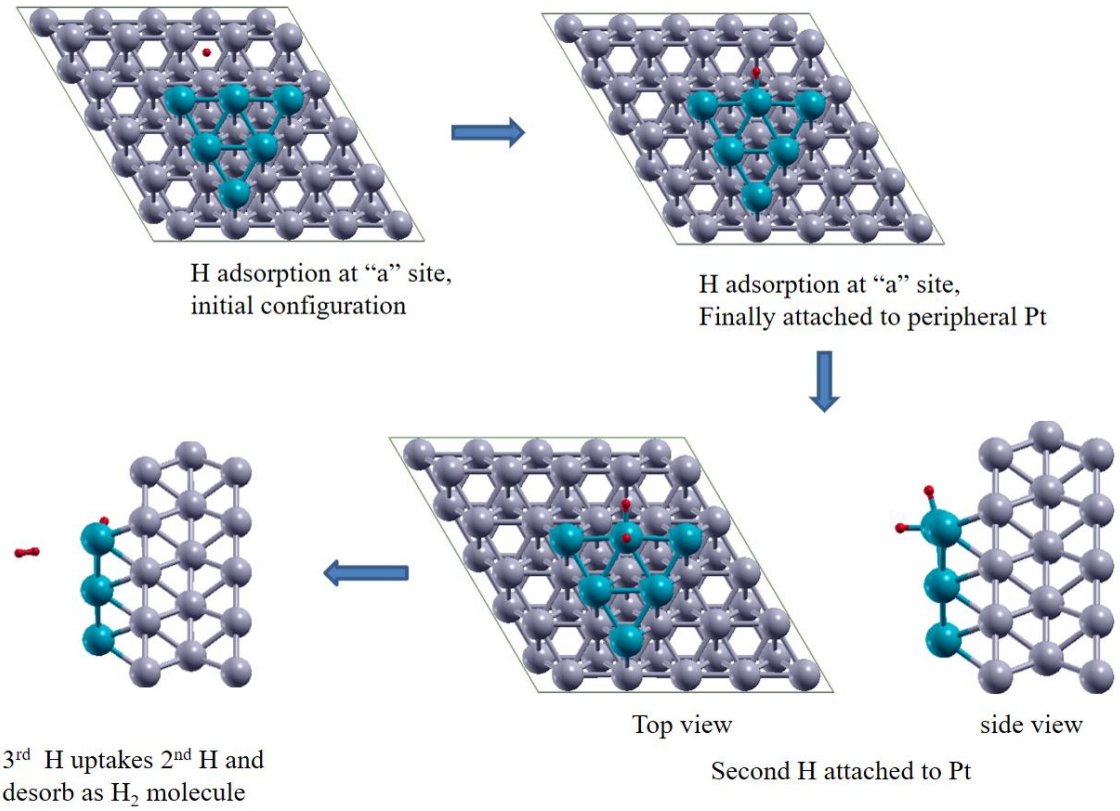

Figure 4.10: Stepwise H atom adsorption and desorption process from site 'a' of $RuPt_6$ surface. (Grey, cyan and red colour represents Ru, Pt and H respectively.)

Upon the chemisorption of Pt on the Ru fcc site, there is a charge transfer from Pt to the Ru–Pt bond shown by the red iso-surface in **Figure 4.11**, accompanied by charge retention on the Ru atoms marked by the absence of an iso-surface on them. The projected density of states **(Figure 4.11d)** for $RuPt_6$ indicates that the occupied electron density at the d orbitals is higher for the Ru atom adjacent to the corner of a Pt island compared to the Ru atoms not in the immediate vicinity of any Pt island. The charge transferred to the hydrogen atom, marked by the red iso-surface on it, is consistent with the observed accumulation of Bader charge of about 0.26*e*, which appears **(Figure 4.11c)** to have been transferred from the Ru–Ru bonds marked by the absence of a red iso-

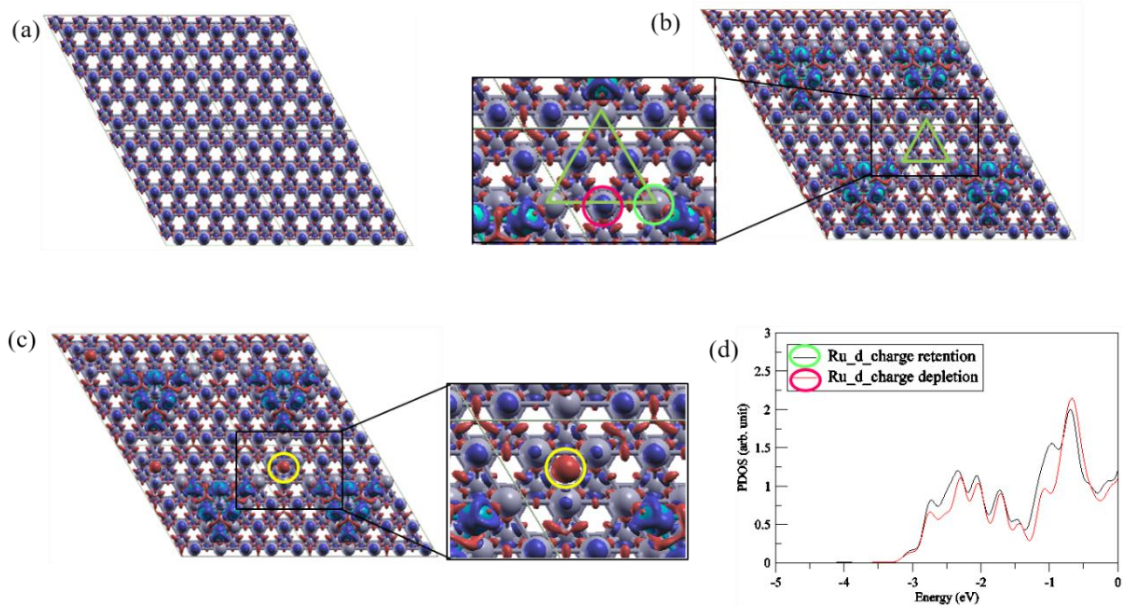

Figure 4.11: The charge density difference in the case of - the pristine Ru(002) surface (a), presence of Pt_6 islands (b), and H adsorbed on the b site in the vicinity of Pt_6 islands (c). The red (blue) iso-surfaces represent electron accumulation (depletion). Projected density of occupied states (d). The "b" site is marked in (b) by a green triangle pointing to charge retention on Ru in $RuPt_6$ (enlarged image) (d). Yellow circle marked in (c) represents the charge accumulation on H atoms. Density of states shown in (d) are projected on the orbitals marked by green and magenta circles in (b).

surface on the bonds. However, the amount of charge on adsorbed H atoms remains unaltered upon the presence of Pt atom in a neighboring fcc site, implying no appreciable change in the nature of chemical bonding upon the adsorption of Pt in the vicinity.However, the energetics of adsorption can still change due to electrostatic interactions. In fact, the retention of charge on Ru atoms in the vicinity of Pt atoms should cause electrostatic repulsion to hydrogen adsorption. With the proximity of three such Ru atoms in the neighborhood of the "b" site in $RuPt_6$, electrostatic repulsion indeed appears to consolidate, leading to a reduction in the strength of adsorption of H by about 10% to 20%, compared to pristine Ru surface, as evident in **Table 4.4**.

Table 4.4 Calculated hydrogen adsorption energy (E_{ads}), and the associated Gibbs free energy change (ΔG) for adsorption of atomic H at the fcc "b" site of Ru to $RuPt_9$ systems.

System	E_{ads} (eV)	ΔG_1 (eV)
Ru	−0.60	−0.24
RuPt	−0.55	−0.22
$RuPt_3$	−0.54	−0.16
$RuPt_6$	−0.49	−0.09
$RuPt_9$	−0.50	−0.13

For a more comprehensive picture of stabilization, we further calculate the change in Gibb's free energy ΔG due to the adsorption of H at the fcc sites. Herein, we have studied two generally accepted HER mechanisms, Volmer–Heyrovsky and Volmer–Tafel, for these catalysts. In the Heyrovsky mechanism, the H^+ from acidic media reacts with adsorbed hydrogen (H*), producing hydrogen gas (H_2), which desorbs from the surface of the catalyst. For the Tafel reaction, two adsorbed H (H*) combine together to desorb as an H_2 molecule, as shown in **Figure 4.12**.

Since the Gibbs free energy (G) of the final step is equal or higher than that of the initial step before the adsorption of atomic hydrogen, lowering of G upon adsorption of implies a subsequent rate limiting (up-hill in G) step, and thereby, requirement of an over-potential to drive the reaction forward to completion. Thus, the higher the lowering of G, the higher the requirement of over-potential and the lower the efficacy of the catalyst. In the case of HER on Ru and $RuPt_n$, ΔG_{Volmer} in all cases is negative, implying that the first step is spontaneous.

However, the strength of the adsorption of hydrogen proportionally determines the value of η required to drive the desorption through. As evident in **Table 4.4** and **Figure 4.12**, ΔG follows the order $RuPt_6 > RuPt_9 > RuPt_3 > RuPt > Ru$, which suggests that $RuPt_6$ is a more efficient catalyst than pristine Ru as well as $RuPt_9$. The reason for this trend, interestingly, is the zero -point energy. With increasing island size, the effect of increasing mass causes softening of phonon modes around the Pt islands, leading to a lowering of the zero-point energy (ZPE) ofthe system, which is a positive contribution to the free energy G. This leads to a lowering of free energy (ΔG), which stabilizes the adsorbed hydrogen non-nominally more in the vicinity of $RuPt_9$ compared to that near $RuPt_6$, while the difference in energetics of H adsorption in the two cases is marginal. As evident from **Figure 4.12**, for this HER pathways, the overpotential for the Heyrovsky mechanism is lower compared to Tafel, as the steric repulsion between the two adsorbed H at neighboring fcc sites at a distance more than 2.7 Å is weak enough to increase the strength of the average binding per H atom compared to the Heyrovsky mechanism, where the second H is not adsorbed at all. However, the aspect that can influence the yield of H_2 more robustly is the availability of active sites.

As evident in **Figure 4.9**, the availability of catalytically active sites increases from $RuPt_1$ to $RuPt_3$ but decreases again for $RuPt_6$. On the other hand, the efficacy of catalysis of the available sites increases at $RuPt_6$ in spite of the drop in the number of active sites. This is because, with the increasing size of Pt islands, the number of "a" type sites along

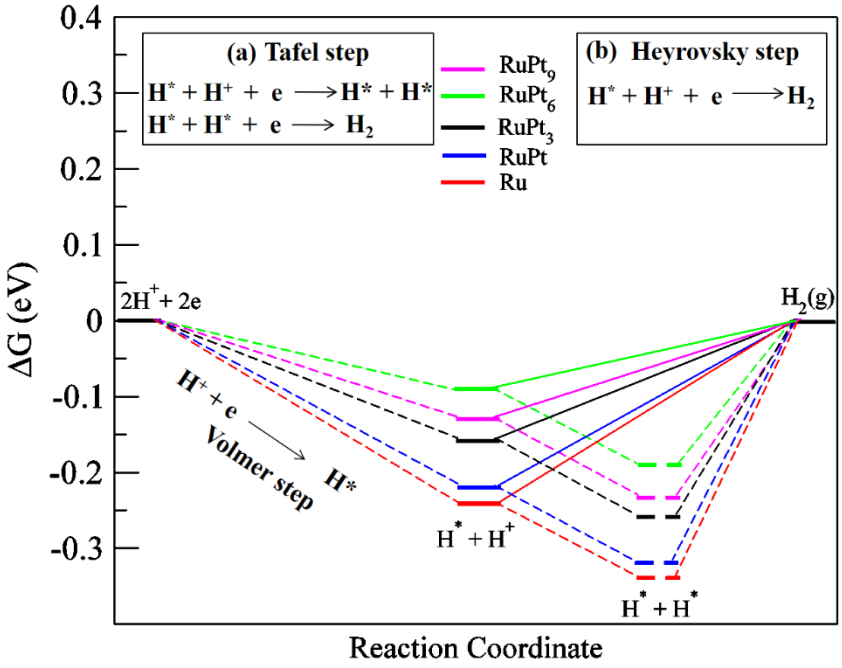

Figure 4.12: Gibbs free energy profile (ΔG) for Ru to $RuPt_9$ catalysts according to the Volmer step followed by the - Tafel route (dashed line) (a) and Heyrovsky route (solid line) (b).

the edge of Pt islands also increases. As already discussed, the under-coordinated peripheral Pt atoms at the edges of the Pt islands consistently block the "a" site.

Thus, larger Pt islands with steps at the edges are expected to lower the yield of H_2 as observed in the experiment. To summarize, it is, therefore, a competitive scenario with increasing Pt island size while some of the Ru fcc sites become more favorable for

catalysis, Ru fcc sites in the vicinity of the islands are rendered unavailable for adsorption of atomic hydrogen by the peripheral Pt atoms. Such a competition supports

Table 4.5 The comparison of overpotential and Tafel slope of the reported materials with the Ru@C/$Pt_{0.5}$.

	Loading density (μgcm^{-2})	Electrolyte	Overpotential at 10 $mAcm^{-2}$ (mV)	Tafel Slope ($mVdec^{-1}$)	Reference
RuP_2@NPC	1000	0.5 M H_2SO_4	38	38	77
PtRu@RFCS	354	0.5 M H_2SO_4	19.7	27.2	78
v-$Pt_{29}Pd_3Ru_{62}Te_6$ AS	285	0.5 M H_2SO_4	39	32	36
Ni@Ni_2P–Ru HNRs	283	0.5 M H_2SO_4	31	35	79
NiRu@N–C	273	0.5 M H_2SO_4	50	36	80
Ru–MoO_2	285	0.5 M H_2SO_4	55	44	81
Ru@Co–SAs/N–C	285	0.5 M H_2SO_4	57	55	82
v-$Pt_{29}Pd_3Ru_{62}Te_6$ AS	285	1 M KOH	22	22	83
Ni@Ni_2P–Ru HNRs	283	1 M KOH	31	41	80
Ru_1CoP/CDs	420	1 M KOH	51	73.4	84
$NiRu_2$@NC-600		0.5 M H_2SO_4	85	45.54	85
$Pt_{0.3}Ru_{0.7}$NP/OMC	0.44 Pt 0.39 Ru	0.5 M H_2SO_4	42.3	37	86
Ru@C/$Pt_{0.5}$	**263**	**0.5 M H_2SO_4**	**32**	**26**	**This work**

the experimental observation that after a stint of decrease in requirement of over-potential with increasing Pt concentrations still within trace amounts, the over-potential requirement picks up again after a certain threshold concentration of Pt, which, within the scope of our computation, would qualitatively correspond to the Pt_6 island, beyond which, not only the over-potential requirement increases again, but also the availability of favorable sites for catalysis drops as well.

4.8 Conclusions

In this work, we have successfully optimized a synthesis method to prepare Ru-PBA and Ru-PBA-derived Ru@C nanoparticles. Also, their composites with platinum at variable concentrations have been prepared, and electrocatalytic performance was evaluated for hydrogen evolution reaction in 0.5 M H_2SO_4. The PXRD, HRTEM, and XPS characterisations clearly signify the formation of metallic Pt nanoparticles that are decorated throughout metallic Ru derived from Ru-PBA. Therefore, the electrocatalytic performance of the composite is primarily due to the formation of the Ru/Pt nanocomposite. Trace amounts of Pt have been used to make this composite, which predominantly improves the electrocatalytic activity of Ru@C nanoparticles over the use of Pt. Among all the electrocatalysts studied in this work, Ru@C/$Pt_{0.5}$ catalyzes the HER efficiently, requiring only 32 and 140 mV overpotential to deliver 10 and 100 mA cm^{-2} current density, respectively, which is lower than the overpotential required by many of the reported materials **(Table 4.5)**. Additionally, Ru@C/$Pt_{0.5}$ showed robust durability during 50 hours of continuous electrolysis, giving a turnover frequency of 5.6 $s^{-1}@\eta_{10\ mA\ cm^{-2}}$ and Tafel slope of 26 mV dec^{-1}. Computational studies from first principles reveal that charge retention on Ru near the corners of the Pt islands causes electrostatic repulsion, which decreases the binding strength of H at the Ru interstitial fcc sites in the vicinity. However, in agreement with experimental results, with the

increasing size of Pt islands, the adsorption of H atoms at the fcc sites starts stabilizing again owing to the softening of phonon modes around the Pt islands, leading to an increase in overpotential. Also, the Ru fcc sites along the edge of the Pt islands are blocked by the under-coordinated peripheral Pt atoms, which in turn over-binds H atoms strongly enough to prevent their easy desorption, thus effectively lowering the number of active Ru fcc sites. The requirement of only a trace amount of Pt is therefore not only sufficient but a necessary condition for optimal catalysis. Hopefully, the efficient catalysis by Ru@C/$Pt_{0.5}$ reported in this work will pave the way for such composites to effectively substitute Pt/C as the primary catalyst, towards rendering commercial water splitting economically viable for mass application.

4.9 References

1. Y. Yang, Z. Lun, G. Xia, F. Zheng, M. He and Q. Chen, *Energy Environ. Sci.*, 2015, **8**, 3563 —3571.
2. C. G. Morales-Guio, L. A. Stern and X. Hu, *Chem. Soc. Rev.*, 2014, **43**, 6555 —6569.
3. Y. Jiao, Y. Zheng, M. Jaroniec and S. Z. Qiao, *Chem. Soc. Rev.*, 2015, **44**, 2060 — 2086.
4. J. A. Turner *Science*, 2004, **305**, 972 —974.
5. C. C. L. McCrory, S. Jung, I. M. Ferrer, S. M. Chatman, J. C. Peters and T. F. Jaramillo, *J. Am. Chem. Soc.*, 2015, **137**, 4347 —4357.
6. M. Zeng and Y. Li, *J. Mater. Chem. A*, 2015, **3**, 14942 —14962.
7. R. K. Tripathy, A. K. Samantara, P. Mane, B. Chakraborty and J. N. Behera, *New J. Chem.*, 2022, **46**, 2730 —2738.

8. J. K. Das, A. K. Samantara, S. Satyarthy, C. S. Rout and J. N. Behera, *RSC Adv.*, 2020, **10**, 4650 —4656.

9. T. Liu, X. Ma, D. Liu, S. Hao, G. Du, Y. Ma, A. M. Asiri, X. Sun and L. Chen, *ACS Catal.*, 2017, **7**, 98 —102.

10. P. Jian, Q. Liu and X. Sun, *Nanoscale*, 2014, 13440 —13445.

11. J. Theerthagiri, G. Durai, K. Karuppasam, P. Arunachalam, V. Elakkiya, P. Kuppusami, T. Maiyalagan and H. S. Kim, *J. Ind. Eng. Chem.*, 2018, **67**, 12 —27.

12. X. Zhang, X. Yu, L. Zhang, F. Zhou, Y. Liang and R. Wang, *Adv. Funct. Mater.*, 2018, **28**, 1706523.

13. C. Du, L. Yang, F. Yang, G. Cheng and W. Luo, *ACS Catal.*, 2017, **7**, 4131 —4137.

14. Y. Y. Zhang, X. Zhang, Z. Y. Wu, B. B. Zhang, Y. Zhang, W. J. Jiang, Y. G. Yang, Q. H. Kong and J. S. Hu, *J. Mater. Chem. A*, 2019, **7**, 5195 —5200.

15. W. Jiang, W. Luo, J. Wang, M. Zhang and Y. Zhu, *J. Photochem. Photobiol., C*, 2016, **28**, 87 —115.

16. D. Wang, K. Lv and Z. Wu, *Mater. Res. Express*, 2018, **5**, 065509.

17. Y. Guo, C. Shang and E. Wang, *J. Mater. Chem. A*, 2017, **5**, 2504 —2507.

18. J. Du, Z. Zou, C. Liu and C. Xu, *Nanoscale*, 2018, **10**, 5163 —5170.

19. F. Ming, H. Liang, Y. Lei, W. Zhang and H. N. Alshareef, *Nano Energy*, 2018, **53**, 11 —16.

20. S. Wei, R. Zhou and G. Wang, *ACS Omega*, 2019, **4**, 15780 —15788.

21. N. Sahu, J. K. Das and J. N. Behera, *Inorg. Chem.*, 2022, **61**, 2835 —2845.

22. Z. Chen, J. Lu, Y. Ai, Y. Ji, T. Adschiri and L. Wan, *ACS Appl. Mater. Interfaces*, 2016, **8** , 35132 —35137.

23. X. Kong, K. Xu, C. Zhang, J. Dai, S. N. Oliaee, L. Li, X. Zeng, C. Wu and Z. Peng, *ACS Catal.*, 2016, **6**, 1487 —1492.

24. K. Xu, P. Chen, X. Li, Y. Tong, H. Ding, X. Wu, W. Chu, Z. Peng, C. Wu and Y. Xie, *J. Am. Chem. Soc.*, 2015, **137**, 4119 —4125.

25. W. Ahn, M. G. Park, D. U. Lee, M. H. Seo, G. Jiang, Z. P. Cano, F. M. Hassan and Z. Chen, *Adv. Funct. Mater.*, 2018, **28**, 1802129.

26. B. Zhao, L. Zhang, D. Zhen, S. Yoo, Y. Ding, D. Chen, Y. Chen, Q. Zhang, B. Doyle, X. Xiong and M. Liu, *Nat. Commun.*, 2017, **8**, 14586.

27. L. Wang, C. Peng, H. Lin and B. Zhao, *Energy Fuels*, 2022, **36**, 11660 —11690.

28. Y. Ouyang, C. Ling, Q. Chen, Z. Wang, L. Shi and J. Wang, *Chem. Mater.*, 2016, **28**, 4390 —4396.

29. P. Q. Liao, J. Q. Shen and J. P. Zhang, *Coord. Chem. Rev.*, 2018, **373**, 22 —48.

30. S. N. Zhao, X. Z. Song, S. Y. Song and H. j. Zhang, *Coord. Chem. Rev.*, 2017, **337**, 80 —96.

31. J. S. Qin, D. Y. Du, W. Guan, X. J. Bo, Y. F. Li, L. P. Guo, Z. M. Su, Y. Y. Wang, Y. Q. Lan and H. C. Zhou, *J. Am. Chem. Soc.*, 2015, **137**, 7169 —7177.

32. X. F. Lu, P. Q. Liao, J. W. Wang, J. X. W, X. W. Chen, C. T. He, J. P. Zhang, G. R. Li and X. M. Chen, *J. Am. Chem. Soc.*, 2016, **138**, 8336 —8339.

33. L. Catala and T. Mallah, *Coord. Chem. Rev.*, 2017, **346** , 32 —61.

34. X. Y. Yu, Y. Feng, Y. Jeon, B. Guan, X. W. D. Lou and U. Paik, *Adv. Mater.*, 2016, **28**, 9006 —9011.

35. L. M. Cao, D. Lu, D. C. Zhong and T. B. Lu, *Coord. Chem. Rev.*, 2020, **407**, 213156.

36. K. Li, Y. Li, Y. Wang, J. Ge, C. Liu and W. Xing, *Energy Environ. Sci.*, 2018, **11**, 1232 —1239.

37. A. S. B. M. Najib, M. Iqbal, M. B. Zakaria, S. Shoji, Y. Cho, X. Peng, S. Ueda, A. Hashimoto, T. Fujita, M. Miyauchi, Y. Yamauchi and H. Abe, *J. Mater. Chem. A*, 2020, **8**, 19788 —19792.

38. E. Demir, S. Akbayrak, A. M. Önal and S. Özkar, *ACS Appl. Mater. Interfaces*, 2018, **10**, 6299 —6308.

39. J. Wang, Z. Wei, S. Mao, H. Li and Y. Wang, *Energy Environ. Sci.*, 2018, **11**, 800 — 806.

40. J. Su, Y. Yang, G. Xia, J. Chen, P. Jiang and Q. Chen, *Nat. Commun.*, 2017, **8**, 1 — 10.

41. X. Liu, F. Liu, J. Yu, G. Xiong, L. Zhao, Y. Sang, S. Zuo, J. Zhang, H. Liu and W. Zhou, *Adv. Sci.*, 2020, **7**, 2001526.

42. W. Dong, Y. Zhang, J. Xu, J. W. Yin, S. Nong, C. Dong, Z. Liu, B. Dong, L. M. Liu, R. Si, M. Chen, J. Luo and F. Huang, *Cell Rep. Phys. Sci.*, 2020, **1**, 100026.

43. H. Zhang, W. Zhou, X. F. Lu, T. Chen and X. W. Lou, *Adv. Energy Mater.*, 2020, **10**, 2000882.

44. Y. Sun, Z. Xue, Q. Liu, Y. Jia, Y. Li, K. Liu, Y. Lin, M. Liu, G. Li and C. Y. Su, *Nat. Commun.*, 2021, **12**, 1369.

45. H. Yu, L. Hui, Y. Xue, Y. Liu, Y. Fang, C. Xing, C. Zhang, D. Zhang, X. Chen, Y. Du, Z. Wang, Y. Gao, B. Huang and Y. Li, *Nano Energy*, 2020, **72**, 104667.

46. W. J. Mitchell, J. Xie, T. A. Jachimowski and W. H. Weinberg, *J. Am. Chem. Soc.*, 1995, **117**, 2606 —2617.

47. J. Mahmood, F. Li, S. M. Jung, M. S. Okyay, I. Ahmad, S. J. Kim, N. Park, H. Y. Jeong and J. B. Baek, *Nat. Nanotechnol.*, 2017, **12**, 441 —446.

48. W. Luo, Y. Wang and C. Cheng, *Mater. Today Phys.*, 2020, **15**, 100274.

49. P. Tan, Z. H. Wei, W. Shyy, T. S. Zhao and X. B. Zhu, *Energy. Environ. Sci.*, 2016, **9**, 1783 —1793.

50. Y. Zheng, Y. Jiao, Y. Zhu, L. H. Li, Y. Han, Y. Chen, M. Jaroniec and S. Z. Qiao, *J. Am. Chem. Soc.*, 2016, **138**, 16174 —16181.

51. B. Fang, N. He, Y. Li, T. Lu, P. He, X. Chen, Z. Zhao and L. Pan, *Electrochim. Acta*, 2023, **448**, 142187.

52. Z. Peng, X. Qiu, Y. Yu, D. Jiang, H. Wang, G. Cai, X. Zhang and Z. Dong, *Carbon*, 2019, **152**, 16 —23.

53. Z. Ding, H. Yu, X. Liu, N. He, X. Chen, H. Li, M. Wang, Y. Yamauchi, X. Xu, M. A. Amin, T. Lu and L. Pan, *J. Colloid Interface Sci.*, 2022, **616**, 210 —220.

54. Y. Ge, P. Dong, S. R. Craig, P. M. Ajayan, M. Ye and J. Shen, *Adv. Energy Mater.*, 2018, **8**, 1800484.

55. J. N. Behera, D. M. D'Alessandro, N. Soheilnia and J. R. Long, *Chem. Mater.*, 2009, **21**, 1922 —1926.

56. M. K. Sahoo, A. K. Samantara and J. N. Behera, *Inorg. Chem.*, 2020, **59**, 12252 — 12262.

57. W. Kohn and L. J. Sham, *Phys. Rev.*, 1965, **140**, A1133.

58. P. Giannozzi , S. Baroni , N. Bonini , M. Calandra , R. Car , C. Cavazzoni , D. Ceresoli , G. L. Chiarotti , M. Cococcioni , I. Dabo , A. Dal Corso , S. De Gironcoli , S. Fabris , G. Fratesi , R. Gebauer , U. Gerstmann , C. Gougoussis , A. Kokalj , M. Lazzeri , L. Martin-Samos , N. Marzari , F. Mauri , R. Mazzarello , S. Paolini , A. Pasquarello , L. Paulatto , C. Sbraccia , S. Scandolo , G. Sclauzero , A. P. Seitsonen , A. Smogunov , P. Umari and R. M. Wentzcovitch , *J. Phys.: Condens. Matter*, 2009, **21**, 395502.

59. D. Vanderbilt *Phys. Rev. B: Condens. Matter Mater. Phys.*, 1990, **41**, 7892.

60. J. P. Perdew, K. Burke and M. Ernzerhof, *Phys. Rev. Lett.*, 1996, **77**, 3865.

61. R. Fletcher *Practical Methods of Optimization*, John Wiley and Sons, 2000.

62. J. K. Nørskov, J. Rossmeisl, A. Logadottir, L. Lindqvist, J. R. Kitchin, T. Bligaard and H. Jónsson, *J. Phys. Chem. B*, 2004, **108**, 17886 —17892.

63. M. W. Chase Jr *NIST-JANAF Thermochemical Tables, Monograph 9*, American Chemical Society, Washington DC, 1998, vol. 9.

64. S. Feng and R. Xu, *Acc. Chem. Res.*, 2001, **34**, 239 —247.

65. C. Debbarma, S. Radhakrishnan, S. M. Jeong and C. S. Rout, *J. Mater. Chem. A*, 2024, **12**, 18674.

66. J. Ohyama, T. Sato, Y. Yamamoto, S. Arai and A. Satsuma, *J. Am. Chem. Soc.*, 2013, **135**, 8016 —8021.

67. R. Q. Huang, W. P. Liao, M. X. Yan, S. Liu, Y. M. Li and X. W. Kang, *J. Electrochem.*, 2023, **29**, 2203081.

68. M. Yin, J. Xu, Q. Li, J. O. Jensen, Y. Huang, L. N. Cleemann, N. J. Bjerrum and W. Xing, *Appl. Catal., B*, 2014, **144**, 112 —120.

69. Z. Z. Jiang, Z. B. Wang, Y. Y. Chu, D. M. Gu and G. P. Yin, *Energy Environ. Sci.*, 2011, **4**, 728 —735.

70. Y. Matsumoto and E. Sato, *Mater. Chem. Phys.*, 1986, **14**, 397 —426.

71. M. G. Walter, E. L. Warren, J. R. McKone, S. W. Boettcher, Q. Mi, E. A. Santori and N. S. Lewis, *Chem. Rev.*, 2010, **110**, 6446 —6473.

72. S. Taylor, E. Fabbri, P. Levecque, T. J. Schmidt and O. Conrad, *Electrocatalysis*, 2016, **7**, 287 —296.

73. J. M. D. Rodríguez, J. A. H. Melián and J. P. Peña, *J. Chem. Educ.*, 2000, **77**, 1195 —1197.

74. M. C. Tavares, S. A. S. Machado and L. H. Mazo, *Electrochim. Acta*, 2001, **46**, 4359 —4369.

75. R. Guo, X. Xu, Y. Xia, W. Huang, Z. Li and B. Teng, *J. Catal.*, 2018, **368**, 379 — 388.

76. A. Raveendran, M. Chandran and R. Dhanusuraman, *RSC Adv.*, 2023, **13**, 3843 — 3876.

77. F. Zhao, C. Li, Q. Yuan, F. Yang, B. Luo, Z. Xie, X. Yang, Z. Zhou and X. Wang, Nanoscale, 2019,11, 19448-19454

78. Z. Pu, I. S. Amiinu, Z. Kou, W. Li and S. Mu, Angew. Chem., 2017, 129, 11717–11722.

79. S. Liu, X. Mu, W. Li, M. Lv, B. Chen, C. Chen and S. Mu, Nano Energy, 2019, 61, 346–351.

80. Y. Liu, S. Liu, Y. Wang, Q. Zhang, L. Gu, S. Zhao, D. Xu, Y. Li, J. Bao and Z. Dai, J. Am. Chem. Soc., 2018, 140, 2731–2734.

81. Y. Xu, S. Yin, C. Li, K. Deng, H. Xue, X. Li, H. Wang and L. Wang, J. Mater. Chem. A, 2018, 6, 1376–1381.

82. P. Jiang, Y. Yang, R. Shi, G. Xia, J. Chen, J. Su and Q. Chen, J. Mater. Chem. A, 2017, 5, 5475–5485.

83. S. Yuan, Z. Pu, H. Zhou, J. Yu, I. S. Amiinu, J. Zhu, Q. Liang, J. Yang, D. He, Z. Hu, G. Van Tendeloo and S. Mu, Nano Energy, 2019, 59, 472–480.

84. H. Song, M. Wu, Z. Tang, J. S. Tse, B. Yang and S. Lu, Angew. Chem. Int. Ed., 2021, 60, 7234–7244.

85. S. Xu, Z. Li, K. Chu, G. Yao, Y. Xu, P. Niu and F. Zheng, Dalt. Trans., 2020, 49, 13647–13654.

86. R. Sachse, D. Bernsmeier, R. Schmack, I. Häusler, A. Hertwig, K. Kraffert, J. Nissen and R. Kraehnert, Catal. Sci. Technol., 2020, 10, 2057–2068.

CHAPTER-5

Ruthenium Cobalt Nanoalloy Derived from its Prussian Blue Analogue (RuCo-PBA) for Efficient Hydrogen Evolution Electrocatalysis

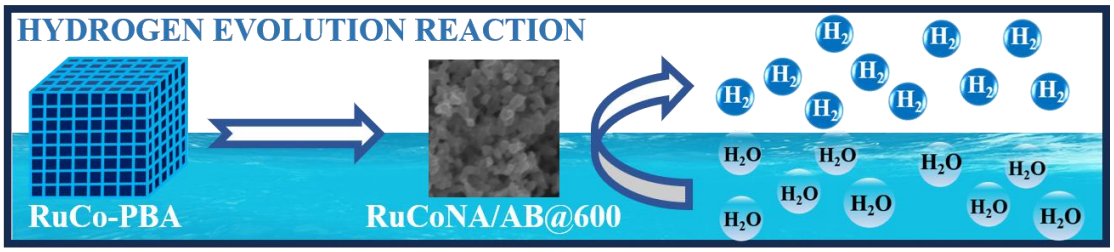

5.1 Abstract

Prussian blue analogue (PBA)-derived electrocatalysts have attracted significant interests for energy conversion applications. They have been extensively used for the production of renewable energy carriers like hydrogen in order to replace platinum based precious materials. We introduced a ruthenium cobalt PBA-derived bimetallic RuCo nano-alloy with the presence of the N-doped graphitised carbon (RuCoNA/AB@T, where T = 500–800 °C), following high temperature annealing in inert atmosphere. By varying the temperature (from 500 to 800 °C) during the annealing process, series of ruthenium cobalt nano-alloy products were obtained: RuCoNA/AB@500, RuCoNA/AB@600, RuCoNA/AB@700, and RuCoNA/AB@800 at 500, 600, 700, and 800 °C temperature, respectively. Temperature variation had a very important role in optimizing the activity of the electro-catalyst toward hydrogen evolution reaction (HER). Amongst different high-temperature annealed products, RuCoNA/AB@600 shows superior electrocatalytic performance due to its distinctive granule like morphology, lower overpotential value, smaller Tafel slope (122 mV/dec), smaller charge transfer resistance (18.69), and larger electrochemically active surface area (7.09 cm^2) that provides a large number of electrochemically active sites. RuCoNA/AB@600 exhibits a lower overpotential of 129 mV to deliver 10 mA cm^{-2} current density. Furthermore, 96 h of long-term stability of the electrocatalyst reflected its practical applicability.

5.2 Introduction

Fossil fuels continue to be the primary energy source for industrial productions globally.[1] The hazardous consequence of using fossil fuels is the drastic change in climate as well as the environmental pollution. The energy situation has become worse due to the rapidly depleting fossil fuel supplies; hence it is imperative to identify alternate green fuel sources. Since hydrogen (H_2) has a high calorific value and emits no toxic combustible products, it has been regarded as one of the most efficient clean energy sources.[2,3] Out of all the existing techniques for producing hydrogen, electrochemical water splitting is a popular and efficient approach that is powered by electricity. However, due to unsatisfactory catalytic performance for non-noble metal materials or the high cost of Pt and IrO_2, which are used for the hydrogen evolution reaction (HER) and oxygen evolution reaction (OER), respectively, it is crucial to produce cost-effective electrocatalysts with strong durability, faster reaction kinetics, and a lower overpotential (η) values.[4]

Various noble and non-noble metal-based electrocatalysts, including transition metal compounds,[5,6] alloys,[7] phosphides[8], oxides[9,10] and carbonaceous nanomaterials[11] have been extensively studied for electrochemical water splitting application. According to the volcano Figure, the H adsorption free energy for HER controls electrocatalytic activity. As a result, this hypothesis implies that no pure metal (with the exception of a few noble metals) has the potential to successfully electrocatalyse the HER.[11] As a result, the only way to utilise low-cost metals for HER electrocatalysis is to mix them with other metals that have weak and strong hydrogen bonding.[11] In this instance, two types of metal hydride bonds can be formed: one strong to promote the H adsorption process and one weak to facilitate H_2 formation. It is widely assumed that H adsorption begins on a metal with a strong M-H bond, and that the adsorbed H can travel via surface diffusion. The

weak M-H bond can be disrupted, allowing an H_2 molecule to exit the electrode surface.[12] Furthermore, as determined in the case of noble metals, the introduction of another metal of a different size modifies the lattice structure, potentially creating active areas for electrocatalysis. Alloying noble metals with other transition metals (TMs) results in extremely efficient catalysts with a favourable cost-competitiveness balance.[13] Therefore, the shift of charge distributions and the ensuing adjustment of surface characteristics during alloy formation might significantly increase the electrocatalytic activities of noble-transition bimetallic alloys in addition to reducing the cost of the materials.[14,15] Ru is being studied extensively towards the electrochemical water splitting application. This is so because, the price of ruthenium is more cost-effective than that of the other Pt-group metals, including Pt, Pd and Ir.[13,16] Also, the bond strength of the Pt and Ru are similar towards H.[16–18] However, the price is just 0.61 times that of Pt. This economic benefit makes it a viable option to Pt. Researchers are also very interested in Co because of its high abundance and affordability.[19] However, because of the strong hydrogen bonding energy of the single Ru and weak hydrogen bonding energy of the Co, both single Co and Ru display inferior catalytic activity when compared to the combining alloy catalyst.[20] The reaction kinetics of the catalyst can be significantly enhanced by alloying Ru with Co.[20–22] In particular, alloy-induced orbital overlap allows for the adjustment of the alloy catalyst's electronic structure.[23] Furthermore, it was anticipated that alloying Co and Ru would result in considerable lattice strain because of their different metallic radii (126 and 132 pm, respectively), which might improve the catalytic efficiency.[24] However, the high cohesive energy causes the alloy nanoparticles to undergo aggregation during the preparation period, and the long-term catalytic process results in substantial performance deterioration.[17] The development of synthetic methods to improve alloy catalyst’s endurance and catalytic activity is required to circumvent this

problem.[20] In light of this, scientists have developed various catalysts using alloys containing several carbon materials, some of which have been extensively researched: graphene,[7] carbon quantum dots,[21] N-doped carbon nanofibers,[25] hollow carbon spheres,[26] acetylene black [28] etc. As a carbon source, acetylene black is an excellent conductor with a carbon content of >99%.[27]

Metal-organic frameworks (MOFs) or porous coordination polymers have evolved into an extensive category of crystalline material with extremely large internal surface area, high structural as well as functional tunability and very high porosity.[28–31] MOF-derived transition metal oxides,[32] phosphides,[33] sulphides,[34] selenides,[35] carbonaceous compounds,[36] and alloy[37] materials are now being extensively used in energy conversion and storage applications. MOF-derived materials excel at electrochemical energy conversion due to their large electrochemical surface area, improved charge transport, tuneable electronic properties, and exposed facets.[29]

Prussian Blue Analogues (PBA) are a subcategory of MOFs which contains a cyanide bridge between two metal ion centres of same or different oxidation states. These two metal ions either can be same or different. PBA-derived materials inherit the tuneable porosity and high surface area of the PBA. PB (Prussian blue) and PBAs (Prussian blue analogues) attract special attention as material precursors because of their simple, reliable, and affordable synthesis. Additionally, PBAs can be made with hollow structures, core-shells, and multi-metal systems. Numerous materials with adjustable properties, including exposed facets, improved electron transport, increased electrochemical surface area, and accessible catalytic sites, can be created utilizing PB or PBA. It has been found that these materials exhibit outstanding electrochemical activity for oxygen evolution, hydrogen evolution, overall water splitting, and oxygen reduction reaction.[38] Additional benefits come from the PBAs' CN bridge, which can

easily burnt off or leached off to create the extremely porous materials. Furthermore, by altering the metallic content and heteroatom doping, the electronic structure of the PB and PBAs can be adjusted. Another method to regulate its electronic properties is post-synthetic alteration of the PBA.[38] These coordination polymers have outstanding thermal and hydrothermal stabilities in addition to significant mechanical resilience. These compounds show better chemical and catalytic stability than the parent frameworks. Additionally, high-temperature carbonization enhances the exposure of active regions and creates high porosity and routes for electrolyte accumulation. The comparatively low conductivity of MOF (PBA) precursors is overcome by MOF-derived (PBA-derived) materials because of their exceptional electrochemical performance, stability, and adaptable nanostructures.[39]

The PBA-derived electrocatalysts will possess some inherent characteristics of the original materials, such as evenly dispersed metal nanoparticles embedded on an amorphous carbon matrix doped with heteroatoms, graphitic, non-graphitized active carbon matrix along with the following advantages (over the direct-route synthesised alloys): firstly, the agglomeration of metals may be effectively controlled by the N-doped graphitized carbon present in the PBA-derived nanoalloys. Second, the N-doped graphitized carbon layers can prevent the corrosion of the metal core from the electrolyte. Third, the catalytic activity can be enhanced by the synergistic action of metals and N-doped graphitised carbon layers.[40] Various PBA-derived electrocatalysts has been studied till date towards the electrochemical water splitting.[41]

In this work we have synthesised a series of ruthenium-cobalt nanoalloys (containing N-doped graphitised carbon i.e. RuCoNA/AB@T) by following the pyrolysis method at a temperature (T) varying from 500-800 °C and studied their electrocatalytic behaviour towards hydrogen evolution reaction.

5.3 Experimental Section

5.3.1 Materials

Potassium hexacyanoruthenate (II) hydrate ($K_4[Ru(CN)_6].xH_2O$), trisodium citrate, acetylene black, and cobalt nitrate hexahydrate ($Co(NO_3)_2.6H_2O$) were purchased from Sigma Aldrich chemicals and used exactly as provided without any modifications. In order to prepare the catalyst ink pure ethanol was bought from Merck and Nafion solution from Alfa Aesar. The DI water was utilised for the entire experiment.

5.3.2 Synthesis of RuCo-PBA

RuCo-PBA has been synthesised by using one of the reported procedure from our previous work.[42] In particular, the co-precipitation approach was utilised to synthesize RuCo-PBA. Typically, 0.2 mmol $K_4[Ru(CN)_6].xH_2O$ (0.0862 g) was added to 10 mL of DI water and the mixture was agitated for 15 minutes leading to the formation of a homogeneous solution. Another solution was prepared by adding 10 mL DI water to 0.46 mmol trisodium citrate (0.134 g) and 0.3 mmol cobalt nitrate hexahydrate (0.0873 g), the obtained solution was then subjected to stirring for 15 minutes. In a dropwise manner, the first solution was added to the second prepared solution while the stirring was on. After complete addition of first solution to the second solution, the stirring was continued for another 30 minutes. After that the stirring was turned off and the precipitate was allowed to age in the mother liquor for 24 hours. The precipitate thus obtained was washed 3 times with DI and then 3 times with the ethanol. The material thus obtained was dried at 60 °C in an oven overnight. A blue coloured material thus obtained was named as RuCo-PBA.

5.3.3 Synthesis of Co-PBA

The aforementioned process of coprecipitation was used to synthesise the Co-PBA. In details 0.2 mmol of $K_3[Co(CN)_6].xH_2O$ was added to 10 mL of DI water and was subjected to stirring for 15 minutes until a homogeneous solution was obtained. Then another solution was made simultaneously by adding 0.2 mmol of $Co(NO)_3.6H_2O$ and 0.46 mmol trisodium citrate into 10 mL DI water and subjecting the mixture to stirring for 15 minutes. The first solution was then added dropwise to the second solution under continuous stirring. After the complete addition of first solution into the second solution, the mixture was further kept for stirring for another 30 minutes. After aging the mixture for 24 hours the obtained precipitate was repeatedly washed 3 times with DI water and then thrice with the ethanol. The obtained material was further dried at 60 °C in an oven overnight. A pink coloured powder material thus obtained was Co-PBA.

5.3.4 Synthesis of Ru-PBA

Ru-PBA was synthesised by using a reported procedure.[43] In details a solvothermal approach was utilised to synthesise the RuPBA. In a typical synthesis, 0.310 mmol $K_4[Ru(CN)_6].xH_2O$ (0.130 g) was added to 10 mL DI water and stirred for 15 minutes. To the above solution 0.620 mmol $Ru(acac)_3$ (0.250 g) was added and the solution was subjected to stirring for 60 minutes. The solution thus obtained was further transferred to a 23 mL autoclave and placed in a hot air oven at 175 °C for 4 days. The autoclave was then allowed to cool down to the room temperature. The obtained material was then washed 3 times each with DI water and ethanol. The material was further dried overnight in an oven at 60 °C. A dark green coloured powder material thus obtained was Ru-PBA.

5.3.5 Synthesis of RuCoNA/AB@T

RuCoNA/AB@T was synthesised by using pyrolysis method. In this method RuCo-PBA and acetylene black (AB) were mixed together with the help of mortar pastel in the ratio 2:1 (20:10 mg) respectively. After mixing for 30 minutes, the obtained material was subjected to annealing at temperature T (500-800 °C) for 3 hours in an inert Ar atmosphere. A black coloured powder material was obtained, named as RuCoNA/AB@T, where T represents the temperature.

5.3.6 Synthesis of RuCoNA@600, CoNP/AB@600, RuNP/AB@600 and AB@600.

For the comparison purpose RuCoNA@600 was synthesised by subjecting RuCo-PBA to annealing at a temperature 600 °C for 3 hours. CoNP/AB@600 and RuNP/AB@600 was synthesised by annealing a mixture of Co-PBA with AB and Ru-PBA with AB respectively in the ratio of 2:1 (20:10 mg) at a temperature of 600 °C for 3 hours in an Ar atmosphere. AB@600 was produced by annealing acetylene black (AB) at a temperature of 600 °C for 3 hours in a non-reactive environment of Ar.

All the obtained materials after the process of annealing were further stored carefully for the measurement and analysis purpose.

5.4 Characterisation

To determine the phase purity and crystallinity of the samples, powder X-ray diffraction measurements were carried out for all the samples using the Bruker D8 advance diffractometer system (XRD) with Cu Kα radiation operating at a wavelength of (λ = 1.5418Å). To determine the functional groups present Perkin Elmer FTIR spectrometer fitted with an attenuated total reflectance (ATR) accessory was used to record Fourier transformed infrared (FTIR) spectra. The surface morphology and elemental

distributions were characterised by transmission electron microscopy (TEM, equipped with HRTEM, JEOL 2100F, at 200kV) and field-emission scanning electron microscopy (FESEM, Zeiss Pvt. Ltd., Germany). A very dilute suspension of the sample in ethanol was prepared for the TEM analysis and cast onto the 200-mesh carbon-coated copper grid. Before being used for morphology analysis, the grid was thoroughly dried under a table lamp. Further, by using X-ray photoelectron spectroscopy (XPS, PHI Versa Probe III) the elemental composition and corresponding oxidation states of the elements present in the synthesized materials were determined. A Raman microscope (Horiba Scientific) with 532 nm laser excitation was utilised to illustrate the graphitic phase and disorderedness of the materials.

5.5 Electrochemical Measurement

All electrochemical experiments were conducted at room temperature in an acidic electrolyte 0.5 M H_2SO_4 using a Biologic SP-200 electrochemical workstation and a typical three-electrode electrochemical cell. The catalyst-casted glassy carbon rotating disc electrode (GCRDE), platinum rod, and Ag/AgCl (sat. KCl) electrodes served as working, counter, and reference electrodes, respectively. The GCRDE was first polished with 0.05 µm alumina slurry in order to obtain a mirror finished smooth surface. The catalyst ink was prepared by the dispersion of 1 mg of the electrocatalyst into a mixture of 95 µL ethanol and 5 µL Nafion. The obtained mixture was then subjected to ultrasonication for 30 minutes. 5 µL of the obtained slurry was then drop-casted onto the surface of the polished GCRDE and then dried prior to the use. Linear sweep voltammetry (LSV) at a scan rate of 5 mV/s was utilised to obtain the polarisation curves. By utilising the geometrical surface area of GCRDE (0.19 cm^2), current was normalised. All the potentials presented in this work have been converted to the RHE (reversible hydrogen electrode) by using the below Nernst equation:[35,44,45]

$E_{RHE} = E_{(Ag/AgCl)} + 0.0591\ (pH) + 0.21$ V.

The pH of the electrolyte was found to be 0.03.

Electrochemical Impedance Spectroscopy (EIS) was carried out at an AC amplitude of 5 mV in a frequency range of 0.1 Hz to 1 MHz. The electrochemically active surface area (ECSA) of the electrocatalysts was determined by employing cyclic voltammetry (CV) at different scan rates (5-150 mV/s) in the non-Faradaic region i.e. in the window range of 0.06-0.21 V vs RHE. Chronopotentiometry test was used to determine the stability of the electrocatalyst.

5.6 Results and Discussion

RuCoNA/AB@500, RuCoNA/AB@600, RuCoNA/AB@700 and RuCoNA/AB@800 were synthesised by using a two-step method as shown in the **Scheme 5.1**. In first step the RuCo-PBA was synthesised in a coprecipitation method. In the second step a mixture of RuCo-PBA and acetylene black (AB) was subjected to annealing at different temperatures ranging from 500 - 800 °C. The phase purity and crystallinity of the

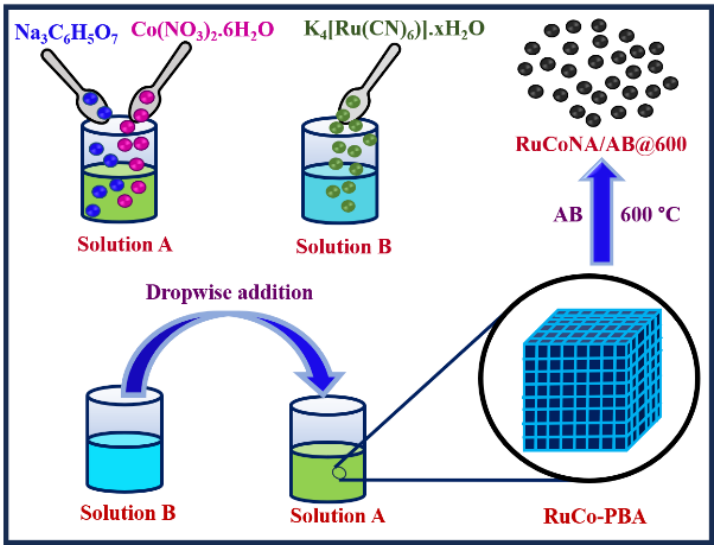

Scheme 5.1: Stepwise synthesis of RuCo-PBA and its derived RuCo-nanoalloy (RuCoNA/AB@600).

synthesised materials were determined through PXRD. **Figure 5.1a** shows the PXRD pattern of RuCo-PBA. The sharp peaks in the PXRD pattern indicate towards the high crystallinity of RuCo-PBA. Also, the absence of any extra peak confirms its high purity. The diffraction peaks at 16.99°, 24.04°, 28.21°, 34.09°, 38.19°, 42.07°, 48.92°, 52.13°,

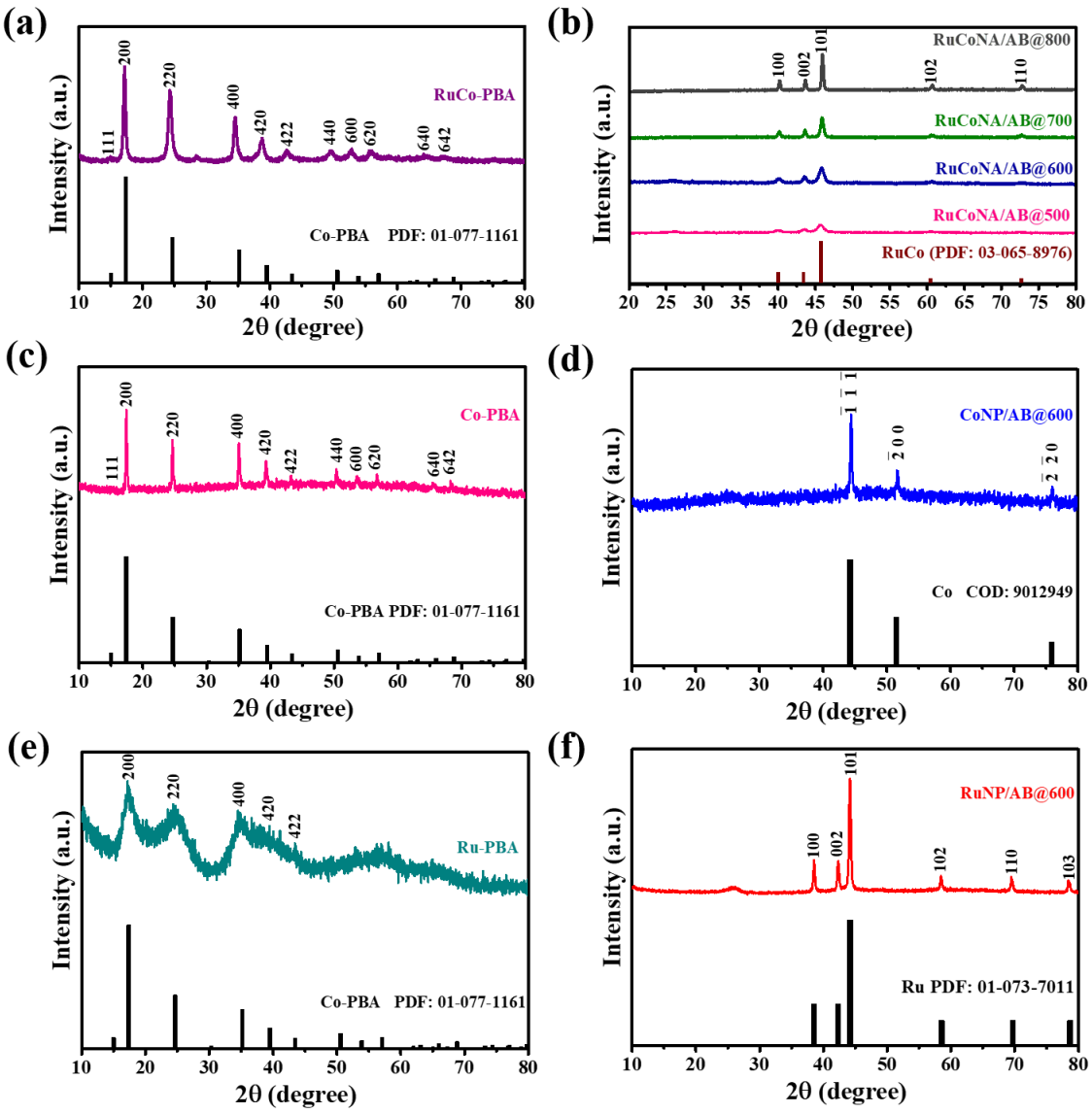

Figure 5.1: PXRD pattern of RuCo-PBA (a), RuCoNA/AB@500, RuCoNA/AB@600, RuCoNA/AB@700, RuCoNA/AB@800 (b), Co-PBA (c), CoNP/AB@600 (d), Ru-PBA (e) and RuNP/AB@600 (f).

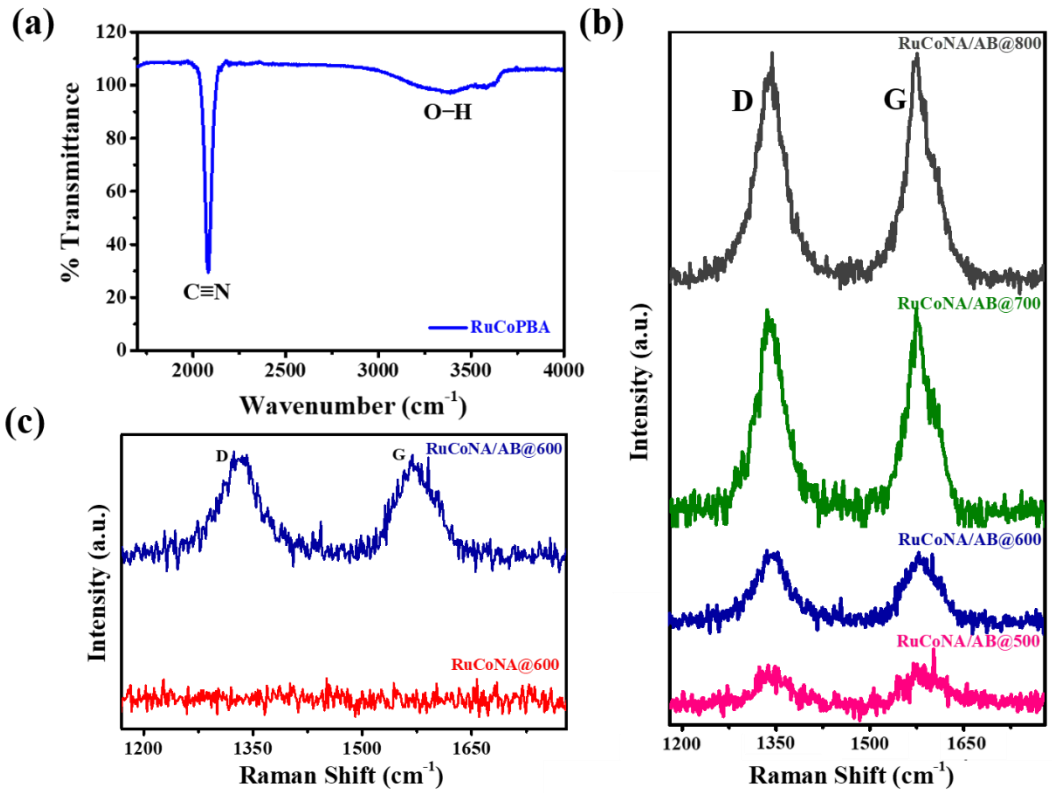

Figure 5.2: FTIR spectrum of RuCo-PBA (a), Raman spectrum for RuCoNA/AB@T (T=500-800 °C) (b) and RuCoNA/AB@600 and RuCoNA@600 (c).

55.24°, 63.67° and 66.46°, were indexed to the 200, 220, 222, 400, 420, 422, 440, 600, 620, 640 and 642 planes of the Co-PBA respectively. The PXRD pattern for RuCo-PBA was matching well with the JCPDS card no. 01-077-1161, for Co-PBA. A slight shift of the peaks towards the lower angles were observed, this can be attributed to the fact that the size of ruthenium ion is bigger as compared to that of Co ion. Hence insertion of Ru leads to enhancement in d spacing value leading to a shift in the PXRD peak position towards lower angle.[46–48] **Figure 5.1b** represents the PXRD pattern of RuCoNA/AB@500, RuCoNA/AB@600, RuCoNA/AB@700 and RuCoNA/AB@800. The diffraction peaks at 40.010°, 43.418°, 45.772°, 60.509° and 72.675° for RuCoNA/AB@T (T=500, 600, 700, and 800 °C) were indexed to the 100, 002, 101, 102 and 110 planes of RuCo . The PXRD pattern was found to be in good agreement with the JCPDS card no. 03-065-8976 for RuCo. No extra peaks were observed in the PXRD

pattern indicating towards the high purity of the materials. As evident from the **Figure 5.1b** the crystallinity of the synthesised electrocatalysts was found to increase with the increase in temperature from the 500-800 °C. The most possible reason for this could be that the high annealing temperatures provide adequate energy for crystallisation to take place at the optimal equilibrium sites, leading to increased intensity of the peaks. **Figure 5.1c** and **Figure 5.1e** represents the PXRD patterns for Co-PBA and Ru-PBA respectively. Similarly, **Figure 5.1d** and **Figure 5.1f** demonstrates the PXRD pattern for CoNP/AB@600 and RuNP/AB@600 respectively. The PXRD pattern for Co-PBA and Ru-PBA was found to match well with the JCPDS file number 01-077-1161 for Co-PBA. Similarly, the PXRD pattern **Figure 5.1e** for CoNP/AB@600 was matching well with the COD number: 9012949 for Co and the PXRD pattern **Figure 5.1f** for RuNP/AB@600 was found to be in good agreement with the JCPDS card number:01-073-7011 for Ru. No impurity was observed in the PXRD pattern of Co-PBA, Ru-PBA, CoNP/AB@600 and RuNP/AB@600 indicating the high purity of the synthesised materials. The crystallinity of the material was found to increase systematically with an increase in the

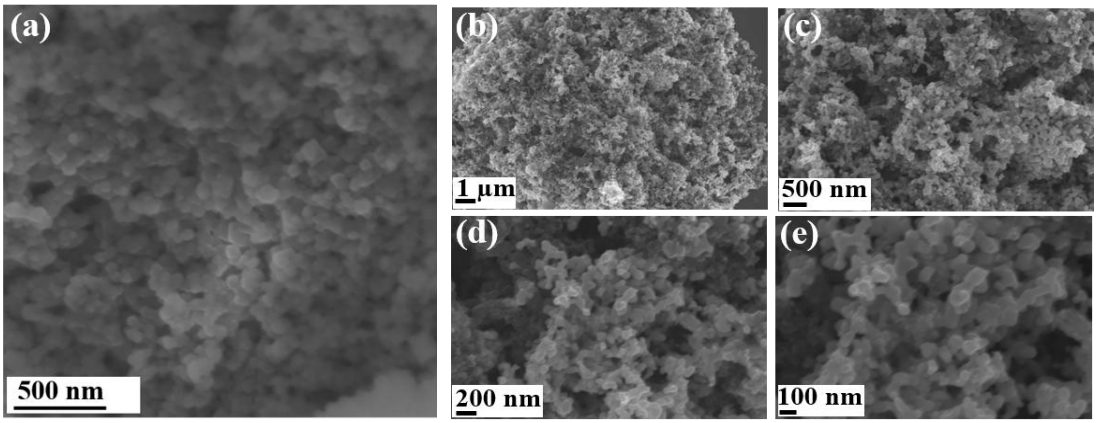

Figure 5.3: FESEM images for RuCo-PBA (a) and RuCoNA/AB@600 at different magnifications (b-e).

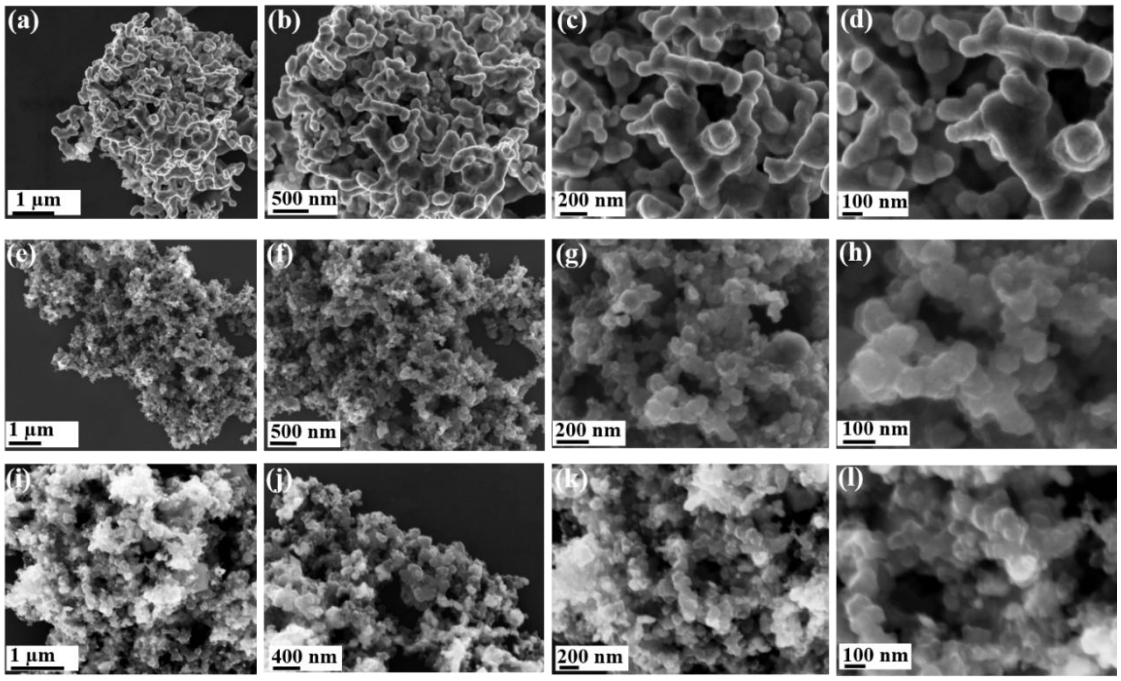

Figure 5.4: FESEM image of RuCoNA/AB@500 (a-d), RuCoNA/AB@700 (e-h) and RuCoNA/AB@800 (i-l) at different magnifications.

annealing temperature from 500 to 800 °C. **Figure 5.2a** represents the FTIR spectrum for RuCo-PBA. The peak at 2083 and 3380 cm^{-1} indicates towards the presence of CN and OH in the RuCo-PBA respectively. The presence of N in the RuCo-PBA precursor is evident from the FTIR spectrum. N-doped graphitized carbon was formed during the annealing of RuCo-PBA with acetylene black due to the rupture of cyanide group.[49] The sp^2 graphitic phase and the disorderedness of the synthesised materials were examined by using Raman spectroscopy. The presence of graphitic carbon in the desired sample is shown by the G band, which represents sp^2 graphitic carbon, while the D band typically denotes disorderedness in the graphite. Two peaks were observed at approximately 1338 and 1579 cm^{-1}, which corresponds to the G and D bands for all of the RuCoNA/AB@T products, as seen in **Figure 5.2b**. Furthermore, RuCoNA/AB@600 has a greater intensity ratio (I_D/I_G = 1.03) than other RuCoNA/AB@T products (0.97 for RuCoNA/AB@500, 1.00 for RuCoNA/AB@700 and 0.94 for RuCoNA/AB@800), indicating more structural defects, which is beneficial for the synthesised material's electrocatalytic performance.

Co tends to catalyse the formation of graphitised carbon because of its poor carbon

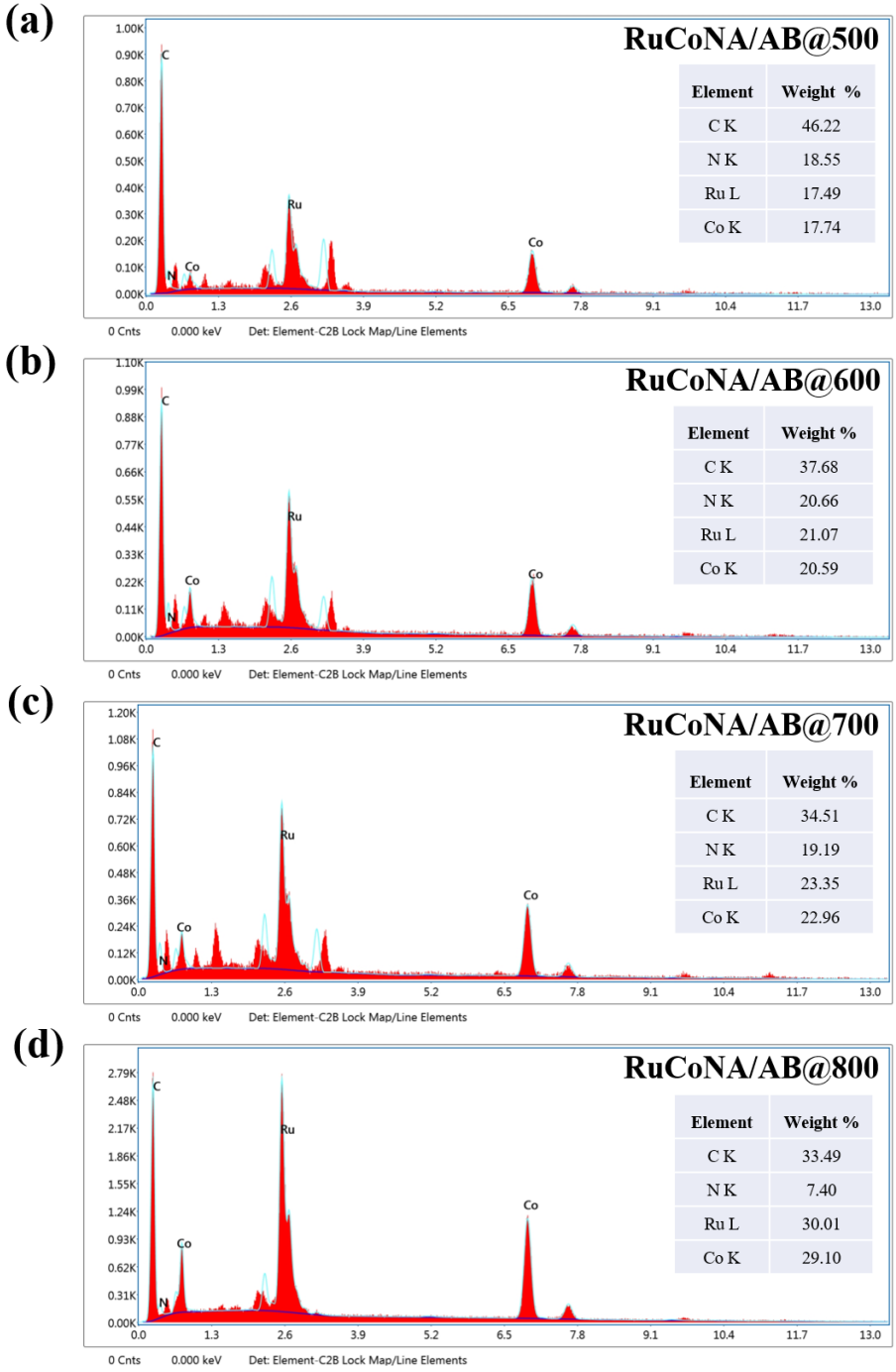

Figure 5.5: EDX spectrum of RuCoNA/AB@500 (a), RuCoNA/AB@600 (b), RuCoNA/AB@700 (c) and RuCoNA/AB@800 (d).

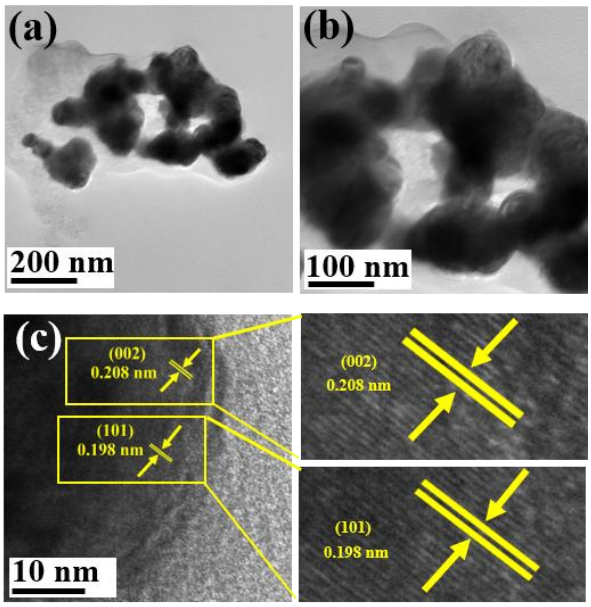

Figure 5.6: TEM images of RuCoNA/AB@600 at different magnifications (a, b) and HRTEM image of RuCoNA/AB@600 (c).

solubility, which limits the damage to carbon layers.[50] During the reduction step of carbon preparation Ru is more prone than Co to produce the defective carbon.[51] These defects along with the presence of doped-N are regarded as active sites which can significantly enhance the electrocatalytic activity of the electrocatalyst.[22] Also the presence of N-doped graphitised C provides protection against the corrosion during the long-term electrolysis.[22] The surface morphology of the RuCo-PBA and its derived RuCo-nanoalloy were verified through Field Emission Scanning Electron Microscopy. The FESEM image **Figure 5.3a** reveals nano-cube like morphology for the RuCo-PBA. Microscopic morphological studies reveal nano-granule like morphology for RuCoNA/AB@500, RuCoNA/AB@600, RuCoNA/AB@700 and RuCoNA/AB@800. As the temperature rises from 500 °C to 600 °C in case of RuCoNA/AB@500 and RuCoNA/AB@600 no significant change in the morphology was observed, which is evident from the FESEM **Figure 5.4a-d** for RuCoNA/AB@500 and **Figure 5.3b-e** for RuCoNA/AB@600. But when the temperature was raised from 600 to 700 °C and then

to 800 °C a significant increase in the agglomeration of the nano-granules was observed which is evident from **Figure 5.4e-h** and **Figure 5.4i-l** which represents the FESEM image for RuCoNA/AB@700 and RuCoNA/AB@800 respectively. The EDX spectrum for RuCoNA/AB@500 **(Figure 5.5a)**, RuCoNA/AB@600 **(Figure 5.5b)**, RuCoNA/AB@700 **(Figure 5.5c)** and RuCoNA/AB@800 **(Figure 5.5d)** reveals the presence of Co, Ru, C and N in the materials. The Transmission Electron Microscopy (TEM) studies reveal granule-like morphology for RuCoNA/AB@600 as shown in **Figure 5.6a and 5.6b** which was found to be in accordance with the FESEM analysis. **Figure 5.6c** shows the High-Resolution Transmission Electron Microscopy analysis for

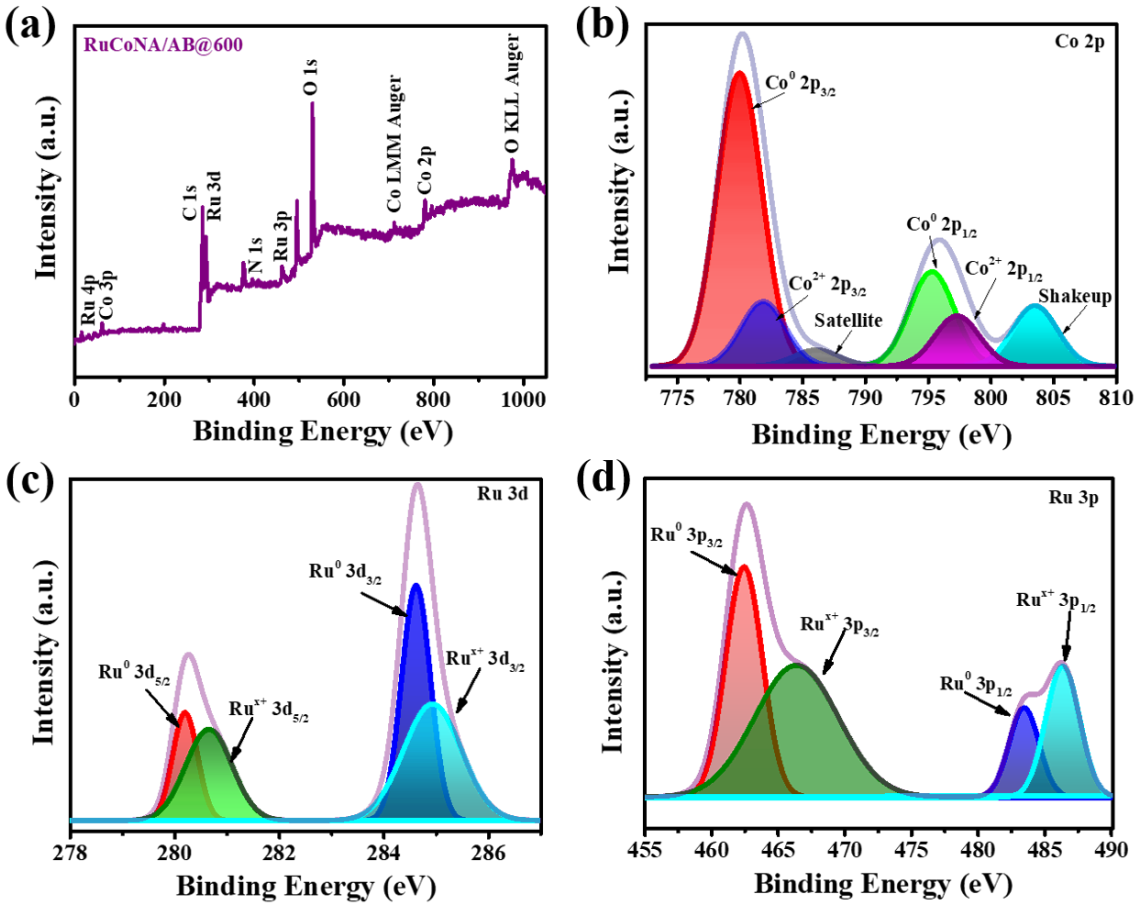

Figure 5.7: Full survey XPS spectrum (a), core level XPS spectrum for Co 2p (b), core level XPS spectrum for Ru 3d (c) and core level XPS spectrum for Ru 3p (d) of RuCoNA/AB@600.

RuCoNA/AB@600, which reveals the presence of two lattice fringes with the interplanar d-spacing value of 0.208 and 0.198 nm which was attributed to the 002 and 101 plane of RuCo nanoalloy respectively. The HRTEM **(Figure 5.6c)** and PXRD **(Figure 5.1b)** of RuCoNA/AB@600 were found to be in good agreement with each other indicating towards the successful synthesis of the RuCo-nanoalloy. In order to offer further details on the surface elemental composition and oxidation states of the elements present in the RuCo nanoalloy (RuCoNA/AB@600) produced by the annealing method, an X-ray photoelectron spectrum (XPS) was also acquired. The full XPS survey spectrum of RuCoNA/AB@600, i.e. **Figure 5.7a** revealed the existence of Co, Ru, C and N. However, the pyrolysis of the PBA linkers produces the N element and the presence of surface oxidized species is what causes the extra oxygen peak. The appearance of the O peak in the XPS spectrum is due to the oxidation of Co and Ru in the presence of atmospheric air. When exposed to air, cobalt oxidation can occur quickly even in a matter of minutes. Although, less reactive than cobalt, ruthenium oxidises when exposed to air, but more slowly.[52] **Figure 5.7b** shows the Co 2p spectrum of RuCoNA/AB@600. XPS assessment of the Co 2p spectrum revealed the presence of two distinct chemical species i.e. Co (0) and Co (II). The existence of Co (II) can be attributed to the inevitable oxidation of metallic Co on its surface during the process of storage and preparation.[52] The presence of two peaks at 781.8 and 797.3 eV corresponds to the existence of Co $2p_{3/2}$ and Co $2p_{1/2}$ orbitals for Co^{2+} species.[26] The remaining two peaks at binding energy value 786 and 803.5 eV were indexed to the satellite shakeup peaks. The peaks at the 779.9 and 795.3 eV are assigned to $2p_{3/2}$ and $2p_{1/2}$ respectively of Co (0).[26] **Figure 5.7c** shows the Ru 3d spectra. The peaks for Ru 3d and C 1s were observed to overlap in **Figure 5.7a**. **Figure 5.7c** reveals the presence of Ru (0) as well as $Ru^{x+.}$ The peaks at the binding energy value 284.6 and 280.2 eV are assigned to the $3d_{3/2}$ and $3d_{5/2}$ peaks of Ru (0)

respectively, confirming the metallic nature of Ru.[40] In **Figure 5.7c** the peaks at 284.9 and 280.7eV were ascribed to the $3d_{3/2}$ and $3d_{5/2}$ peaks of Ru^{x+}. **Figure 5.7d** depicts the

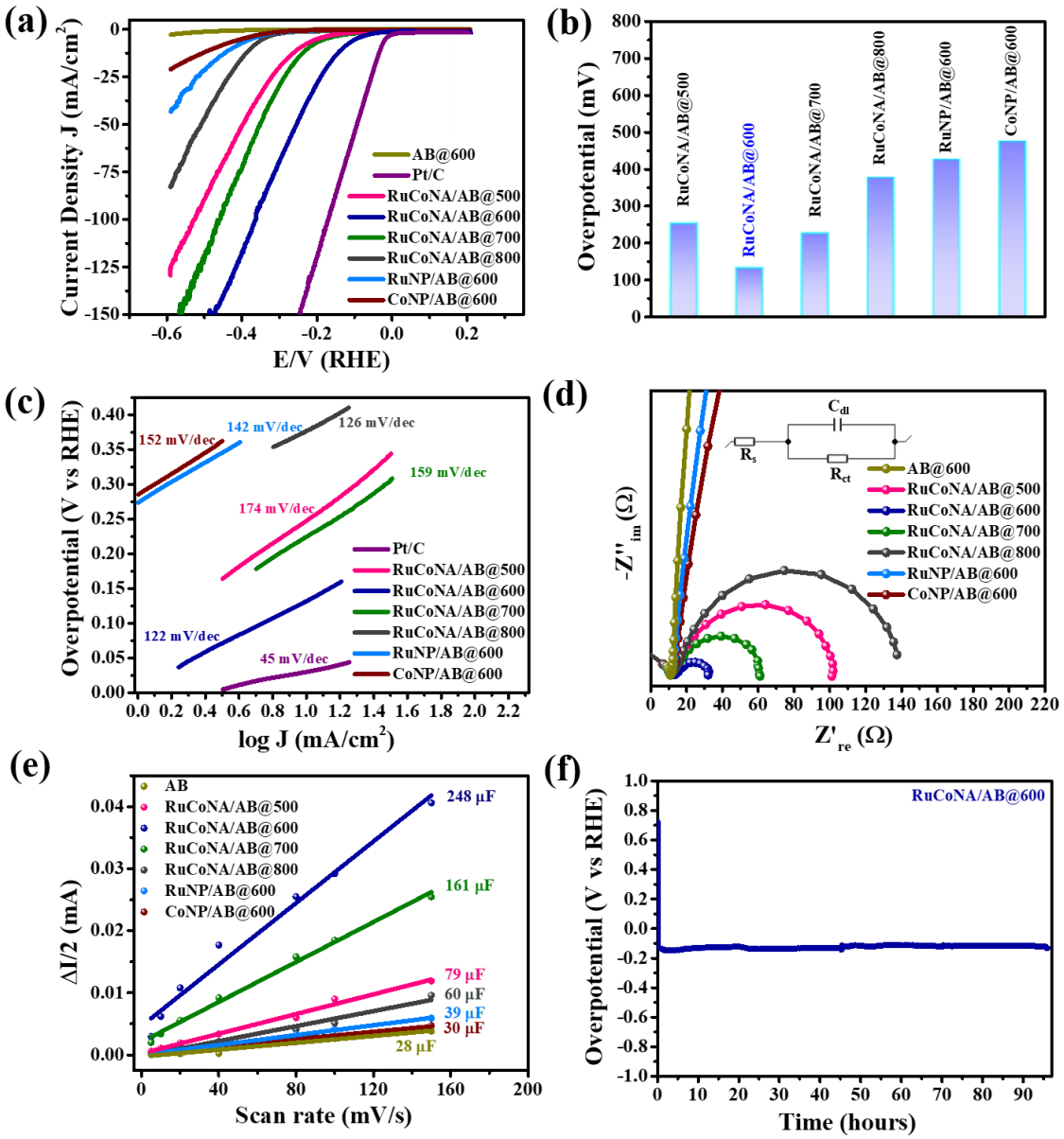

Figure 5.8: Linear sweep voltammogram (a), overpotential comparision (b), Tafel (c), EIS , the inset shows the circuit diagaram (d), C_{dl} values of RuCoNA/AB@T, RuNP/AB@600, CoNP/AB@600, AB@600 (e) and chronopotentiometric measurement plot of RuCoNA/AB@600 (f). The linear sweep voltammograms are recorded at sweep rates of 5 mV/s.

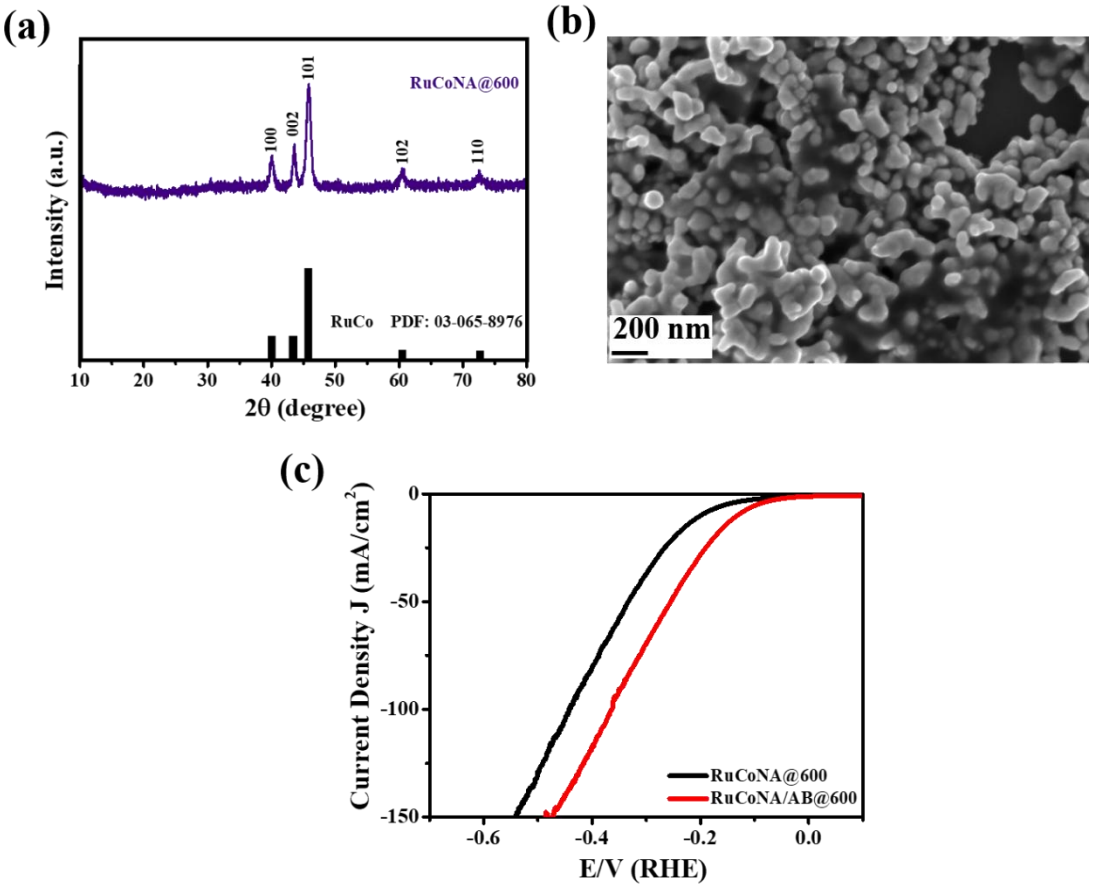

Figure 5.9: Powder XRD pattern of RuCoNA@600 (a), FESEM image of RuCoNA@600 (b) and LSV of RuCoNA@600 and RuCoNA /AB@600 (c).

Ru 3p spectrum, where the peaks at 462.2 and 466.3 eV were assigned to the $3p_{3/2}$ of metallic Ru and Ru^{x+} respectively.[46] Similarly, the remaining peaks at 483.5 and 486.3 eV were attributed to the $3p_{5/2}$ of metallic Ru and Ru^{x+} respectively.[53]

The electrochemical behaviour of all the synthesised materials were investigated towards water reduction reaction under an acidic electrolytic condition (0.5 M H_2SO_4). All the measurements were carried out in a three-electrode setup with material coated glassy carbon electrode, platinum rod and Ag/AgCl (sat. KCl) electrode as working, counter, and reference electrodes respectively. To analyse the performance of the electrocatalysts, the activity was compared to that of the state-of-the-art catalyst Pt/C for HER in acidic medium of 0.5 M H_2SO_4. The obtained linear sweep voltammograms (LSVs) were then

normalised to the working electrode's geometrical surface area (0.19 cm^2). All the LSV curves presented in this research work are non-iR compensated. The LSV plot as shown in **Figure 5.8a** reveals that RuCoNA/AB@600 requires a low overpotential of 129 mV to produce a current density of 10 mA/cm^2. The overpotential required by RuCoNA/AB@500, RuCoNA/AB@700, RuCoNA/AB@800 and Pt/C was found to be 250, 225, 377 and 29 mV respectively. The value of overpotential of RuCoNA/AB@600 was found to be lower as compared to that of the other synthesised materials RuCoNA/AB@500, RuCoNA/AB@700 and RuCoNA/AB@800. In order to analyse the performance of the RuCo-PBA-derived RuCo-nanoalloy, we have synthesised Co-PBA derived Co nanoparticles (CoNP/AB@600) and the Ru-PBA-derived Ru nanoparticles (RuNP/AB@600) for comparison. **Figure 5.8a** demonstrates that CoNP/AB@600 and RuNP/AB@600 requires an overpotential of 478 and 429 mV respectively to produce the bench-mark current density of 10 mA/cm^2. Further the performance of RuCoNA/AB@600 (RuCo-nanoalloy synthesised by pyrolyzing a mixture of RuCo-PBA and AB in a ratio of 2:1) was compared with the performance of RuCoNA@600 (RuCo-nanoalloy synthesised by pyrolyzing RuCo-PBA without AB). The crystallinity and phase purity of the synthesised RuCoNA@600 was determined through PXRD. **Figure 5.9a** reveals high purity and successful synthesis of the RuCoNA@600 which is found to be in good agreement with the JCPDS card number 03-065-8976 of RuCo. Also, nanogranules like morphology was observed for the RuCoNA@600 through FESEM **(Figure 5.9b)**. **Figure 5.9c** demonstrates that RuCoNA@600 requires an overpotential of 198 mV to produce 10 mA/cm^2 current density. The poor performance of RuCoNA@600 can be ascribed to the absence of the N-doped graphitised C as well as the defects as evident from the **Figure 5.2c**. Also, the performance of RuCoNA/AB@600 was compared with the AB@600 (AB pyrolyzed at 600 °C). AB@600 was not able to

produce the bench-mark current density of 10 mA/cm^2. From the LSV plots we can clearly conclude that RuCoNA/AB@600 requires the least value of overpotential in comparison to other synthesised materials which are RuCoNA/AB@500, RuCoNA/AB@700, RuCoNA/AB@800, RuCoNA@600, RuNP@600, CoNP@600 and AB@600. **Figure 5.8b** shows the comparison of overpotential values of all the synthesised materials. Further Tafel slopes was determined for all the synthesised materials by fitting the linear region of the plot between log J vs overpotential by following the equation:

$$\eta = a + b \log J$$

(η is overpotential value, a is the Tafel constant, b is Tafel slope and J is the current density).[54] **Figure 5.8c** demonstrates that the temperature optimised RuCoNA/AB@600 had a small Tafel slope of 122 mV/dec, which indicates faster surface kinetics leading to an improved electrochemical activity towards HER. **Figure 5.8c** shows the calculated Tafel slope values for RuCoNA/AB@500, RuCoNA/AB@700, RuCoNA/AB@800, CoNP/AB@600 and RuNP/AB@600 were found to be 174, 159, 126, 152 and 142 mV/dec respectively. This concludes that faster reaction kinetics are occurring in case of RuCoNA/AB@600 as compared to the other synthesised electrocatalysts. Nyquist plot or EIS was employed and data was recorded at an AC amplitude of 5 mV and in the frequency region of 0.1 Hz to 1 MHz at a potential of -0.16 V vs RHE in order to determine the charge transfer dynamics of all the synthesised materials. **Figure 5.8d** shows the EIS of RuCoNA/AB@500, RuNP/AB@600 and AB@600. **Figure 5.8d** shows that all of the RuCoNA/AB@T, CoNP/AB@600, RuNP/AB@600 samples had relatively similar solution resistance (R_s) at the high frequency range. R_s is a mixture of electrolyte resistance, intrinsic resistance and contact resistance of the employed electrode. Smaller is the diameter of the semicircle, smaller will be the charge transfer resistance (R_{ct}). R_{ct}

value was observed to be 88.78, 18.69, 46.94 and 125.9 Ω for RuCoNA/AB@500, RuCoNA/AB@600, RuCoNA/AB@700 and RuCoNA/AB@800 respectively.

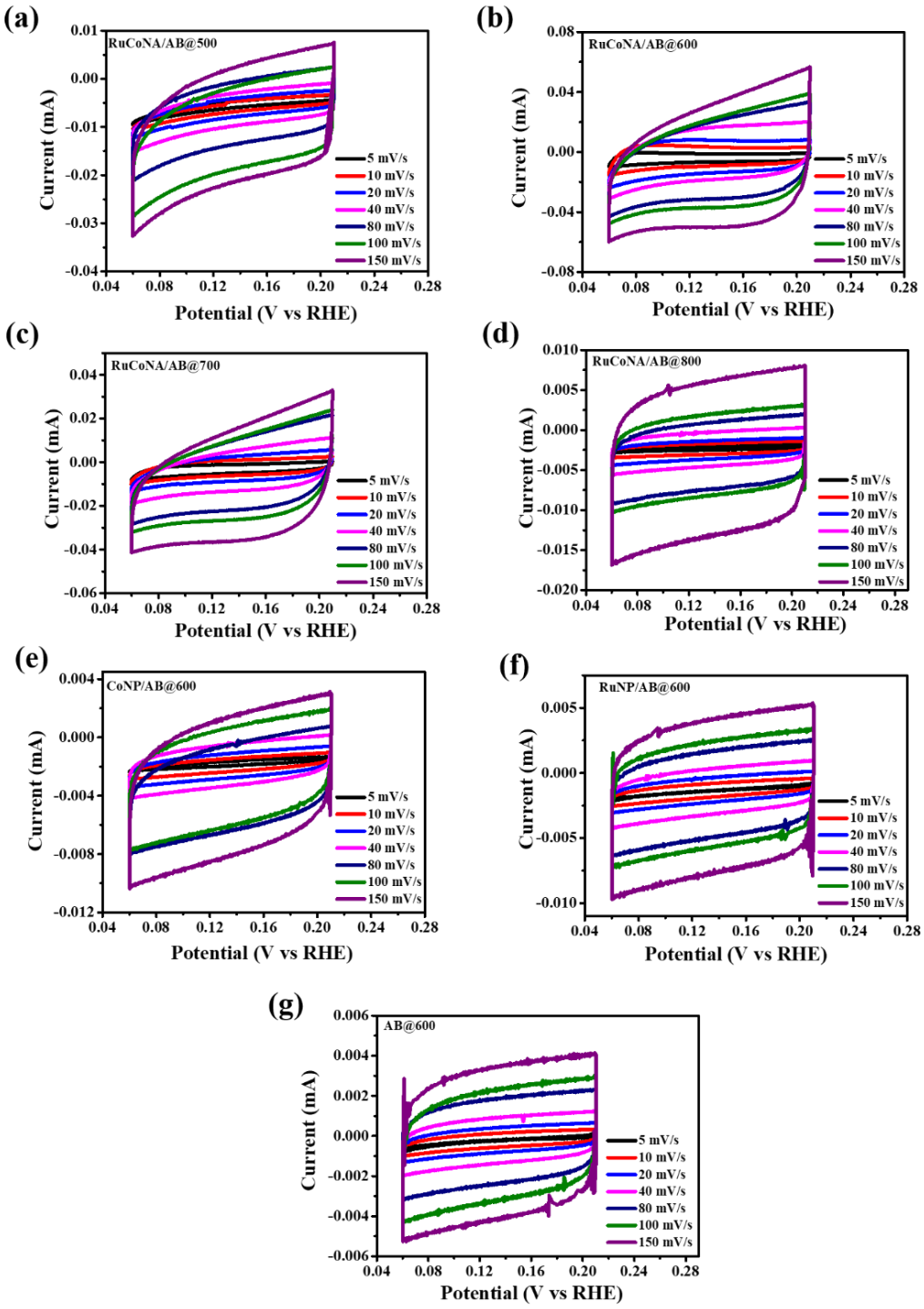

Figure 5.10: CV curves for RuCoNA/AB@500 (a), RuCoNA/AB@600 (b), RuCoNA/AB@700 (c), RuCoNA/AB@800 (d), CoNP/AB@600 (e), RuNP/AB@600(f), and AB@600 (g) at different scan rates.

RuCoNA/AB@600 poses a smaller R_{ct} value as compared to the other comparing materials. A lower value of R_{ct} suggests a faster reaction kinetics between the electrolyte solution and electrode surface resulting into enhanced performance towards the water reduction reaction.[33] The lower value of overpotential, Tafel slope and R_{ct} can be attributed to the presence of RuCo-nanoalloy along with the N-doped graphitised C. In acidic environments, the reduction of H_3O^+ (hydronium ions) to H_2 (gaseous dihydrogen) is the cathodic reaction of water electrolysis. The first step of the reaction is the Volmer step which involves the reduction of a proton on the catalyst's active site. Then the second step involves the evolution of molecular H_2 either by a second proton/electron transfer (Heyrovsky step) or through the process of recombination of two adsorbed hydrogen (Tafel step).

$H_3O^+ + e^- + * = H^* + H_2O$ (Volmer)

$H^* + H_3O^+ + e^- = H_2 + H_2O$ (Heyrovsky)

$2H^* = H_2$ (Tafel)

Here * denotes an active site of the catalyst and H* indicates the adsorbed H on the active site of the catalyst.[44] In particular, it was observed that adding Co and Ru together to create the RuCo alloy efficiently altered the electronic structure through the overlap of d-orbitals, which could control intermediate adsorption energies and improve catalytic activity.[56] The as-synthesised RuCo-nanoalloy can efficiently alter the distribution of electron on the carbon surface, thus regulating the local function for active intermediates and provides an appropriate active surface for the splitting of water and adsorption/desorption of its related reactive species.[26] To further analyse the electrocatalytic activity of the synthesised electrocatalysts their electrochemically accessible surface area (ECSA) was determined. The ECSA provides insights on the

electrocatalytic activity of the electrocatalyst. However, ECSA is used to determine the accessible units of electrochemical active sites and has a direct correlation with the electrocatalyst's double layer capacitance (C_{dl}).[42] ECSA is determined by using the following equation:

ECSA: C_{dl}/C_s

Where C_{dl} is the double layer capacitance of the electrocatalyst and C_s is the specific capacitance of the atomically smooth surface of metal nanoparticles. C_s value is 35 μF in an acidic electrolyte.[39] A standard cyclic voltammetry (CV) method was used to determine the C_{dl} value in the non-Faradaic region. The CV curves for RuCoNA/AB@500, RuCoNA/AB@600, RuCoNA/AB@700, RuCoNA/AB@800, CoNP/AB@600, RuNP/AB@600 and AB@600 has been presented in the **Figure 5.10**. To determine C_{dl} values various scan rates were plotted against half of the anodic current and cathodic current differential (i.e. $\Delta I = I_a - I_c$) and the corresponding slopes were calculated. The obtained C_{dl} values from **Figure 5.8e** are 248, 79, 161, 60, 30, 39 and 28 μF for RuCoNA/AB@600, RuCoNA/AB@500, RuCoNA/AB@700, RuCoNA/AB@800, CoNP/AB@600, RuNP/AB@600 and AB@600 respectively. The ECSA value obtained by using the above-mentioned equation was found to be 7.09, 2.26, 4.6, 1.71, 0.86, 1.11 and 0.8 cm^2 for RuCoNA/AB@600, RuCoNA/AB@500, RuCoNA/AB@700, RuCoNA/AB@800, CoNP/AB@600, RuNP/AB@600 and AB@600 respectively. RuCoNA/AB@600 outperformed the other temperature-varying ruthenium cobalt nano-alloy compounds, including RuCoNA/AB@600, RuCoNA/AB@500, RuCoNA/AB@700, RuCoNA/AB@800, as well as the nanoparticles CoNP/AB@600, RuNP/AB@600 along with the AB@600 in terms of more number of electrochemical active sites and accessible surface area for the desired reaction to take place **(Figure 5.8e)**. Materials with higher ECSA value generally

produces higher value of current density at a particular overpotential. This is due to the availability of larger ECSA, a greater number of proton reduction reactions can occur resulting in the better performance of the electrocatalyst, which is an essential parameter for material's application towards HER. The excellent electrochemical performance of the RuCoNA/AB@600 can also be attributed to its high ECSA value.[43] Both CoNP/AB@600 and RuNP/AB@600 exhibits poor performance towards the HER. The poor performances of CoNP/AB@600 and RuNP/AB@600 can be attributed to the weak and strong hydrogen bonding energy of Co and Ru respectively.[20] The weak hydrogen bonding energy of Co leads to the poor catalytic performance of CoNP/AB@600 and the strong interaction between the Ru and H makes the desorption of H_2 difficult leading towards the poor performance of RuNP/AB@600.[20] CoNP/AB@600 and RuNP/AB@600 requires very high overpotential of 478 and 429 mV to produce a bench mark current density of 10 mA/cm^2. Also, the higher Tafel slope value for CoNP/AB@600 (152 mV/dec)

and RuNP/AB@600 (142 mV/dec) indicates the slower kinetics at the electrode and

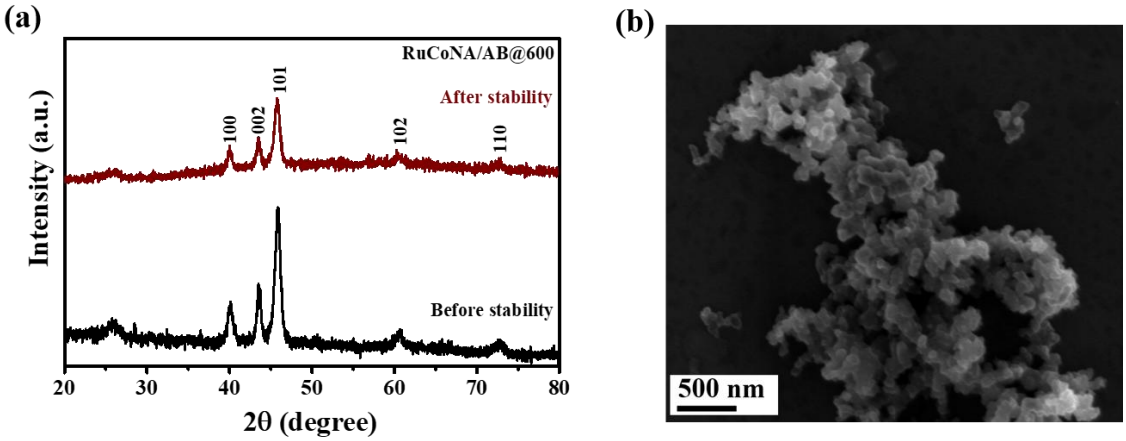

Figure 5.11: PXRD pattern (a) and FESEM image (b) after the long-term stability of RuCoNA/AB@600.

electrolyte interface. The electrochemically active surface area for both the material is

very low indicating towards the lesser number of active sites leading to the poor performance of the materials. The poor performance of the materials can be attributed to the absence of synergistic effect of the metal centres which provides optimized conditions for the dissociation of water and adsorption/desorption process of the involved intermediates and products.[20–24] One of the most important factors pertaining to the material's practical application is its stability. Following a thorough examination of the HER activity, chronopotentiometry is used to verify the catalyst's electrochemical stability. **Figure 5.8f** displays the long-term stability of RuCoNA/AB@600 in acidic medium for 96 hours. The electrocatalyst was found to be stable during the long-term stability test for 96 hours. A negligible change in the performance of the electrocatalyst was observed after the long-term electrolysis for 96 hours. The small increase in the overpotential can be due to the loss of electrocatalyst from the surface of electrode. This might be due to the mechanical force involved in the gas bubble's rupturing, which further supports its dynamic electrochemical stability. Moreover, powder X-ray diffraction and FESEM **(Figure 5.11a** and **5.11b)** were employed to examine any structural or phase changes of the catalyst following catalysis. The phase which demonstrates the catalyst's structural integrity, was found to remain unchanged and the FESEM images showed little bit agglomeration of particles due to the long-term electrolysis. This indicates towards the robustness of RuCoNA/AB@600 as an electrocatalyst for HER.

Performance of RuCoNA/AB@600 has been compared with various novel, PBA-derived and Ru Co based materials in **Table 5.1**. The exceptional performance of the electrocatalyst can be attributed to multiple factors. Firstly, the synthesised RuCo-nanoalloy have the ability to modify the distribution of the electrons on the carbon surface which can further control the local function of the active species. This offers

a suitable active surface for the process of water dissociation as well as the adsorption and desorption of the related reactive species.[22,26] Secondly, the alloying between the Co and Ru along with the presence of N-doped graphitised C greatly decreased the catalyst's vulnerability to corrosion during the long-term electrolysis.[20,22] Thirdly, the uniform distribution of nano granules like particles exposes a large number of active sites for the reaction to take place which is also evident from the large ECSA value obtained for RuCoNA/AB@600. This uniform distribution of the nano granules like particles also promoted the adequate electrolyte diffusion and for the smooth progression of HER shorten the electron transfer path. In our present study PBA performed a crucial role by providing the uniform distribution of the nano-granules like particles throughout the electrocatalyst's surface. The enhanced electrochemical performance of RuCoNA/AB@600 along with its aforementioned systematic characterisation implies that RuCoNA/AB@600 can be utilised as an effective alternative to the most expensive electrocatalyst for hydrogen evolution reaction. Our current work suggests a new strategy for synthesising RuCo-nanoalloy electrocatalyst through RuCo-PBA for use in electrochemical water splitting processes.

Table 5.1. Comparison of metal based electrocatalysts for HER.

Sl. No.	Electrocatalysts	Overpotential at 10 mA cm^{-2} (mV)	Tafel Slope (mV dec^{-1})	Electrolyte	Reference
1	CoNi@NC	142	104	0.1 M H_2SO_4	57
2	$NiCo_2S_4$	345	60	0.5 M H_2SO_4	58
3	CoSAs-MoS_2/TiN NRs	187.5	56.9	0.5 M H_2SO_4	59
4	CoS_2 nanowires	145	51.6	0.5 M H_2SO_4	60
5	Zn-Co_9S_8@CF-(1-1)	278	85.2	0.5 M H_2SO_4	61
8	P-$CoNiO_2$@NC	64.6	55	0.5 M H_2SO_4	62
9	W electrode	320	25	0.5 M H_2SO_4	63
10	$CoWO_4$@rGO	570	142	0.5 M H_2SO_4	64
11	**RuCoNA/AB@600**	**129**	**122**	**0.5 M H_2SO_4**	**This work**
PBA-derived electrocatalysts for HER					
12	MoS_2-Co	155	55	0.5 M H_2SO_4	44
13	Co_2P/Ni_2P/CNT-3	151	41.64	0.5 M H_2SO_4	65
14	Ni–Co–MoS_2	155	51	0.5 M H_2SO_4	66
15	C/Fe-CoS_2-350	151	66.21	0.5 M H_2SO_4	67
16	NGQD/CoFeP	70	56	0.5 M H_2SO_4	26
Ru and Co based electrocatalysts for HER (synthesised by following 2 or more steps)					
17	$CoRu_{0.25}$@N-C	94	64	0.5 M H_2SO_4	68
18	RuCo@HCS	57	48	0.5 M H_2SO_4	69
19	Ru−CoSe NCs	152	37	0.5 M H_2SO_4	70
20	Ru@Co/N-CNTs	92	45	0.5 M H_2SO_4	71
21	CoRu@NG-3	52	65	0.5 M H_2SO_4	72

5.7 Conclusion

In summary, we have synthesised a series of RuCo nanoalloy with N-doped graphitised carbon derived from a bimetallic PBA RuCo-PBA, by varying the annealing temperature from 500-800 °C (i.e. RuCoNA/AB@T, T= 500-800). The optimised product RuCoNA/AB@600 requires a low overpotential value of 129 mV to produce the bench-mark current density of 10 mA/cm^2 and has an excellent durability in the harsh acidic condition during the long-term electrolysis for 96 hours. The obtained Tafel slope value and charge transfer resistance value are also small indicating the faster reaction kinetics between the electrolyte and electrode surface. Altering the annealing temperature had a major impact on optimising the morphology as well as the electrochemically active surface area of the resulting nanoalloy products. The remarkable catalytic performance is due to the presence of N-doped graphitised carbon along with the alloying of Ru and Co. Specifically, it was demonstrated that incorporating Co and Ru together for the formation of RuCo alloy effectively changed the electronic structure by causing the d-orbitals to overlap. The presence of N-doped graphitised C protected the catalyst during the long term chronopotentiometry test. This might potentially regulate intermediate adsorption energies and enhance the electrocatalytic activity of RuCoNA/AB@600 for HER. The synthesis of RuCoNA/AB@600 through a facile annealing process which involves the annealing of RuCo-PBA precursor along with acetylene black creates a new pathway for the development of ruthenium cobalt nano-alloy with N-doped graphitised carbon which acts as an exceptional electrocatalyst for the H_2 production.

5.8 References

1. X. Zhou, X. Yang, M. N. Hedhili, H. Li, S. Min, J. Ming, K. W. Huang, W. Zhang, L. J. Li, *Nano Energy*, 2017, **32**, 470–478.
2. V. D. Nithya, *Int. J. Hydrogen Energy*, 2021, **46**, 36080–36102.
3. G. W. Crabtree, M. S. Dresselhaus, *MRS Bull.*, 2008, **33**, 421–428.
4. B. Wang, F. Yang, L. Feng, *Small*, 2023, **19**, 2302866.
5. D. Damien, A. Anil, D. Chatterjee, M. M. Shaijumon, *J. Mater. Chem. A*, 2017, **5**, 13364–13372.
6. R. Zhang, X. Wang, S. Yu, T. Wen, X. Zhu, F. Yang, X. Sun, X. Wang, W. Hu, *Adv. Mater.*, 2017, **29**, 1605502.
7. S. Jeong, K. Hu, T. Ohto, Y. Nagata, H. Masuda, J. I. Fujita, Y. Ito, *ACS Catal.*, 2020, **10**, 792–799.
8. J. Zhao, Y. Zhang, Y. Xia, B. Zhang, Y. Du, B. Song, H. L. Wang, S. Li, P. Xu, *Appl. Catal. B*, 2023, **328**, 122447.
9. S. Niu, S. Li, J. Hu, Y. Li, Y. Du, X. Han, P. Xu, *Chem. Comm.*, 2019, **55**, 14649–14652.
10. G. Ma, F. Wang, R. Jin, B. Guo, H. Huo, Y. Dai, Z. Liu, J. Liu, S. Li, *Int. J. Mol. Sci.*, 2025, **26**, 1582.
11. Y. Zheng, Y. Jiao, Y. Zhu, L. H. Li, Y. Han, Y. Chen, A. Du, M. Jaroniec, S. Z. Qiao, *Nat. Commun.*, 2014, **5**, 3783.
12. A. Eftekhari, *Int. J. Hydrogen Energy*, 2017, **42**, 11053–11077.
13. J. Su, Y. Yang, G. Xia, J. Chen, P. Jiang, Q. Chen, *Nat. Commun.*, 2017, **8**, 1–10.
14. J. Chen, G. Xia, P. Jiang, Y. Yang, R. Li, R. Shi, J. Su, Q. Chen, *ACS Appl. Mater. Interfaces*, 2016, **8**, 13378–13383.

15. A. F. Pedersen, E. T. Ulrikkeholm, M. Escudero-Escribano, T. P. Johansson, P. Malacrida, C. M. Pedersen, M. H. Hansen, K. D. Jensen, J. Rossmeisl, D. Friebel, A. Nilsson, I. Chorkendorff, I. E. L. Stephens, *Nano Energy*, 2016, **29**, 249–260.

16. F. Xu, Y. J. Li, C. Huang, H. C. Xu, *ACS Catal.*, 2018, **8**, 3820–3824.

17. Y. Liu, X. Yong, Z. Liu, Z. Chen, Z. Kang, S. Lu, *Adv. Sustainable Syst.*, 2019, **3**, 1800161.

18. L. Huang, X. Zhang, Q. Wang, Y. Han, Y. Fang, S. Dong, *J. Am. Chem. Soc.*, 2018, **140**, 1142–1147.

19. D. Yang, W. Hou, Y. Lu, W. Zhang, Y. Chen, *J. Energy Chem.*, 2021, **52**, 130 138.

20. W. Li, Y. Zhao, Y. Liu, M. Sun, G. I. N. Waterhouse, B. Huang, K. Zhang, T. Zhang, S. Lu, *Angew. Chem. Int. Ed. Engl.*, 2021, **60**, 3290–3298.

21. Y. Liu, X. Li, Q. Zhang, W. Li, Y. Xie, H. Liu, L. Shang, Z. Liu, Z. Chen, L. Gu, Z. Tang, T. Zhang, S. Lu, *Angew. Chem.*, 2020, **132**, 1735–1743.

22. C. Gao, H. Wang, S. Li, B. Liu, J. Yang, J. Gao, Z. Peng, Z. Zhang, Z. Liu, *Electrochim. Acta*, 2019, **327**, 134958.

23. Y. Sun, B. Huang, Y. Li, Y. Xing, M. Luo, N. Li, Z. Xia, Y. Qin, D. Su, L. Wang, S. Guo, *Chem. Mater.*, 2019, **31**, 8136–8144.

24. M. Luo, S. Guo, *Nat. Rev. Mater.*, 2017, **2**, 17059.

25. M. Li, H. Wang, W. Zhu, W. Li, C. Wang, X. Lu, *Adv. Sci.*, 2020, **7**, 1901833.

26. H. Wang, C. Gao, R. Li, Z. Peng, J. Yang, J. Gao, Y. Yang, S. Li, B. Li, Z. Liu, *ACS Sustainable Chem. Eng.*, 2019, **7**, 18744–18752.

27. A. O. Dudoladov, A. V. Grigorenko, V. Kumar, M. S. Vlaskin, *Theor. Found. Chem. Eng.*, 2022, **56**, 988–996.

28. X. Cao, C. Tan, M. Sindoro, H. Zhang, *Chem. Soc. Rev.*, 2017, **46**, 2660 2677.

29. J. Liu, D. D. Zhu, C. X. Guo, A. Vasileff, S. Z. Qiao, *Adv. Energy Mater.*, 2017, **7**, 1700518.

30. Y. V. Kaneti, S. Dutta, M. S. A. Hossain, M. J. A. Shiddiky, K. L. Tung, F. K. Shieh, C. K. Tsung, K. C. W. Wu, Y. Yamauchi, *Adv. Mater.*, 2017, **29**, 1700213.

31. S. Fu, C. Zhu, J. Song, D. Du, Y. Lin, *Adv. Energy Mater.*, 2017, 1700363.

32. J. Zhou, Y. Dou, A. Zhou, L. Shu, Y. Chen, J. R. Li, *ACS Energy Lett.*, 2018, **3**, 1655–1661.

33. L. Yan, L. Cao, P. Dai, X. Gu, D. Liu, L. Li, Y. Wang, X. Zhao, *Adv. Funct. Mater.*, 2017, **27**, 1703455.

34. X. Zhang, S. Liu, Y. Zang, R. Liu, G. Liu, G. Wang, Y. Zhang, H. Zhang, H. Zhao, *Nano Energy*, 2016, **30**,93–102.

35. N. Sahu, J. K. Das, J. N. Behera, *Inorg. Chem.*, 2022, **61**, 2835–2845.

36. W. Jiang, W. Luo, J. Wang, M. Zhang, Y. Zhu, *J. Photochem. Photobiol.*, 2016, **28**, 87–115.

37. Y. Yang, Z. Lun, G. Xia, F. Zheng, M. He, Q. Chen, *Energy Environ. Sci.*, 2015, **8**, 3563–3571.

38. Q. Wu, M. Luo, J. Han, W. Peng, Y. Zhao, D. Chen, M. Peng, J. Liu, F.M. F. De Groot, Y. Tan, *ACS Energy Lett.*, 2020, **5**, 192–199.

39. M. K. Sahoo, J. N. Behera, *Dalton Trans.*, 2023, **52**, 10876–10884.

40. L. M. Cao, D. Lu, D. C. Zhong, T. B. Lu, *Coord. Chem. Rev.*, 2020, **407**, 213156.

41. Y. Xue, Q. Yan, X. Bai, Y. Xu, X. Zhang, Y. Li, K. Zhu, K. Ye, J. Yan, D. Cao, G. Wang, *J. Colloid Interface Sci.*, 2022, **612**, 710–721.

42. M. Sadangi, J. N. Behera, *Dalton Trans.*, 2024, **53**, 6667–6675.

43. J. N. Behera, D. M. D'Alessandro, N. Soheilnia, J. R. Long, *Chem. Mater.*, 2009, **21**, 1922–1926.

44. S. Chandrasekaran, E. Arumugam, C. Karuppiah, S. Karuppaiah, A. S. Haidyrah, B. Chandran, C. C. Yang, *Mater. Lett.*, 2021, **300**, 130274.

45. S. Xu, J. Xu, Y. Z. Liu, Y. Hua, Z. Duan, Y. Wang, A. Neville, X. Gao, *ACS Appl. Energy Mater.*, 2019, **2**, 8974–8984.

46. A. Bleuzen, J. D. Cafun, A. Bachschmidt, M. Verdaguer, P. Münsch, F. Baudelet, J. P. Itié, *J. Phys. Chem. C*, 2008, **112**, 17709–17715.

47. S. Kjeldgaard, I. Dugulan, A. Mamakhel, M. Wagemaker, B. B. Iversen, A. Bentien, *R. Soc. Open Sci.*, 2021, **8**, 201779.

48. S. F. A. Kettle, E. Diana, E. M. C. Marchese, E. Boccaleri, P. L. Stanghellini, *J. Raman Spectrosc.*, 2011, **42**, 2006–2014.

49. Z. Yao, C. Wang, Y. Wang, R. Lu, S. Su, J. Qin, H. Wei, Q. Wang, *J. Mater. Sci.*, 2019, **54**, 11841–11847.

50. Y. Zhu, H. A. Tahini, Y. Wang, Q. Lin, Y. Liang, C. M. Doherty, Y. Liu, X. Li, J. Lu, S. C. Smith, C. Selomulya, X. Zhang, Z. Shao, H. Wang, *J. Mater. Chem. A*, 2019, **7**, 14222–14232.

51. G. Li, N. Wei, Y. Wang, *Appl. Surf. Sci.*, 2023, **610**, 155459.

52. J. Wang, Q. Yu, H. Li, R. Li, S. Zeng, Q. Yao, Z. Guo, H. Chen, K. Qu, *Chem. Comm.*, 2021, **57**, 7284–7287.

53. J. K. Das, A. K. Samantara, A. K. Nayak, D. Pradhan, J. N. Behera, *Dalton Trans.*, 2018, **47**, 13792–13799.

54. N. Dubouis, A. Grimaud, *Chem. Sci.*, 2019, **10**, 9165–9181.

55. Y. Liu, S. Sun, X. Zheng, D. Li, J. Zhu, M. Zhang, D. Jiang, *Inorg. Chem.*, 2022, **61**, 17557–17567.

56. J. K. Das, A. K. Samantara, S. Satyarthy, C. S. Rout, J. N. Behera, *RSC Adv.*, 2020, **10**, 4650–4656.

57. J. Deng, P. Ren, D. Deng, X. Bao, *Angew. Chem., Int. Ed.*, 2015, **54**, 2100 2104.

58. U. Aftab, A. Tahira, R. Mazzaro, V. Morandi, M. Ishaq Abro, M. M. Baloch, C. Yu, Z. H. Ibupoto, *RSC Adv.*, 2020, **10**, 22196–22203.

59. T. L. L. Doan, D. C. Nguyen, S. Prabhakaran, D. H. Kim, D. T. Tran, N. H. Kim, J. H. Lee, *Adv. Funct. Mater.*, 2021, **31**, 2100233.

60. M. S. Faber, R. Dziedzic, M. A. Lukowski, N. S. Kaiser, Q. Ding, S. Jin, *J. Am. Chem. Soc.*, 2014, **136**, 10053–10061.

61. B. Dong, J.-Y. Xie, N. Wang, W.-K. Gao, Y. Ma, T.-S. Chen, X.-T. Yan, Q.-Z. Li, Y.-L. Zhou, Y.-M. Chai, *Renew. Energy*, 2020, **157**, 415–423.

62. P. Zhao, Y. Zhao, H. Liang, X. Song, B. Yu, F. Liu, A. J. Ragauskas, C. Wang, *Chem. Eng. J.*, 2023, **466**, 143140.

63. G. M. Abd El-Hafez, N. H. Mahmoud, A. Walcarius, A. M. Fekry, *Int. J. Hydrogen Energy*, 2019, **44**, 16487–16496.

64. G. Chen, W. F. Dong, B. L. Li, Y. H. Deng, X. H. Wang, X. F. Zhang, H.Q. Luo, N. B. Li, *Electrochim. Acta*, 2018, **276**, 81–91.

65. Z. Ding, H. Yu, X. Liu, N. He, X. Chen, H. Li, M. Wang, Y. Yamauchi, X. Xu, M. A. Amin, T. Lu, L. Pan, *J. Colloid Interface Sci.*, 2022, **616**, 210–220.

66. X. -Y. Yu, Y. Feng, Y. Jeon, B. Guan, X. W. D. Lou, U. Paik, *Adv. Mater.*, 2016, **28**, 9006–9011.

67. B. Fang, N. He, Y. Li, T. Lu, P. He, X. Chen, Z. Zhao, L. Pan, *Electrochim. Acta*, 2023, **448**, 142187.

68. W.-S. Lin, M. Rinawati, W.-H. Huang, C.-Y. Chang, L.-Y. Chang, Y.-S. Cheng, sC.-C. Chang, J.-L. Chen, W.-N. Su, M.-H. Yeh, *J. Colloid Interface Sci.*, 2024, **654**, 677–687.

69. Z. Wei, Y. Liu, Z. Peng, H. Song, Z. Liu, B. Liu, B. Li, B. Yang, S. C. Lu, *ACS Sustain. Chem. Eng.*, 2019, **7**, 7014–7023.

70. M. Wang, Z. Dang, M. Prato, U. Petralanda, I. Infante, D. V. Shinde, L. De Trizio, L. Manna, *ACS Appl. Nano Mater.*, 2019, **2**, 5695–5703.

71. Z. Liu, X. Yang, G. Hu, L. Feng, *ACS Sustain. Chem. Eng.*, 2020, **8**, 9136 9144.

72. H. Wang, M. Zhou, X. Bo, L. Guo, *Electrochim. Acta*, 2021, **382**, 138337.

CHAPTER-6

Prussian Blue Analogue (PBA)-Derived Ru-$NiSe_2$ Nanogranules as Robust and Efficient Electrocatalysts for Alkaline Hydrogen Evolution

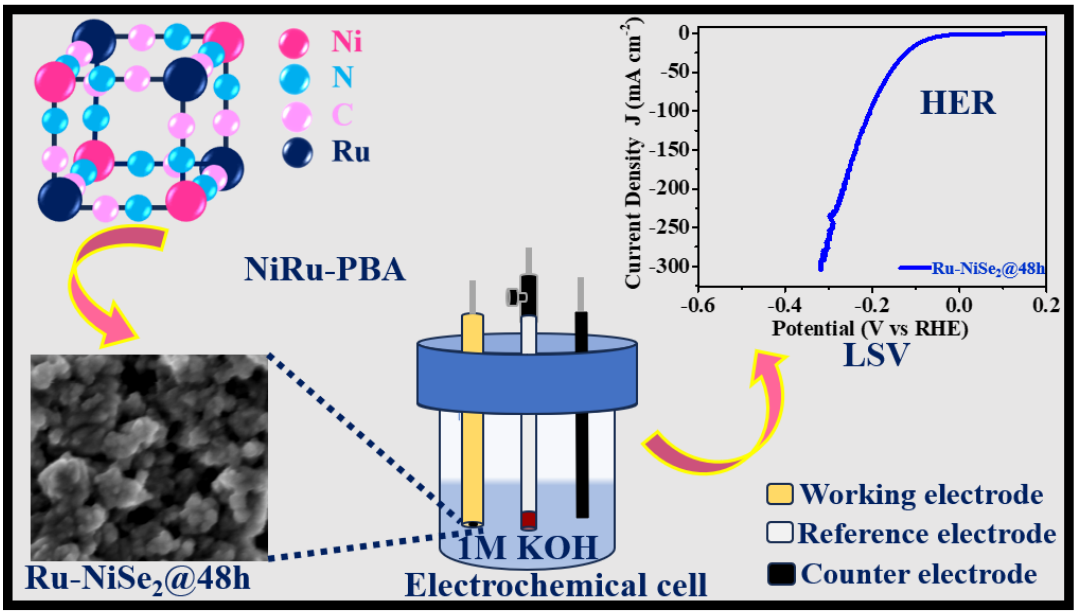

6.1 Abstract

The development of robust and efficient electrocatalysts for the hydrogen evolution reaction (HER) in alkaline media remains a critical challenge for large-scale hydrogen production. Herein, we report the synthesis of a series of Ru-incorporated nickel selenide nanogranules (Ru-$NiSe_2$@T, T = 24, 48, and 72h) derived from a NiRu–Prussian Blue Analogue (NiRu–PBA) precursor via a controlled hydrothermal selenization strategy. The optimized Ru-$NiSe_2$@48h catalyst exhibits an exceptionally low overpotential of 84 mV at 10 mA cm^{-2}, a small Tafel slope of 89 mV dec^{-1}, and excellent long-term durability over 72 h in 1.0 M KOH. Structural and spectroscopic analyses confirm the successful incorporation of Ru into the $NiSe_2$ lattice, inducing partial lattice distortion and defect formation that enhance charge transfer and active site density. XPS studies reveal the coexistence of Ru^0 and Ru^{3+} species, indicating strong interfacial electronic interactions that optimize the hydrogen adsorption–desorption energetics. The superior performance of Ru-$NiSe_2$@48h arises from the synergistic effects between Ru and $NiSe_2$, improved conductivity, and an enlarged electrochemically active surface area. The reaction time optimization has played an important role in enhancing the performance of the material

by providing an optimized morphology for the desired reaction to occur. The presence of small-sized nanogranule-like particles and their uniform distribution throughout the surface of the material exposed a larger area of the material for the reaction to happen. The incorporated Ru gives the electrocatalyst exceptional stability in an alkaline environment by inhibiting particle aggregation. This work provides an unique approach for designing Prussian Blue Analogue–derived transition metal chalcogenides with tailored electronic structures for efficient and durable hydrogen evolution in alkaline media.

6.2 Introduction

The accelerating depletion of conventional fossil fuels, coupled with their substantial contribution to environmental degradation, has driven intensive research into sustainable energy conversion and storage technologies. To mitigate these challenges, developing environmentally friendly systems such as water-splitting devices, metal–air batteries, and fuel cells has become imperative.[1–4] Among these, hydrogen, a clean, renewable, and high-energy-density fuel, has emerged as a promising candidate to meet the rising global energy demand while minimizing greenhouse gas emissions.[5] Electrochemical water splitting offers a green and efficient pathway for producing ultra-pure hydrogen using renewable electricity, thereby reducing fossil fuel dependency and facilitating carbon neutrality.[6] Among the various approaches, alkaline water electrolysis has gained considerable attention owing to its low corrosion rate, high durability, and reduced acid fog generation.[6] However, the overall water-splitting process, which involves the hydrogen evolution reaction (HER) and the oxygen evolution reaction (OER), typically requires large overpotentials due to sluggish reaction kinetics.[7,8] The water electrolysis can be carried out either in an acidic or alkaline medium. Although proton exchange membranes (PEMs) have demonstrated some advantages in acid water electrolysis, but

their high cost and the slow reaction kinetics of the anodic oxygen evolution reaction (OER) in the acidic medium continue to prevent their widespread application. When electrolysis is carried out in an alkaline medium, the aforementioned issues can be lessened. The much slowed cathodic hydrogen evolution reaction (HER) kinetics in alkaline conditions, however, is a new disadvantage.[9] In order to reduce energy losses and improve catalytic performance, it is essential to build robust and effective electrocatalysts that can function at high current densities.

Pt/C and IrO_2 are the benchmark catalysts for HER and OER, respectively, due to their high cost, scarcity, instability during long-term electrolysis, etc. we need a suitable substitute for them. Although significant progress has been achieved in developing non-precious transition metal–based catalysts as alternatives to noble metals (Pt/C for HER and IrO_2 for OER), most of these substitutes still fail to maintain long-term operational stability under practical conditions.[6,10] Transition metal compounds such as oxides,[11] chalcogenides,[12,13] carbides,[14,15] hydroxides,[16,17] and phosphides[18] have been widely explored as potential candidates for overall water splitting. Among them, transition metal chalcogenides, particularly selenides, have garnered increasing attention due to their superior electrical conductivity, optimal d-orbital configuration, and tunable electronic structure.[6] Nickel-based selenides are especially attractive because of their narrow bandgap, high electrical conductivity, strong metal–anion covalency, and excellent catalytic activity.[19,20] With increasing atomic number in the chalcogenide series, the electronegativity of the chalcogen decreases, leading to enhanced covalent character in M–X bonds (X = S, Se, Te). This improved covalency promotes better alignment of valence and conduction band levels with water redox potentials, thereby accelerating redox kinetics at transition metal centers.[21] However, because of their high hydrogen adsorption energies and limited number of electrochemically active sites, their catalytic

efficacy still trails that of cutting-edge noble metal catalysts.[6] Furthermore, a major worry for long-term operation is the catalyst's deterioration brought on by corrosion, surface reconstruction, or agglomeration during extended electrolysis.

In alkaline media, the HER mechanism proceeds via two key steps: (i) water dissociation into adsorbed hydrogen (H_{ads}) and hydroxide ions (OH^-) (Volmer step), followed by (ii) hydrogen gas evolution through either the Heyrovsky (electrochemical desorption) or Tafel (recombination) pathway.[22] The extra water dissociation step significantly restricts reaction rates even for platinum, whose HER activity in alkaline media is two to three orders of magnitude lower than in acidic environments.[22,23] Therefore, obtaining good HER performance in alkaline electrolytes requires improving water dissociation kinetics. Innovative material engineering techniques that combine conductivity enhancement, electronic structure modification, and structural robustness are highly needed.

Strategies such as heterostructure construction, elemental doping, strain modulation, and defect engineering have been employed to improve catalytic efficiency.[6] Among these, electronic modulation via cation incorporation is particularly effective, as introducing secondary metal species can alter the crystal field, optimize hydrogen adsorption free energy, and synergistically enhance reaction kinetics.[20] Additionally, decorating catalysts with sub-nanometer metal or metal oxide clusters has proven beneficial, as these clusters exhibit quantum confinement effects, expose more active sites, and significantly boost water dissociation capability.[6] Ruthenium-based catalysts are among the most promising alternatives to platinum for HER, owing to their comparable hydrogen binding energy and substantially lower cost.[24–28] However, metallic Ru suffers from dissolution and instability under electrochemical operating conditions.[29] Incorporating Ru into bimetallic systems or heterostructures has been shown to stabilize the active phase and tune the electronic structure for improved durability and activity.[19,29] Notably, Ru

nanoclusters can effectively modulate the d-band centre toward the Fermi level, thereby enhancing water dissociation and accelerating HER kinetics.[6] To achieve scalable synthesis of such advanced materials, bimetallic metal–organic frameworks (MOFs) and their subclass, Prussian Blue Analogues (PBAs), have emerged as ideal precursors. These frameworks consist of metal centres bridged by cyanide ligands, offering high surface area, adjustable porosity, and versatile composition.[30,31] Upon thermal or chemical conversion, PBAs yield highly porous and compositionally tunable electrocatalysts with excellent structural integrity and enhanced conductivity, making them attractive templates for water splitting applications.

In light of these challenges, the current work focuses on rational catalyst design to enhance intrinsic catalytic activity, charge transfer behaviour, and active-site utilisation, thus offering a different approach to the production of hydrogen that is both economically feasible and sustainable. In the present work, we report the hydrothermal synthesis of a series of Ru-incorporated $NiSe_2$ nanogranules (Ru-$NiSe_2$@T, T = 24, 48, and 72 h) using a NiRu–PBA as a precursor, with the reaction time systematically varied to optimize structural and electrochemical properties. The resulting catalysts were extensively evaluated for their HER performance in alkaline media, demonstrating how Ru incorporation and time-dependent structural evolution synergistically enhance catalytic activity and durability. The bimetallic PBA provided the two metal centers simultaneously which reduced the number of reaction steps and made the reaction feasible. Due to the optimised electronic interactions, synergistic catalytic effects, and a greater number of electroactive sites for the reaction to occur because of uniformly dispersed nanogranule-like morphology, the time optimised material Ru-$NiSe_2$@48h exhibits better HER kinetics. The catalyst showed exceptional stability during the long-

term electrolysis owing to the incorporated Ru, which gives the material resilience against corrosion and agglomeration.

6.3 Experimental Section

6.3.1 Materials

Potassium hexacyanoruthenate (II) hydrate ($K_4[Ru(CN)_6].xH_2O$), potassium hydroxide (KOH 90% flakes), hydrazine monohydrate $H_2NNH_2.H_2O$, trisodium citrate ($Na_3C_6H_5O_7$) and nickel nitrate hexahydrate ($Ni(NO_3)_2.6H_2O$) were purchased from Sigma Aldrich chemicals, and Se powder was purchased from TCI chemicals. All chemicals were used exactly as specified with no changes. For the preparation of catalyst ink pure ethanol was bought from Merck and Nafion solution from Alfa Aesar. The experiment was carried out entirely with DI water.

6.3.2 Synthesis of NiRu-PBA

NiRuPBA was synthesised by utilizing a facile coprecipitation method. Firstly, a solution was made by adding 87 mg of nickel nitrate hexahydrate ($Ni(NO_3)_2.6H_2O$) and 134 mg of trisodium citrate ($Na_3C_6H_5O_7$) to 10 mL of DI H_2O. Then a second solution was prepared by adding 86 mg of potassium hexacyanoruthenate hydrate ($K_4[Ru(CN)_6].xH_2O$) to 10 mL of DI H_2O. The second solution was then added to the firstly prepared solution in a slow dropwise manner while stirring continuously. After the complete addition of the second solution to the first solution, the mixture was allowed to stir for another 15 minutes. Then the resultant solution was kept for 24 hours at room temperature and then the obtained precipitate was washed 3 times with DI H_2O, then it was allowed to dry at 60 °C. The resultant faded cyan colour powder thus obtained is the NiRu-PBA.

6.3.3 Synthesis of Ru-$NiSe_2$@T Nanoparticles

35 mg of NiRu-PBA was added to 8 mL of DI H_2O. After complete dispersion of the NiRu-PBA into the DI H_2O, 35 mg of Se powder was added to the solution. After 30 minutes of stirring 3 mL of hydrazine monohydrate was added to the mixture. Then the solution was transferred in a 23 mL Teflon lined-stainless steel autoclave. The autoclave was kept in a preheated oven at 200 °C for 24, 48 and 72 hours. After cooling the autoclave to the room temperature, the obtained product was washed three times with DI H_2O. Then all the samples were dried at 60 °C and then stored for the further measurements. The black coloured powder materials thus obtained were Ru-$NiSe_2$@T. The samples synthesised at 24, 48 and 72 hours of time period were named as Ru-$NiSe_2$@24h, Ru-$NiSe_2$@48h and Ru-$NiSe_2$@72h respectively.

6.3.4 Synthesis of $NiSe_2$@48h

$NiSe_2$@48h was further synthesised by following the above procedure. In place of NiRu-PBA, $Ni(NO_3)_2.6H_2O$ was used for the reaction process. In detail 35 mg of $Ni(NO_3)_2.6H_2O$ was added to 8 mL of DI H_2O, to this solution 35 mg of Se powder was added. After 30 minutes 3 mL of hydrazine monohydrate was added to the solution in a dropwise manner. The resultant solution was then transferred to a Teflon lined stainless steel autoclave. The autoclave was kept in a preheated oven at 200 °C for 48 hours. After allowing the autoclave to cool down at room temperature, the obtained solution was washed 3 times with DI H_2O. Then the product was allowed to dry at 60 °C. The material thus obtained is $NiSe_2$@48h and it was stored for future use.

6.4 Characterisation

Powder X-ray diffraction measurements were performed for all the synthesised samples using the Bruker D8 advanced diffractometer system (XRD) with Cu Kα radiation at a wavelength of (λ = 1.5418Å) to assess phase purity and crystallinity. The surface morphology and elemental distributions of the synthesised samples were studied using transmission electron microscopy (TEM, equipped with HRTEM, JEOL 2100F, at 200kV) and field-emission scanning electron microscopy (FESEM, Zeiss Pvt. Ltd., Germany). A dilute suspension of the material in ethanol was prepared for the TEM analysis and cast onto the 200-mesh carbon-coated copper grid. Similarly, a dilute suspension was drop casted on the Si wafer for the FESEM analysis. Before being used for morphology analysis, the copper grid as well as the Si wafer was thoroughly dried under a table lamp. Additionally, the elemental composition and associated oxidation states of the elements contained in the synthesised materials were ascertained through the use of X-ray photoelectron spectroscopy (AXIS Supra Kratos analytical) equipped with a monochromatic X-ray source, Al Ka, of 1486.6 eV). As a known carbon calibration, the C 1s peak was fixed at 284.6 eV, and the other data were computed according to that value. By using Brunauer−Emmett−Teller (BET) desorption/adsorption study using Quanta Chrome Instruments (version 5.21) at 77 K, the specific surface area of the as synthesised materials was determined.

6.5 Electrochemical Measurements

A Biologic SP-200 electrochemical workstation and a standard three-electrode electrochemical cell were used for all electrochemical studies, which were carried out at room temperature in an alkaline electrolyte (1.0 M KOH). The working, counter, and reference electrodes were a catalyst-casted glassy carbon rotating disc electrode

(GCRDE), graphite rod, and Hg/HgO, respectively. To achieve a mirror-finished smooth surface, the GCRDE was first polished using alumina slurry. 1 mg of the electrocatalyst was added to a mixture of 95 µL ethanol and 5 µL Nafion to prepare the catalyst ink. After that, the mixture was ultrasonically treated for half an hour. The polished GCRDE's surface was then drop-cast with 5 µL of the freshly prepared slurry, which was subsequently dried before the measurements. Linear sweep voltammetry (LSV) was employed at a scan rate of 5 mV s^{-1} and at a rotation speed of 2000 RPM to get the polarisation curves. The current was normalised by using the geometrical surface area of GCRDE (0.19 cm^2). All the electrochemical potentials were calibrated to a reversible hydrogen electrode (RHE) using the following equation:[32]

$$E_{RHE} = E^0_{Hg/HgO} + 0.0591\ (pH) + E_{Hg/HgO}$$

The pH of the electrolyte was found to be 13.7. The Tafel slope is calculated by using the following equation:

$$\eta = a + b\log J,$$

where η is the overpotential, a is the Tafel constant, b is the Tafel slope and J represents the current density. Electrochemical impedance spectroscopy (EIS) was performed in the frequency range of 0.1 Hz to 1 MHz with an AC amplitude of 5 mV. In the non-Faradaic region, or the window range of 0.124 - 0.424 V versus RHE, cyclic voltammetry (CV) was performed to measure the electrochemically active surface area (ECSA) of the electrocatalysts at various scan rates (40-200 mV s^{-1}). Chronopotentiometry test was carried out at a constant current density of 20 mA cm^{-2}. To perform the chronopotentiometry test, 1.25 mg of the catalyst was added to a mixture of ethanol (95 µL) and Nafion (5 µL). The mixture was then sonicated for 30 minutes and drop-cast on a glassy carbon plate electrode (2 × 1 cm^2) by covering only 1 × 0.5 cm^2 of it. The

chronopotentiometry measurement was carried out by applying 10 mA of current, i.e. 20 mA cm^{-2} current density. The substance was carefully scraped from the electrode surface following the stability test. Gas chromatography was used to analyse the produced H_2 gas (Agilent 990 Micro GC).

6.6 Results and Discussion

The Ru-$NiSe_2$@T (T = 24, 48, and 72 h) nanogranular electrocatalysts were synthesized following a two-step strategy **(Scheme 6.1)**. Initially, a NiRu–Prussian Blue Analogue (NiRu-PBA) was obtained via a facile coprecipitation route. Subsequently, the as-prepared PBA was subjected to a hydrothermal selenization process in the presence of Se powder and hydrazine monohydrate at 200 °C for different durations (24–72 h) to yield Ru-$NiSe_2$@T. Powder X-ray diffraction (PXRD) confirmed the crystalline nature and phase

purity of the products. The PXRD pattern of NiRu-PBA **(Figure 6.1a)** exhibited sharp peaks consistent with the NiCo–PBA structure (JCPDS No. 89-3738), verifying its high crystallinity and purity. The slight shift in the diffraction peaks toward lower 2θ values indicates lattice expansion due to the substitution of larger Ru ions for Co, leading to an increased d-spacing.[23] Similarly, the PXRD patterns of Ru-$NiSe_2$@24h, Ru-$NiSe_2$@48h,

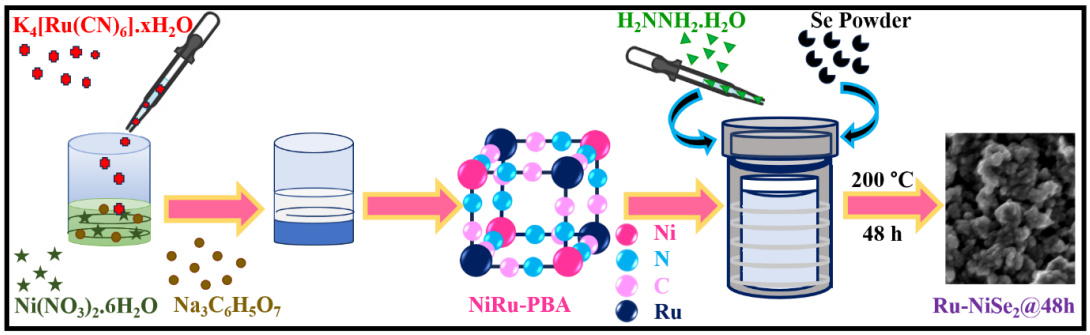

Scheme 6.1: Stepwise synthesis of NiRu-PBA and its derived Ru incorporated $NiSe_2$ i.e. Ru-$NiSe_2$@48h.

and Ru-$NiSe_2$@72h **(Figure 6.1b)** matched well with $NiSe_2$ (COD No. 9012537), confirming successful phase formation. The absence of distinct Ru peaks suggests homogeneous incorporation of Ru into the $NiSe_2$ lattice rather than the formation of a Ru single-atom cluster, catalyst or nanoparticle.[15] The diffraction peak intensity decreased with increasing reaction time, implying reduced crystallinity and enhanced defect formation at longer durations. For comparison, pristine $NiSe_2$@48h was synthesized under identical conditions using $Ni(NO_3)_2 \cdot 6H_2O$ as the Ni source. Its PXRD pattern **(Figure 6.1c)** also matched that of $NiSe_2$, though with higher peak intensity, indicating greater crystallinity. The reduced crystallinity of Ru-$NiSe_2$@48h is advantageous, as lattice imperfections and edge defects can act as active sites, improving mass transport and catalytic performance.[17,25,26] Field-emission scanning electron microscopy (FESEM)

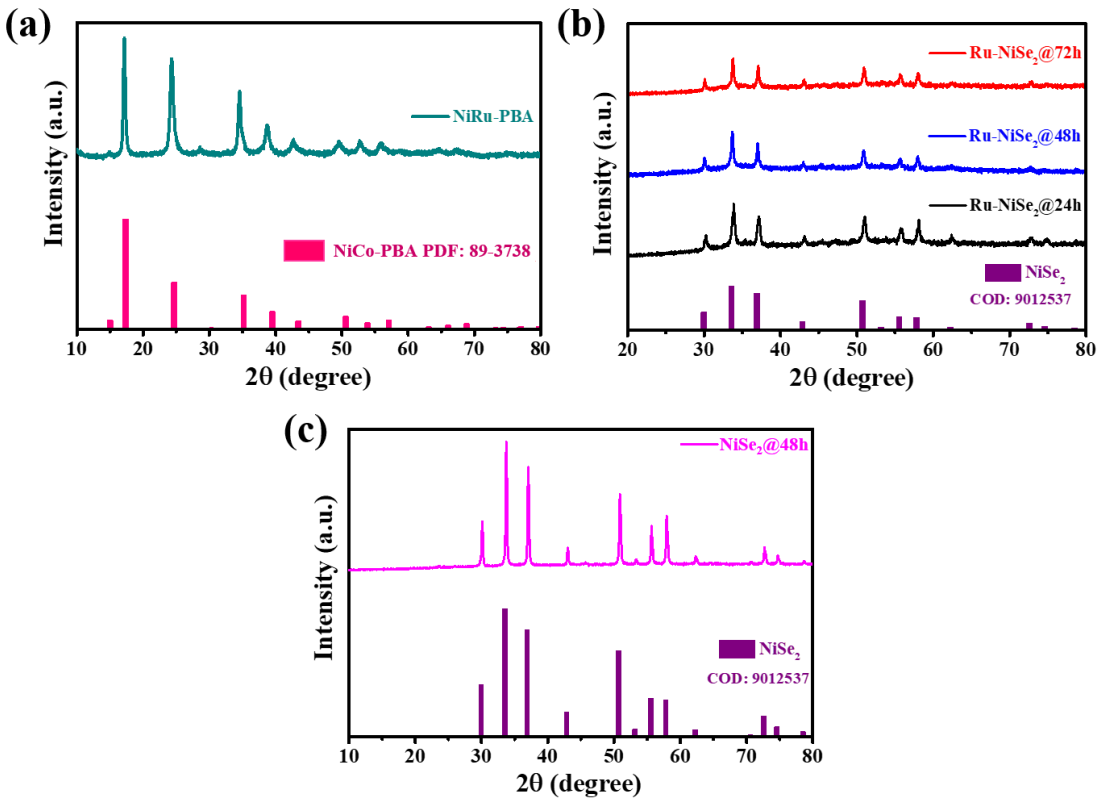

Figure 6.1: Powder X-Ray diffraction pattern of NiRu-PBA (a), NiRu-PBA-derived Ru-$NiSe_2$@24h, Ru-$NiSe_2$@48h, Ru-$NiSe_2$@72h (b) and $NiSe_2$@48h (c).

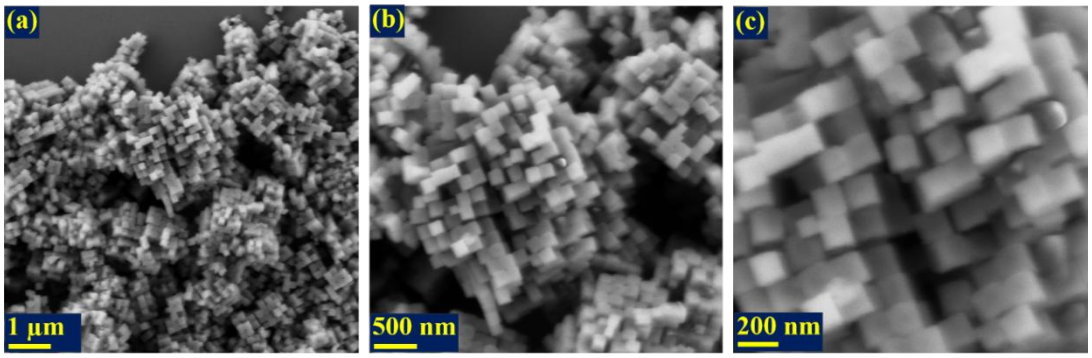

Figure 6.2: FESEM images of NiRu-PBA at different scales (a-c).

revealed nanocube-like morphology for NiRu-PBA **(Figure 6.2a–c)**. After selenization, Ru-$NiSe_2$@48h exhibited a uniform nanogranular morphology **(Figure 6.3a–c)**, while Ru-$NiSe_2$@24h and Ru-$NiSe_2$@72h **(Figures 6.3d-f** and **6.3g-i)** showed denser agglomeration of larger granules. Pristine $NiSe_2$@48h **(Figure 6.4a-c)** displayed significantly larger and more aggregated particles, suggesting fewer accessible active sites compared with Ru-$NiSe_2$@48h. The optimized nanoscale morphology of Ru-$NiSe_2$@48h is expected to enhance the electrochemically active surface area and facilitate charge transfer during catalysis. Energy-dispersive X-ray spectroscopy (EDX) mapping **(Figure 6.5)** confirmed homogeneous distribution of Ni, Ru, Se, C, and N elements throughout the Ru-$NiSe_2$@48h surface, without noticeable phase segregation. The atomic and weight percentages **(Figure 6.5h)** verified successful Ru incorporation. Similar uniform elemental distributions were also observed for Ru-$NiSe_2$@24h and Ru-$NiSe_2$@72h **(Figures 6.6** and **6.7)**. Transmission electron microscopy (TEM) further corroborated the nanogranular morphology of Ru-$NiSe_2$@48h **(Figure 6.8a,b)**. High-resolution TEM (HRTEM) images **(Figure 6.8c,d)** displayed clear lattice fringes with interplanar d-spacings of 0.1797, 0.267, and 0.243 nm, corresponding to the $(\bar{3}\bar{1}\bar{1})$, $(\bar{2}\bar{1}0)$, and $(\bar{2}\bar{1}\bar{1})$ planes of $NiSe_2$, respectively. The absence of distinct Ru lattice fringes implies lattice incorporation rather than discrete Ru nanoparticles. Remarkably, **Figure 6.8d** shows that the $NiSe_2$ phase's lattice fringes are discontinuous and partially absent,

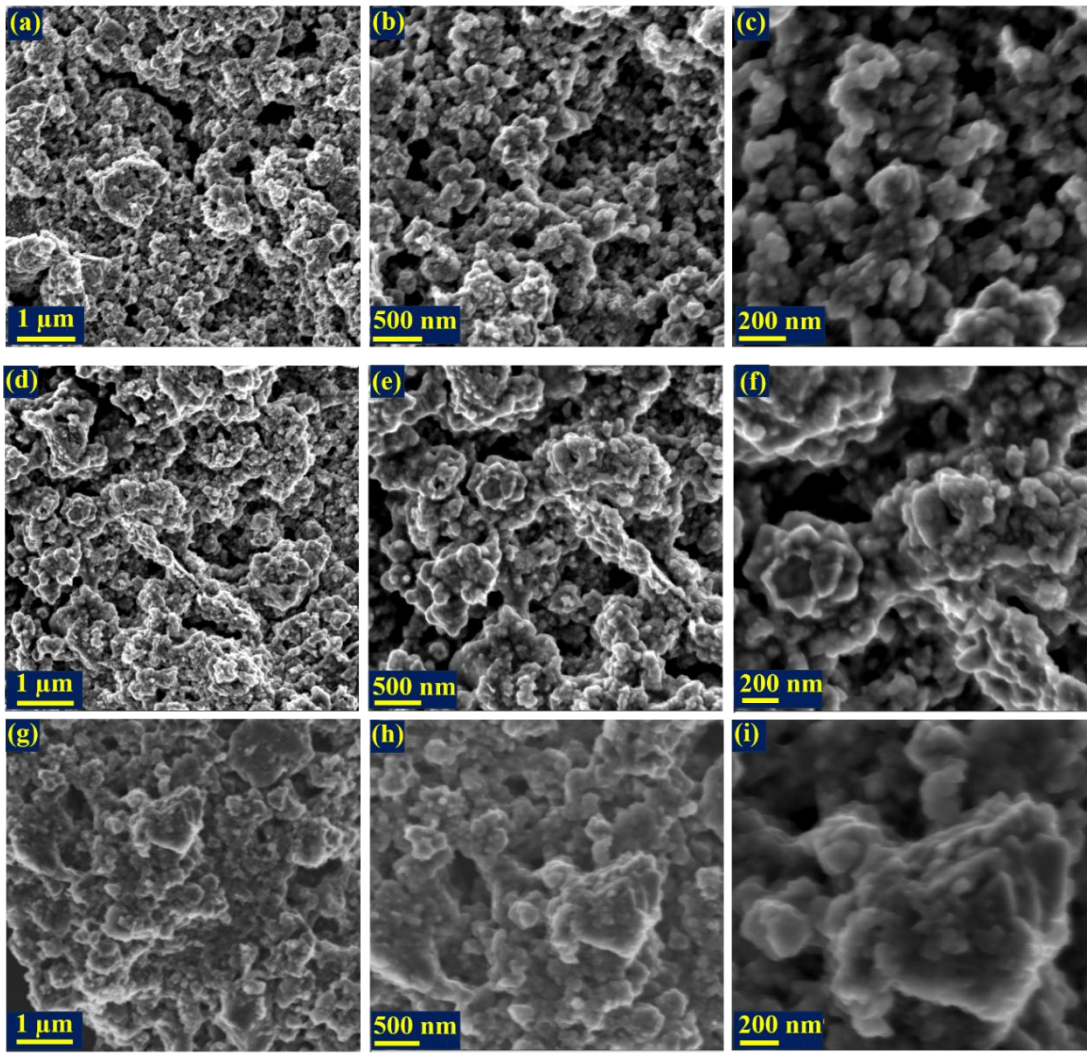

Figure 6.3: FESEM images of Ru-$NiSe_2$@48h (a-c), Ru-$NiSe_2$@24h (d-f) and Ru-$NiSe_2$@72h (g-i) at different scales.

suggesting that a large number of defects gets formed in the $NiSe_2$ phase following the integration of Ru into the host lattice.[17] The discontinuous fringes observed in $NiSe_2$ regions indicate defect generation upon Ru insertion, which can further enhance catalytic activity by facilitating ion diffusion and active site exposure. The SAED (Selected Area Electron Dispersion) pattern shown in **Figure 6.8e** further confirmed the crystalline nature of the sample. X-ray photoelectron spectroscopy (XPS) was used to probe the oxidation states and surface chemical environment of Ru-$NiSe_2$@48h. The survey spectrum **(Figure 6.9)** confirmed the presence of Ni, Ru, Se, C, N, and minor surface

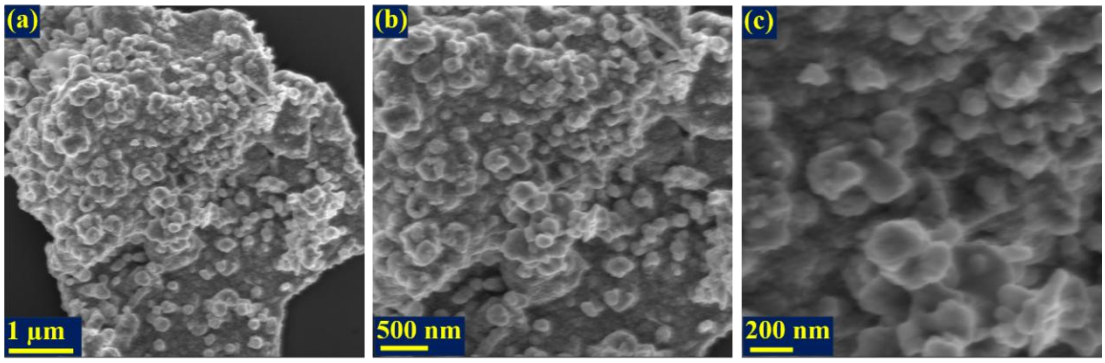

Figure 6.4: FESEM images of $NiSe_2$@48h at different scales (a-c).

oxygen species. The existence of oxygen peak is due to the surface oxidation of the Ru-$NiSe_2$@48h sample or inevitable oxygen species after exposure to air. **Figure 6.10a** shows that the Ni 2p spectrum at the core level is deconvoluted into four peaks. The peaks present at the binding energy of 855.5 eV and 873.3 eV are assigned to the Ni^{2+} $2p_{3/2}$ and Ni^{2+} $2p_{1/2}$ respectively.[27] Conversely, the peaks at 860.7 and 879 eV are the two satellite peaks. This confirms the presence of Ni in the +2 oxidation state. The core level Ru 3p spectrum **(Figure 6.10b)** shows the presence of four peaks.[28] The two peaks at 461.6 and 483.9 eV were ascribed to the $3p_{3/2}$ and $3p_{1/2}$ of the metallic Ru.[17] Similarly,

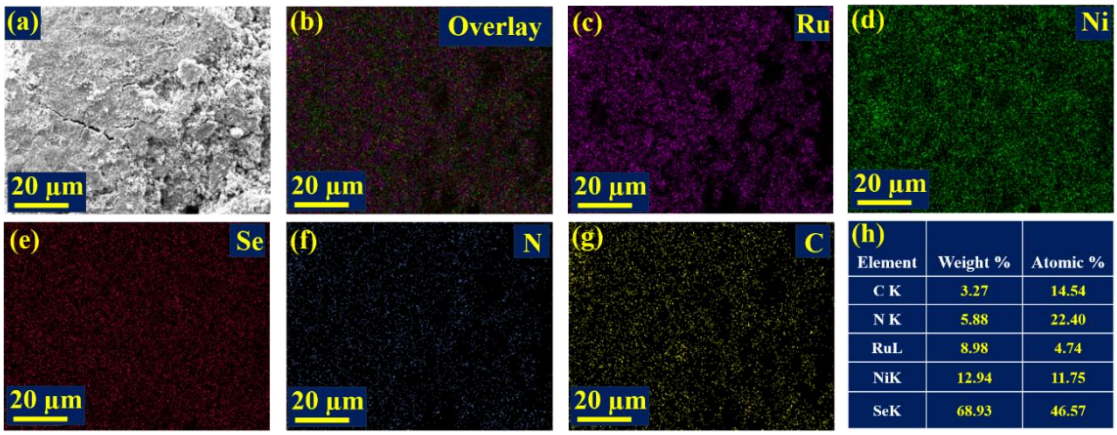

Figure 6.5: FESEM image (a), overlay (b), elemental mapping (c-g) and weight and atomic percentage of elements (h) in Ru-$NiSe_2$@48h.

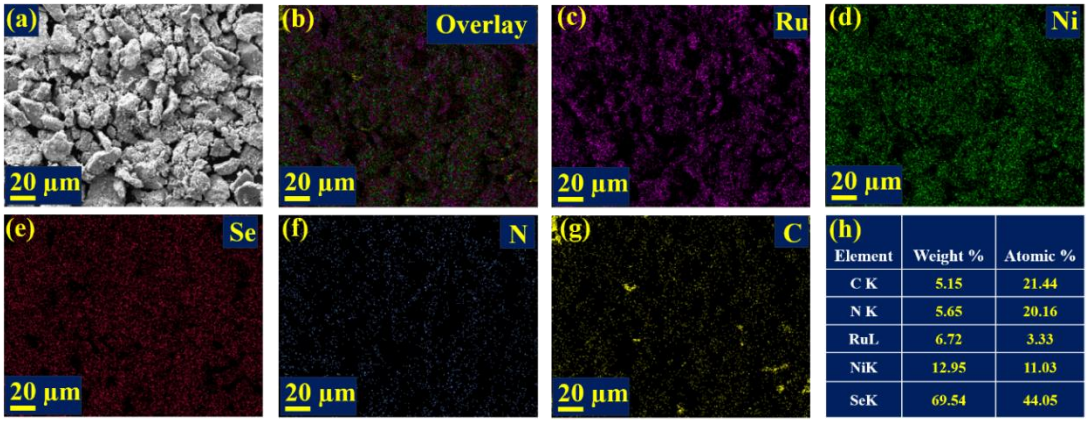

Figure 6.6: FESEM image (a), overlay (b), elemental mapping (c-g) and weight and atomic percentage of elements (h) in Ru-$NiSe_2$@24h.

the other two peaks at 463.1 and 485.4 eV were assigned to the $3p_{3/2}$ and $3p_{1/2}$ of the Ru^{3+}.[29] The Ru 3d spectrum **(Figure 6.10c)** reveals the presence of two peaks at 280.5 and 284.6 eV which corresponds to the $3d_{5/2}$ and $3d_{3/2}$ of metallic Ru respectively.[30] The aforementioned findings show that Ru is present in the Ru-$NiSe_2$@48h catalyst in both Ru^0 and Ru^{3+} states, with Ru^{3+} content being comparatively low in relation to Ru^0. **(Figure 6.10d)** shows the Se 3d spectrum with peaks at 54.7 and 55.5 eV are indexed to Se_2^{2-} in Ni–Se bonds.[1,3,27] Specifically, the two peak's binding energy difference is nearly

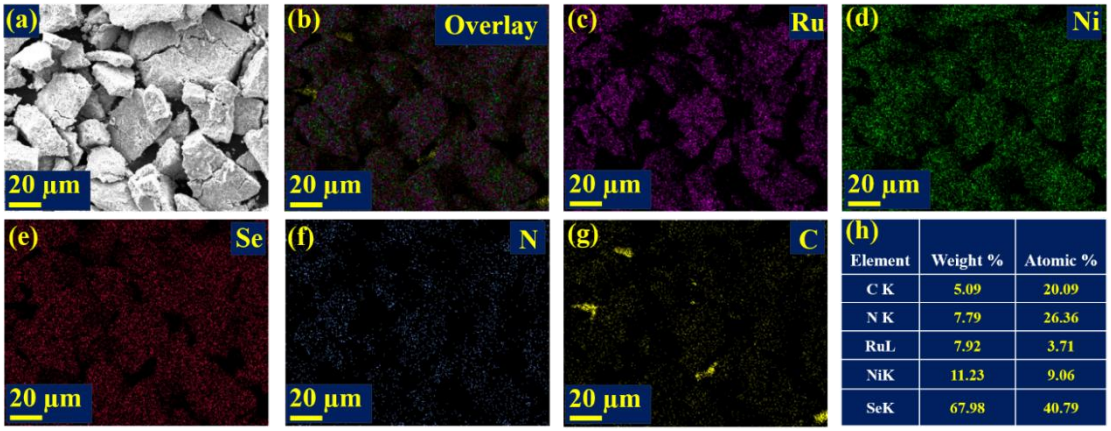

Figure 6.7: FESEM image (a), overlay (b), elemental mapping (c-g) and weight and atomic percentage of elements (h) in Ru-$NiSe_2$@72h.

0.8 eV, which is in accordance with the standard outcome. This reveals the formation of only one metal–selenide bond.[17] Further, the existence of oxidative selenium species is indicated by the presence of a distinct peak at 58.7 eV.[1,3,27] When selenides are exposed to air, they readily oxidize. This leads to the simultaneous transfer of partial electrons from Se to O and minimizes the electron-electron repulsion between Se and Ni. This will optimise the distribution of the localised π-symmetry electrons among Se and Ni at the interface and hence the adsorption/desorption process during the catalytic reactions. The strong electronic interaction between Ru and $NiSe_2$ causes a redistribution of charges at the interface and the synergistic impact between Ru and $NiSe_2$ further boosts the electrocatalytic activity of the catalyst.[17] The coexistence of Ru^0 and Ru^{3+} facilitates redox flexibility, enhancing H* adsorption and reaction kinetics during HER. These results confirm that Ru incorporation alters the electronic environment of $NiSe_2$, optimizing charge redistribution at the interface and improving intrinsic catalytic activity.. Furthermore, to determine the specific surface area of the synthesised materials, we carried out a BET measurement. Figure S9 reveals the adsorption-desorption plot for Ru-$NiSe_2$@24h, Ru-$NiSe_2$@48h and Ru-$NiSe_2$@72h. **Figure 6.11** clearly reveals that

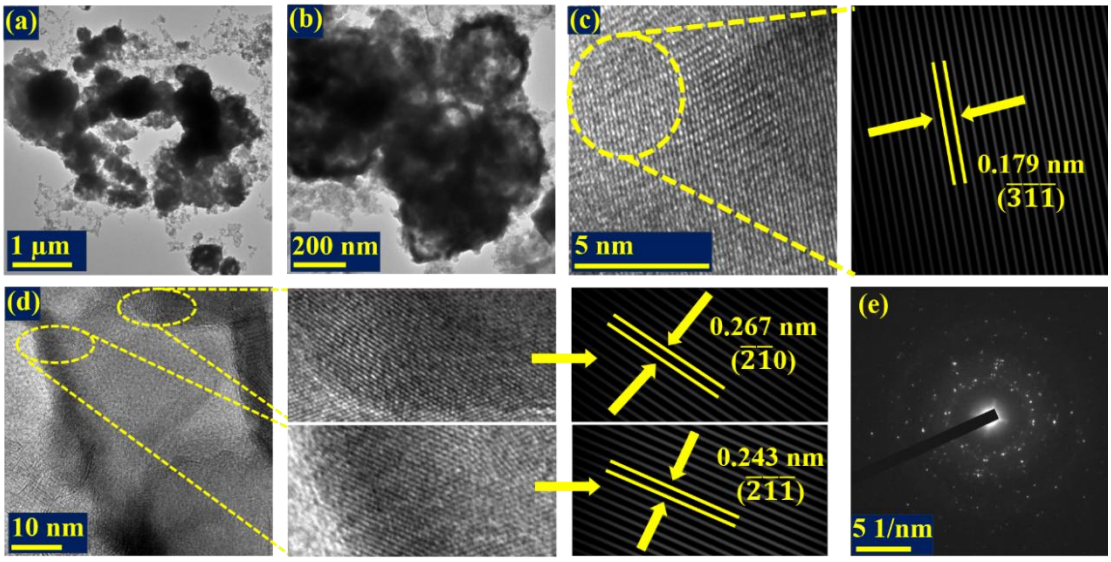

Figure 6.8: TEM images (a, b), HRTEM images (c, d) and SAED (e) of Ru-$NiSe_2$@48h.

the surface area was found to be highest for Ru-$NiSe_2$@48h (65.6 m^2 g^{-1}) compared to Ru-$NiSe_2$@24h (54.1 m^2 g^{-1}) and Ru-$NiSe_2$@72h (37 m^2 g^{-1}). It has been found that optimising the reaction time plays a significant role in providing a high surface area, which can ultimately enhance the electrocatalytic performances of Ru-$NiSe_2$@48h toward HER.

After the systematic characterisation, the electrochemical performance of all the synthesised materials were studied. Additionally, the activity of the electrocatalysts was assessed in relation to that of the state-of-the-art catalyst Pt/C for water reduction in an alkaline medium of 1 M KOH in order to compare their performance. **Figure 6.12a** shows the LSV curves of the Pt/C, $NiSe_2$@48h, NiRu-PBA and derived Ru-$NiSe_2$@T products synthesized by time variation. . All the LSVs are iR compensated. The LSV plot clearly reveals that the Ru-$NiSe_2$@48h displayed the lowest overpotential of 84 mV to achieve 10 mA cm^{-2} current density, outperforming Ru-$NiSe_2$@24h (97 mV), Ru-$NiSe_2$@72h (125 mV), $NiSe_2$@48h (330 mV), and NiRu-PBA (749 mV). The performance was also compared to that of the benchmark catalyst Pt/C which shows an overpotential of 64 mV to produce the benchmark current density. Remarkably, Ru-

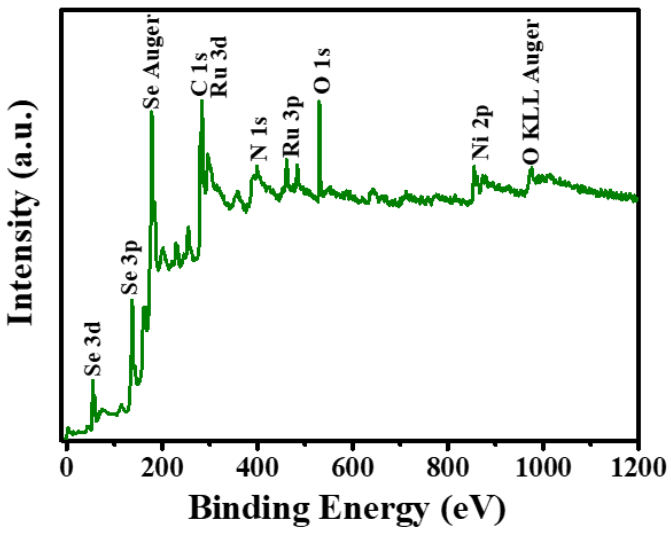

Figure 6.9: XPS full survey spectrum of Ru-$NiSe_2$@48h.

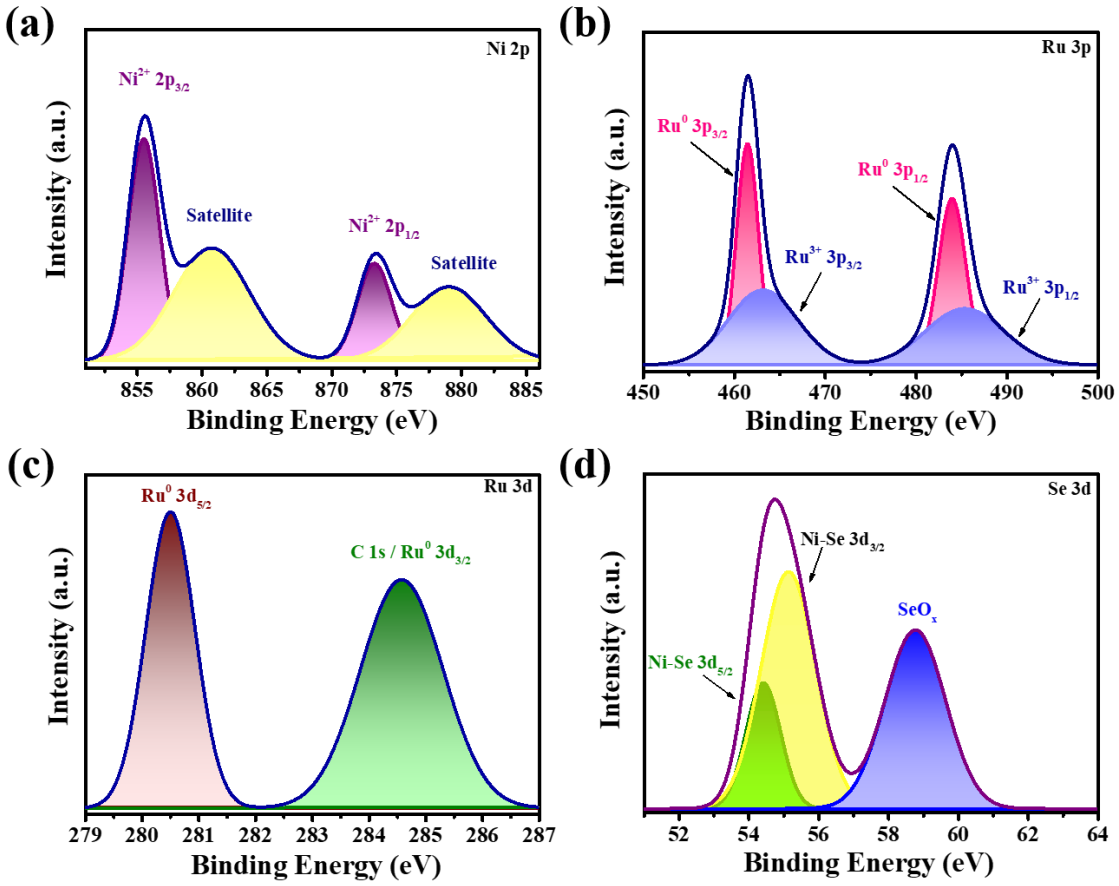

Figure 6.10: XPS spectrum for Ni 2p (a), Ru 3p (b), Ru 3d (c) and Se 3d (d) of Ru-$NiSe_2$@48h.

$NiSe_2$@48h sustained current densities up to 300 mA cm^{-2} under identical conditions, highlighting its superior catalytic efficiency. The optimized reaction time (48 h) proved critical for achieving balanced crystallinity, morphology, and defect concentration. **Figure 6.12b** shows the overpotential comparison of all the Ru-$NiSe_2$@T products, NiRu-PBA, $NiSe_2$@48h and Pt/C. A comparison of the Ru-$NiSe_2$@48h catalyst with other extremely effective electrocatalysts is displayed in **Table 6.1**. Each sample's Tafel slope was evaluated, which corresponds to the electrocatalyst's kinetics at the interface. The reaction kinetics of an active electrocatalyst for the generation of H_2 are faster when the Tafel slope value is smaller. The Tafel slope obtained after fitting the linear region of the plot between log of current density vs overpotential was found to be 106, 89, 116,

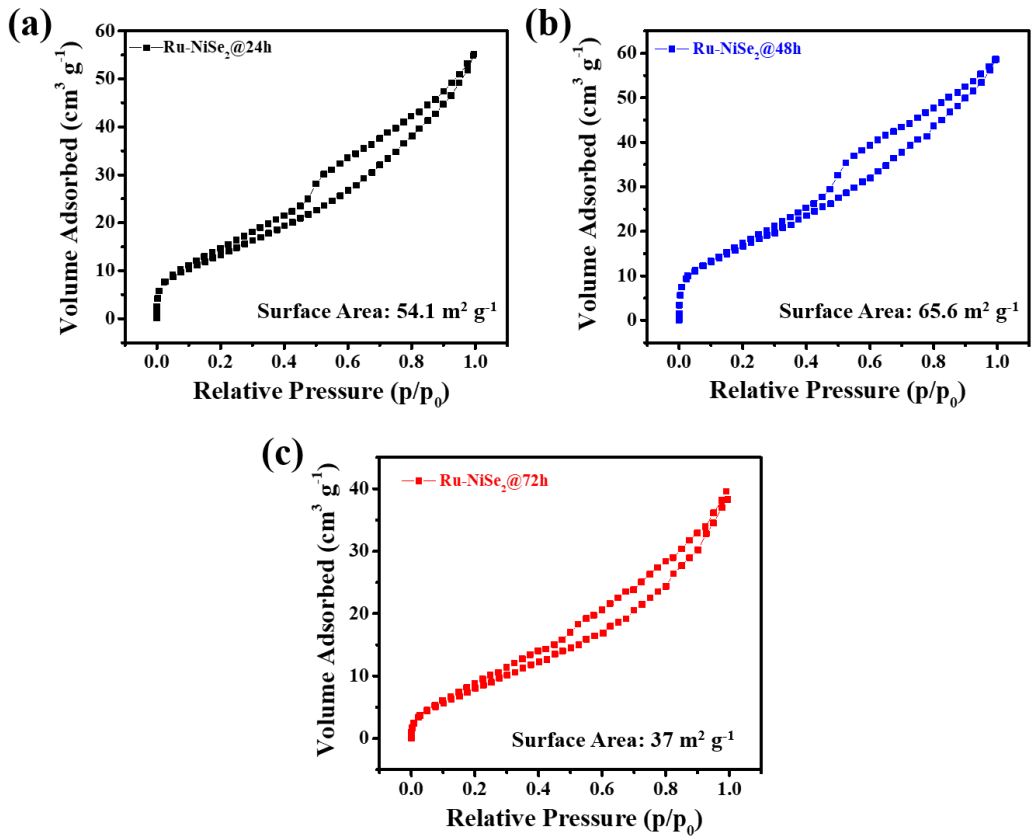

Figure 6.11: Nitrogen adsorption desorption isotherm for (a) Ru-$NiSe_2$@24h, (b) Ru-$NiSe_2$@48h, (c) Ru-$NiSe_2$@72h.

143, 109 and 48 mV dec^{-1} for Ru-$NiSe_2$@24h, Ru-$NiSe_2$@48h, Ru-$NiSe_2$@72h, $NiSe_2$@48h, NiRu-PBA and Pt/C respectively **(Figure 6.12c)**. The lower Tafel slope value for Ru-$NiSe_2$@48h indicates towards its faster reaction kinetics for H_2 evolution in comparison to other synthesised materials. In the alkaline media, two pathways: Volmer-Heyrovsky and Volmer-Tafel have been proposed to explain the HER mechanism. In an alkaline medium, H_2 gas evolution takes place in the successive processes listed below:[31–33]

The Volmer step: $H_2O + e^- \longrightarrow H_{ad} + OH^-$

The Heyrovsky step: $H_2O + H_{ad} + e^- \longrightarrow H_2 + OH^-$

Or, the Tafel step: $H_{ad} + H_{ad} \longrightarrow H_2$

Here H_{ad} is the adsorbed H on the catalyst's surface. 30, 40 and 120 mV dec^{-1} Tafel slope values corresponds to the Tafel, Heyrovsky and Volmer step as the rate determining step.[17,34] The obtained Tafel slope value for Ru-$NiSe_2$@48h is 89 mV dec^{-1}. This suggests that the rate determining step is the Volmer step and the catalyst follows the Volmer-

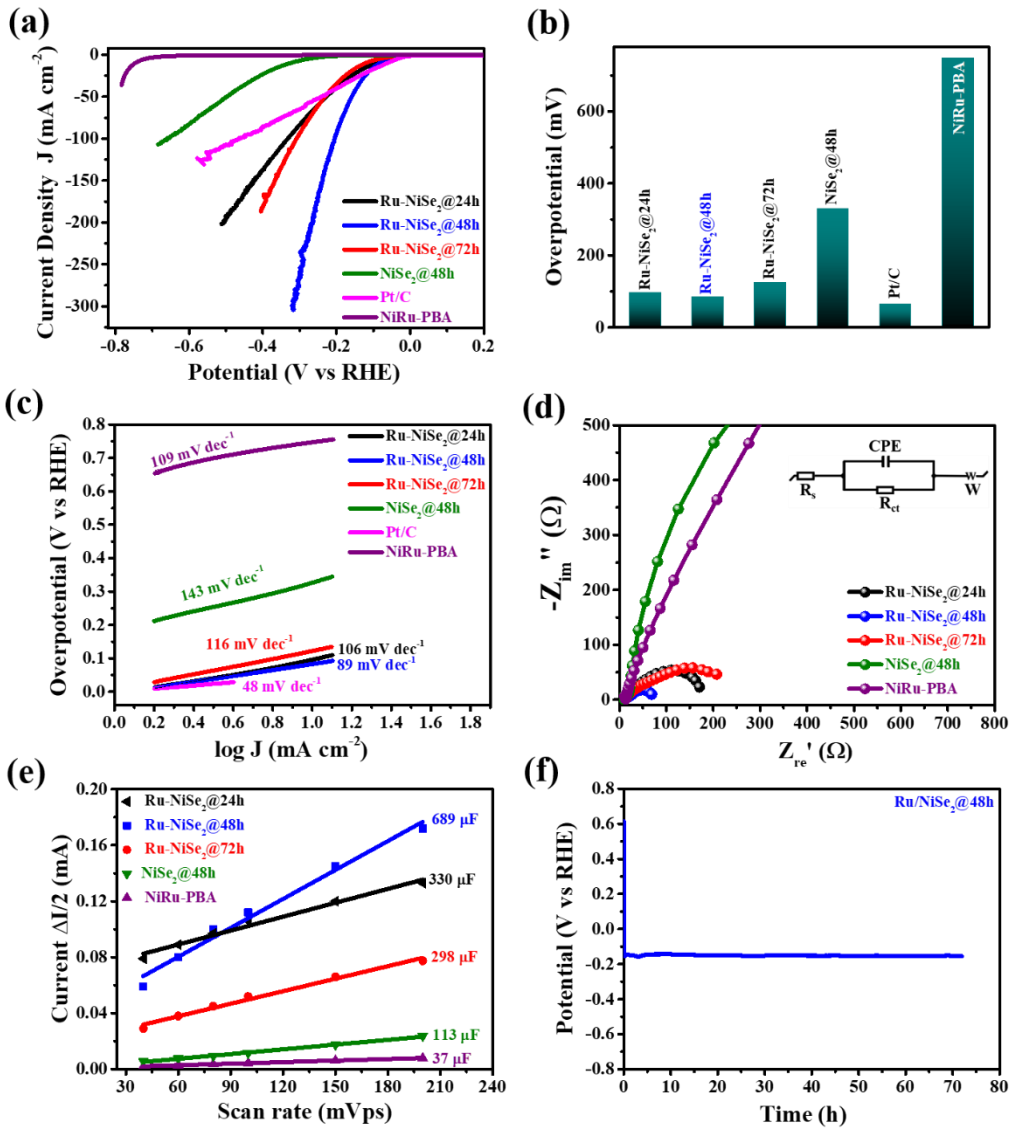

Figure 6.12: LSVs (a), bar graph for overpotential comparison (b) and Tafel slopes (c) of NiRu-PBA, $NiSe_2$@48h, Ru-$NiSe_2$@T products, and Pt/C. PEIS comparison (d) and estimated double-layer capacitance of NiRu-PBA, $NiSe_2$@48h and Ru-$NiSe_2$@T products (e). Chronopotentiometry test of Ru-$NiSe_2$@48h in an alkaline solution (1 M KOH) (f).

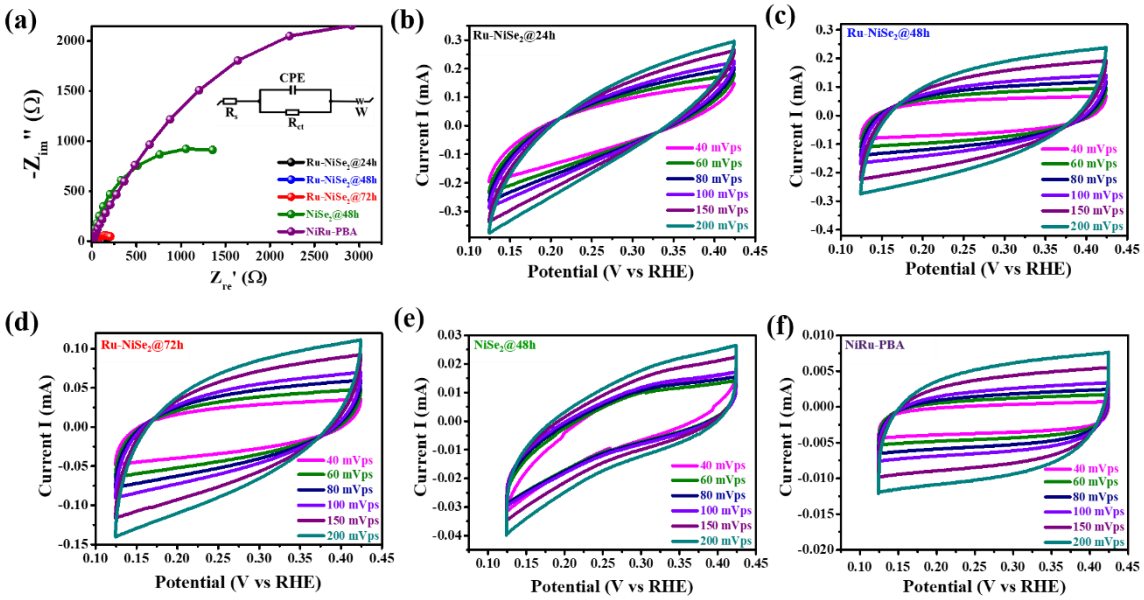

Figure 6.13: PEIS comparison of NiRu-PBA, $NiSe_2$@48h and Ru-$NiSe_2$@T products (a). CV curves of Ru-$NiSe_2$@24h (b), Ru-$NiSe_2$@48h (c), Ru-$NiSe_2$@72h (d), $NiSe_2$@48h (e) and NiRu-PBA (f).

Heyrovsky pathway for the H_2 production. EIS or Nyquist plot was applied to evaluate the charge transfer kinetics of the as-prepared HER active electrocatalysts.[35] EIS data were obtained by supplying an AC amplitude of 5 mV in a frequency region of 1 MHz to 0.1 Hz at a potential of 0.141V vs RHE for all the compared samples. **Figure 6.12d** makes it clear that all of the Ru-$NiSe_2$@T, $NiSe_2$@48h and NiRu-PBA samples had comparatively similar solution resistance (R_s) at the high frequency area. R_s is a combination of contact resistance, electrolyte resistance, and intrinsic resistance of all the utilised electrodes. Smaller diameter of the semicircle indicates towards the lower value of the charge transfer resistance (R_{ct}) leading towards the faster transfer of electrons at the electrode-electrolyte interface.[36] It is evident from **Figure 6.12d** that Ru-$NiSe_2$@24h, Ru-$NiSe_2$@48h and Ru-$NiSe_2$@72h displays a R_{ct} of 170, 57 and 218 Ω respectively. **Figure 6.13a** reveals that $NiSe_2$@48h and NiRu-PBA possess higher value of R_{ct} in comparison to all the synthesised materials. Lower R_{ct} value of Ru-$NiSe_2$@48h

indicates towards its better charge transfer ability and electrocatalytic performance as compared to the other time-varied synthesised materials. A modified Randles equivalent circuit comprising solution resistance (R_s), charge transfer resistance (R_{ct}), a Warburg diffusion element (W), and a constant phase element (CPE) that accounts for non-ideal double-layer capacitance was used to fit the impedance spectra. During electrocatalysis, coupled charge transfer and mass transport processes are confirmed by the appearance of a depressed semicircle followed by a low-frequency diffusion tail. By using electrochemical active surface area (ECSA) measurements, the enhanced catalytic behaviour of the Ru-$NiSe_2$@48h electrocatalyst was further illustrated. The electrochemically accessible surface area (ECSA) of the synthesized materials was measured in order to further analyse their electrocatalytic activity. Conversely, ECSA is used to determine the accessible units of electrochemical active sites and is directly correlated with the double layer capacitance (C_{dl}) of electrocatalyst.[37,38] The ECSA is calculated by using the following equation:

$$ECSA=C_{dl}/C_s$$

Here C_{dl} represents the double layer capacitance and C_s represents the specific capacitance of the atomically smooth surface of metal nanoparticles. In an alkaline electrolyte the C_s value is 40 μF cm^{-2}.[39] The C_{dl} value in the non-Faradaic region was ascertained using a conventional cyclic voltammetry (CV) technique. In **Figure 6.13b-f**, the CV curves for Ru-$NiSe_2$@24h, Ru-$NiSe_2$@48h, Ru-$NiSe_2$@72h, $NiSe_2$@48h, and NiRu-PBA are presented. In order to calculate the C_{dl} values, the slopes were determined by plotting the different scan rates against the half of the difference of the anodic current and cathodic current (i.e. $\Delta I = I_a - I_c$) at 0.274 V vs RHE. The C_{dl} value obtained are 330, 689, 298, 113, and 37 μF for Ru-$NiSe_2$@24h, Ru-$NiSe_2$@48h, Ru-$NiSe_2$@72h, bare-$NiSe_2$@2D, and NiRu-PBA respectively **(Figure 6.12e)**. In terms of the accessible

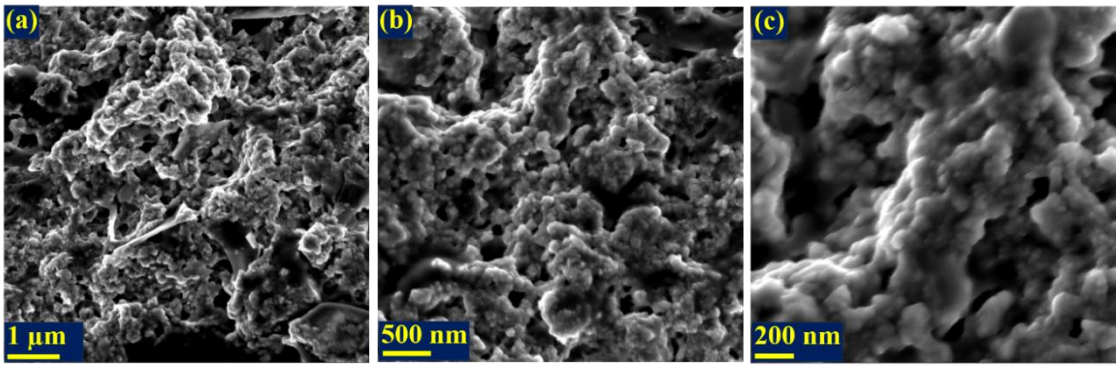

Figure 6.14: FESEM images of post-catalytic Ru-$NiSe_2$@48h at different scales (a-c).

surface area and number of electrochemical active sites for the envisioned reaction to occur, Ru-$NiSe_2$@48h performed better than the other time-varying electrocatalysts, such as Ru-$NiSe_2$@24h and Ru-$NiSe_2$@72h, as well as the other materials i.e. $NiSe_2$@48h and NiRu-PBA. The stability of the electrocatalyst in the alkaline condition is one of the most crucial aspects of its practical use. The electrochemical stability of the catalyst is confirmed by chronopotentiometry after a comprehensive analysis of the HER activity. **Figure 6.12f** displays the stability of Ru-$NiSe_2$@48h over a 72-hour period in an alkaline medium. After 72 hours of prolonged electrolysis, there was a slight decrease in the electrocatalyst's performance. The loss of electrocatalyst from the electrode surface may be the cause of the little increase in the overpotential. This might be due to the mechanical force involved in the gas bubble's rupturing, which further supports its dynamic electrochemical stability. Further, the concentration of hydrogen gas produced by the catalyst Ru-$NiSe_2$@48h was examined by gas chromatography after running the chronopotentiometry experiment for 30 minutes at a current density of 10 mA cm^{-2} which was found out to be 2568 ppm. The exceptional performance of the Ru-$NiSe_2$@48h in comparison to the other time varied Ru-$NiSe_2$@24h and Ru-$NiSe_2$@72h materials can be attributed to the optimised morphology of the Ru-$NiSe_2$@48h. The uniform distribution of small granules like particles provides larger surface area as well as larger

number of electroactive sites for the HER reaction to take place. This is evident from the high C_{dl} value of Ru-$NiSe_2$@48h **(Figure 6.12e).** Also, the lower R_{ct} value of Ru-$NiSe_2$@48h suggest it's faster charge transfer ability at the electrode-electrolyte interface which ultimately enhances the hydrogen evolution process. As illustrated in **Figure 6.12a-e** longer or shorter reaction times of 24 and 72 h respectively are unfavourable to the catalytic activities, at the reaction time of 48 hours, the prepared sample possesses the best catalytic activity. Again, the performance of Ru-$NiSe_2$@48h is exceptionally better when compared to $NiSe_2$@48h. The insertion of Ru into the $NiSe_2$ lattice modifies its electronic structure and optimises the intermediate adsorption energies which ultimately enhances the catalytic activity. Also, the crystallinity of Ru-$NiSe_2$@48h **(Figure 6.1b)** was observed to be low in comparison to $NiSe_2$@48h **(Figure 6.1c)** which is due to the incorporation of Ru into the $NiSe_2$. The HRTEM image **(Figure 6.8d)**

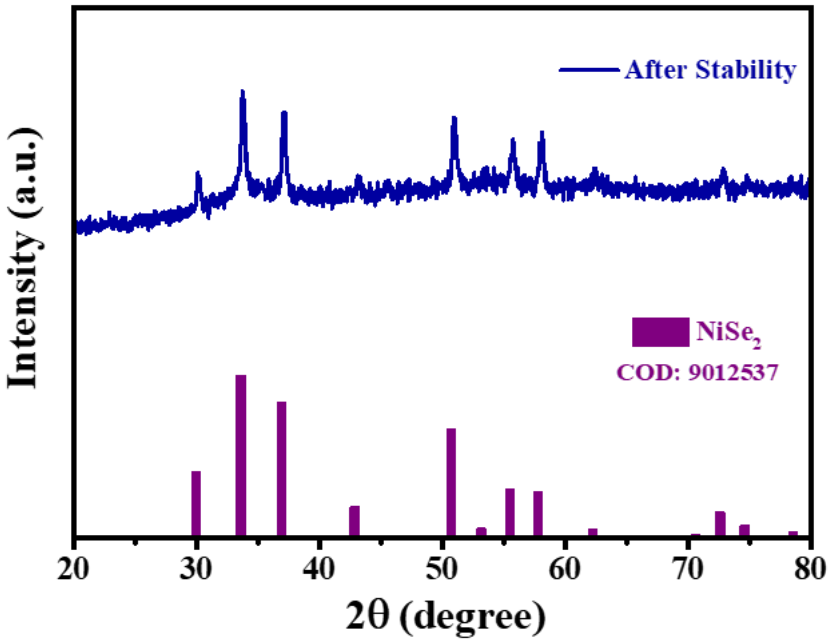

Figure 6.15: PXRD pattern of Ru-$NiSe_2$@48h after stability test.

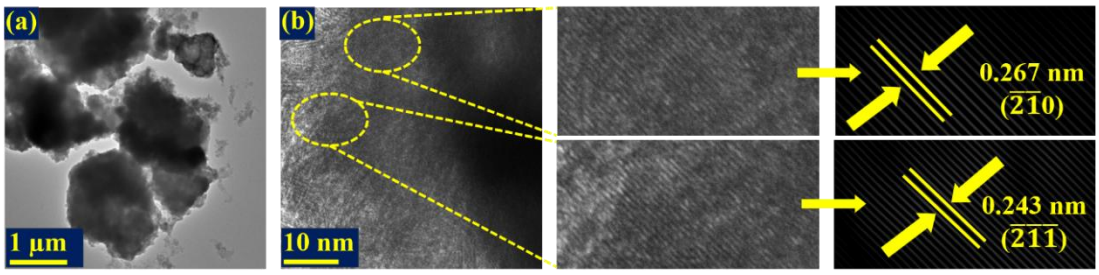

Figure 6.16: TEM (a) and HRTEM (b) image of post-catalytic Ru-$NiSe_2$@48h.

demonstrates the discontinuous and partially absent lattice fringes of the $NiSe_2$ phase. This suggests that a large number of defects are being generated in the host lattice $NiSe_2$ as a result of Ru incorporation. This is crucial for boosting mass transport and number of active sites in electrochemical hydrogen evolution process. The FESEM image **(Figure 6.4a-c)** reveals bigger size and highly agglomerated particles for $NiSe_2$@48h when compared to Ru-$NiSe_2$@48h. This leads towards lower number of electroactive site and lesser exposure of surface area for the required reactions to occur which is also evident from the lower C_{dl} value of $NiSe_2$@48h **(Figure 6.12e)**. Also, the presence of carbon and nitrogen in Ru-$NiSe_2$@48h was confirmed from **Figures 6.5** and **6.9** which enhances the electronic conductivity and provides stability to the material during the long-term

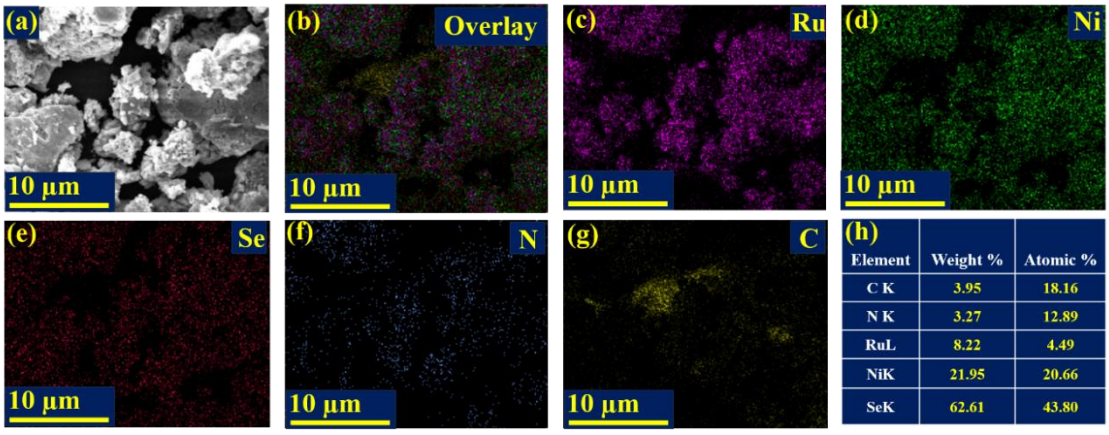

Figure 6.17: FESEM image (a), overlay (b), elemental mapping (c-g) and weight and atomic percentage of elements (h) in post-catalytic Ru-$NiSe_2$@48h.

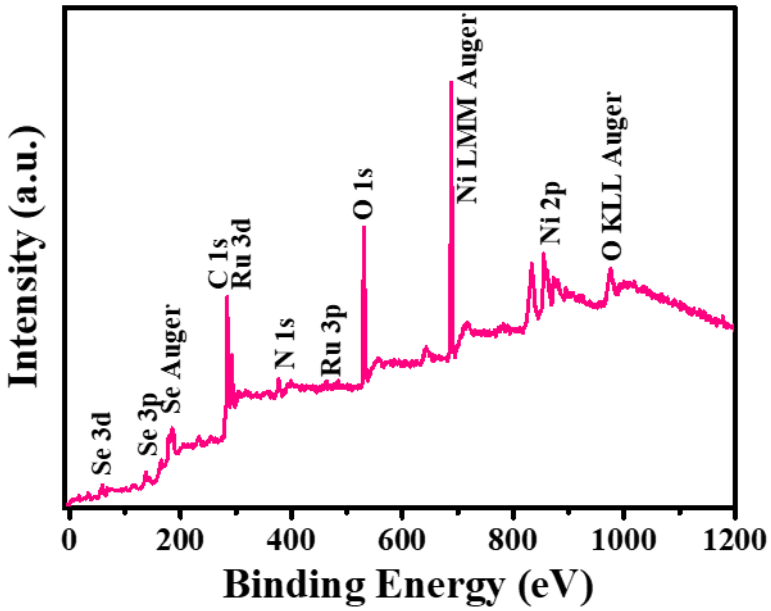

Figure 6.18: XPS full survey spectrum of post-catalytic Ru-$NiSe_2$@48h.

electrolysis from corrosion. The absence of C and N in $NiSe_2$@48h results in the poor conductivity and eventually the performance of $NiSe_2$@48h. Additionally, the higher Tafel slope and R_{ct} value confirms the slower kinetics and smaller charge transfer ability respectively of the $NiSe_2$@48h. All the aforementioned facts support the poor performance of $NiSe_2$@48h.

Furthermore, to investigate any structural or phase changes of the catalyst after catalysis, FESEM and powder X-ray diffraction **(Figure 6.14a-c** and **6.15)** were utilized. Very little particle agglomeration was visible in the FESEM pictures as a result of the prolonged electrolysis. The distinctive peaks of Ru-$NiSe_2$@48h catalyst post electrolysis are weakened and broadened after the HER stability test, indicating that the crystallinity of the catalyst is reduced. TEM image **(Figure 6.16a)** of the post-catalytic sample was found in accordance with the FESEM images. Lattice fringes were observed in the HRTEM **(Figure 6.16b)** image. The d-spacing values of 0.267 and 0.243 nm were

ascribed to the $(\bar{2}\bar{1}0)$ and $(\bar{2}\bar{1}\bar{1})$ planes of $NiSe_2$. In the EDX analysis **Figure 6.17a** reveals the FESEM image and **Figure 6.17b-h** reveals the uniform distribution of Ru, Ni, Se, C and N along with the atomic and weight percentages in the post-catalytic Ru-$NiSe_2$@48h material. XPS survey spectrum **(Figure 6.18)** confirmed the existence of Ni, Se, Ru, C and N elements in the post catalytic Ru-$NiSe_2$@48h. No significant changes in the peak positions were observed for all the four peaks in the Ni 2p core level spectrum **(Figure 6.19a)**. In Ru 3p spectrum **(Figure 6.19b)** Ru $3p_{3/2}$ and Ru $3p_{1/2}$ peaks were observed for metallic Ru only. This suggests that the Ru^{3+} are converted into the Ru^0 during the long-term electrolysis process. In the Ru 3d spectrum **(Figure 6.19c)** the peak position for Ru $3d_{5/2}$ and Ru $3d_{3/2}$ were observed to remain unchanged. Further, no

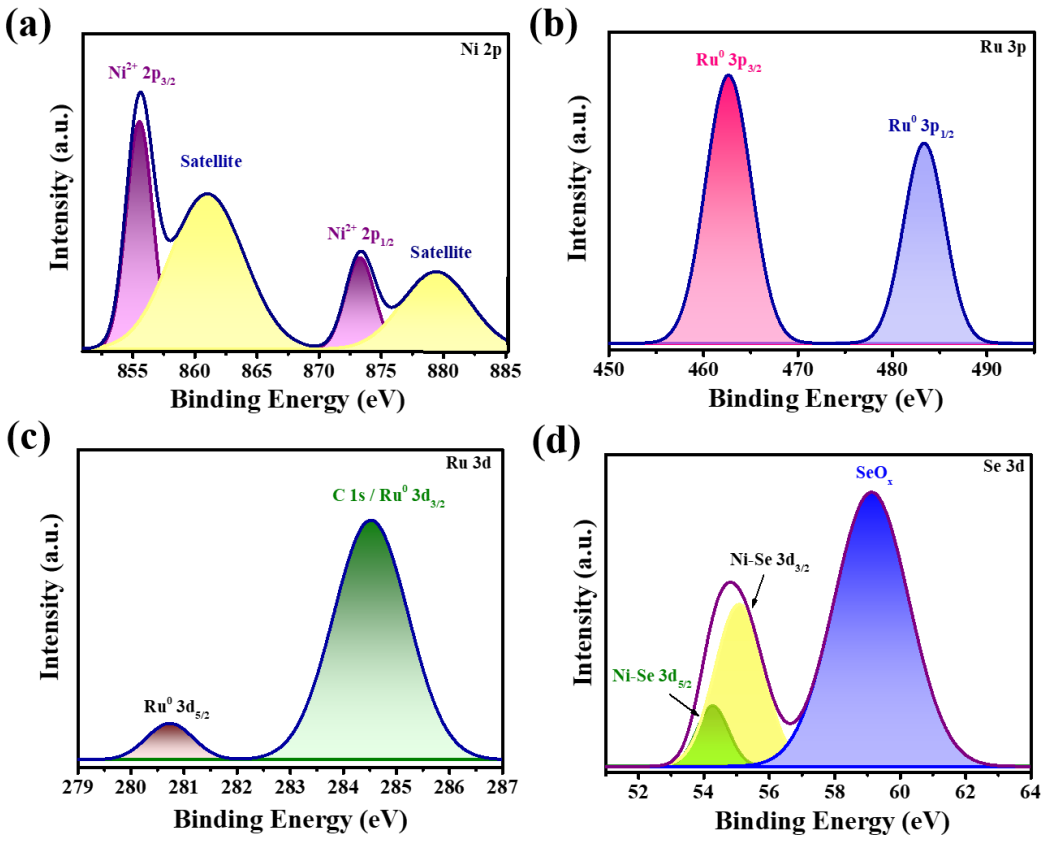

Figure 6.19: XPS spectrum for Ni 2p (a), Ru 3p (b), Ru 3d (c) and Se 3d (d) of post-catalytic Ru-$NiSe_2$@48h

noticeable changes in the peak position were observed in Se 3d XPS spectrum **(Figure 6.19d)**. This indicates Ru-$NiSe_2$@48h resilience as an electrocatalyst for HER. This implies that the Ru-$NiSe_2$@48h is stable in an alkaline environment.

The following elements are responsible for the as-synthesised electrocatalyst's exceptional catalytic activity and durability. Firstly, the synergistic effect of both metal ions is responsible for the enhanced electrocatalytic efficacy in Ru-$NiSe_2$@48h, which would prudently regulate the electronic properties and optimise free energy during the HER process.[16] Secondly, the insertion of Ru into the $NiSe_2$ lattice led to a decrease in the crystallinity of $NiSe_2$ which favoured formation of defects which are helpful for enhancing the electrochemical performance of the catalyst. Thirdly, the homogeneous distribution of the nanogranules-like particles across the surface also contributed significantly, exposing a large number of electrochemically active sites and increasing the electrochemically active surface area, which allows the appropriate electrolyte diffusion and shortens the electron transfer path for the smooth progression of HER. Fourth, the NiRu-PBA played an important role by providing uniformly distribution of Ru incorporated $NiSe_2$ (Ru-$NiSe_2$@48h) throughout the surface. Fifth, the Ru incorporation helps in maintaining the long-term stability of the electrocatalyst by avoiding the material from getting agglomerated or corroded in the alkaline environment. Additionally, the presence of carbon and nitrogen in the material facilitates the electronic conductivity which led to the better performance and stability of Ru-$NiSe_2$@48h during the long-term electrolysis. The aforementioned systematic characterisation and findings suggest that transition metal schalcogenide combined with noble metal particles can provide highly HER active surfaces, opening up an intriguing avenue for the development of effective and commercially feasible HER electrocatalysts.

Table 6.1 Comparison of various electrocatalysts for HER in 1.0 M KOH and 0.5 M H_2SO_4 electrolyte.

Sl. No.	Electrocatalysts	Overpotential at 10 $mAcm^{-2}$ (mV)	Tafel Slope ($mVdec^{-1}$)	Electrolyte	Reference
1	**Ru-$NiSe_2$@48h**	**107**	**108**	**1 M KOH**	**This work**
2	Ru, $WeNiSe_2$/NF	100	119.7	1 M KOH	40
3	$Zn_{0.1}Co_{0.3}Ni_{0.6}Se_2$	121	35.3	0.5 M H_2SO_4	16
4	Ru-Ni_3Se_2	24	45	1 M KOH	17
5	NiFeSe/CFP	186	52	1 M KOH	41
6	RuO_2-Fe_2O_3	148	43	1 M KOH	42
7	Ru-NiFe LDH-F/NF	115.6	125.1	1 M KOH	43
8	V-Ni_3Se_2/NF	191	83	1 M KOH	44
9	Ni_3S_2@NGCLs/NF	134	84	1 M KOH	45
10	Ni_3S_2-NiOx/NF	104	64	1 M KOH	46
11	MoS_2/Ni_3S_2@CA	96	61	1 M KOH	47

6.7 Conclusions

In summary, a series of Ru-incorporated $NiSe_2$ nanogranular electrocatalysts (Ru-$NiSe_2$@T, T = 24, 48, and 72 h) were successfully synthesized via a hydrothermal approach using NiRu-PBA as a bimetallic precursor. The optimized Ru-$NiSe_2$@48h catalyst exhibits remarkable HER activity in alkaline media, requiring only 84 mV to

achieve 10 mA cm^{-2} with a Tafel slope of 89 mV dec^{-1} and a low R_{ct} of 57 Ω. The catalyst maintained excellent durability over 72 h of continuous electrolysis with minimal structural degradation. The enhanced catalytic performance originates from Ru-induced electronic modulation, structural defect generation, and increased surface area, which together accelerate water dissociation and hydrogen evolution. This study demonstrates that rationally designed Ru-incorporated $NiSe_2$ derived from Prussian Blue Analogues can serve as an efficient, durable, and scalable non-platinum catalyst for sustainable hydrogen production in alkaline environments.

6.8 References

1. H. Leng, Y. Shuai, P. He, S. Liu and Y. Liu, *Inorg. Chem.*, 2025, **64**, 13429–13437.
2. Y. Liu, X. Li, Q. Zhang, W. Li, Y. Xie, H. Liu, L. Shang, Z. Liu, Z. Chen, L. Gu, Z. Tang, T. Zhang and S. Lu, *Angew. Chem.*, 2020, **132**, 1735–1743.
3. A. Muthurasu, L. Natarajan, T. W. Kim, T. H. Ko, Y. J. Lee and H. Y. Kim, *ACS Appl. Mater. Interfaces*, 2025, **17**, 25237–25252.
4. Y. Xu, S. Yin, C. Li, K. Deng, H. Xue, X. Li, H. Wang and L. Wang, *J. Mater. Chem. A*, 2018, **6**, 1376–1381.
5. T. Kim, W. Lee, H. Choi, V. G. Parale, U. M. Patil, K. Kanamori, J. G. Seo, Y. S. Bae, S. W. Kim and H. H. Park, *Int. J. Energy Res.*, 2024, **2024,** 1.
6. Q. Hu, K. Gao, X. Wang, H. Zheng, J. Cao, L. Mi, Q. Huo, H. Yang, J. Liu and C. He, *Nat. Commun.*, 2022, **13**, 3958.
7. Y. Zhu, Q. Lin, Y. Zhong, H. A. Tahini, Z. Shao and H. Wang, *Energy Environ. Sci*. 2020, **13**, 3361–3392.
8. J. Xie, J. Zhang, S. Li, F. Grote, X. Zhang, H. Zhang, R. Wang, Y. Lei, B. Pan and Y. Xie, *J. Am. Chem. Soc.*, 2013, **135**, 17881–17888.

9. A. Muthurasu, B. Dahal, T. Mukhiya, K. Chhetri and H. Y. Kim, *ACS Appl. Mater. Interfaces*, 2020, **12**, 41704–41717.

10. R. Liu, M. Anjass, S. Greiner, S. Liu, D. Gao, J. Biskupek, U. Kaiser, G. Zhang and C. Streb, *Chem. - Eur. J.*, 2020, **26**, 4157–4164.

11. O. Rabi, E. Pervaiz, R. Zahra, M. Ali and M. B. K. Niazi, *Mol. Catal*., 2020, **494**, 111116.

12. A. Yuan, J. Du, Y. Zheng, H. Liu, H. Zhang, H. Li and L. Chen, *J. Colloid. Interface Sci.*, 2025, **684**, 243–250.

13. B. H. R. Suryanto, Y. Wang, R. K. Hocking, W. Adamson and C. Zhao, *Nat. Commun.*, 2019, **10**, 5599.

14. A. Muthurasu, T. H. Ko, T. W. Kim, K. Chhetri and H. Y. Kim, *Adv. Funct. Mater.*, 2024, **34**, 2404254.

15. S. Verma, L. Singh, A. Goyal, B. Singh and A. Draksharapu, *ACS Appl. Nano Mater.*, 2025, **8**, 13522–13531.

16. A. Kareem, H. Mohanty, K. Thenmozhi, S. Pitchaimuthu and S. Senthilkumar, *ACS Appl. Nano Mater.*, 2024, **7**, 4886–4894.

17. R. Li, L. Chen, H. Zhang, M. Humayun, J. Duan, X. Xu, Y. Fu, M. Bououdina and C. Wang, *Nanoscale*, 2023, **15**, 19604–19616.

18. N. Mahmood, Y. Yao, J. W. Zhang, L. Pan, X. Zhang and J. J. Zou, *Adv. Sci*., 2018, **5**, 1700464.

19. Z. W. She, J. Kibsgaard, C. F. Dickens, I. Chorkendorff, J. K. Nørskov and T. F. Jaramillo, *Science*. 2017, **355**, 6321.

20. Y. Feng, S. Zhang, L. Zhu, G. Li, N. Zhao, H. Zhang and B. H. Chen, *Int. J. Hydrogen Energy*, 2022, **47**, 39853–39863.

21. M. Wang, Z. Dang, M. Prato, U. Petralanda, I. Infante, D. V. Shinde, L. De Trizio and L. Manna, *ACS Appl. Nano Mater.*, 2019, **2**, 5695–5703.

22. M. Sadangi, C. Chakravarty, J. Bhattacharjee and J. N. Behera, *Dalton Trans.*, 2024, **53**, 16384–16396.

23. M. Sadangi and J. N. Behera, *ChemCatChem*, 2025, **17**, e202500178.

24. A. Sahu, M. Sadangi and J. N. Behera, *Sustain. Energy Fuels*, 2025, **9**, 2718–2728.

25. Y. Zhang, H. Guo, M. Song, L. Sun and R. Song, *J. Mater. Chem. A*, 2023, **11**, 3584–3593.

26. X. Luo, P. Ji, P. Wang, R. Cheng, D. Chen, C. Lin, J. Zhang, J. He, Z. Shi, N. Li, S. Xiao and S. Mu, *Adv. Energy Mater.*, 2020, **10**, 1903891.

27. H. H. Do, Q. Van Le, T. H. Lee, S. H. Hong, S. H. Ahn, H. W. Jang and S. Y. Kim, *Int. J. Energy Res.*, 2021, **45**, 20463–20473.

28. N. Sahu, J. K. Das and J. N. Behera, *Inorg. Chem.*, 2022, **61**, 2835–2845.

29. J. Su, Y. Yang, G. Xia, J. Chen, P. Jiang and Q. Chen, *Nat. Commun.*, 2017, **8**, 1–10.

30. K. Wang, B. Li, J. Ren, W. Chen, J. Cui, W. Wei and P. Qu, *Inorg. Chem. Front.*, 2022, **9**, 3885–3897.

31. Q. Lu, G. S. Hutchings, W. Yu, Y. Zhou, R. V. Forest, R. Tao, J. Rosen, B. T. Yonemoto, Z. Cao, H. Zheng, J. Q. Xiao, F. Jiao and J. G. Chen, *Nat. Commun.*, 2015, **6***,* 6567.

32. B. He, L. Chen, M. Jing, M. Zhou, Z. Hou and X. Chen, *Electrochim. Acta*, 2018, **283**, 357–365.

33. H. Jin, J. Wang, D. Su, Z. Wei, Z. Pang and Y. Wang, *J. Am. Chem. Soc.*, 2015, **137**, 2688–2694.

34. A. Loiacono, S. Díaz-Coello, G. García, G. I. Lacconi, J. Luis Rodriguez, E. Pastor and E. A. Franceschini, *J. Electroanal. Chem.,* 2024, **952***,* 117973.

35. K. Ao, J. Dong, C. Fan, D. Wang, Y. Cai, D. Li, F. Huang and Q. Wei, *ACS Sustain. Chem. Eng.*, 2018, **6**, 10952–10959.

36. A. K. Samantara, J. K. Das, S. Ratha, N. K. Jena, B. Chakraborty and J. N. Behera, *ACS Appl. Mater. Interfaces*, 2021, **13**, 35828–35836.

37. Z. Huang, J. Liu, Z. Xiao, H. Fu, W. Fan, B. Xu, B. Dong, D. Liu, F. Dai and D. Sun, *Nanoscale*, 2018, **10**, 22758–22765.

38. N. Sahu, J. K. Das and J. N. Behera, *Sustain. Energy Fuels*, 2021, **5**, 4992–5000.

39. P. Babar, A. Lokhande, H. H. Shin, B. Pawar, M. G. Gang, S. Pawar and J. H. Kim, *Small*, 2018, **14**, 1702568.

40. Y. Dang, G. Wang, X. Li, X. Ma, F. Yue, C. Wang, L. Gao and F. Fu, *Int J. Hydrogen Energy*, 2023, **48**, 17035–17044.

41. Y. Guo, Y. Liu, Y. Liu, C. Zhang, K. Jia, J. Su and K. Wang, *Catalysts*, 2022, **12**, 739.

42. H. Mosallaei, H. Hadadzadeh, A. Foelske, M. Sauer, H. Amiri Rudbari and O. Blacque, *Dalton Trans.*, 2022, **51**, 6314–6331.

43. Y. Wang, P. Zheng, M. Li, Y. Li, X. Zhang, J. Chen, X. Fang, Y. Liu, X. Yuan, X. Dai and H. Wang, *Nanoscale*, 2020, **12**, 9669–9679.

44. D. He, L. Cao, J. Huang, Y. Feng, G. Li, D. Yang, Q. Huang and L. Feng, *ACS Sustain. Chem. Eng.*, 2021, **9**, 12005–12016.

45. B. Li, Z. Li, Q. Pang and J. Z. Zhang, *Chemi. Eng. J.*, 2020, **401**, 126045.

46. Z. Huang, L. He, W. Zhang, W. Huang, Q. Mo, L. Yang, Q. Fu and Q. Gao, *J. Colloid. Interface Sci.*, 2022, **622**, 728–737.

47. B. Zhang, H. Luo, B. Ai, Q. Gou, J. Deng, J. Wang, Y. Zheng, J. Xiao and M. Li, *Small*, 2023, **19**, 2205431.

Chapter-7

Thesis Summary and Future Perspectives

By keeping an eye on the current state of the energy sector, the finite supply of fossil fuels, and the anticipated energy-related combat-like situation in the near future, the primary focus of the thesis is the requirement for the development of effective energy conversion materials that can produce H_2 in a pollution-free and economically viable manner. The conclusion of this thesis study is described below.

Ru-containing Prussian blue analogues have been used as precursors for developing a variety of electrocatalysts, such as alloy, composite, and chalcogenides based on Ru and transition metals. PBA and its derived materials have been synthesised using a variety of reaction procedures, such as coprecipitation, hydrothermal/solvothermal, annealing, and reduction techniques. A straightforward coprecipitation technique was used to synthesise RuCo-PBA and NiRu-PBA at room temperature. Ru-PBA was synthesised by using the hydrothermal method.

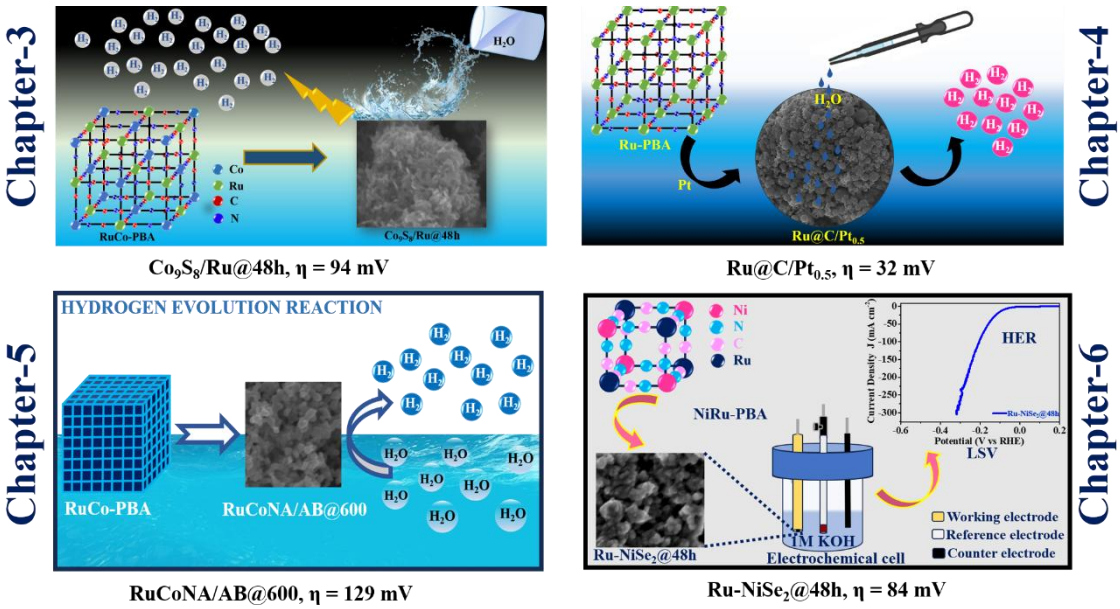

Figure 7.1: Pictorial representation of thesis summary.

The RuCo-PBA-derived Ru-doped Co_9S_8 nanosheets synthesised at a duration of 48 hours i.e. Co_9S_8/Ru@48h by following the solvothermal method required the least value of overpotential (94 mV) compared to the other synthesised materials to produce the benchmark current density in the acidic electrolytic condition of 0.5 M H_2SO_4. Further, the Ru-PBA-derived Ru-Pt nanocomposite exhibited excellent performance towards the HER in 0.5 M H_2SO_4. Among all the synthesised nanocomposites, the catalyst with optimised Pt concentration i.e. Ru@C/$Pt_{0.5}$ required only 32 mV of overpotential to reach the current density of 10 mA cm^{-2}. At higher current density, it outperforms the benchmark catalyst Pt/C. Then the RuCo-PBA-derived Ru-Co nanoalloys with N-doped graphitised carbon synthesised by following the annealing method show good performance towards HER in acidic medium. The temperature optimised electrocatalyst RuCoNA/AB@600 produced 10 mA cm^{-2} of current density by requiring only 129 mV of the overpotential. All these materials reveal good performance and stability in the acidic electrolytic environment. Lastly, NiRu-PBA-derived ruthenium incorporated nickel selenide was synthesised by utilising the solvothermal method. The time-optimised electrocatalyst Ru-$NiSe_2$@48h synthesised at a duration of 48 h, exhibited excellent performance in the alkaline electrolytic condition of 1 M KOH. It required an overpotential of only 84 mV at a current density of 10 mA cm^{-2}. **Figure 7.1** represents the pictorial representation of all the works.

The presence of Ru in the PBA precursor played a significant role in optimising the overall performance of the electrocatalysts. The PBA precursor helps in achieving the homogeneous distribution of nanoparticles throughout the surface of the material. The doping, incorporation, composite formation and alloying of Ru in the derived catalysts with/into other metals as a result of the derivatisation process modulates the electronic structure of the final materials. This further results into the optimisation of the

adsorption/desorption energy of the intermediates during the HER process. This is attributed to the Ru's similar H binding properties as compared to that of Pt. Further, the presence of Ru prevents the aggregation and corrosion of the material particles during the long-term stability measurements.

Future Scope

PBAs, a family of metal-organic frameworks made up of metal ions and cyanide ligands through coordination bonds, have given new life to modern green energy conversion and storage technologies. The thesis examines the use of novel PBA-based materials for the hydrogen evolution reaction (HER). Even though these materials' HER performance has been investigated, there are still opportunities to enhance their performance, some of which are included below.

- **Fabrication of Catalyst and their Engineering:**
  i. Heteroatom-doped carbon rich metal selenides, sulphides, or phosphides can be made using the sealed tube method, which uses a lower temperature than traditional high-temperature furnace heating and doesn't require the use of a solvent or reducing agent (as is typically the case with hydrothermal/solvothermal methods).
  ii. Low Ru-containing materials can be synthesised by varying the concentration during the synthesis of the precursor. This will further lower the catalysts' production cost.
  iii. Strong multi-metal adjustability, together with carbon and nitrogen components in M-N and M-C bonding manner, is the characteristic feature of PBAs. In the future, ongoing efforts should be made to investigate novel single-atom catalysts,

which may demonstrate significant importance and high efficiency in energy conversion devices.

iv. The fabrication of catalysts derived from high-entropy PBA is expected to be revolutionary by embracing the synergistic effects of multimetallic compositions to improve mechanical robustness, electrical conductivity, and catalytic performance. This compositional variability offers remarkable opportunity to optimise catalyst microenvironments and customise active sites when paired with accurate dopant control and heterostructure engineering. Furthermore, by enhancing active surface areas and promoting fast ion transport, nanostructuring techniques like controlled defect introduction and hierarchical pore manufacturing can solve basic kinetic restrictions.

- **Integration of Devices and Scaling Up:**

  All the derived electrocatalysts in the present thesis are studied towards the water reduction reaction. Further, their application towards the energy storage performances and overall water splitting application can also be explored. Additionally, adding PBA-based catalysts to hybrid or tandem systems that combine energy conversion and storage capabilities - like integrated electrolyser storage units and rechargeable metal-air batteries could take advantage of their multifunctionality to improve overall system durability, efficiency, and economic viability.

- **Multidisciplinary Characterisation and Modelling:**

  It is recommended to use highly advanced in-situ characterisation techniques such as Raman spectroscopy, infrared spectroscopy, X-ray absorption spectroscopy, and TEM to gain more understanding of the structure evolution and related mechanism. Additionally, the combination of theoretical computation and experimental findings

will provide important direction for the development of PBAs and the high-performance active materials developed from them for energy-related applications.

- **Metal-Ion Batteries:**

  Ion transmission is facilitated by the hollow architecture of metallic compounds generated from PB/PBA. Previous research has demonstrated that the ability of PB/PBAs to function in various metal-ion batteries depends on the coordination of crystal lattice defects and metal centres. One of the best ways to solve the existing issues is to build a metal compound and carbon nanocomposite formed from PB and PBA. The carbon material can improve the electroactive material's electrical conductivity and effectively reduce strain, such as volume variations during repeated desalination and fossilisation.

- **Supercapacitors:**

  PB/PBAs derivatives have emerged as a potential material for high-property electrochemical supercapacitors due to their superior conductivity, plentiful REDOX reaction sites, and other benefits. The PB/PBAs' metal centres enhance the charge storage capacity by offering Faraday reflexes redox reaction active sites. Wearable supercapacitors can also be made by growing metallic compounds derived from PB and PBA on a substrate. Metallic compounds derived from PB/PBA can be coated on carbon fibre yarn using electrodeposition technology.

- **Artificial Intelligence and Data-Driven Discovery:**

  A paradigm shift in the search for catalytic materials is represented by the growing fields of artificial intelligence and machine learning. AI algorithms may quickly identify promising PBA/PBAD compositions and processing parameters by analysing large experimental and computational datasets to find subtle structure-property connections. The discovery process will be optimised by high-throughput

computer screening and experimental validation, allowing for quick iteration and improvement. Additionally, AI-guided synthesis planning and predictive modelling of electrochemical behaviour will significantly lessen the requirement for trial-and-error methods, increasing efficiency and repeatability.